Transactions of the ASME

FLUIDS ENGINEERING DIVISION
Technical Editor
FRANK M. WHITE (1984)
Executive Secretary
L. T. NELSON (1984)
Calendar Editor
M. F. ACKERSON

Associate Editors
Fluid Machinery
AWATEF A. HAMED (1985)
WILLIAM E. THOMPSON (1984)
Fluid Measurements
THEODORE R. HEIDRICK (1984)
Fluid Mechanics
SHLOMO CARMI (1984)
CHARLES DALTON (1983)
KIRTI N. GHIA (1984)
THOMAS J. MUELLER (1985)
Fluid Transients
M. HANIF CHAUDHRY (1983)
Multiphase Flow
JOHN T. JUREWICZ (1985)
OKITSUGU FURUYA (1984)
Review Articles
RICHARD A. BAJURA (1985)

FOREIGN CORRESPONDENTS
Europe and Russia
JACQUES CHAUVIN
Europe and Russia
JOHN H. HORLOCK
India and Middle East
ARUN PRASAD
Japan and China
YASUTOSHI SENOO

BOARD ON COMMUNICATIONS
Chairman and Vice President
MICHAEL J. RABINS

Members-at-Large
W. BEGELL, W. G. GOTTENBERG,
D. KOENIG, M. KUTZ, F. LANDIS,
J. W. LOCKE, J. ORTLOFF, C. PHILLIPS,
H. C. REEDER, K. REID

President, FRANK M. SCOTT
Executive Director
PAUL ALLMENDINGER
Treasurer,
ROBERT A. BENNETT

PUBLISHING STAFF
Mng. Dir. Publ., J. J. FREY
Dep. Mng. Dir. Publ.,
JOS. SANSONE
Managing Editor, CORNELIA MONAHAN
Editorial Production Assistant,
BETH DARCHI

The Journal of Fluids Engineering (USPS 278-480) is published quarterly for $72 per year by The American Society of Mechanical Engineers, 345 East 47th Street, New York, NY 10017. Second class postage paid at New York, NY and additional mailing offices. POSTMASTER: Send address changes to The Journal of Fluids Engineering, c/o THE AMERICAN SOCIETY OF MECHANICAL ENGINEERS, P.O. Box 3199, Grand Central Station, New York, NY 10163.
CHANGES OF ADDRESS must be received at Society headquarters seven weeks before they are to be effective. Please send old label and new address.
PRICES: To members, $36.00, annually: to nonmembers, $72.00. Single copies, $24.00 each. Add $6.00 for postage to countries outside the United States and Canada.
STATEMENT from By-Laws. The Society shall not be responsible for statements or opinions advanced in papers or . . . printed in its publications (B7.1, Par. 3),

INDEXED by the Engineering Index, Inc.

Journal of Fluids Engineering

Published Quarterly by The American Society of Mechanical Engineers

VOLUME 105 • NUMBER 3 • SEPTEMBER 1983

A Review of Near-Wall Similarity Models in Three-Dimensional Turbulent Boundary Layers

F. J. Pierce
Professor,
Mechanical Engineering,
Virginia Polytechnic Institute
and State University
Blacksburg, Va. 24061

J. E. McAllister
Research Engineer,
Savannah River Laboratory.

M. H. Tennant
Research Supervisor.

E.I. du Pont de Nemours & Company,
Aiken, S.C.

Eleven near-wall similarity models for three-dimensional turbulent boundary layers which have been identified in the literature are reviewed. Each model summary includes a brief review of its derivation, discusses limitations in the derivation, estimates the applicable y^+ range, and compares differences among the models. This review of three-dimensional similarity models was developed as part of a larger study which tests the validity of ten of these different models by comparison with experimental data which includes the direct and simultaneous measurement of the local wall shear stress direction and magnitude in a three-dimensional turbulent flow. A direct force measurement of local wall shear stress is necessary to test the local wall shear-shear velocity relationship, $\tau_0 = \rho q^{*2}$, generally assumed in three-dimensional flows. This review is necessary to acquaint the reader with the similarities and differences among the models tested in companion papers since differences among some of the models are significant, particularly in the coordinate systems of the vector models.

Introduction

Near-wall similarity refers to the experimentally determined "sameness" of velocity profiles in the wall region of a broad class of turbulent boundary layer flows when these are plotted in suitably nondimensionalized coordinates. For two-dimensional turbulent boundary layers[1] the concept of near-wall similarity is well accepted and is reviewed in Pierce, McAllister, and Tennant [1].

For a large portion of the near-wall similarity region where measurements can usually be made with ease (and accuracy) in a 2DTBL, a generally accepted form of the law of the wall is written as

$$u^+ = \frac{1}{\kappa} \ln y^+ + C \tag{1}$$

where $u^+ = u/u^*$, $y^+ = yu^*/\nu$ and $u^* = \sqrt{\tau_0/\rho}$. Unlike a rigorous mathematical similarity analysis, κ and C are experimentally determined constants (that change with roughness and suction/blowing) and sometimes appear to have at least a weak but not well defined dependence on other variables. Apparent systematic variations in κ and C are often within the experimental uncertainty of the data itself and this causes difficulty in fixing the universality of these two parameters and thier possible dependence on other variables. A discussion of the university of the constant appears in reference [1]. Different forms of this equation have been proposed to account for pressure gradients [2, 3, 4, 5], transpiration blowing [6], very small y^+ values [6, 7], rough walls [8, 9, 10], and compressible flow [11].

For the three-dimensional case the concept of near-wall similarity is not so well established. To date, 11 models for the velocity profile in the near-wall region have been found in the literature. Six of these models are simpler scalar models where only one component or the total scalar velocity value is used. The remaining five models recognize in some more elaborate way the vector character of the 3DTBL velocity profile where the vector can turn continuously down to the wall.

The direct force measurement of local wall shear stress is an absolute requirement in any serious study of the near-wall similarity question in three-dimensional flows. This is an essential requirement since the several near-wall similarity models proposed in the literature for the 3DTBL case all require the local wall shear stress (or some component of it) in the necessary nondimensionalizing of experimental data. While the use of indirect wall shear devices has been reported in some 3DTBL flows (e.g., see references [12-19]), all such devices reported to date have used only two-dimensional calibrations in three-dimensional flows. This, in effect, assumes *a priori* and without proof the validity of the two-dimensional near-wall similarity law in three-dimensional flow – and this is wholly unacceptable in any attempt at a definitive study of near-wall similarity in a three-dimensional flow. The use of a two-dimensional calibration in a three-dimensional flow presumes far more than is acceptable in a near-wall similarity study in 3DTBL flows.

In summary, in the 2DTBL case near-wall similarity concerns itself with the experimentally determined sameness of the flow from the wall itself. This excludes the large outer

[1] The short forms 2DBTL and 3DTBL are used as convenient for the two- and three-dimensional turbulent boundary layers.

Contributed by the Fluids Engineering Division for publication in the JOURNAL OF FLUIDS ENGINEERING. *Manuscript received by the Fluids Engineering Division, May 1982.*

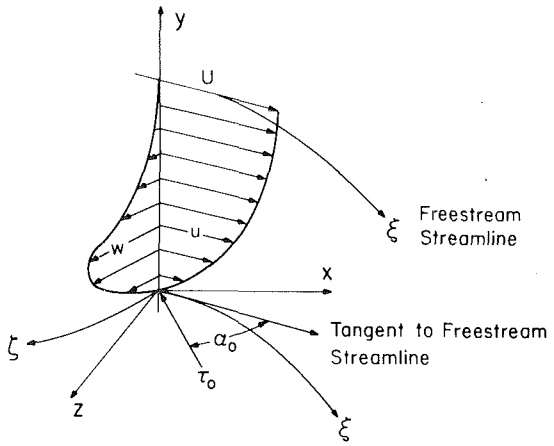

Fig. 1(*a*) Typical pressure-driven three-dimensional boundary layer

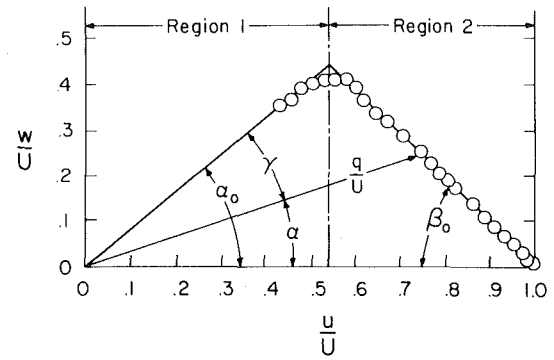

Fig. 1(*b*) Typical polar plot used to construct the six simpler similarity models

portion of the velocity profile where the wake character is strong. Practical experimental difficulties in making accurate and repeatable measurements very close to the wall suggest the exclusion of the very near-wall data in two-dimensional near-wall similarity studies. Since all the three-dimensional near-wall similarity models give the two-dimensional logarithmic form of the law of the wall in the limit of vanishing secondary flow and since in the two-dimensional case an approximate y^+ range of 50 to 300 is suggested for modest pressure gradient flows, it would seem reasonable to focus attention on a similar interval in a first look at the existence of near-wall similarity in the three-dimensional case.

Review of Similarity Models

Three-Dimensional Flows.

1. Scalar Models. The first six models consider only one velocity or velocity component and are described as scalar models. For a three-dimensional turbulent boundary layer an *equivalent* scalar velocity is used in the two-dimensional near-wall similarity law. The logarithmic form of equation (1) would collapse the velocity profiles, with

Table I

Model	$q_{\text{equivalent}}$	q^*
Coles [20]	$q \cos \gamma$	$\sqrt{\tau_0/\rho}$
Johnston [22]	$u/\cos \alpha_0$	$\sqrt{\tau_0/\rho}$
Hournung and Joubert [23]	u	$\sqrt{\tau_0/\rho}$
Pierce and Krommenhoek [12]	u	$\sqrt{\tau_0 \cos \alpha_0/\rho}$
Prahlad [13]	q	$\sqrt{\tau_0/\rho}$
East and Hoxey [14]	$q/\cos\alpha_1$	$\sqrt{\tau_0/\rho}$

$\alpha_1 = \sin^{-1}\{(U_0/K_1 q^*)\sin\beta_1\} - \beta_1$

$\beta_1 = -\tan^{-1}(\delta_2/\delta_1), \quad K_1 = 19.45$

U_0 = a "working section reference velocity"

δ_1, δ_2 = streamwise and transverse displacement thickness

$$q^+ = \frac{q_{\text{equivalent}}}{q^*} = \frac{1}{\kappa} \ln \frac{y q^*}{\nu} + C. \tag{2}$$

where q^* and the various equivalent velocity terms are defined in Table 1 for the six models. Unlike the two-dimensional case, there is no body of experimental evidence relating the wall shear stress to the shear velocity to provide an empirical basis for this identification. At this point one simply seeks a suitable nondimensionalizing constant to collapse a velocity profile – that such a nondimensionalizing constant is uniquely identified with the local wall shear stress is yet to be established. At least for small deviations from two-dimensional flows, this seems to be a reasonable approach, but the assertion that $q^* = \sqrt{\tau_0/\rho}$ is without vertification, and it should be noted that a parameter q^* might collapse the velocity profile without being related to the wall shear stress. It is this identification of the nondimensionalizing shear velocity with the wall shear stress which is the critical assumption in near-wall similarity in the 3DTBL. This identification is empirical and it must be *experimentally* demonstrated that the local wall shear stress is in fact identified with the nondimensionalizing shear velocity. The symbol q^* is used to distinguish the shear velocity in the 3DTBL from its u^* counterpart in the 2DTBL case.

Figure 1(*a*) shows a sketch of a three-dimensional turbulent boundary layer velocity profile skewed in one direction only and Fig. 1(*b*) shows a typical polar plot of such a velocity profile. Both notation and the coordinate systems are also shown. Note that the approximate triangular shape of the polar plot presumes a near-wall collateral flow. Such a polar plot is closely identified with the six scalar similarity models. Note that Fig. 1 is valid only for profiles where the boundary layer skew is unilateral or in one direction only.

The first of the simpler scalar models was introduced by

Nomenclature

C = law of the wall constant
h_1 = streamwise metric coefficient
p = pressure
q = velocity in the xz or $\xi\zeta$ plane
u = streamwise velocity component
u_ξ = velocity component in the local wall shear direction
u^+ = u/u^* or u/q^*
u^* = $\sqrt{\tau_0/\rho}$ for 2DTBL; $\sqrt{\tau_{0\,\text{streamwise}}/\rho}$ for 3DTBL
q^* = $\sqrt{\tau_0/\rho}$ for 3DTBL
w = transverse velocity component in streamwise coordinates
w_ζ = velocity component normal to the local wall shear direction
w^+ = w/q^*
y = distance from wall
y^+ = $u^* y/\nu$ or $q^* y/\nu$ or $q_\xi^* y/\nu$
κ = law of the wall constant
ξ = wall shear coordinate direction
ζ = transverse coordinate normal to the local wall shear direction
ρ = density
τ_0 = wall shear stress
ν = kinematic viscosity

Coles in 1956 [20] who suggested that the velocity vector, $\mathbf{q}=\mathbf{u}+\mathbf{w}$, could be expressed as the sum of a wall, $\mathbf{q}_w$, and a wake, $\mathbf{q}_{\text{wake}}$, component. He reasoned that: (1) near the wall the wake component would be small, (2) that the direction of the mean flow near the surface is also the direction of the wall shear, τ_0, as well as the direction of the wall velocity component, and (3) that the wall velocity component in the direction of the wall shear stress could be described by the two-dimensional logarithmic similarity law.

Coles used the data of Kuethe, McKee, and Curry [21] on a swept airfoil to test his model. Though the velocity profiles seemed to be fairly well represented by Coles' model, no direct or indirect measurements of wall shear stress were included. No y^+ range was suggested for this three-dimensional model but a range similar to the two-dimensional log law would seem a reasonable first estimate.

In 1960 Johnston [22] introduced a second similarity model by noting the existence of an apparently collateral region very near the wall. He proposed that the angle which the near-wall velocity vector has with respect to the freestream approaches the angle α_0 in a presumed collateral region, where α_0 is the limiting wall streamline angle and coincident with the wall shear direction.

When q is along α_0, $u/\cos\alpha_0$ is equal to the physically real q. When q is not along α_0, $u/\cos\alpha_0$ gives a fictitious velocity. Johnston based his model on the experimental measurements of Kuethe et al. [21] discussed previously, Gruschwitz who gave data in a turning passage of a rectangular duct, and his own study over a flat wall bounding a two-dimensional air jet impinging against a perpendicular back wall. He noted from his data that the applicability of equation (1) would be from the outer portion of Region I into the inner portion of Region II of the polar plot in Fig. 1(*b*). It is difficult to specify a specific y^+ range for this model since Johnston's data suggested Region I was within the viscous sublayer while Hornung and Joubert [23] have since shown Region I to have y^+ ranges which were well outside the viscous sublayer.

Both Cole's and Johnston's models suggest that in at least a thin layer the mean flow near the surface is in the same direction as the wall shear stress. Much of the early data plotted as the polar plot in Fig. 1(*b*) shows two, three, or more velocity points in the very near-wall region which appear to have the same direction, suggesting the existence of a collateral near-wall flow. The very careful measurements of Rogers and Head [24] and Hebbar and Melnik [25] using very small instrumentation and emphasizing spatial resolution showed no region of near-wall collateral flow. In addition, Pierce and East [26] and Klinksiek and Pierce [27] have demonstrated with a finite difference solution to a pressure-driven 3DTBL flow where the viscous stresses were retained in the motion equations that no near-wall collateral flow was predicted in a computer solution. Since only the viscous equations were being solved in the very near-wall region where the turbulent stresses vanish, the Reynolds stress model used is immaterial and the existence of a collateral region appears to be inconsistent with the governing equations. Prahlad [28] also presented work supporting these computer results where he noted local streamline turning in the immediate neighborhood of the wall which "suggests the possibility of a fairly large variation in the flow direction within the viscous sublayer." These results cloud the question of the accurate measurement of the limiting wall streamline direction by surface type probes.

In 1963 Hornung and Joubert [23] presented the results of a study of the flow around a circular cylinder with trailing edge standing on a plate. Their measurements seemed to confirm Johnston's polar plot, but in contrast to Johnston's assumption, they found the polar plot peak did not necessarily lie within the viscous sublayer. Hornung and Joubert suggested that the streamwise profile follows the two-dimensional logarithmic similarity law, nondimensionalizing with a shear velocity based on the local wall shear stress as in the earlier two cases. From their work (their Fig. 15) it appears that the equivalent velocity is the streamwise velocity component. They indicated that their model applied "up to the point where the boundary layer becomes yawed," usually to $y^+ < 150$.

A fourth model is a similar model of unknown origin first reported by Pierce and Krommenhoek [12] in 1968. In this case the streamwise component of the three-dimensional velocity profile was assumed to follow the two-dimensional similarity law with a shear velocity defined from a component of the wall shear stress in the streamwise direction.

In 1968 Prahlad [13] introduced a fifth scalar similarity model[2] which assumes that the equivalent velocity is the magnitude of the skewed velocity vector. Prahlad used his own data to verify his model and found good agreement in a two-dimensional law of the wall coordinate system. For adverse or positive pressure gradients the y^+ range of similarity was approximately 20 to 300, while for highly favorable or negative pressure gradients the y^+ range was reduced considerably, depending on the gradient magnitude.

Based on their own experiments in a pressure-driven 3DBTL, East and Hoxey [14] in 1969 proposed yet another similarity model based on the Johnston triangular polar plot. They noted Hornung and Joubert's [23] work which extended Johnston's finding that Region I of Fig. 1(*b*) was within the viscous sublayer and cited their own experimental results showing the triangle apex taking on larger widely varying y^+ values.

2. *Complex Models.* The last five models tend to become more complicated and while not all are in vector form, they explicitly treat the vector nature of the 3DTBL velocity profile in contrast to the first six models which are in essence scalar models. These last models will be discussed briefly in order of perceived ascending complexity. The complications encountered in these last models come about through consideration of some or all of the following: (1) separate consideration of velocity components, (2) pressure gradients, (3) wall shear gradients, and (4) wall shear angle gradients.

In 1976 Chandrashekhar and Swamy [29] proposed a model characterized by separate, two-dimensional-like logarithmic equations for the streamwise and transverse velocity components. Examining the data of East and Hoxey for a pressure-driven 3DTBL, Chandrashekhar and Swamy observed that logarithmic functions could be applied separately to the streamwise and crossflow components of velocity with

$$u^+ = \frac{u}{u^*} A \log_{10} \frac{yu^*}{\nu} + B \tag{3}$$

$$w^+ = \frac{w}{w^*} = C \log_{10} \frac{yw^*}{\nu} + D \tag{4}$$

where $A=5.4$, $B=4.9$, $C=1.0$, and $D=11.8$ with the values of A, B, C, and D determined from the East and Hoxey [14] data. The nondimensionalizing shear velocities u^* and w^* are from the components of the wall shear stress where $u^*=\sqrt{\tau_0 \cos\alpha_0/\rho}$ or $u^* = q^*\sqrt{\cos\alpha_0}$ and $w^* = q^*\sqrt{\sin\alpha_0}$. Note that the streamwise similarity law is essentially identical to the scalar Pierce and Krommenhoek [14] streamwise model.

Chandrashekhar and Swamy show similarity results for the streamwise equation with data in the approximate region of $9 < y^+ < 900$. For $y^+ > 300$ (an approximate value) the data

[2] It was recently pointed out to the authors that H. G. Hornung used this model as early as 1962 in his M.E. Sc. thesis at the University of Melbourne.

exhibit a two-dimensional wake behavior and for $y^+ < 9$ the agreement is poor so that a y^+ range of approximately $9 < y^+ < 300$ would be reasonable from their work. The y^+ range for equation (4) was not specified but an examination of the transverse similarity plots showed data in the range $1 < y^+ < 60$, with the best fit appearing in the $1 < y^+ < 15$ range. For $y^+ > 15$ the data points fell consistently below the analytical model line.

The second of the complex similarity models was proposed by White, Lessmann, and Christoph [30] in 1975 to provide a velocity profile expression for use in their integral boundary layer analysis. This model uses a streamwise or freestream streamline coordinate system and the streamwise profile $u(y)$ is related to the pressure gradient using the mixing length theory to obtain

$$\tau \simeq \tau_0 + \frac{1}{h_1}\frac{\partial p}{\partial \xi} y \simeq \rho \kappa^2 y^2 \left|\frac{\partial u}{\partial y}\right| \frac{\partial u}{\partial y}$$

Introducing a streamwise shear velocity, u^*, based on the freestream component of the wall shear, then $u^+ = u/u^*$, $y^+ = yu^*/\nu$, and the above can be integrated to give

$$u^+ = \frac{1}{\kappa}\left\{2(S - S_0) + \ln\left(\frac{S-1}{S+1}\,\frac{S_0+1}{S_0-1}\right)\right\} \quad (5)$$

where

$$\alpha = \frac{\nu}{\rho u^{*3}}\frac{1}{h_1}\frac{\partial p}{\partial \xi},\quad S = (1+\alpha_\xi y^+)^{1/2},$$

$$\text{and } S_0 = (1 + e^{-\kappa C} y^+)^{1/2}.$$

White et al. noted that attempts at developing a crossflow profile with reasoning as for the u^+ profile were without success. They ultimately suggested a form based on the unilateral hodograph model of Mager [31] with

$$w^+ = u^+ \tan \alpha_0 (1 - y^+/\delta^+)^2 \quad (6)$$

where δ^+ is the nondimensional boundary layer thickness. It was noted that this form does not accommodate bilateral crossflow profiles.

No similarity plots were given by White et al. for this two-component model as it was developed as part of a larger computational study not aimed specifically at near-wall similarity. The approximate y^+ range of equation (5) was inferred by White et al. when they defined S_0 such that for zero pressure gradient the two-dimensional logarithmic law of the wall is returned. This would suggest an initial look at a y^+ range of approximately 50 to 300. There does not appear to be any simple way to estimate the y^+ range for the transverse similarity model.

In 1965 Perry and Joubert [32] developed a near-wall model using similarity arguments and treating the near-wall region as an equilibrium layer. Townsend's (33) local similarity concept led Perry and Joubert to an isotropic eddy viscosity model relating the shear stresses and strain rates in a three-dimensional flow. Their analysis provided for streamwise and transverse pressure gradient effects and gives an integral form to the similarity law with

$$\frac{q_d}{q^*} = \frac{1}{\kappa}\int_1^{y^+} \frac{1}{y^+}[1 + 2\omega\cos\theta + \omega^2]^{1/4}\, dy^+ + C. \quad (7)$$

where $q^* = \sqrt{\tau_0/\rho}$, $\omega = y^+ \alpha\nu/q^{*3}$, $y^+ = yq^*/\nu$ and $\alpha = 1/\rho\,[(\partial p/\partial x)^2 + (\partial p/\partial z)^2]^{1/2}$ is a local pressure gradient parameter. The velocity q_d in equation (7) is the developed velocity or length of arc from the origin in a polar or hodograph figure, that is

$$q_d = \int_0 \left(1 + \left(\frac{dw}{du}\right)^2\right)^{1/2} du.$$

For better consistency with the equations of motion, θ here is the supplement of the angle used in Perry and Joubert [32] and corresponding changes have been made in equation (7).

The effect of the pressure gradient parameter, $\alpha\nu/q^{*3}$, is to cause deviations from the two-dimensional logarithmic line to shift bodily up and down along this line. It should be noted that θ depends on *a priori* knowledge of the direction of local wall shear and pressure gradient.

The upper y^+ limit for this model is identified with the apex of the Johnston polar plot. While Johnston [22] originally set the apex of the polar model as $y^+ \simeq 15$, Hornung and Joubert [23] subsequently found this apex to approach $y^+ \simeq 150$ and still later Perry and Joubert show three-dimensional similarity plots with this apex as high as $y^+ \simeq 2000$. All this suggests a relatively large possible y^+ range for this similarity model, from as low as about 10 to 2000 or more.

In 1973 van den Berg [5, 15, 34] developed a two-component similarity model that includes both pressure gradient and inertial effects. His development begins with the 3DTBL motion equations in Cartesian coordinates oriented in arbitrary directions. Van den Berg noted that a considerable simplification of the acceleration terms and the subsequent mathematics occurs if the similarity model is developed for components of velocity along and normal to the local wall shear stress directions which can be designated ξ and ζ. These are in effect rotated Cartesian coordinates not to be confused with more frequent usage as orthogonal curvilinear coordinates identified with the streamwise flow. This choice of coordinate system requires the *a priori* knowledge of the local wall shear direction.

Utilizing a mixing length hypothesis, nondimensionalizing both the u_ξ^+ and w_ζ^+ components with a shear velocity defined as $q^* = \sqrt{\tau_0/\rho}$, and evaluating inertia terms using his earlier two-dimensional similarity model, van den Berg develops the following two component similarity model with the restrictions that $|\alpha| y^+ << 1$ and $|\beta|(\ln y^+)^2 y^+ << 1$. Thus the form of the model which includes both inertial and pressure gradient effects is restricted to either small pressure gradients and shear gradients or to relatively small y^+ values, and is given by

$$u_\xi^+ = \frac{1}{\kappa}\left[\ln y^+ + \kappa C + \frac{1}{2}\alpha_\xi y^+ + \frac{1}{2}\beta_\xi \frac{(\ln y^+)^2 y^+}{\kappa^2}\right] \quad (15)$$

$$w_\zeta^+ = \frac{1}{\kappa}\left[\alpha_\zeta (y^+ + b) + \beta_\zeta \frac{(\ln y^+)^2 y^+}{\kappa^2}\right] \quad (16)$$

where

$$u_\xi^+ = u_\xi/q^*, \qquad w_\xi^+ = w_\xi/q^*, \qquad \alpha_\xi = \frac{\nu}{\rho q^{*3}}\frac{\partial p}{\partial \xi},$$

$$\alpha_\zeta = \frac{\nu}{\rho q^{*3}}\frac{\partial p}{\partial \zeta}, \qquad \beta_\xi = \frac{\nu}{q^{*2}}\frac{\partial q^*}{\partial \xi}, \qquad \beta_\zeta = \frac{\nu}{q^*}\frac{\partial \phi}{\partial \zeta}$$

and ϕ is the wall shear stress angle relative to the x coordinate and $b = 13$.

When only pressure gradient effects are considered, the van den Berg model is not restricted in pressure gradient magnitude or y^+ values. This analysis is somewhat similar to that of Perry and Joubert, and White, Lessmann, and Christoph.

In 1972 East [35] proposed the most complex three-dimensional similarity model for the general case of compressible flows which requires stress distribution information through the boundary layer and considers the nonalignment of the velocity gradient and shear stress vectors. This last feature appears to have been included to adapt the model into Bradshaw's [36] computational scheme which also treats this nonalignment.

The East model consists of six partial differential equations and two algebraic equations. Two of the partial differential equations were derived by taking into account the variation in the orientation of the shear stress vector near the wall, two

were derived by relating the velocity vector magnitude and magnitude of the velocity gradient, and the remaining two were modifications of Bradshaw's [36] turbulent stress transport equations. For compressible flow two algebraic equations are needed to provide for density and viscosity distributions in the boundary layer. This system of equations was solved numerically by East as part of Bradshaw's program in the range $0 < y^+ < 10{,}000$. No comparisons with experimental data were presented.

East presents results in q^+ and y^+ coordinates for his model for the compressible 2DTBL case and shows excellent agreement with well accepted results for this case, noting that the closeness of fit of other results to his is dependent on the choice of the law of the wall constants κ and C. East also presents graphical results for the incompressible three-dimensional case with strong cross flow. These results are in terms of two parameters, the direction of the viscous shear relative to the wall shear, and the gradient value at the wall of the total shear vector angle. The practical difficulties in measuring these parameters made it impossible to attempt to validate these graphical results. It is worth noting that for East's model no effect on the similarity law for the log-like region is seen until values of $y^+ > 200$, near the upper limit of where similarity is likely to be expected in the three-dimensional case. No experimental data was used to verify this model.

Summary

It is convenient to view the 11 similarity models in two groups. The first group of six models can be described collectively as simple scalar models following the two-dimensional similarity law or law of the wall. In the form of equation (2), the differences among these scalar models are in the equivalent velocity or velocity component which is defined in the q^+ term. Except for the streamwise model, each equivalent velocity is nondimensionalized by a shear velocity assumed to be related to the local wall shear stress as in the two-dimensional case with $q^* = \sqrt{\tau_0/\rho}$. In the limit of vanishing skew, these models all become identical. None of these six models attempts to include explicitly any pressure gradient or inertial effects on the similarity model equation.

In comparing experimental three-dimensional data to any of these six models, the q^+, y^+ pair appropriate to each model is in effect compared to the two-dimensional similarity law – the uniqueness of each of these models lies in the particular definition of q^+ and y^+ for each of the models. Since the analytical or model line for these six scalar models is the two-dimensional law of the wall, any convenient form of this wall law can be used. For example, the model line for all of these six cases could be the one, the two, or the three formula law of the wall, or the Spalding third or fourth order single formula where the role of the u^+ and y^+ variable are interchanged with $y^+ = f(u^+)$.

In general, specific y^+ ranges of applicability of these six scalar models are not given. In the case of the Johnston model subsequent measurements have shown his proposed upper limit of $y^+ = 50$ might well be raised significantly. As a generalization, since these six models are all variations of the logarithmic form of the two-dimensional law of the wall, a first look for similarity in the three-dimensional case would focus on the range of y^+ from approximately 50 to 300, with the upper limit expected to be sensitive to pressure gradient magnitude (Patel [37], Patel and Head [38]) with the exact effect of pressure gradient direction not generally predictable.

In the second group of the five more complex or vector similarity models, the Chandrashekhar and Swamy model is the simplest. Like the scalar models, it treats no explicit pressure gradient effects and it results from the empirical fitting of some 3DTBL data.

The van den Berg, Perry and Joubert, and White, Lessmann, and Christoph models require the explicit input of pressure gradient information. Whether the inclusion of pressure gradient information in these models can help the model's predictive capability is a question which can only be answered by an experimental program. A common feature in the van den Berg, Perry, and Joubert, and White et al. model derivations is the use of mixing length or eddy viscosity hypotheses. The van den Berg model is demanding in that it requires not only the local wall shear direction but the vector shear gradient in the plane of the flow as well. The East model, even in the case of an incompressible flow, contains parameters which, at this time, are judged as extremely difficult if not impossible to measure and hence this model could not be tested here.

A basic but untested assumption common to all eleven proposed models is the existence of some friction velocity q^* that is uniquely related to the local wall shear stress. Unlike the two-dimensional case, there is no body of experimental data relating the wall shear stress to the shear velocity to provide an empirical basis for this identification. Up to this point one simply seeks a suitable nondimensionalizing constant to collapse a velocity profile – that such a nondimensionalizing constant is uniquely identified with the local wall shear stress has not been established. At least for small deviations from two-dimensional flows this seems to be a reasonable approach, but the assertion that $q^* = \sqrt{\tau_0/\rho}$ for 3D flows is without experimental verification, and it should be noted that a parameter q^* might collpase the velocity profiles without being related to the local wall shear stress. It is this identification of the nondimensionalizing shear velocity with the wall shear stress which is the critical assumption in near-wall similarity in the 3DTBL. This identification is empirical and it must be experimentally demonstrated that the local wall shear stress is in fact identified with the nondimensionalizing shear velocity.

Evidence (1) to validate the existence of near-wall similarity in a 3DTBL, (2) of the existence of a shear velocity related to the local wall shear stress as with $q^* = \sqrt{\tau_0/\rho}$, (3) that pressure gradient information is necessary in an adequate similarity model, and/or (4) that mixing length theory is sufficient to develop an adequate similarity model in the three-dimensional flow, is difficult to obtain. *A posteriori* support for one or more of these proposed models would come from the validation of these models using experimental data including the simultaneous direct force measurement of the local wall shear stress magnitude and direction. The authors have completed an extensive experimental program which tests the predictive capability of the first ten of the eleven models reviewed here. Results are presented in the two companion papers.

Conclusions

Eleven proposed models for near-wall similarity for 3DTBL flows have been reviewed. Six of these models are relatively simple scalar models and five are more complex and/or two-component vector models. Ten of these models can be tested as to their validity or predictive capability using measured mean velocity field, wall pressure field, and direct wall shear stress field (magnitude and direction) data. One of the models cannot be tested because of its dependence on two parameters which currently are extremely difficult (if not impossible) to measure. This overview will facilitate the understanding of the results of the test of these models presented in companion papers.

Acknowledgment

This work was initiated under NSF Grant sponsorship and has more recently been supported under NASA Grant NSG2301 monitored by J. G. Marvin at the NASA-Ames Research Center.

References

1 Pierce, F. J., McAllister, J. E., and M. H. Tennant, "Near-Wall Similarity in Three-Dimensional Turbulent Boundary Layers—Part I Model Review," in *Three Dimensional Turbulent Shear Flows*, ASME, New York, 1982.

2 Dean, R. B., "A Single Formula for the Complete Velocity Profile in a Turbulent Boundary Layer," ASME JOURNAL OF FLUIDS ENGINEERING, Vol. 98, Dec. 1976, pp. 723-727.

3 Musker, A. J., "Explicit Expression for the Smooth Wall Velocity Distribution in a Turbulent Boundary Layer," *AIAA Journal*, Vol. 17, No. 6, June 1979, pp. 655-657.

4 Townsend, A. A., "Equilibrium Layers and Wall Turbulence," *Journal of Fluid Mechanics*, Vol. 11, 1961, pp. 97-120.

5 van den Berg, B., "The Law of the Wall in Two- and Three-Dimensional Turbulent Boundary Layers," National Aerospace Laboratory, TR 72111 U, Netherlands, Jan. 1973.

6 Kleinstein, G., "Generalized Law of the Wall and Eddy-Viscosity Model for Wall Boundary Layers," *AIAA Journal*, Vol. 5, No. 8, Aug. 1967, pp. 1402-1407.

7 Spalding, D. B., "A Single Formula for the Law of the Wall," ASME *Journal of Applied Mechanics*, Vol. 83, Sept. 1961, pp. 455-458.

8 Clauser, F. H., "The Turbulent Boundary Layer," *Advances in Applied Mechanics*, Vol. 4, 1956, pp. 1-51.

9 Hinze, J. O., *Turbulence*, 2 ed., McGraw-Hill, New York, 1975.

10 Townsend, A. A., *The Structure of Turbulent Shear Flow*, 2 ed., Cambridge University Press, Cambridge, 1976.

11 White, F. M., and G. H. Christoph, "A Simple Theory for the Two-Dimensional Compressible Turbulent Boundary Layer," ASME Paper No. 72-FE-15, 1972.

12 Pierce, F. J., and D. H. Krommenhoek, "Wall Shear Stress Diagnostics in Three-Dimensional Turbulent Boundary Layers," Interim Technical Report No. 2 ARO-D Project 6858E, Virginia Polytechnic Institute and State University, 1968.

13 Prahlad, T. S., "Wall Similarity in Three-Dimensional Turbulent Boundary Layers," *AIAA Journal*, Vol. 6, No. 9, 1968, pp. 1772-1774.

14 East, L. F., and R. P. Hoxey, "Low-Speed Three-Dimensional Turbulent Boundary Layer Data," Parts 1 and 2, Aeronautical Research Council R & M 3653, 1969.

15 van den Berg, B., "Investigations of Three-Dimensional Incompressible Turbulent Boundary Layers," National Aerospace Laboratory, TR 76001 U, Netherlands, 1976.

16 Dechow, R., and K. O. Felsch, "Measurements in the Mean Velocity and the Reynolds Stress Tensor in a Three-Dimensional Turbulent Boundary Layer Enclosed by a Cylinder Standing in a Flat Wall," Symposium on Turbulent Shear Flows, Pennsylvania State University, University Park, Pa., 1977, pp. 9.11-9.20.

17 Higuchi, H., and D. J. Peake, "Bi-Directional Buried-Wire Skin-Friction Gage," NASA TM 78531, 1978, Ames Research Center.

18 Higuchi, H., and M. Rubesin, "An Experimental and Computational Investigation of the Reynolds Stress in an Axisymmetric Swirling Boundary Layer," AIAA Paper 81-0416, Jan. 1981.

19 Pontikos, N., and P. Bradshaw, "Miniature Pressure Probe for Measuring the Surface-Shear-Stress Vector in Turbulent Flow," *Aero. Quarterly*, Feb. 1981, pp. 43-47.

20 Coles, D., "The Law of the Wake in the Turbulent Boundary Layer," *Journal of Fluid Mechanics*, Vol. 1, 1956, pp. 191-227.

21 Kuethe, A., McKee, P., and W. Curry, "Measurements in the Boundary Layer with Zero Pressure Gradient," NACA TN 1946, 1949.

22 Johnston, J. P., "On Three-Dimensional Turbulent Boundary Layer Generated by Secondary Flow," ASME *Journal of Basic Engineering*, Vol. 82, Mar. 1960, pp. 233-248.

23 Hornung, H. G., and P. N. Joubert, "The Mean Velocity in Three-Dimensional Turbulent Boundary Layers," *Journal of Fluid Mechanics*, Vol. 15, Part 3, 1963, pp. 368-384.

24 Rogers, B. K., and M. R. Head, "Measurement of Three-Dimensional Turbulent Boundary Layers," *The Aero. Journal of the Royal Aero. Society*, Vol. 73, Sept. 1969, pp. 796-798.

25 Hebbar, K. S., and W. L. Melnik, "Measurements in the Near-Wall Region of a Relaxing Three-Dimensional Low Speed Turbulent Air Boundary Layer," University of Maryland, T. R. No. AE-76-1, 1976.

26 Pierce, F. J., and J. L. East, "Near-Wall Collateral Flow in Three-Dimensional Turbulent Boundary Layers," *AIAA Journal*, Vol. 10, No. 3, Mar. 1972, pp. 334-336.

27 Klinksiek, W. F., and F. J. Pierce, "A Finite Difference Solution of the Two- and Three-Dimensional Incompressible Turbulent Boundary Layer Equations," ASME JOURNAL OF FLUIDS ENGINEERING, Vol. 95, Sept. 1973, pp. 445-458.

28 Prahlad, T. S., "Mean Velocity Profiles in Three-Dimensional Incompressible Turbulent Boundary Layers," *AIAA Journal*, Vol. 11, No. 3, Mar. 1973, pp. 359-365.

29 Chandrashekhar, N., and N. V. C. Swamy, "Wall Shear Stress Inference for Three-Dimensional Turbulent Boundary Layer Velocity Profiles," ASME *Journal of Applied Mechanics*, Vol. 43, Mar. 1976, pp. 20-27.

30 White, F. M., Lessmann, R. C., and G. H. Christoph, "A Three-Dimensional Integral Method for Calculating Incompressible Skin Friction," ASME JOURNAL OF FLUIDS ENGINEERING, Vol. 97, Dec. 1975, pp. 550-557.

31 Mager, A., "Generalization of Boundary Layer Momentum Integral Equations to Three-Dimensional Flows, Including Those of a Rotating Disk," NACA TN 2310, 1951.

32 Perry, A. E., and P. N., Joubert, "A Three-Dimensional Turbulent Boundary Layer," *Journal of Fluid Mechanics*, Vol. 22, Part 2, 1965, pp. 285-304.

33 Townsend, A. A., "Equilibrium Layers and Wall-Turbulence," *Journal of Fluid Mechanics*, Vol. 11, 1961, pp. 97-120.

34 van den Berg, B., "A Three-Dimensional Law of the Wall for Turbulent Shear Flows," *Journal of Fluid Mechanics*, Vol. 70, Part 1, 1975, pp. 149-160.

35 East, L. F., "A Prediction of the Law of the Wall in Compressible Three-Dimensional Turbulent Boundary Layers," Royal Aircraft Establishment Technical Report 72178, 1972.

36 Bradshaw, P., "Calculation of Three-Dimensional Turbulent Boundary Layers," *Journal of Fluid Mechanics*, Vol. 46, Part 3, 1972, pp. 417-445.

37 Patel, V. C., "Calibration of the Preston Tube and Limitations on Its Use in Pressure Gradients," *Journal of Fluid Mechanics*, Vol. 23, Part 1, 1965, pp. 185-208.

38 Patel, V. C., and M. R. Head, "Reversion of Turbulent to Laminar Flow," *Journal of Fluid Mechanics*, Vol. 34, Part 2, 1968, pp. 371-392.

F. J. Pierce
Professor
Mechanical Engineering,
Virginia Polytechnic Institute
and State University,
Blacksburg, Va. 24061

J. E. McAllister
Research Engineer,
Savannah River Laboratory.

M. H. Tennant
Research Supervisor.

E. I. du Pont de Nemours & Company,
Aiken, S.C.

Near-Wall Similarity in a Pressure-Driven Three-Dimensional Turbulent Boundary Layer

Ten of eleven three-dimensional near-wall similarity models identified in the literature are evaluated with direct wall shear, velocity field, and pressure gradient data from a three-dimensional pressure-driven boundary layer flow. In a primary focus in the interval $50 < y^+ < 300$ graphical results indicate that six simpler models and the streamwise component of one complex model are adequate for profiles with monotone increasing skew up to about 15 deg. The three remaining complex models provide a better predictive capability (for the main flow component) for monotone increasing skew up to almost 20 deg but these require significantly more input. One of three transverse models shows reasonably good predictive capability. Similar general results also appear for profiles with increasing-decreasing skew as occurs with freestream streamline recurvature with the maximum skew limited to about 10 deg. In a secondary focus in the interval of $y^+ < 50$ there is a very strong tendency for the data to follow the well accepted, two-dimensional like behavior often identified with a transition or buffer region below the two-dimensional log-like law.

Introduction

The motivation for establishing the existence of and limits on near-wall similarity in the 3DTBL[1] case is much the same as in the 2DTBL case. The importance of local near-wall similarity laws in 3DTBL and channel flows grows when one recognizes that the empirical eddy viscosity and mixing length models often rely on wall similarity information, especially in the near-wall behavior. The question is even more critical in current applications of higher order modeling of the Reynolds stresses where in many existing numerical solution techniques only turbulent stresses are included in the motion equations. These techniques exclude any near-wall calculations where viscous stresses exist by using a patch or match to a similarity model. A good knowledge of and limits on local three-dimensional near-wall similarity laws are crucial to these kinds of solution techniques.

The direct force measurement of local wall shear stress is an absolute requirement in any serious study of the near-wall similarity question in three-dimensional flows. The wall shear stress is required since a key question in the test of similarity models in three-dimensional flow is whether or not the local wall shear stress is related to some form of a three-dimensional shear velocity as in $q^* = \sqrt{\tau_0/\rho}$, analogous to the two-dimensional case. This is an essential requirement since the several near-wall similarity models proposed in the literature for the 3DTBL case all require the local wall shear stress (or some component of it) in the necessary non-dimensionalizing of experimental data.

The literature contains at least 11 models proposed to describe near-wall similarity in three-dimensional flows. Six of these models (Coles [1], Johnston [2], Hornung and Joubert [3], Pierce and Krommenhoek [4], Prahlad [5], and East and Hoxey [6]) are relatively simple scalar models using various forms of an equivalent velocity in the two-dimensional similarity law. Five of these models (Chandrashekhar and Swamy [7], White, Lessmann, and Christoph [8], Perry and Joubert [9], van den Berg [10], and East [11]) are more complex and are either two-component models or recognize the vector character of a three-dimensional flow. These 11 models are reviewed in a companion paper by Pierce, McAllister, and Tennant [12]. In the following figures these models are designated by letter symbols as summarized in Table 1.

Ten of these models were tested in their predictive capability by comparison with experimental data including the simultaneous direct force wall shear magnitude and

Table 1 Three-dimensional similarity model designations

Model	Short Forms
Coles [1]	C
Johnston [2]	J
Prahlad [5]	P
Hornung and Joubert [3]	HJ
Freestream Profile Pierce and Krommenhoek [4]	F
East and Hoxey [11]	EH
Perry and Joubert [9]	PJ
van den Berg [10]	B
Chandrashekhar and Swamy [7]	CS
White, Lessmann, and Christoph [8]	WLC

[1] The short forms 3DTBL and 2DTBL will be used as convenient for the three- and two-dimensional turbulent boundary layers.

Contributed by the Fluids Engineering Division for publication in the JOURNAL OF FLUIDS ENGINEERING. Manuscript received by the Fluids Engineering Division, May 1983.

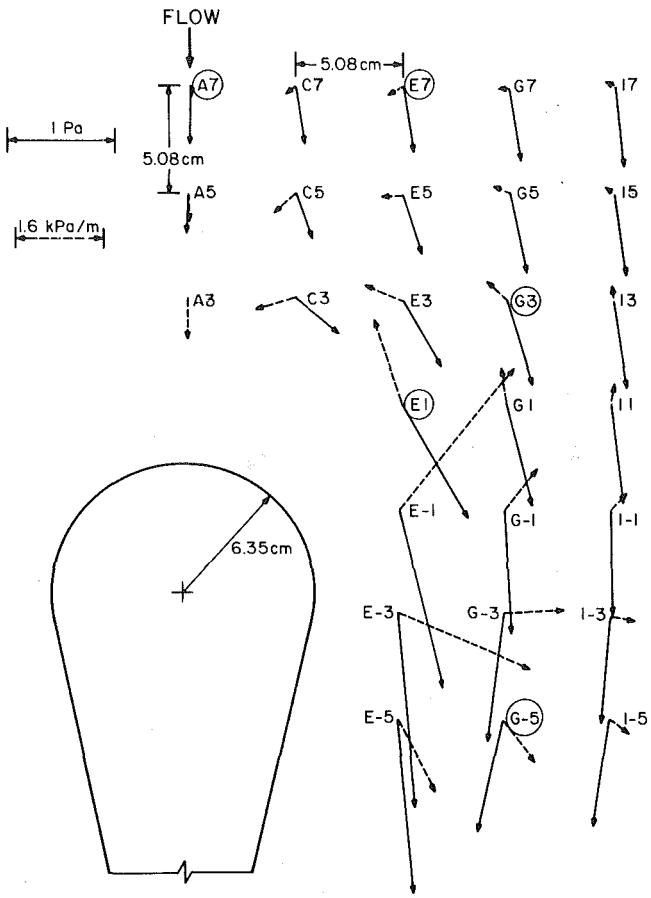

Fig. 1 Flow field showing data stations and the wall shear and *pressure gradient vectors*

direction measurements for a pressure-driven three-dimensional flow generated by a teardrop cylinder placed normal to a flat plate. This flow contains a wide variety of wall shear and wall pressure gradient orientations as shown in Fig. 1. The vectors in this figure are shown to scale. Details on the direct force shear meter are presented in Tennant, Pierce, and McAllister [13] and on the wall shear measurements in McAllister, Pierce, and Tennant [14]. Three of the models tested use wall shear and/or pressure gradient parameters unique to each model as defined in the companion paper [12]. The value of the van den Berg pressure gradient parameter, α, is specified in the captions of Figs. 2–6. Caution is advised on generalizations based on the pressure gradient parameter, α, alone since this parameter does not clearly reflect wall shear-pressure gradient vector orientations.

Measurements of mean velocity field, wall pressure field, and simultaneous direct force wall shear magnitude and direction were made to allow the evaluation of 10 of these proposed models at 25 stations as shown in Fig. 1. Data stations were identified by a letter-number pair. Letter increments correspond to one-inch increments in the transverse direction where the A series is on the flow line-of-symmetry. Numbers represent distances relative to the leading edge of the

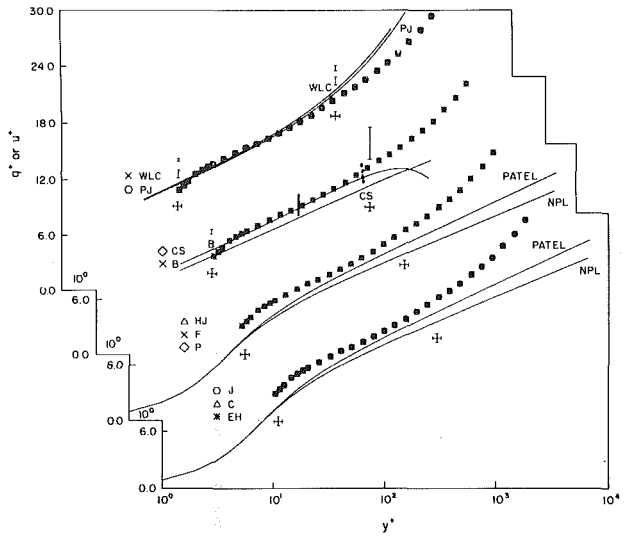

Fig. 2 Simple and complex (mainflow component) model similarity plots for A7, nominal plane of symmetry flow, $|\alpha| = 8.7 \times 10^{-3}$

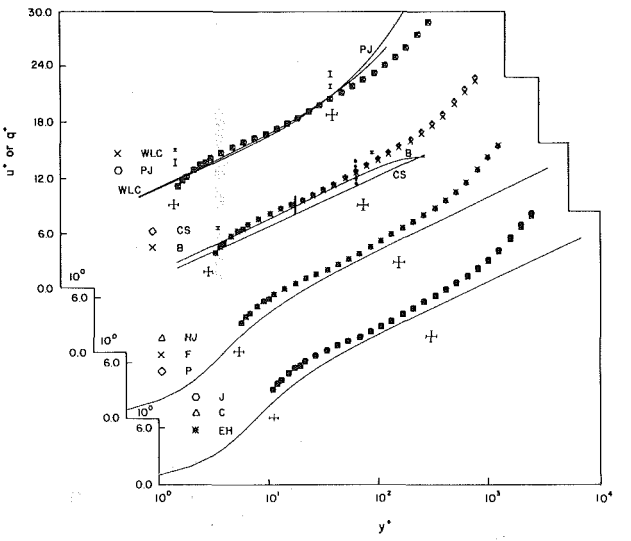

Fig. 3 Simple and complex (mainflow component) model similarity plots for E7, maximum skew 5-15 deg, $|\alpha| = 8.7 \times 10^{-3}$

cylinder with zero corresponding to the leading edge and plus in the upstream direction.

In the following, because of space limitations, comparisons will be made with experimental data at five stations judged representative of the wide variety of flow conditions examined. These results are for stations A7, E7, G3, E1, and G-5. Results for all the stations are contained in Pierce and McAllister [15]. It is noted that in this reference the experimental velocity data points shown for the transverse or w^+ van den Berg model should be multiplied by -1. That is, these data points should be shown as their mirror images with respect to the y^+ axis.

In making an assessment of the validity of any near-wall similarity model for a three-dimensional flow, an early

Nomenclature

q^* = friction velocity, $\sqrt{\tau_0/\rho}$
q^+ = nondimensional developed velocity profile
u^+ = nondimensional mainflow velocity (unique to each similarity model)
w^+ = nondimensional transverse velocity (unique to each complex model)
y = distance from wall
y^+ = nondimensional distance, yq^*/ν
α = pressure gradient parameter, $\nu|\text{grad}\, p|/\rho q^{*3}$
ρ = density
τ_0 = wall shear stress
ν = kinematic viscosity

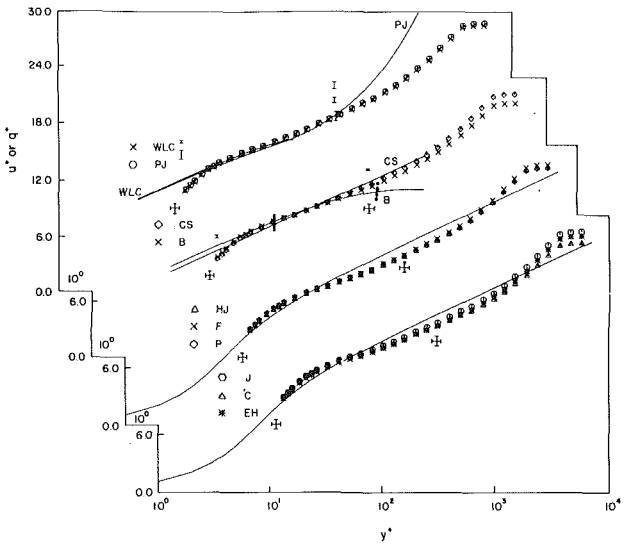

Fig. 4 Simple and complex (mainflow component) model similarity plots for G3, maximum skew 5·15 deg, $|\alpha| = 10.7 \times 10^{-3}$

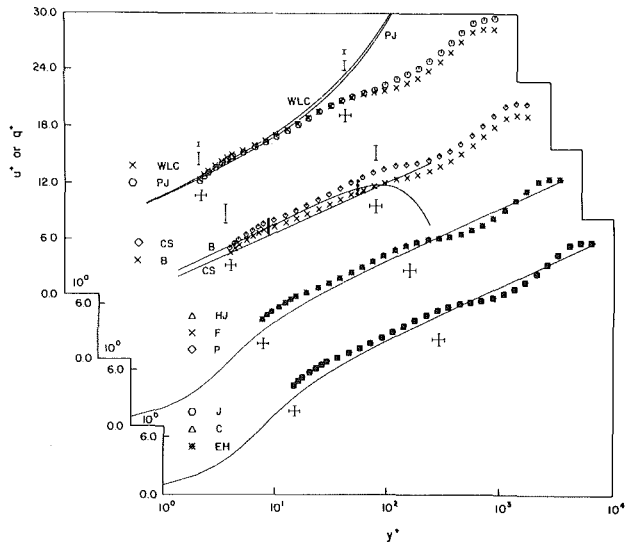

Fig. 6 Simple and complex (mainflow component) model similarity plots for G·5, modest bilateral skewing, $|\alpha| = 14.4 \times 10^{-3}$

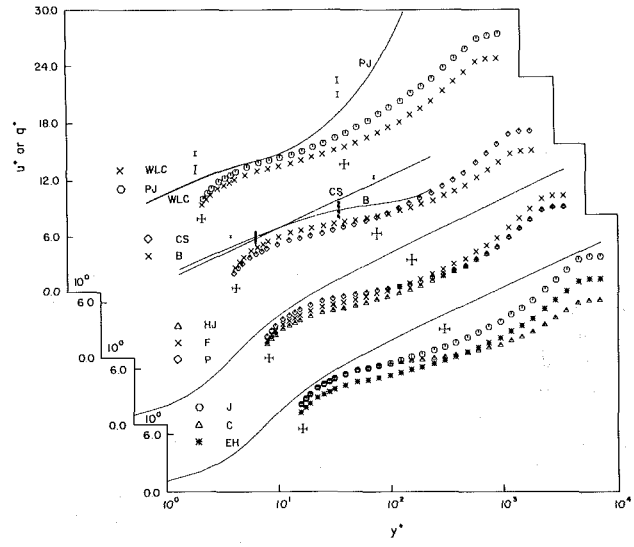

Fig. 5 Simple and complex (mainflow component) model similarity plots for E1, maximum skew greater than 15 deg, $|\alpha| = 19.6 \times 10^{-3}$

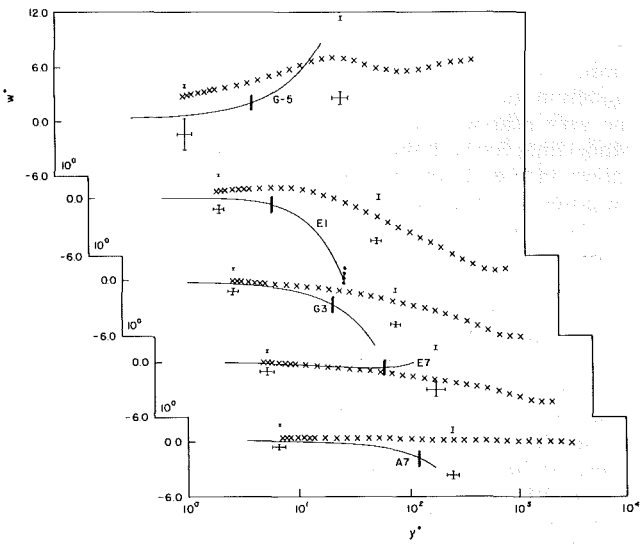

Fig. 7 Transverse van den Berg (B) similarity model

question that arises is that of over what range of y^+ values one might expect to find similarity. In his extensive study of 2DTBL data, Coles [1, 16] suggests that consistent similarity behavior begins at about y^+ of 50 and for moderate pressure gradient flows extends to about 300. Questions on possible inaccuracies in velocity measurements arising from high-turbulence effects, wall interference or wall proximity and other effects, in the range of $y^+ < 50$ for two-dimensional flows would also seem likely for these three-dimensional flows as well. It is also noted that the upper limit of $y^+ \simeq 300$ is reduced in adverse pressure gradient flows and tends to increase in favorable pressure gradient flows.

For the three-dimensional data in this study this two-dimensional experience will be used as a guide in the test for similarity. For the six simpler similarity models, the PJ model, and for the principal flow component of the CS, WLC and B models, the primary focus will be on data in the $50 < y^+ < 300$ range. Clearly this upper limit of 300 must be considered flexible just as in the two-dimensional case. One might also expect that as in the 2DTBL, the pressure gradient will strongly affect the range of similarity for the six simpler models. Some of the more complex models incorporate pressure gradient information and in these cases the agreement with experimental velocity-wall shear data might be expected to be maintained at these higher y^+ values.

It is worth noting, however, that in the early study of three-dimensional flows with indirect wall shear measurements with Preston tubes (which presumes the existence of two-dimensional like near-wall similarity in three-dimensional flows), Prahlad [5] showed a high degree of velocity profile data consistency in the $y^+ < 50$ range (though not with the logarithmic-like law). Such consistency was also found in the velocity data of a few others including Ezekwe [17] and Brown [18]. It will prove to be useful to evaluate these simlarity models in a secondary focus in this $y^+ < 50$ range as well.

In the case of the three models which propose a transverse component of the flow (in the coordinate system unique to each model), there is no firm basis for a choice as to the y^+ region to focus on in looking for near-wall similarity.

The test of the suitability of the ten similarity models evaluated here is a graphic or visual test. In each case an analytical or similarity *model* line is shown as a solid line of q^+ (or u^+ and w^+) vs. y^+. In some cases (PJ, B, and WLC) input from experimental data is required to construct this model line while in the others this line is independent of any

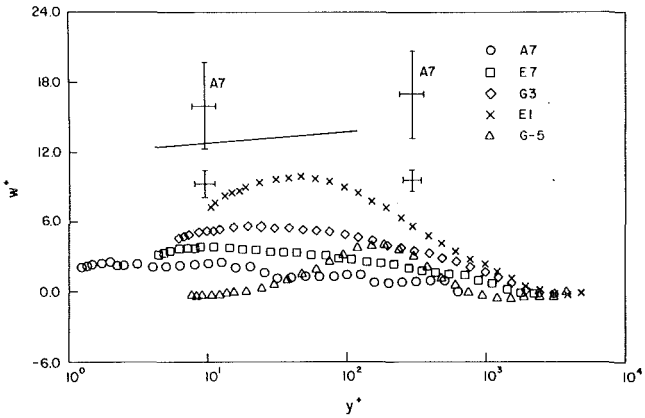

Fig. 8 Transverse Chandrashekhar and Swamy (CS) similarity model

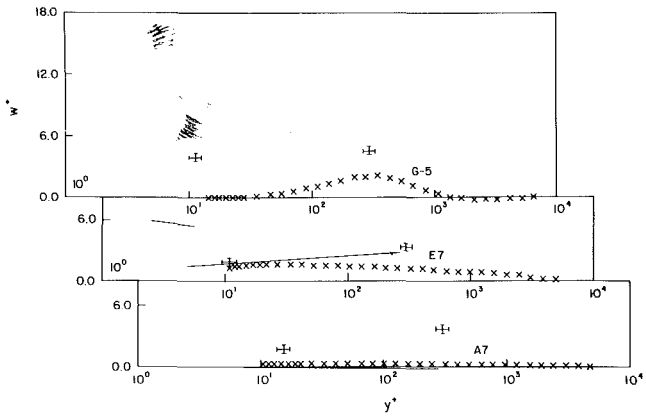

Fig. 9 Transverse White, Lessman, and Christoph (WLC) similarity model

experimental data input. Next, the experimentally measured velocity profile and local wall shear stress are combined as the various models specify to provide pairs of q^+ (or u^+ and w^+) and y^+ coordinates and these are shown as symbols. For the six simpler models the model line is here arbitrarily taken to be the Spalding [19] third-order two-dimensional near-wall similarity law. This choice allows a comparison of these models in the $50 < y^+ < 300$ range of principal focus as well as the very near-wall interval of $y^+ < 50$ of secondary focus. Model lines for both the NPL [20] and Patel [21] constants are shown in Fig. 2 for the six simpler models for comparison purposes with the Patel constants used in all other cases. For the PJ, B, and WLC models only the model lines for the Patel constants are shown. For the CS model specific constants are given by the model authors. Additionally, since for vanishing secondary flow these four models all return the two-dimensional logarithmic law, the q^+ or u^+ model lines are arbitrarily shown in the $5 < y^+ < 1000$ interval. The same lower limit is used for the transverse velocity model lines as well. In some instances the flow parameters were such that the u^+ model line was terminated early and the w^+ model line could not be drawn because of a negative square root problem in the WLC model. The reader is cautioned again that the *two-component similarity models do not use the same* coordinate systems and this should be recognized in any attempted generalizations.

Uncertainties. The q^+ (or u^+ or w^+) and y^+ uncertainties in plotting the results from the same experimental data generally vary among the similarity models because of the different ways the data are manipulated in each of these several models. Additionally, the uncertainties for a given model vary as one moves throughout the boundary layer.

In the three-dimensional case a comparison of experimental data with a similarity model can involve two kinds of uncertainty. Such a comparison requires that for each of the models an experimentally determined q^+ (or u^+ or w^+), y^+ pair be calculated. This uncertainty is here called an *experimental* uncertainty in q^+ (or u^+ or w^+) and y^+.

In the case of the six simpler models and one of the two component models (CS), the analytical q^+ (or u^+ or w^+) and y^+ values (the solid lines) require no experimental data input hence for *given* constants κ and C there is no uncertainty identified with the analytical or model line. However, in the three complex models of WLC, PJ, and B, the analytical or model line requires the input of specific experimentally measured data such as a measured pressure gradient vector, a wall shear vector, or gradients in the magnitude and direction of the wall shear vector. By inputting experimental data into the calculation of a model line there is introduced into that model prediction an uncertainty here called a *model* uncertainty. Note that this model uncertainty is different from what has been called the experimental uncertainty in calculating a q^+ (or u^+ or w^+), y^+ pair from velocity profile and wall shear data, although both these kinds of uncertainties arise from various possible measurement errors. The total uncertainty for the WLC, B, and PJ comparisons in the similarity figures discussed here would combine the model uncertainty and the experimental uncertainty as defined above.

It should be noted that each of these models includes two empirical constants. The question of the uniqueness and accurate specification of these two constants in the two-dimensional case is documented in the literature by the large number of different constants, and these ambiguities should also be recognized here. Finally, the uncertainties reported for the local wall shear measurements include no pressure gradient effects. This is due to the lack of agreement among proposed corrections (and no corrections in pressure gradient flows should be included as one of these possible corrections).

In Figs. 2 through 8 experimental uncertainties in q^+ (or u^+ or w^+) and y^+ are shown *below* the model lines for the data point nearest the wall and at a y^+ value of about 300. Model uncertainties were calculated at fixed y^+ values of 10 and 300 and these uncertainties in q^+ (or u^+ or w^+) are shown *above* the model lines. In the case of the PJ and WLC model lines in Figs. 2 through 6, the WLC model uncertainties are shown above the PJ values. In Fig. 9 only, the experimental uncertainties are shown above the model lines. Computational difficulties did not allow calculation of model uncertainties for this figure. All uncertainties are at nominal 20:1 odds and the model uncertainties reflect the most recent estimates in the data reduction process. The method of Kline and McClintock [22] was used in the calculation of these uncertainties.

Similarity Model Results. In an attempt to organize the comparisons the pressure-driven velocity profiles are divided into four categories based on the skewing of the local velocity vector relative to the local freestream direction. The first category is for the nominal plane of symmetry with skew angles approximately 1 deg or less, the second two categories are for monotone increasing skew angles from 5 to 15 deg, and for more than 15 deg, and the last category is for profiles with first increasing and then decreasing skew angles. In all cases the changes in skew angle are with respect to an increasing distance from the local freestream direction. Of the velocity profiles in this last group, only the profile at station I-5 reported in Pierce and McAllister [15] is (slightly) s-shaped or bilaterally skewed.

The pseudo two-dimensional, nominal plane of symmetry

profiles along the A column, stations A7, A5, and A3, show the total velocity vector skewing less than 1.5 deg. Results for station A7 are shown in Fig. 2. As expected, the six simpler models gave identical results, with the measured velocities larger than the model line predictions. The CS model behaves essentially the same way. The complex models of B, PJ, and WLC, all of which include pressure gradient parameters, all show good agreement for a modest y^+ interval. The possibility of a pressure gradient effect in the wall shear measurement must be noted since the slightly higher q^+ values shown for the simpler models could result from a low wall shear and this would intuitively be the direction of such an error for these stations.

The better agreement for the PJ, WLC, and B models supports the accuracy of the wall shear measurements and suggests that the ability to include pressure gradient effects is important. With the nearly zero skew measured, none of the transverse model comparisons in Figs. 7-9 would appear to be meaningful but are included for completeness.

The second group of profiles considered all showed a monotone increasing skew angle relative to the local freestream direction and limited to 15 deg. The E7 data with a maximum skew of 7 deg is characterized by a positive pressure gradient while the G3 data has a maximum skew of 12 deg and is characterized by negative pressure gradient. The six simpler models give essentially identical results with the adverse pressure gradient results in Fig. 3 riding consistently above the model line, while the favorable pressure gradient results in Fig. 4 tend to fall below the model line. In both these cases the slope of the data is noticeably less than that of the model line. The mainflow CS model is similar to these simple model results for E7 in Fig. 3, but shows better agreement for station G3 in Fig. 4.

The B, PJ, and WLC results in Figs. 3 and 4 are nearly identical and show good agreement with the measured data for the primary y^+ region of comparison. The effect of both the magnitude and the sign of the pressure gradient appears to be well accounted for in these three models for the mainflow velocity components.

For all ten models the data shows a very consistent behavior for $y^+ < 50$ with the data dropping below the log-like model line and following the form of the empirical Spalding two-dimensional line.

For both the E7 and G3 profiles only a modest transverse flow is present. The WLC w^+ model in Fig. 9 shows good agreement for E7 in the $10 < y^+ < 100$ range. The WLC transverse model for G3 could not be evaluated because of a negative argument in a square root quantity. This quantity arose from determining the nondimensional boundary layer thickness by evaluating the freestream model at the boundary layer edge as suggested by the model authors.

For the transverse components of the E7 and G3 profiles the CS model shows very poor agreement. The choice of the principal flow direction in the B model results in an especially small transverse component for y^+ less than 300. The data and model line both agree well, but the small transverse flow offers a questionable test of the transverse model.

The third flow category is represented by the E1 data in Figs. 5 and 7-9. For E1 with its largest skew angle of 25 deg, the six simpler models begin to show significant differences as a result of the way the experimental data are manipulated to generate the equivalent q^+ values. The poor agreement between the data and model line is a clear indication that the mixing length theory which these models implicitly support tends to produce poor results for large skewing. The poor performance of the B, PJ, and WLC models in Fig. 5 should also be no surprise as these models explicitly use a mixing length in their development. It appears that the mixing length model can be useful for skew up to about 20 deg as shown by results in Pierce and McAllister [15] where for station E3 the PJ model and the mainflow component models of B, WLC, and CS show good agreement in the y^+ interval from 50 to 100. Since the pressure gradients for stations E1 and E3 are nearly equal, the breakdown in the model performance appears to lie in the large increase in the skew angle.

The transverse WLC model could not be compared with the data because of the negative square root argument discussed earlier. The CS transverse model results for E3 are as poor as for E1 shown in Fig. 8. The B transverse model results for E3 are much better than the E1 results shown in Fig. 7.

Again, the choice of a coordinate system aligning itself with the wall shear in the B model leads to small transverse velocities in the region where similarity would be expected even for these cases of large skew.

The fourth group of data is for local velocity vector skew angles which first increase and then decrease with respect to the local freestream velocity vector direction. The station G-5 data in Figs. 6 and 7-9 are representative of the model predictions for this data grouping. The data in the lower y^+ range for the six simple models tend to ride high. There is also a small tendency for the velocity data to suggest a lower slope to the log line. In the plane of symmetry case this has been attributed to lateral streamline divergence but such streamline divergence is more difficult to identify clearly in this velocity profile.

The PJ model and WLC mainflow model in Fig. 6 show good agreement over the $50 < y^+ < 200$ range. The transverse WLC model in Fig. 9 shows relatively poor agreement. The CS and B u^+ models also demonstrate relatively good agreement with the data. The transverse B model also shows good agreement with the data while the CS transverse model shows poor agreement.

The van den Berg (B) model tested here includes both inertial and pressure gradient effects and, as such, is restricted to $|\alpha| y^+ << 1$ and $|\beta|(1n y^+)^2 y^+ << 1$ where α and β are pressure and wall shear gradient parameters defined in the companion paper [12]. For the range of these variables in the data reported here this model should be restricted to y^+ values of about 100 or less in all cases of both the u^+ and the w^+ plots. For this model, a short vertical line was placed across both the u^+ and w^+ model lines at the y^+ values where $|\alpha| y^+ = 1$ or $|\beta|(1n y^+)^2 y^+ = 1$ to suggest a generous upper limit beyond which this model including both inertial and pressure gradient effects is not expected to be applicable. A solid line shows the α limit and a dotted line is used to show the β limit.

Summary

For the six simpler models, negligible differences among the model lines exist for skew angles less than about 15 deg. The model predictions are nearly identical but tend to show consistent good agreement with the data only for $y^+ < 50$. Agreement is good in the $50 < y^+ < 300$ range only for the near zero pressure gradients. For skew angles above about 15 deg, the simpler models show poor agreement with the measured data for all y^+ values.

The mainflow CS model tends to agree with the data in the $50 < y^+ < 300$ interval for skew angles under 15 deg where the pressure gradient is near zero or negative. When the pressure gradient is positive, agreement is not as good. The transverse CS model shows poor agreement with the data for all the flow stations shown in Fig. 1.

Good agreement with the data is shown for the PJ and the mainflow B and WLC models in the $50 < y^+ < 300$ interval for both moderately favorable and moderately adverse pressure gradients for skew angles up to about 20 deg. For larger pressure gradients with skew angles under 20 deg, the upper limit on the y^+ range is reduced only slightly for the mainflow component of the B model, with a larger reduction for the PJ

and the mainflow component of the WLC models. Since the B, PJ, and WLC models all incorporate pressure gradient parameters, their better agreement with the data is not surprising. No noticeable benefit appears to result from the inclusion of inertial effects in the B model for the flow conditions encountered here. The failure of the PJ and the mainflow B and WLC models at higher skew angles is probably due to the failure of the mixing length model together with the large pressure gradients generally present with these large skew angles.

Neither the B or WLC transverse flow models is adequate for all the flow conditions encountered here. The nature of the B model formulation results in small transverse velocity component with corresponding small w^+ values.

A comparison of the pressure gradient vector and wall shear vector relative orientation shown in Fig. 1 for A7, E7, G-5, and G3 reveals the importance of the pressure gradient term in a three-dimensional near-wall similarity model. At station A7, the pressure gradient and wall shear vectors are collinear as in an adverse pressure gradient 2D flow, while the angle between these is about vectors 90 deg for E7, about 45 deg for G-5, and about 135 deg for G3. The six simple scalar models show varying degrees of agreement for these three stations while the B, PJ, and WLC models generally show much better agreement. Questions concerning possible pressure gradient effects on the wall shear meter and consequent q^* values are only partially answered in the literature [15]. The better predictive ability of the B, PJ, and WLC models indicates that models with a pressure gradient parameter are needed to accurately predict near-wall flow behavior.

Acknowledgment

This work was initiated under NSF Grant sponsorship and has more recently been supported under NASA Grant NSG2301 monitored by J. G. Marvin at the NASA-AMES Research Center.

References

1 Coles, D., "The Law of the Wake in the Turbulent Boundary Layer," *Journal of Fluid Mechanics*, Vol. 1, 1956, pp. 191–227.

2 Johnston, J. P., "On the Three-Dimensional Turbulent Boundary Layer Generated by Secondary Flow," ASME *Journal of Basic Engineering*, Vol. 82, Mar. 1960, pp. 233–248.

3 Hornung, H. G., and Joubert, P. N., "The Mean Velocity in Three-Dimensional Turbulent Boundary Layers," *Journal of Fluid Mechanics*, Vol. 15, Part 3, 1963, pp. 368–384.

4 Pierce, F. J., and Krommenhoek, D. H., "Wall Shear Stress Diagnostics in Three-Dimensional Turbulent Boundary Layers," Interim Technical Report No. 2, ARO-D Project 6858E, Virginia Polytechnic Institute and State University, Sept. 1968.

5 Prahlad, T. S., "Wall Similarity in Three-Dimensional Turbulent Boundary Layers," *AIAA Journal*, Vol. 6, No. 9, 1968, pp. 1772–1774.

6 East, L. F., and Hoxey, R. P., "Low-Speed Three-Dimensional Turbulent Boundary Layer Data," Parts 1 and 2, Aeronautical Research Council R & M 1653, Mar. 1969.

7 Chandrashekhar, N., and Swamy, N. V. C., "Wall Shear Stress Inference for Three-Dimensional Turbulent Boundary Layer Velocity Profiles," ASME *Journal of Applied Mechanics*, Vol. 43, Mar. 1976, pp. 20–27.

8 White, F. M., Lessmann, R. C., and Christoph, G. H., "A Three-Dimensional Integral Method for Calculating Incompressible Turbulent Skin Friction," ASME JOURNAL OF FLUIDS ENGINEERING, Vol. 97, Dec. 1975, pp. 550–557.

9 Perry, A. E., and Joubert, P. N., "A Three-Dimensional Turbulent Boundary Layer," *Journal of Fluid Mechanics*, Vol. 22, Part 2, 1965, pp. 285–304.

10 van den Berg, B., "A Three-Dimensional Law of the Wall for Turbulent Shear Flows," *Journal of Fluid Mechanics*, Vol. 70, Part 1, 1975, pp. 149–160.

11 East, L. F., "A Prediction of the Law of the Wall in Compressible Three-Dimensional Turbulent Boundary Layers," Royal Aircraft Establishment Technical Report 72178, 1972.

12 Pierce, F. J., McAllister, J. E., and Tennant, M. H., "A Review of Near-Wall Similarity Models in Three-Dimensional Turbulent Boundary Layers," ASME JOURNAL OF FLUIDS ENGINEERING, Vol. 105, September 1983, pp. 251–256.

13 Tennant, M. H., Pierce, F. J., and McAllister, J. E., "An Omnidirectional Wall Shear Meter," ASME JOURNAL OF FLUIDS ENGINEERING, Vol. 102, Mar. 1980, pp. 21–25.

14 McAllister, J. E., Pierce, F. J., and Tennant, M. H., "Direct Force Wall Shear Measurements in Pressure-Driven Three-Dimensional Turbulent Boundary Layers," ASME JOURNAL OF FLUIDS ENGINEERING, Vol. 104, June 1982, pp. 150–155.

15 Pierce, F. J., and McAllister, J. E., "Near-Wall Similarity in a Pressure-Driven Three-Dimensional Turbulent Boundary Layer," Report VPI-E-80.32, Mechanical Engineering, Virginia Polytechnic Institute and State University, Blacksburg, Va., Sept. 1980.

16 Coles, D., "The Young Person's Guide to the Data," *Proceedings Computation of Turbulent Boundary Layers - 1968*, AFOSR-IFP-Stanford Conference, Vol. II, pp. 1–45, 1968.

17 Ezekwe, C. I., "Turbulent Stress Tensor in a Three-Dimensional Boundary Layer," Dissertation, Virginia Polytechnic Institute and State University, Blacksburg, Va., 1974.

18 Brown, K. C., "Three-Dimensional Turbulent Boundary Layers," Dissertation, University of Melbourne, Australia, 1971.

19 Spalding, D. B., "A Single Formula for the Law of the Wall," ASME *Journal of Applied Mechanics*, Vol. 83, Sept. 1961, pp. 455–458.

20 Staff of the N. P. L., "On the Measurement of Local Surface Friction on a Flat Plate by Means of Preston Tubes," N. P. L. Report No. 3185, May 1958.

21 Patel, V. C., "Calibration of the Preston Tube and Limitations on Its Use in Pressure Gradients," *Journal of Fluid Mechanics*, Vol. 23, Part 1, 1965, pp. 185–208.

22 Kline, S. J., and McClintock, F. A., "Describing Uncertainties in Single-Sample Experiments," *Mechanical Engineering*, Jan. 1953, pp. 3.

F. J. Pierce
Professor,
Mechanical Engineering,
Virginia Polytechnic Institute
and State University,
Blacksburg, Va. 24061

J. E. McAllister
Research Engineer,
Savannah River Laboratory,
E. I. du Pont de Nemours & Company,
Aiken, S. C.

Near-Wall Similarity in a Shear-Driven Three-Dimensional Turbulent Boundary Layer

Ten of eleven proposed three-dimensional similarity models identified in the literature are evaluated with direct wall shear, velocity field, and pressure gradient data from a three-dimensional shear-driven boundary layer flow. Results define an upper limit on velocity vector skewing for each model's predictive ability. When combined with earlier results for pressure-driven flows, each model's predictive ability with and without pressure gradients is summarized.

Introduction

The variety of three-dimensional near-wall similarity models presented in the literature is documented in Pierce, McAllister, and Tennant [1] where eleven models are reviewed.

The predictive abilities of ten proposed three-dimensional similarity models were previously evaluated for a pressure-driven flow (Pierce, McAllister, and Tennant [2] and Pierce and McAllister [3]). This paper evaluates these same ten models using experimental data from a shear-driven three-dimensional flow. The flow is described as shear-driven or shear-dominated to contrast it with the flow described in the earlier work [2, 3] where secondary flow is dominated by pressure forces and hence described as pressure-driven. In the earlier work the authors have examined the predictive ability of these models in a pressure-driven flow over a variety of pressure gradients and wall shear orientations. This shear-driven flow approaches a downstream near-zero pressure gradient condition. The model evaluations with the shear-driven data can provide some insight into each model's ability to predict the local velocity magnitude and direction in a three-dimensional turbulent boundary layer without the added complexity of the larger pressure gradients reported in reference [2]. Comparing the model evaluations from this flow with the model evaluations from the earlier pressure-driven flow should provide the reader with a broader perspective as to the predictive abilities and restrictions of the proposed models tested for two broad classes of three-dimensional flows.

The need for the direct measurement of wall shear stress magnitude and direction by a floating element device, the key to an experimental study of three-dimensional similarity, raises the question of possible pressure gradient effects on the measured wall shear data. The presence of minimal (near-zero) pressure gradients in portions of the shear-driven flow suggests less uncertainty in the necessary direct wall shear measurements. The results of Pierce, McAllister, and Tennant [2] and Pierce and McAllister [3] suggest that any pressure gradient effects on the direct force-sensing floating element shear meter (Tennant, Pierce, and McAllister [4]) used to take these wall shear measurements are small. A shear-driven flow should reduce any possible pressure gradient effects on the wall shear data and result in greater confidence in the model comparisons.

Contributed by the Fluids Engineering Division for publication in the JOURNAL OF FLUIDS ENGINEERING. Manuscript received by the Fluids Engineering Division, May 1983.

Flow Geometry

The three-dimensional shear-driven flow was created by a 3.8 cm high step yawed at a 30 deg angle. Figure 1 shows the step, the data stations, and the wall shear and pressure gradient vector directions. The limiting wall velocity and wall shear vectors are shown in Fig. 2. Note that the pressure gradient, wall shear, and nearest wall velocity vectors in Figs. 1 and 2 are shown to scale. Values of the van den Berg [5] parameter, α, are given in the captions of Figs. 3–7. The nominal reattachment line is shown as a broken line paralleling the step trailing edge. The tunnel used to obtain the experimental data is described in McAllister, Pierce, and Tennant [6], the floating element device in Tennant, Pierce, and McAllister [4], and the remaining equipment in Pierce and McAllister [3].

The data stations in Fig. 1 are located on a 5.08 cm grid. The station identification consists of two groups of digits where the first group indicates the distance in inches from the tunnel centerline while the second number indicates the centerline distance from the step's trailing edge. Measurements indicated a nominal 2DTBL two meters upstream of the step. Reattachment behind the step was estimated as at 10.2 cm behind the step on the tunnel centerline and paralleling the step by observing yarn tufts. The stability of the wall shear meter behavior and the velocity measurements at station 0 6 was consistent with the flow visualization results. Velocity profiles indicated that spanwise invariance did not exist downstream of the step.

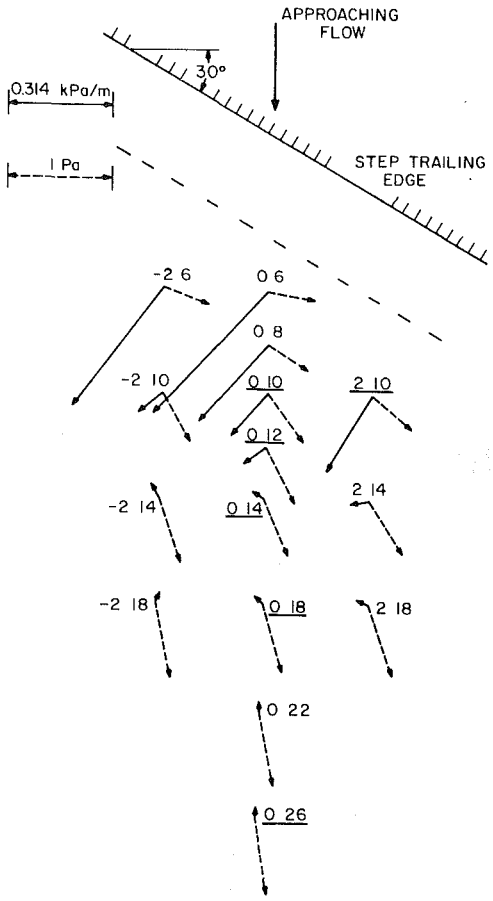

Fig. 1 Flow geometry with wall shear vector and pressure gradient vector map

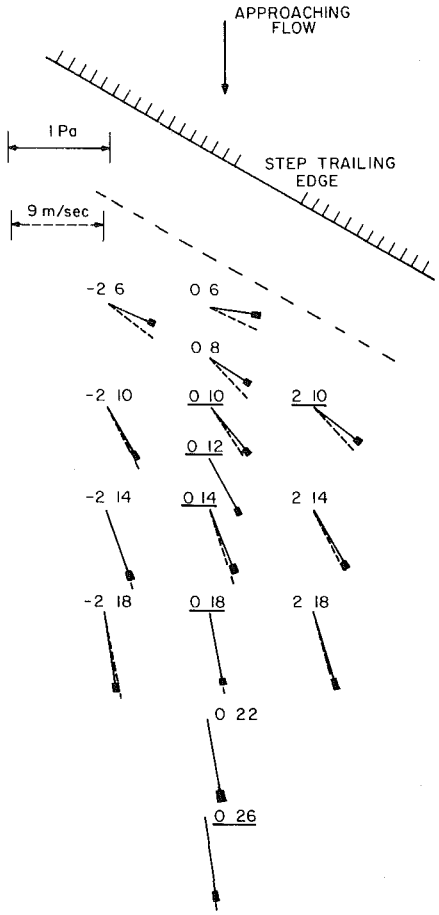

Fig. 2 Wall shear vector and limiting wall velocity map

Experimental Results

Velocity profiles, direct wall shear, and pressure gradient data were obtained for the step flow in Fig. 1. The velocity profiles nearest the step exhibited 67 deg of skew and in general were characteristic of other velocity data behind steps. The local freestream directions for each velocity profile were nominally aligned with the tunnel centerline, regardless of the distance behind the step.

The wall shear vector orientations in Fig. 1 indicate a gradual increase in magnitude as one initially moves downstream from the step. Simultaneously, the vector direction gradually relaxes from its initial skew relative to the tunnel centerline and approaches a nominally two-dimensional flow circumstance where the tunnel centerline and wall shear stress vectors are aligned.

In comparing the wall shear and limiting wall velocity vectors in Fig. 2, the flow stations closest to the step show large angle differences between the two vectors. The limiting wall velocity vectors were measured at 0.254 mm from the wall with a miniature claw probe. The velocity angle uncertainty of ± 1.0 deg and the wall shear stress uncertainties, which are shown as curvilinear rectangles at the tip of the stress vectors in Fig. 2, cannot account for these angle differences for all the data stations. These results support the earlier work reported by Pierce, McAllister, and Tennant [2] which suggests the existence of noncollateral, near-wall flow in pressure-driven three-dimensional turbulent boundary layers where strong pressure gradients exist. Further downstream from the trailing edge (for the series 14 stations and downstream) the pressure gradient becomes essentially zero and the wall shear and nearest wall velocity direction become more nearly collateral, and well downstream the wall shear and velocity vectors gradually align themselves as expected for a skewed flow relaxing to a two-dimensional state in a zero pressure gradient field.

The pressure gradient vector field downstream of the step in Fig. 1 shows that the vectors closest to the step have the largest magnitudes and are nominally normal to the step trailing edge. The pressure gradient vectors quickly reduce to the nominal tunnel two-dimensional pressure gradient (near-zero) value and direction of − 14 Pa/m at station 0 26. When compared to the pressure gradient magnitudes in Pierce, McAllister, and Tennant [2] which in a first approximation were assumed to have a small effect on the wall shear data, the pressure gradient magnitudes in this study are from 4 to 100 times smaller for most flow stations. Any possible pressure gradient effects on the wall shear data in McAllister, Pierce,

Nomenclature

q^* = friction velocity, $\sqrt{\tau_0/\rho}$
q^+ = nondimensional developed or velocity magnitude profile
u^+ = nondimensional mainflow velocity (unique to each similarity model)
w^+ = nondimensional transverse velocity (unique to each complex model)
y = distance from wall
y^+ = nondimensional distance, yq^*/ν
α = pressure gradient parameter, $\nu \mid \text{grad}\, p \mid /\rho q^{*3}$
ρ = density
τ_0 = wall shear stress
ν = kinematic viscosity

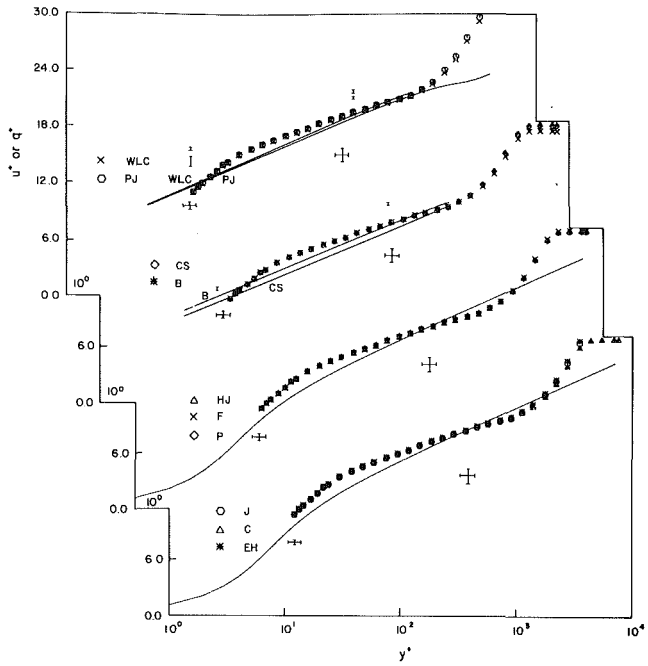

Fig. 3 Simple and complex (mainflow component) model similarity plots for station 0 26, maximum skewing less than 15 deg, $|\alpha| = 0.37 \times 10^{-3}$

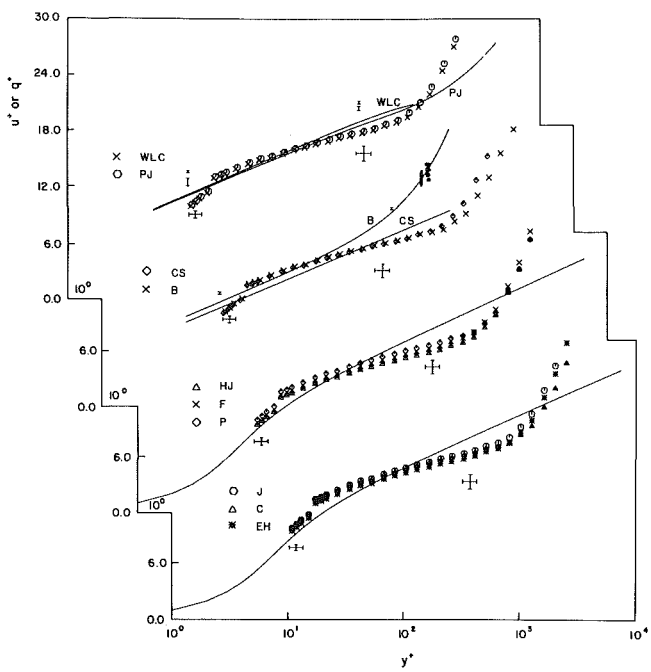

Fig. 4 Simple and complex (mainflow component) model similarity plots for station 0 18, maximum skewing less than 15 deg, $|\alpha| = 0.69 \times 10^{-3}$

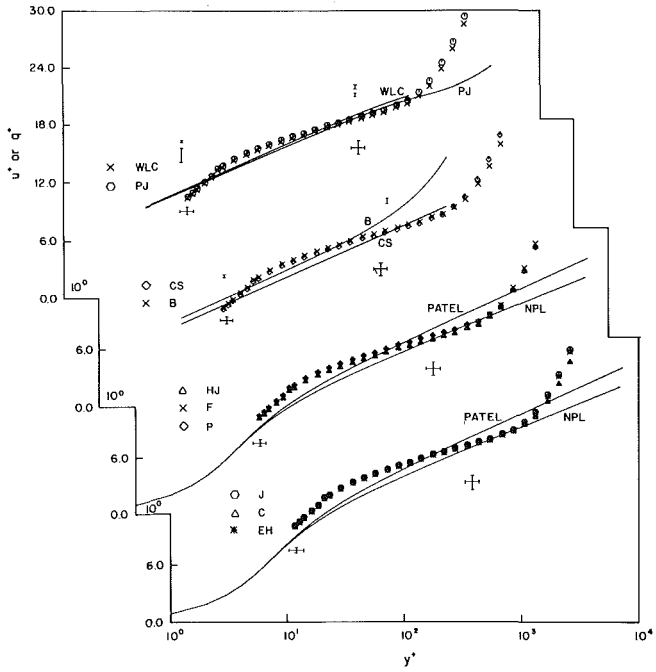

Fig. 5 Simple and complex (mainflow component) model similarity plots for station 0 14, maximum skewing less than 15-30 deg, $|\alpha| = 1.61 \times 10^{-3}$

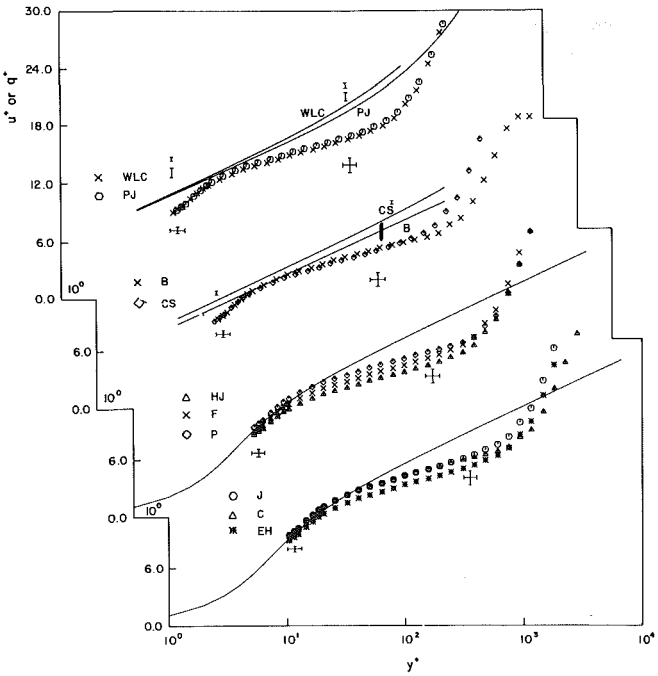

Fig. 6 Simple and complex (mainflow component) model similarity plots for station 0 12, maximum skewing less than 15-30 deg, $|\alpha| = 3.2 \times 10^{-3}$

and Tennant [6] would presumably be essentially negligible for much of the shear-driven flow data reported here.

Background

In discussing the ten similarity models, the same model notation used in the companion paper of Pierce, McAllister, and Tennant [2] is used. Data are shown as symbols and the analytical or model lines are shown as solid lines in the figures. As discussed in the companion paper, one must consider both an experimental and a model uncertainty in this visual comparison. In Figs. 3 through 10 experimental uncertainties in q^+ (or u^+ or w^+) and y^+ pairs are shown below the model lines for the data point nearest the wall and at a y^+ value of about 300. Model uncertainties were calculated at fixed y^+ values of 10 and 300 and these uncertainties in q^+ (or u^+ or w^+) are shown above the model lines. In the case of the PJ and WLC model lines in Figs. 3 through 8, the WLC uncertainties are shown above the PJ values. In Fig. 3 the results for the six simpler models are compared to the model lines for both the NPL and Patel constants, κ and C. In all other cases only the model line for the Patel constants is shown. Computational difficulties did not allow calculation of model uncertainties for Fig. 11. All uncertainties are at

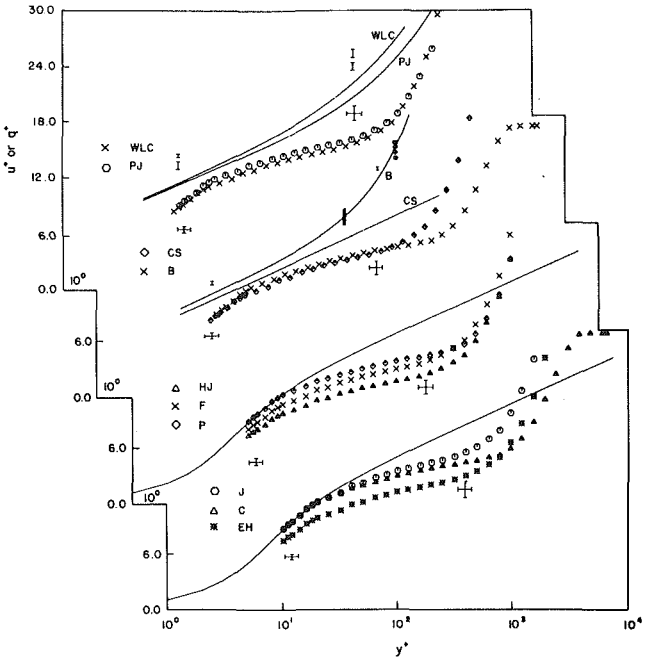

Fig. 7 Simple and complex (mainflow component) model similarity plots for station 0 10, maximum skewing less than 30 deg, $|\alpha| = 7.88 \times 10^{-3}$

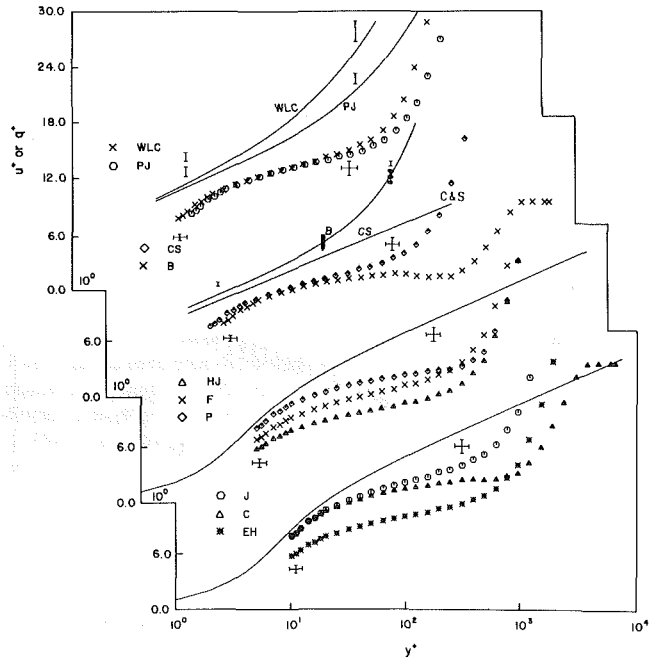

Fig. 8 Simple and complex (mainflow component) model similarity plots for station 2 10, maximum skewing less than 30 deg, $|\alpha| = 13.6 \times 10^{-3}$

nominal 20:1 odds and the method of Kline and McClintock [7] was generally followed in the calculation of these uncertainties.

Similarity Model Comparisons

The complex model comparisons are divided into three arbitrary groups based on the total skewing of the local velocity vector relative to the freestream direction and note that only monotone increasing skewing occurs in these data. The first group of profiles is for maximum skew angles ranging from 0 to 15 deg, the second group is for maximum

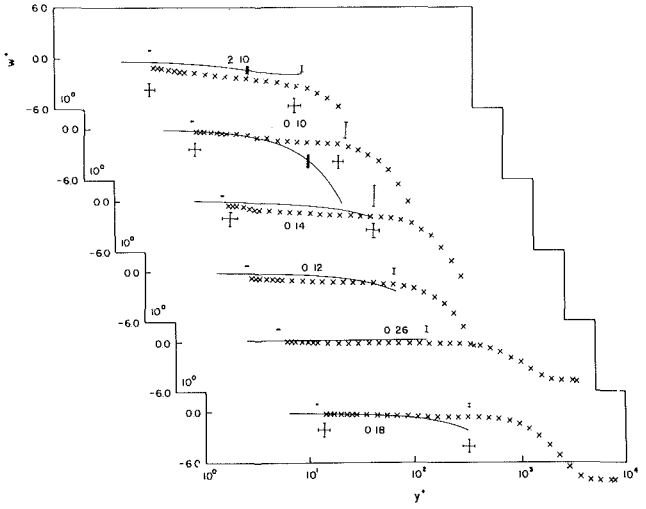

Fig. 9 Transverse van den Berg (B) similarity model

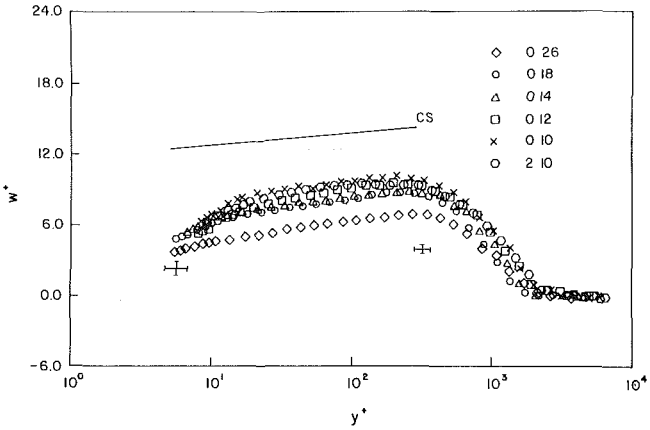

Fig. 10 Transverse chandrashekhar and Swamy (CS) similarity model

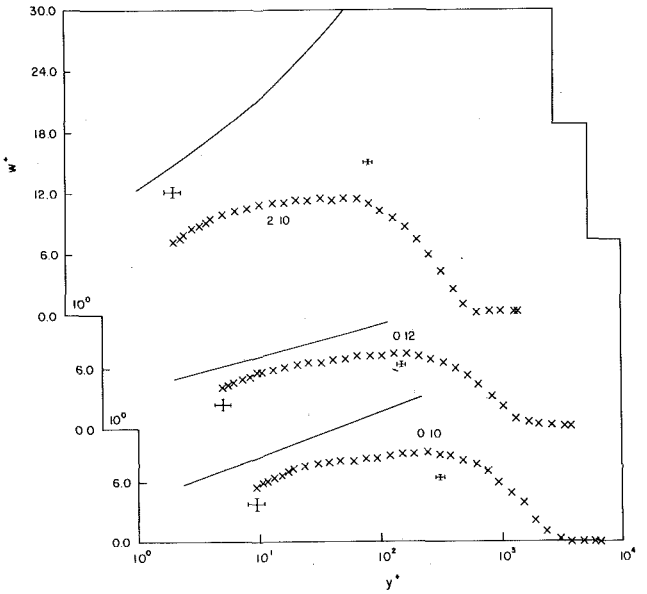

Fig. 11 Transverse White, Lessman, and Christoph (WLC) similarity model

skew between 15 to 30 deg, and the last group is for maximum skew over 30 deg. Two representative data stations for each of the three skewing categories are presented here while similarity plots for all the data are reported in McAllister [8]. As in Pierce, McAllister, and Tennant [2], for the van den

Berg model, a short vertical line was placed across both the u^+ and w^+ model lines at the y^+ values where $|\alpha| y^+ = 1$ or $|\beta| (\ln y^+)^2 y^+ = 1$ to suggest a generous upper limit beyond which this model including both inertial and pressure gradient effects is not expected to be applicable. A solid line shows the α limit and a dotted line is used to show the β limit. It should be noted that the region of validity of this model is considerably expanded in much of this shear-driven flow. As in the earlier reported pressure-driven flow results, the pressure gradient limit is generally the critical restriction. However for this shear-driven flow the pressure gradients gave an upper limit on y^+ of at least 300 at station 0 12, and greater than 600 for the other three downstream profiles. Thus the range of the test of the validity of the B model was considerably extended.

The six simpler models can be discussed collectively for the three skew groupings. Figures 3–8 show that the models generally show a poor level of agreement for the data over the $50 < y^+ < 300$ interval with the slope of the data less than the model line and with the data dipping below the model line. This behavior is not unlike some reattaching two-dimensional flows indicating this behavior may not be caused by three-dimensional effects. For the $y^+ < 50$ range, the data tends to follow the damped mixing length model line. For skew of less than 30 deg the six models show similar levels of weak agreement with the model lines. For larger skew angles, only the P, C, and J models show reasonable agreement. The general level of agreement seen here is similar to that shown for these models in the pressure-driven flow described in Pierce, McAllister, and Tennant [2], and the behavior is typical of the plane of symmetry and small monotone skew cases. In that latter case the existence of a pressure gradient effect possibly resulting in a too-low measured wall shear was considered. Here in a near-zero pressure gradient field, such an effect is more difficult to accept. Agreement in the $50 < y^+ < 300$ range could be improved by changing the slope of the model line but it is felt that the rapid drop-off in the velocity with increasing wall distance, while somewhat similar to the earlier described plane of symmetry flow, is here more a reflection of the larger local velocity defect that the step develops in the lower portions of the velocity profile. As is well known the outer regions of a boundary layer flow have a slower response and longer memory to such disturbances with the near-wall flow responding much more rapidly. The PJ and mainflow components of the WLC, CS, and B models somewhat underpredict the data.

For monotone increasing skew with maximum skew angles less than 15 deg, Figs. 3 and 4 show that the PJ and the mainflow components of the WLC, B, and CS models show similar results. This is partly due to the small value of the pressure gradient and its corresponding small effect on the three models which include this effect. These four models tend to underpredict the measured data with somewhat poorer agreement than in the pressure-driven flow for similar skew conditions and somewhat larger $|\alpha|$ values.

The WLC transverse model predictions could not be plotted for either station 0 26 or 0 18 because of the negative square root problem discussed in reference [2]. The CS transverse model comparisons in Fig. 10 are poor while the B transverse model comparison in Fig. 9 for station 0 18 is relatively good.

Station 0 14 (20 deg maximum skew) and station 0 12 (25 deg maximum skew) fall into the second skewing group. For station 0 14, Fig. 5 shows the data agrees with the B model only in the $20 < y^+ < 100$ range, while the PJ and mainflow WLC models increase this range to $20 < y^+ < 300$. The mainflow CS model shows only fair agreement with the data.

The poorer agreement for the complex models for station 0 12 in Fig. 6 reflects the breakdown in the predictive ability for the larger skew angles. The station E1 (also with 25 deg of maximum skew) results in reference [2] are similar to the poor agreement shown in Fig. 6 here. Since station E1 has a favorable pressure gradient while station 0 12 has an adverse pressure gradient, the breakdown in the complex models predictive ability is dependent on the magnitude rather than the direction of the pressure gradient. The results indicate the models tend to lose their predictive ability for maximum skewing above 20 deg.

The transverse CS model in Fig. 10 shows poor agreement for both the 0 14 and 0 12 data in contrast to the B transverse model for station 0 14 which shows good agreement. The WLC transverse model could only be calculated for station 0 12 and the agreement in Fig. 11 is only fair.

Stations 0 10 (35 deg skew) and 2 10 (44 deg skew) fall into the last skew category. Figures 7 and 8 show that none of the models shows good agreement with the data for these stations.

As for the previous data stations, the CS transverse model predictions for stations 0 10 and 2 10 are poor. The WLC model predictions in Fig. 11 are also poor but the B transverse model predictions in Fig. 9 are relatively good. For the large transverse velocities for these data, the B transverse model agreement is significant and should not be overlooked. However, the coordinates of this model tend to result in small transverse velocities in the y^+ regions of expected similarity.

Summary

The six data stations discussed in this paper all had monotone increasing skew from 7 to 45 deg. As for the pressure-driven flows described in Pierce, McAllister, and Tennant [2], model and data agreement generally deteriorated with increasing skew angle. This would suggest that the equilibrium concepts and mixing length theory in which these models find their origin are not adequate for three-dimensional turbulent boundary layers with large and rapidly changing crossflow.

The six simpler models show generally poor agreement with the data in the range of primary focus. Only for station 0 12 does good agreement occur, but in the secondary region of comparison, $y^+ < 50$. While the simpler models show somewhat better agreement with the data for the pressure-driven flow [2], these models could not predict the large velocity defect behind the step.

For the complex models, the mainflow CS model shows poor agreement with the data. The PJ and mainflow WLC and B models tend to show better agreement with the data for maximum skewing up to 20 deg. Above 20 deg maximum skewing, none of the complex models shows good agreement with the data, regardless of the pressure gradient magnitude or direction. Poor predictive ability by the PJ and mainflow WLC and B models is not attributed to the increased pressure gradient magnitude of station 0 10 when compared to station 0 12 since pressure gradients of similar magnitudes in the pressure-driven flow did not result in such relatively poor model performance. The pressure-driven flow results in Pierce, McAllister, and Tennant [2] indicate that pressure gradient input is necessary for more accurate model predictions, yet the pressure gradients in this study are apparently small enough that their magnitude and/or direction is immaterial.

The transverse CS and WLC models show poor agreement with the data for all flow stations. Within the experimental uncertainties, the transverse B model shows the best agreement with the data.

Restrictions noted in at least some of these similarity model derivations support the limited predictive ability found here and in the companion paper on pressure-driven flows. For example, van den Berg limits his model to small skew in the sense of limited pressure and wall shear magnitude gradients.

While it is one of the better complex models tested, its poor predictive ability at stations 0 10 and 2 10 is not surprising since the y^+ upper limit of applicability is relatively small. A similar reduced range of applicability with a similar decrease in predictive ability was also noted in the pressure-driven flow. The region of y^+ within which this model is proposed as valid is shown in the various figures. For the four downstream minimum pressure gradient profiles the range of this model for both u^+ and w^+ is quite large. While not explicitly stated for other models, it appears that similar restrictions on at least skew magnitude, if not pressure gradient, should be considered as well.

The CS and six simpler models do not predict three-dimensional flows as well as the WLC, B, and PJ models. These latter three models take into account significantly more flow information than the CS or six simpler models. In particular, the six simpler models seem to agree reasonably well with all the data for the lower range of $y^+ < 50$ which is the boundary layer region where the velocity vector turns through a relatively smaller range and is thus more nearly collateral, i.e., a scaler-like quantity. Since these models are scalar in nature, this small y^+ region agreement is not surprising. What is somewhat surprising here is the strong consistency in much of the data for modest skewing (< 20 deg), and in some instances even for stronger skewing, to follow the two-dimensional-like buffer or transition region similarity models in the very near-wall flow. In the two-dimensional case data in this very-near wall region is characterized by more scatter and uncertainty attributed to various near-wall effects such as shear gradients, low Reynolds number effects, wall proximity effects, turbulence effects, etc. This consistency in very near-wall flow is also noted in the work of Prahlad [9], Ezekwe [10], Brown [11], and some others.

Discussion and Conclusions

In comparing the pressure driven results from Pierce, McAllister, and Tennant [2] and the shear-driven results of this study, the following conclusions may be drawn.

For monotone increasing skew:

1. With skewing up to about 15 deg, all of the simpler models, the PJ, and the mainflow component of the complex models are useful over modest y^+ ranges. Both the WLC and B transverse models are reasonable, but the transverse velocity components are small for this range of skew angles.
2. For skewing greater than 15 deg, the six simpler models deteriorate in their predictive ability, although the HJ, P, and C models offer some utility in the $y^+ < 50$ range. The PJ and the mainflow WLC and B models are somewhat better than the CS model for a limited y^+ range with the models which require pressure gradient input tending to predict the near-wall profile trends more accurately. The B transverse model is somewhat better than the WLC model, while the CS transverse model is generally poor.
3. For skewing above 20 deg, none of the 10 models tested appeared to consistently predict the measured velocity data well.

For increasing and decreasing skew:

1. For skews of less than 10 deg, the six simpler models, the PJ, and the main flow components of the WLC, CS, and B models can be useful over a limited y^+ range. The B and WLC transverse models appear reasonable but the transverse velocity components for this case were so small as to offer a weak test of the models.

It is worth noting the relatively small y^+ regions where similarity is perceived for the wide range of flow conditions surveyed. The region of reasonably predicted similarity is well below the y^+ of 300 upper limit for nominally zero pressure gradient two-dimensional flows (which should be no surprise), often with an upper limit of y^+ of about 100, depending on the pressure gradient, wall shear, and skewing in the local flow, but not easily correlated with these variables.

All ten models can trace their origin directly to the classic Townsend equilibrium concept for two-dimensional turbulent boundary layers and subsequent variations of the classic mixing length hypothesis. It appears that skewing in the three-dimensional case taxes the applicability of this basically two-dimensional approach with an approximate upper limit of 15–20 deg of skew. It is encouraging to see the strong tendency of many of these data for modest skewing (< 20 deg), and in some instances for stronger skewing, to follow the two-dimensional-like buffer or transition region similarity models in the very near-wall flow ($y^+ < 50$). This is especially clear in the case of the six simpler models where the Spalding third order single formula wall law was (arbitrarily) chosen to represent the model line. Within this upper skew limit for these flows it appears that the local wall shear stress and nondimensionalizing shear velocity for the various similarity plots are related within a modest uncertainty. This implies that at least an approximate *magnitude* of local wall shear stress would be inferred from such similarity models in a Clauser chart type of approach as developed by Pierce and Zimmerman [12] for at least the simpler similarity models reviewed and tested here. This would also imply that indirect diagnostic devices which are not strongly sensitive to yaw angles (such as small Preston tubes and surface heat meters) would, using a *two*-dimensional calibration, also give a reasonably good approximation to the *magnitude* of the wall shear stress in such modestly skewed flow as well. Note that without the supporting results of this study with directly measured local wall shear stresses, such use of a two-dimensional calibration in a three-dimensional flow would be speculative at best. Inferring a local shear velocity with a assumed similarity model guarantees a good similarity plot fit for the region of velocity data used to infer the shear velocity but this goodness of fit should *not* be taken as evidence of accuracy in the shear velocity value. Based on this study which used direct force local wall shear measurements it appears that such Clauser chart inferences and indirect wall shear measurements using two-dimensional flow calibrations can give the local wall shear stress *magnitudes* to about ± 5 to 10 percent – the uncertainties in this experiment do not appear to warrant any narrower limits.

The same relative insensitivity of yaw which would allow the use of such indirect wall shear devices in a skewed flow would, however, render such devices as relatively poor in indicating the local wall shear or limiting wall streamline direction. It would appear that for modestly skewed flows the combination of, for instance, a small Preston tube or surface heat meter (using a two-dimensional calibration) together with an established wall flow visualization technique would do a reasonably satisfactory job in mapping a three-dimensional wall shear field. The combination of an indirect wall shear magnitude sensing device and a flow visualization technique for direction would be significantly easier to use than a direct force sensing three-dimensional wall shear meter such as used in this study.

Finally, as in all graphical evaluations, what one sees is wholly subjective, and conclusions tendered are based on

these individual perceptions from various frames of reference. As a result the strongly interested reader is urged to study these and the more complete results in order to form his/her own individual conclusion.

Acknowledgments

This work was initiated under an NSF grant monitored by Dr. George Lea and subsequently supported in part under an NASA grant monitored by Mr. Joseph G. Marvin of the Ames Research Laboratory.

References

1 Pierce, F. J., J. E. McAllister, and M. H. Tennant, "A Review of Near-Wall Similarity Models in Three-Dimensional Turbulent Boundary Layers," ASME JOURNAL OF FLUIDS ENGINEERING, Vol. 105, September 1983, pp. 251–256.

2 Pierce, F. J., J. E. McAllister, and M. H. Tennant, "Near-Wall Similarity in a Pressure-Driven Three-Dimensional Turbulent Boundary Layer," ASME JOURNAL OF FLUIDS ENGINEERING, Vol. 105, September 1983, pp. 257–262.

3 Pierce, F. J., and J. E. McAllister, "Near-Wall Similarity in a Pressure-Driven Three-Dimensional Turbulent Boundary Layer," Report VPI-E-80.32, Mechanical Engineering, Virginia Polytechnic Institute and State University, Blacksburg, Va., Sept. 1980.

4 Tennant, M. H., F. J. Pierce, and J. E. McAllister, "An Omnidirectional Wall Shear Meter," ASME JOURNAL OF FLUIDS ENGINEERING, Vol. 102, No. 1, Mar. 1980, pp. 21–25.

5 van den Berg, B., "A Three-Dimensional Law of the Wall for Turbulent Shear Flows," *Journal of Fluid Mechanics*, Vol. 70, Part 1, 1975, pp. 149–160.

6 McAllister, J. E., F. J. Pierce, and M. H. Tennant, "Direct Force Wall Shear Measurements in Pressure-Driven Three-Dimensional Turbulent Boundary Layers," ASME JOURNAL OF FLUIDS ENGINEERING, Vol. 104, 1975, pp. 149–160.

7 Kline, S. J., and F. A. McClintock, "Describing Uncertainties in Single-Sample Experiments," *Mechanical Engineering*, Jan. 1953, p. 3.

8 McAllister, J. E., "Near-Wall Similarity in Two- and Three-Dimensional Turbulent Boundary Layers," Dissertation, Virginia Polytechnic Institute and State University, Blacksburg, Va., Dec. 1979.

9 Prahlad, T. S., "Wall Similarity in Three-Dimensional Turbulent Boundary Layers," *AIAA Journal*, Vol. 6, No. 9, 1968, pp. 1772–1774.

10 Ezekwe, C. I., "Turbulent Stress Tensors in a Three-Dimensional Boundary Layer," Dissertation, Virginia Polytechnic Institute and State University, 1974.

11 Brown, K. C., "Three-Dimensional Turbulent Boundary Layers," Dissertation, University of Melbourne, Australia, 1971.

12 Pierce, F. J., and B. B. Zimmerman, "Wall Shear Stress Inference from Two- and Three-Dimensional Turbulent Boundary Layer Velocity Profiles," ASME JOURNAL OF FLUIDS ENGINEERING, Vol. 95, 1973, pp. 61–67.

Blade Boundary Layer Effect on Turbine Erosion and Deposition

M. Menguturk
Associate Professor.

D. Gunes
Graduate Student.

H. K. Mimaroglu
Graduate Student.

Department of Mechanical Engineering,
Bogazici University,
Istanbul, Turkey

E. F. Sverdrup
Advisory Engineer,
Westinghouse R & D,
Pittsburgh, Pa.

As an extension to the inviscid gas flow particle trajectory model presented in earlier papers, a complementary model has been developed to establish the effect of the blade boundary layer on the trajectories of particles and thus on the resulting erosion and/or deposition. The method consists essentially in tracing particles inside the boundary layer with initial conditions taken from the inviscid flow model. The flow data required for the particle trajectory calculations are obtained by using a compressible boundary layer flow computer program.

This model has been applied to the first stage stator of a large electric utility gas turbine operating with coal gas. Results are compared with the predictions of the inviscid flow model. It is shown that the effect of the boundary layer on the trajectories of particles smaller than 6 μm is important. Since the hot gas cleaning system of a pressurized fluidized-bed gasifier system is projected to remove particles larger than 6 μm diameter effectively, it is concluded that an accurate assessment of turbine erosion and deposition requires inclusion of the boundary layer effect. Although these results emphasize the relative importance of the blade boundary layer, the absolute accuracy of the method remains to be demonstrated and is thought to be largely dependent on the basic data concerning the erosivity and sticking probability of particles.

Introduction

The successful development of the coal based energy projects which involve the concept of combined cycle power generation is dependent to a large extent on the efforts to protect the high speed turbines against erosion, corrosion and deposition caused by particulate matter present in hot combustion gases. When particles of diverse physical/chemical formation find their way to turbine surfaces, particularly to blade surfaces, they may give rise to one or a combination of these problems. The quantity and quality of particles arriving at a certain point on the surface along with the physical and chemical characteristics of the surface and the gaseous environment determine the nature and the extent of the damage.

Although erosion, corrosion, and deposition appear to be local phenomena occurring in the immediate vicinities of the locations where particles reach the blade surfaces, previous histories of particles are of prime importance in the establishment of not only the locations but also the conditions of contact with surface, and thereby, in the evolution of the subsequent "surface" phenomena. Therefore, it is not surprising to see that a great deal of research is now directed toward understanding the mechanisms which bring particles in touch with blade surfaces.

Particles may be transported to blade surfaces under the action of a wide variety of forces. Among the most important of these forces are inertial force arising from particles' own acceleration, viscous drag force exerted by gaseous medium in motion, diffusive forces due to molecular activities, turbulent eddies and temperature gradients, gravitational force, buoyancy force, electric and magnetic forces.

The above list, despite being far from exhaustive, serves to illustrate the complexity of the problem. Attraction and adhesion forces between particles have been excluded from the list considering that particle concentrations are bound to be very small in practical applications. Shear lift forces and material attraction forces between particles and blade surface are again neglected on the basis that these forces will come into play only when particles have come within touching distance to the surface.

The classical approach to the problem of particle motion has been to write Newton's second law in the form

$$\Sigma \mathbf{F}_i = m_p \mathbf{a} \tag{1}$$

where the right-hand side represents the inertial force and the left-hand side is the sum of all the other forces acting on the particle.

Obviously, the resulting equation is extremely complicated and will not lend itself to practical solution, if all the forces mentioned above are to be included. Fortunately, however, it is possible in most instances to neglect the majority of these forces and to consider only the prevailing few mechanisms. In fact, electric and magnetic field forces can be directly omitted in the absence of such fields. In gas turbines, the gravitational force turns out to be quite negligible in comparison to the inertial and/or diffusive forces, because turbines are being made to operate at very high gas velocities in the spirit of the modern technological trends toward hotter and more efficient

Contributed by the Fluids Engineering Division and presented at the Joint AIAA/ASME Fluids, Plasma, Thermophysics, and Heat Transfer Conference, St. Louis, Mo., June 7-11, 1982, of The American Society of Mechanical Engineers. Manuscript received by the Fluids Engineering Division, August 5, 1982.

turbines. Buoyancy forces are also insignificant if the particle density to gas density ratio is very large.

The problem is amenable to further simplification in that there is usually little interaction between diffusive and inertial transport mechanisms. Therefore, separate treatments of these mechanisms are usually permissible. Very small particles (typically in the submicron range) are carried to blade surfaces by diffusion, whereas large particles are captured through direct inertial impactions.

In earlier papers [1, 2, 3] we presented models that calculate inertial and diffusive motions of particles in gas turbines.

The inertia model solves a set of equations which expresses a balance of inertial and drag forces and calculates trajectories of particles in blade passages based on inviscid flow data. This model was used [1] to determine the frequency and locations of particle impacts with the blades of a large electric utility turbine. The resutling erosion damage was calculated through use of a semiempirical erosion model assuming that all particles rebound. There are two underlying assumptions in this model. First of all, as evidenced by the omission of diffusion terms from the equations of motion, particles are assumed to be large enough so that diffusion has negligible influence on their motion. Secondly, it is assumed, implicitly through the use of inviscid gas flow data in calculations, that relaxation times of particles are too large for viscous boundary layers around blades to significantly effect their trajectories. The numerical application of the model indicated that the latter assumption may not be valid for particles smaller than 10 μm in diameter.

The inertia model was used [2] to estimate the erosion damage on the first stage rotor blades of a redesigned turbine tested by the Aeronautical Research Laboratories of Australia [4]. The applicability of the model was tested by comparing the model predictions with the experimental results. The predicted erosion distributions along the blade surfaces exhibited good agreement with the observed erosion patterns.

The diffusion model [3] considers laminar and turbulent diffusion of small particles inside blade boundary layer. Inertial deviation of particles from mean streamlines is neglected and particle transport is assumed to take place by convection and diffusion. Inertia is taken into account merely in establishing the condition on particle flux near surface according to the stopping distance theory of Friedlander and Johnstone [5]. Application of the diffusion model showed that the stopping distances corresponding to particles smaller than 1 μm in diameter are small in comparison to the local boundary layer thicknesses. These results appear to justify the assumption that inertial deviations of particles in this size range are negligible. Near the trailing edges of blades, the stopping distance of 3 μm particles reaches the local boundary layer thickness. This means that diffusion has negligible contribution to collection of larger particles, because inertia will be sufficient anyway to drive these particles all the way to surface. However, it is imperative to note that such particles may still spend considerable time in blade boundary layer, and consequently, their impact conditions may differ from those predicted by the inviscid-flow inertia model.

The above results lead to an interesting size spectrum of particle transport. It appears that transport of particles smaller than about 1 μm in diameter is solely governed by diffusion. 1-3 μm particles are transported by diffusion and inertia. Diffusion loses its importance in motions of particles larger than about 3 μm. Furthermore, it is understood that inertial motions of particles in the size range 1 μm–10 μm will be influenced to a varying degree by the presence of blade boundary layer. Trajectories and impact conditions calculated by the inviscid flow inertia model can be quite erroneous for these medium size particles.

The objective of the present study is to present a model which calculates inertial motions of particles inside blade boundary layers.

Equations of Inertial Particle Motion

In the presence of inertial and viscous drag forces alone, the equations of particle motion in a blade passage can be written as [6]

$$\ddot{x}=G(U-\dot{x})$$
$$\ddot{\theta}=\frac{G}{r}(V-r\dot{\theta})-\frac{2\dot{r}}{r}(\dot{\theta}+\omega) \tag{2}$$
$$\ddot{r}=-G\dot{r}+r(\dot{\theta}+\omega)^2$$

The coordinate system is shown in Fig. 1. x, θ, and r denote, respectively, the axial, tangential and radial coordinates of particle. U and V are, respectively, the axial and tangential gas velocity components relative to the blade under consideration. In axial turbines the radial gas velocity component is small. ($\dot{}$) denotes differentiation with respect to time. ω is the angular velocity of the blade.

The coefficient G in equations (2) is given by

$$G=\frac{3}{4}C_D\mathrm{Re}\frac{\mu}{\rho_p d_p^2} \tag{3}$$

where μ, ρ_p, and d_p are gas viscosity, particle density and particle diameter, respectively. Re is the particle Reynolds number defined based on the velocity difference $|\mathbf{W}_g-\mathbf{W}_p|$ as follows

$$\mathrm{Re}=\frac{\rho d_p|\mathbf{W}_g-\mathbf{W}_p|}{\mu} \tag{4}$$

Nomenclature

$\mathbf{a}$ = acceleration vector, m/s^2
C_D = viscous drag coefficient given by equation (5)
d_p = particle diameter, m
E = erosion rate, m^3/kg
$\mathbf{F}_i$ = forces acting on particle other than inertial force, N
G = coefficient defined by equation (3)
K_1, K_2 = ductile and brittle mode amplitudes of erosion, (m^3/kg)/(m/s)$^{2.5}$
m = velocity exponent of erosion
m_p = particle mass, kg
n = coordinate normal to blade surface, m
r = radial coordinate, m
Re = particle Reynolds number defined by equation (4)
s = surface coordinate measured from blade leading edge, m
U = axial gas velocity component, m/s
V = tangential gas velocity component, m/s
W = particle impact velocity, m/s
$\mathbf{W}_g$ = gas velocity vector relative to blade, m/s
$\mathbf{W}_p$ = particle velocity vector relative to blade, m/s
x = axial coordinate, m
y = tangential coordinate, m
α = angle between surface tangent and x-axis, deg
β = particle impact angle, deg
β_0 = erosion reference angle, deg
Δ = local momentum thickness, m
η = Levy-Lees coordinate defined by equation (6)
θ = tangential coordinate, rad
μ = viscosity, N-s/m^2
ξ = Levy-Lees coordinate defined by equation (6)
ρ = gas density, kg/m^3
ρ_p = particle density, kg/m^3
ω = rotational speed, rad/s

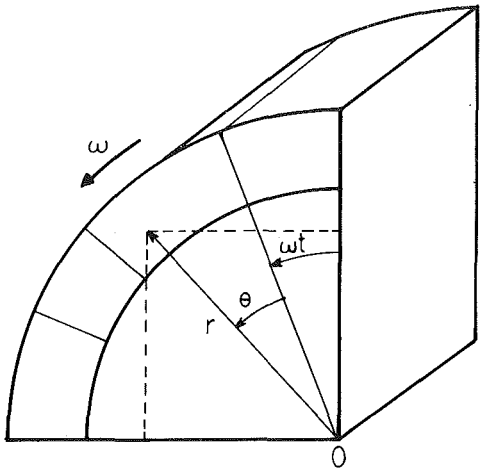

Fig. 1 Coordinate system for particle motion in axial turbomachine

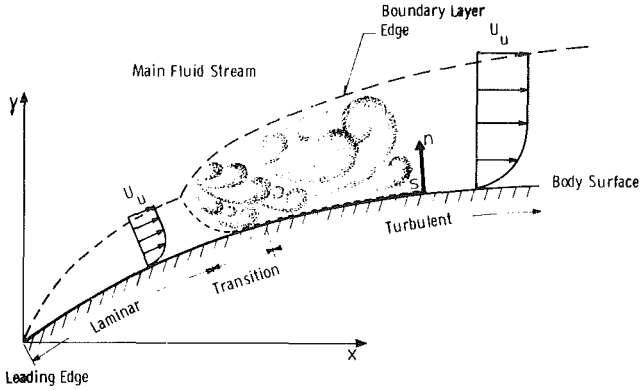

Fig. 2 Flow geometry

where ρ denotes the gas density, $\mathbf{W}_g$ the gas velocity and $\mathbf{W}_p$ the particle velocity.

C_D appearing in equation (3) is the drag coefficient and is equal to 24/Re for Stokes' flow. Correlations obtained by Morsi and Alexander [7] are used for large Re:

$$
\begin{aligned}
&C_D = 24/\mathrm{Re} && (0 < \mathrm{Re} \le 0.1)\\
&C_D = 22.73/\mathrm{Re} + 0.0903/(\mathrm{Re})^2 + 3.69 && (0.1 < \mathrm{Re} \le 1)\\
&C_D = 38.80/\mathrm{Re} - 12.65/(\mathrm{Re})^2 + 0.36 && (1 < \mathrm{Re} \le 10)\\
&C_D = 46.50/\mathrm{Re} - 116.667/(\mathrm{Re})^2 + 0.61667 && (10 < \mathrm{Re} \le 100) \qquad (5)\\
&C_D = 98.33/\mathrm{Re} - 2778/(\mathrm{Re})^2 + 0.3644 && (100 < \mathrm{Re} \le 1000)\\
&C_D = 148.62/\mathrm{Re} - 47500/(\mathrm{Re})^2 + 0.35713 && (1000 < \mathrm{Re} \le 5000)
\end{aligned}
$$

Equation (2) with the variable coefficient G given by equation (3) must be solved numerically for each particle entering blade boundary layer. The geometry of boundary layer flow is illustrated in Fig. 2 where s denotes the surface coordinate measured from the leading edge, n is the coordinate normal to the surface, and x and y are the axial and tangential coordinates ($y = r\theta$). α is the angle that a surface tangent makes with the x-axis ($\tan\alpha = dy/dx$).

Calculation of Boundary Layer Flow

The "mean field closure type" Cebeci-Smith computer program [8] is used to calculate two-dimensional compressible boundary layer flows around axial turbine blades. The outer flow conditions required as input to this program are obtained from the Katsanis inviscid flow computer program [9]. The Cebeci-Smith boundary layer program solves the continuity, momentum and energy equations in mass averaged form with respect to a coordinate system obtained by the Levy-Lees transformation. The Levy-Lees transformation is written as

$$
\begin{aligned}
d\xi &= \rho_e \mu_e U_e ds\\
d\eta &= \frac{\rho U_e}{(2\xi)^{1/2}} dn
\end{aligned}
\qquad (6)
$$

where ρ_e, μ_e, and U_e denote, respectively, the density, viscosity, and velocity of gas at the outer edge of the boundary layer.

In the Cebeci-Smith program the location of the transition point is specified as an external input by the user. For the calculations presented here, the transition location input was estimated by using Horlock's criterion [10].

$$
(\mathrm{Re}_\Delta)_{\text{transition}} = \frac{\rho_e U_e \Delta}{\mu_e} = 250 \qquad (7)
$$

where Δ is the local momentum thickness.

Calculation of Particle Trajectories

A computer program was developed to calculate particle trajectories in blade boundary layers. The program accepts boundary layer flow data generated by the Cebeci-Smith program in the Levy-Lees coordinate system and transforms it back into the $x-y$ system. A typical example of this transformation is given in Fig. 3 where i and j denote vertical and horizontal mesh line indices, respectively. In this example, 60 vertical and 100 horizontal meshlines are used. It is noted that the spacing between horizontal mesh lines is decreasing toward the blade surface to provide a better account of large velocity gradients near solid boundary. It is also noted that the rectangular grids of the Levy-Lees coordinate system transform into a curved mesh structure in the $x-y$ coordinate system. The flow data is known at the mesh points of this structure.

The transformation of the geometry and the gas velocity components into the $x-y$ plane is actually carried out in two steps. First, integrating equations (6) points in the Levy-Lees plane are transformed into the surface coordinate system defined by the coordinates s and n. The velocity components are unaffected by this mapping. In the second and final step, points and velocities are mapped into the $x-y$ plane by making use of the local surface angle, as described in Fig. 4.

Since the gas flow is given in discrete form, integration of the particle equations of motion (2) is not a straightforward task. At each step of integration, gas properties and velocity components must be interpolated. A three-point interpolation method is used for this purpose. Figure 5 illustrates a typical situation where the particle is enclosed by a triangle having its vertices at the mesh points (i, j), $(i, j-1)$ and $(i-1, j)$. Any quantity P can, then, be interpolated by using the following equation [11].

$$
P = a_1 P_{i,j} + a_2 P_{i,j-1} + a_3 P_{i-1,j} \qquad (8)
$$

where

$$
\begin{aligned}
a_1 &= |(x_{i,j-1} - x)(y_{i-1,j} - y) - (x_{i-1,j} - x)(y_{i,j-1} - y)|/d\\
a_2 &= |(x_{i-1,j} - x)(y_{i,j} - y) - (x_{i,j} - x)(y_{i-1,j} - y)|/d\\
a_3 &= |(x_{i,j} - x)(y_{i,j-1} - y) - (x_{i,j-1} - x)(y_{i,j} - y)|/d\\
d &= (x_{i,j-1} - x_{i,j})(y_{i-1,j} - y_{i,j}) - (x_{i-1,j} - x_{i,j})(y_{i,j-1} - y_{i,j})
\end{aligned}
$$

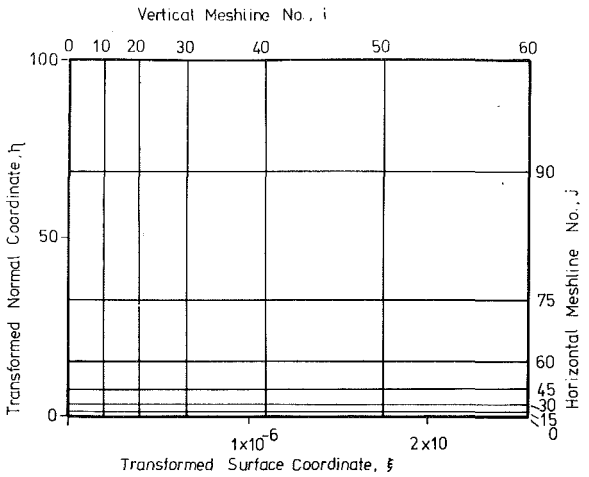

Fig. 3(*a*) $\xi - \eta$ plane

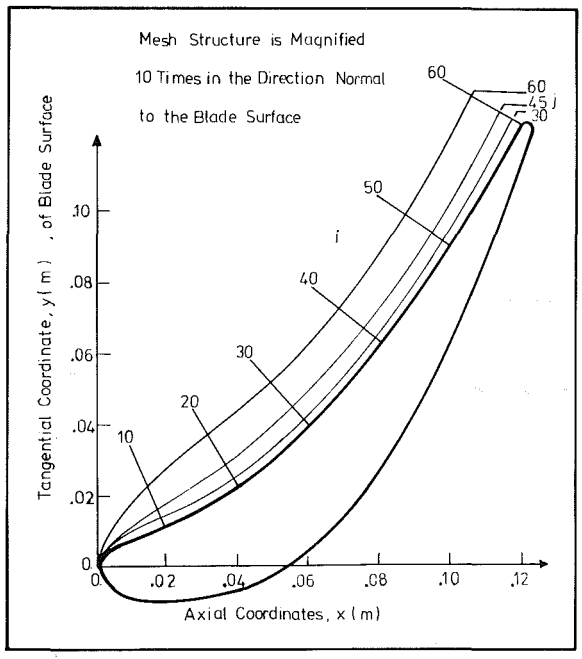

Fig. 3(*b*) $x - y$ plane

Fig. 3 Finite-difference mesh structure

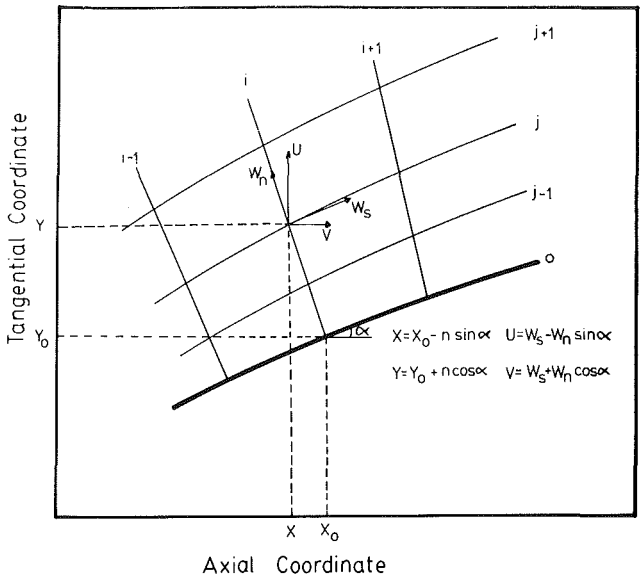

Fig. 4 Transformation from $s-n$ coordinate system into $x-y$ coordinate system

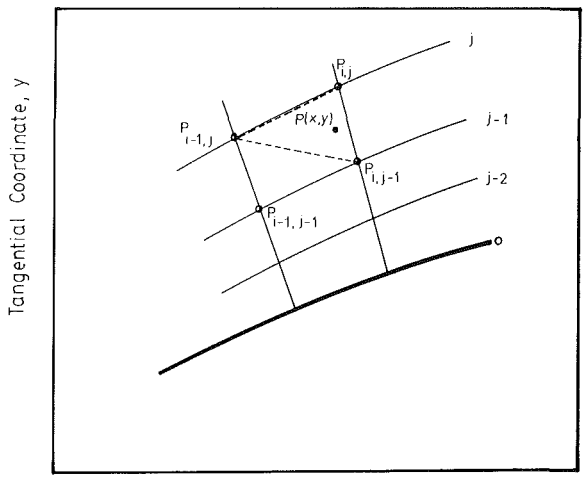

Fig. 5 Triangular cell used in gas data interpolation

The analysis is carried out as follows. The inviscid flow trajectory program [1] is used to calculate the trajectory of a given particle in the blade passage until the particle crosses the boundary layer edge. The coordinates and velocity at the point of entry to the boundary layer are specified to the boundary layer trajectory program as initial conditions. The fluid properties at this position are calculated by locating the triangle enclosing the particle and by applying the three-point interpolation equation (8). Once the coefficient G is evaluated, equations (2) are integrated by using Hamming's algorithm [12] to yield the new position and velocity. The new data is used to proceed a step further. This routine is continued until the particle reaches the blade surface. If the particle goes beyond the surface, the integration step is systematically reduced and the equations are reintegrated from the last position until the particle lands on the surface.

Application to the First Stage Stator of a Large Turbine

The boundary layer inertia model was applied to the first stage stator of the electric utility turbine considered in our earlier papers [1, 3].

The velocity distribution along the pressure surfaces of the stator blades calculated by the Katsanis program [9] and the corresponding boundary layer thickness distribution calculated by the Cebeci-Smith program [8] are shown in Fig. 6.

Figure 7 shows the trajectories of 3 μm particles (2500 kg/m^3 density) in the stator passage based on inviscid flow data. The trajectories of these particles calculated with the boundary layer inertia model is shown in Fig. 8 in a very small region (0.009 m $\times$ 0.012 m) near the trailing edge of the blade pressure surface.

The velocities at which particles in the 2 μm-6 μm size range impact the blade surface are shown in Figure 9. It is noted that large particles having high inertia lag behind gas velocity variations (i.e., acceleration along blade surface or deceleration across boundary layer), while small particles possessing low inertia follow the velocity variations closely. In the limit, the high inertia particles are expected to impact the blade with the same velocities at which they enter the blade passage. On the other hand, the low inertia particles are expected, toward the limit, to reach the surface at creeping velocities due to the damping effect of the boundary layer.

The impact angles shown in Fig. 10 suggest that larger

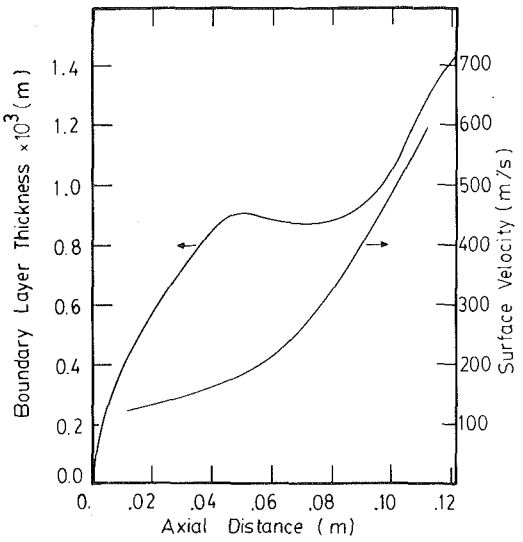

Fig. 6 Boundary layer thickness and surface velocity distribution along blade pressure surface

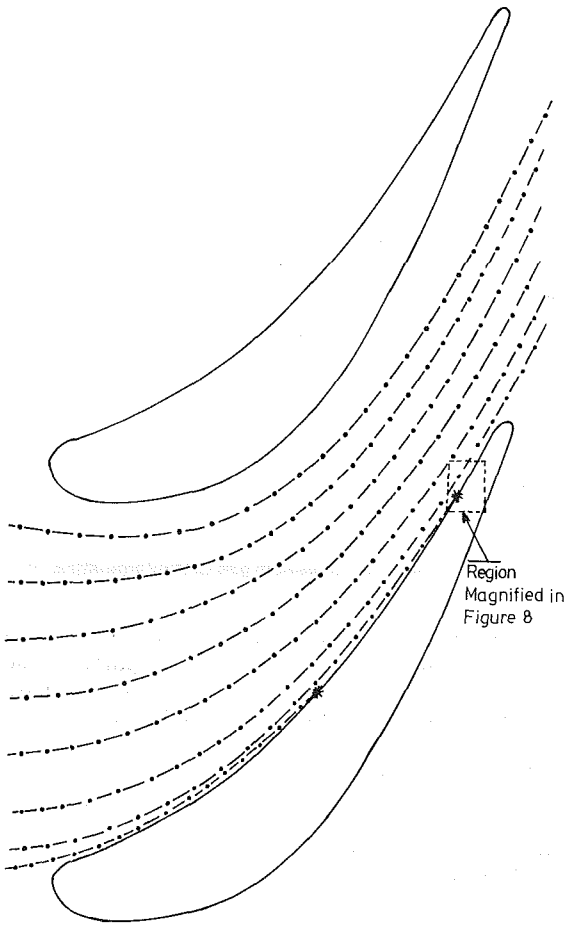

Fig. 7 Trajectories of 3 μm particles calculated based on inviscid flow data

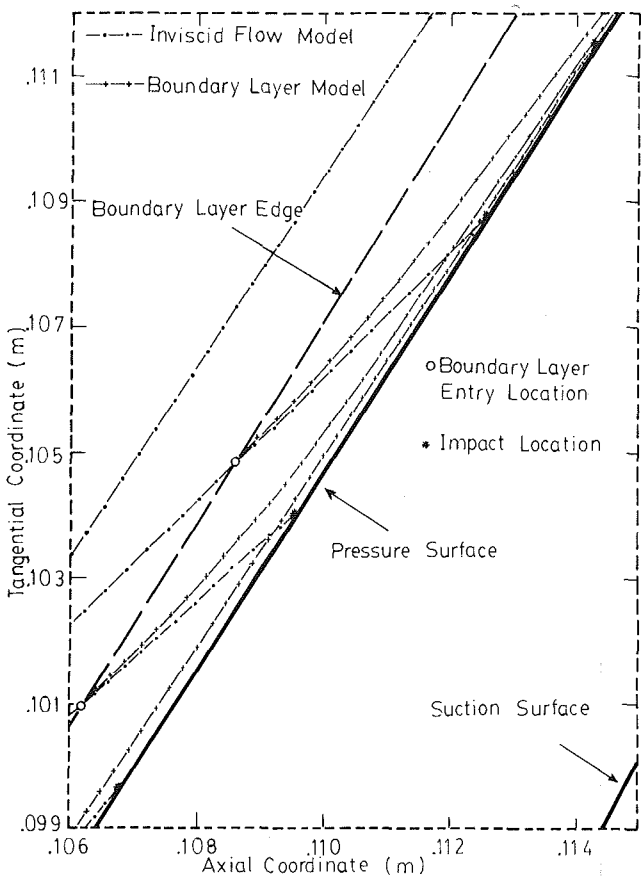

Fig. 8 Trajectories of 3 μm particles near trailing edge of blade pressure surface

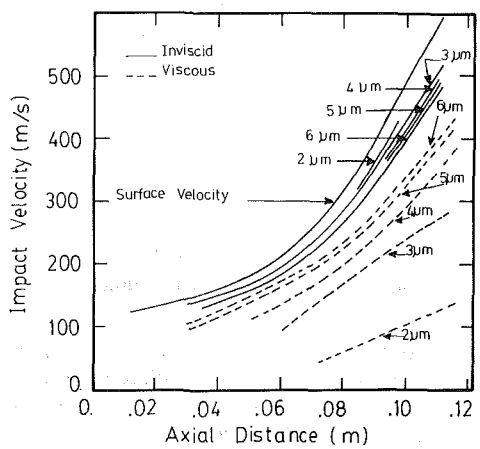

Fig. 9 Particle impact velocities along blade pressure surface

particles impact the blade at larger angles, and that the difference between the inviscid and the boundary layer model predictions increases as particle diameter decreases.

The effect of the boundary layer on particle impact conditions can be better seen when the impact velocities and angles at a given point on the surface are plotted as a function of particle diameter. Figure 11 gives these plots at an axial distance 0.10 m from the leading edge. It is clear that the boundary layer will have negligible effect on particles larger than 10 μm.

Erosion Rates. To see the effect of boundary layer flow on erosion, the semiempirical erosion model used in the inviscid flow inertia model [1] is assumed.

$$E = K_1(W\cos\beta)^m \sin n\beta + K_2(W\sin\beta)^m \text{ for } \beta \le \beta_0$$
$$E = K_1(W\cos\beta)^m + K_2(W\sin\beta)^m \text{ for } \beta > \beta_0 \quad (9)$$

where W and β are, respectively, the impact velocity and angle; K_1 and K_2 are the amplitudes, respectively, of ductile and brittle modes of erosion; m is an exponent expressing the velocity dependence of erosion; β_0 is a reference angle and $n = 2\pi/\beta_0$.

The following data [1] is used in the calculations.

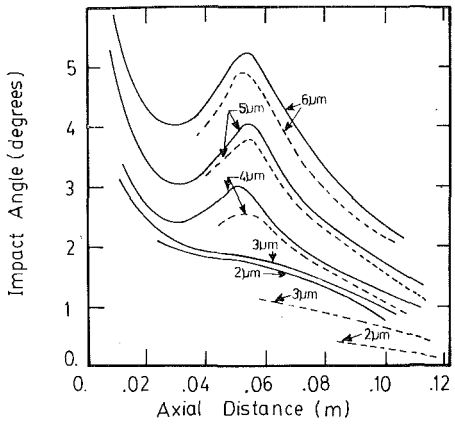

Fig. 10 Particle impact angles along blade pressure surface

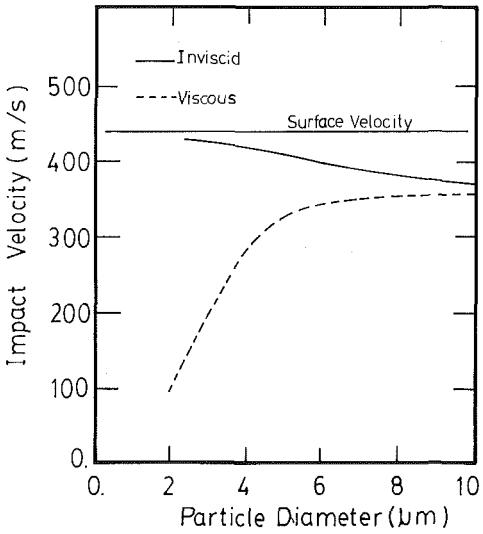

Fig. 11(*a*)

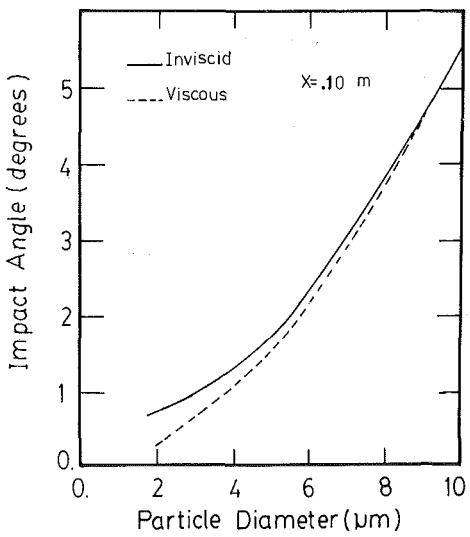

Fig. 11(*b*)

Fig. 11 Impact velocity and angle at 0.10 m from leading edge as a function of particle diameter

$$K_1 = 6.51 \times 10^{-14}\ (\mathrm{m^3/kg})/(\mathrm{m/s})^{2.5}$$
$$K_2 = 1.87 \times 10^{-14} (\mathrm{m^3/kg})/(\mathrm{m/s})^{2.5}$$
$$\beta_0 = 22.7°, \qquad m = 2.5$$

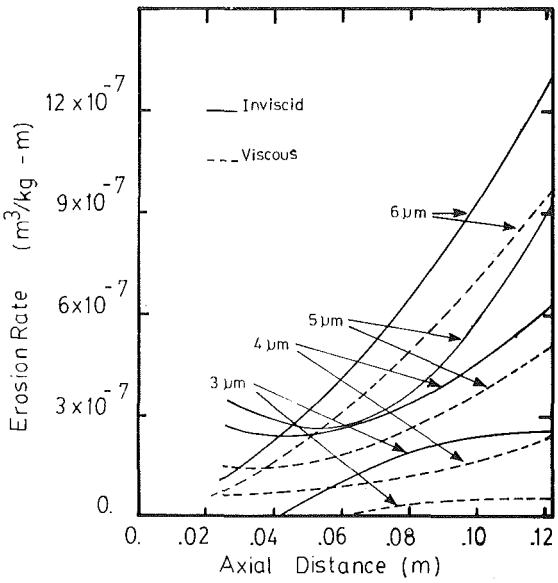

Fig. 12 Erosion rates along blade pressure surface

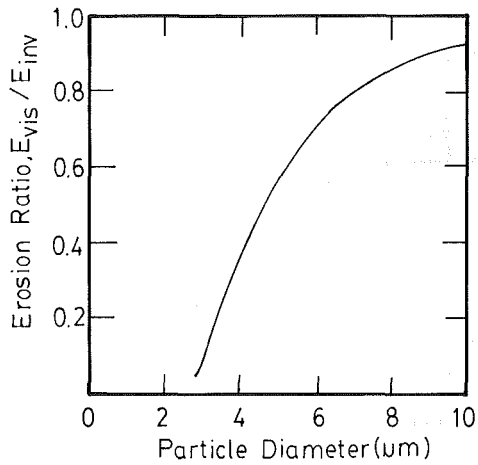

Fig. 13 Erosion ratio at trailing edge as a function of particle diameter

Results with and without boundary layer correction are compared in Fig. 12 which gives erosion rates as a function of axial distance from the leading edge. Figure 13 shows the ratio of the erosion rates at the trailing edge calculated by the boundary layer and inviscid flow models as a function of particle diameter. It is clearly seen that negligence of boundary layer effects in the calculation of the erosion rates due to particles smaller than 10 μm may lead to very serious errors. The erosion ratio falls below 75 percent for particles smaller than 6 μm.

Arrival Rates. It is of interest to compare the particle arrival rates calculated by the present model with the diffusive arrival rates [3]. For this purpose, particle impact frequency is converted into "deposition" velocity defined as the ratio of particle arrival flux to inlet particle concentration. This conversion is accomplished by multiplying the local impact frequency per unit surface area by the inlet volume flow rate per blade passage.

Figure 14 shows the deposition velocity at trailing edge as a function of particle diameter in the range 0.01 μm–10 μm. It is noted that particles larger than 3 μm reach the blade trailing edge predominantly by their own inertia while particles smaller than 0.5 μm are transported by diffusion. In the transition range (0.5 μm–3μm), both mechanisms are in effect, in which case the assumptions of the diffusion and

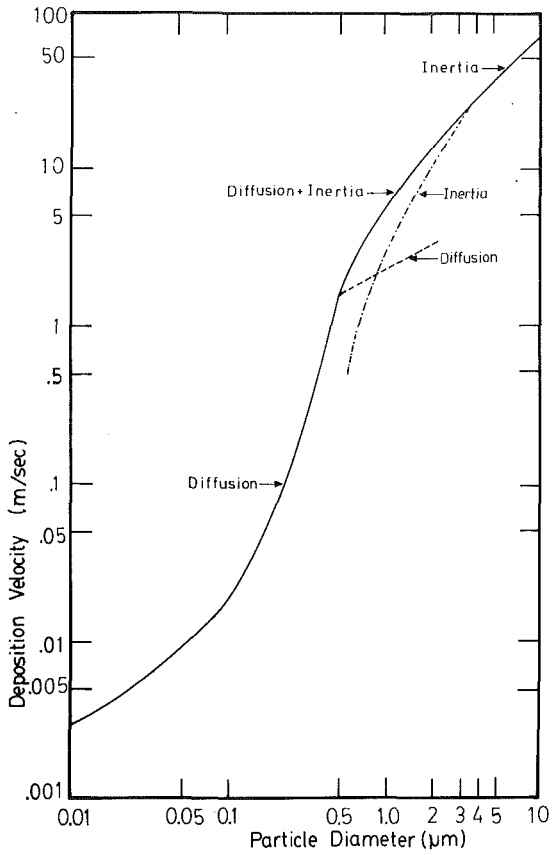

Fig. 14 Deposition velocity at trailing edge as a function of particle diameter

inertia models become questionable. However, the curve obtained by direct superposition of the results appears to be connecting the diffusion and inertia regimes smoothly.

Conclusions

A computer model calculating particle trajectories in blade boundary layers has been developed. This model determines frequency, angle and velocity of particle impacts with blade surfaces and can be used to predict erosion and/or deposition rates when combined with information regarding the erosion response of the blade material and the sticking probability of particles to the surface. The model accepts flow data calculated from computer programs available in the public domain. The authors would caution that the flow calculations neglect three-dimensional effects such as end wall boundary layers, passage vortices and radial flows. Ulke and Rowleau [13] reported that these effects may be significant.

Application of the model to a large-scale gas turbine has indicated that the effect of boundary layer on the trajectories of particles smaller than 6 μm is important. Since a great majority of particles leaving the particle filtration system of a pressurized fluidized-bed gasifier system are expected to be smaller than 6 μm, it is concluded that a reliable assessment of turbine erosion/deposition requires incorporation of boundary layer effects.

Comparing the particle arrival rates at blade surface as calculated by the boundary layer inertia model with the diffusive arrival rates presented in an earlier paper [3], it has been shown that particles larger than 3 μm reach blades by virtue of their own inertia while particles smaller than 0.5 μm are transported by diffusion. In the transition range (0.5 μm–3 μm), where inertial and diffusive mechanisms act together, the assumptions of both models become questionable, and yet, direct superposition of results appears to provide a smooth transition between diffusion and inertia regimes.

All the comparisons in the present paper are made to models previously published by the same authors. Therefore, the results should be interpreted as to indicate the relative importance of the blade boundary layer. The absolute accuracy of these predictions remains to be tested experimentally and is thought to be largely dependent on the basic data concerning the erosivity and sticking probability of particles.

References

1 Menguturk, M., and Sverdrup, E. F., "Calculated Tolerance of a Large Electric Utility Turbine to Erosion Damage by Coal Ash Particles," *Erosion Prevention and Useful Applications*, ASTM STP 664, Adler, W. F. (ed.), 1979, pp. 193–224.

2 Menguturk, M., Sverdrup, E. F., Elkabes, V., and Gunes, D., "Computer Erosion Assessment of an Experimental Turbine," *I. Mech. E.*, c70/81, 1981.

3 Menguturk, M., and Sverdrup, E. F., "A Theory of Fine Particle Deposition in 2-D Boundary Layer Flows and Application to Gas Turbines," ASME *Journal of Engineering for Power*, Vol. 104, No. 1, Jan. 1982, pp. 69–76. (Paper No. 81-GT-54)

4 McCay, F. L., "The Coal Burning Gas Turbine Project," Report of the Interdepartmental Gas Turbine Steering Committee, Australian Government Publishing Service, Canberra, 1973.

5 Friedlander, S. K., and Johnstone, H. F., "Deposition of Suspended Particles from Turbulent Gas Streams," *Ind. and Engr. Chem.*, Vol. 49, No. 7, 1957.

6 Hussein, M. F., and Tabakoff, W., "Dynamic Behaviour of Solid Particles Suspended by Polluted Flow in Turbine Stage," *Journal of Aircraft*, Vol. 10, No. 7, July 1973, pp. 434–440.

7 Morsi, S. A., and Alexander, A. J., "Theoretical Low Speed Particles Collision with Symmetrical and Cambered Aerofoils," ASME Paper 72-WA/FE-35, 1972.

8 Cebeci, T., Smith, A. M. O., and Wang, L. C., "A Finite-Difference Method for Calculating Compressible Laminar and Turbulent Boundary Layers," Donnel Douglas Aircraft Company, Report No. DAC-67131, Parts 1 and 2, 1969.

9 Katsanis, T., "Fortran Program for Calculating Transonic Velocities on a Blade-to-Blade Stream Surface of a Turbomachine," NASA TN.D. No. 5427, 1969.

10 Horlock, J. H., *Flow Research on Blading*, Ed. by Dzung, L. S., Amsterdam, Elsevier, 1970.

11 Young, D. M., and Gregory, R. T., *A Survey of Numerical Mathematics*, Vol. 1, p. 340, Addison-Wesley, 1972.

12 Hamming, R. W., *Numerical Methods for Scientists and Engineers*, McGraw-Hill, New York, 1962.

13 Ulke, A. and Rowleau, W. T., "The Effect of Secondary Flows on Turbine Blade Erosion," ASME Paper 76-GT-74, 1976.

M. Murakami
Professor,
Department of Mechanical Engineering.

K. Minemura
Associate Professor,
College of General Education.

Nagoya University,
Nagoya, Japan

Behavior of Air Bubbles in an Axial-Flow Pump Impeller

Motion of air bubbles in a high-specific-speed axial-flow pump impeller was analyzed on the basis of measured streak lines of air bubbles in the impeller. The results were compared with those obtained by a numerical solution of the bubble motion equations for three dimensional flow. Governing factors of the bubble motion are the drag force due to the surrounding water and the force due to the pressure gradient. Trajectories of the bubbles deviate somewhat from the streamlines of water, and the amount of the deviation is dependent on the bubble diameter and also on specific-speeds of the pumps and flow rate of water.

Introduction

Knowledge of the behavior of air bubbles in centrifugal pumps has recently become increasingly important, relevant to safety analyses for the loss of coolant accidents in pressurized water reactors, and also to the improvement of waste-treatment plants where sewage pumps conduct air-water mixtures. In order to investigate the behavior of bubbles entrained in the pumps, the previous paper [1] obtained the fundamental motion equations of air bubble flowing through an impeller of arbitrary shape, and gave a numerical procedure to evaluate the resulting bubble motion. This method was also applied to the flow in a radial-flow impeller pump, and the effects of the bubble diameter on its motion were discussed.

In the present paper, the same method is applied to an axial-flow pump with high specific-speed, and the flow pattern in the impeller is clarified under air admitting conditions. The results of the numerical analysis coincides well with experiments. The bubble motion in the impeller is also discussed in relation to the specific speeds and water capacities of pumps currently used.

Experimental Apparatus and Measured Results

Experimental Apparatus. The general arrangement of the experimental apparatus is the same as that used in the previous study [2]. The impeller of the axial pump is designed on the base of a free vortex flow pattern in the impeller. The pump discharges 8.80 m^3/min of water (ϕ = 0.260) at its normal speed of 1340 rpm under the head of 3.28 m; the specific speed being 1630 (rpm, m, m^3/min). In order to observe the motion of bubbles in the pump, the upper parts of the casing were made transparent. The piping system including the pump was made in a closed type in order to enable adjustment of the field pressure.

Air was drawn from the atmosphere into the piping system as is shown in Fig. 1. The entrained air is transformed to fine bubbles with which the locus of the flow in the impeller can easily be traced. The air tube was made adjustable to accord with various axial and circumferential locations.

Flow and Experimental Conditions of Pump. In advance of the experiments using air admission, the distributions of water velocities at sections both just before and after the impeller were measured in a single phase flow by a Pitot tube with three holes. For water capacity lying in the range of $0.20 \leqq \phi \leqq 0.290$, the meridian streamlines were nearly parallel to the pump axis. The data thus obtained, of the flow angle at the impeller outlet, was used to decide boundary conditions for the numerical calculations of the water flow.

The air entrained at the upstream section of the pump rises upward in the suction pipe and gathers at the top as is indicated by hatch lines in Fig. 1. To avoid the effect of this accumulation of air, an opening of the air pipe was provided directly above the pump axis and 35 mm ahead of the impeller, where the flow was not influenced by the upstream bend of the pump casing. The air admission opening was placed at a radial distance of $r = 98.75$ mm ($r/r_2 = 0.806$),

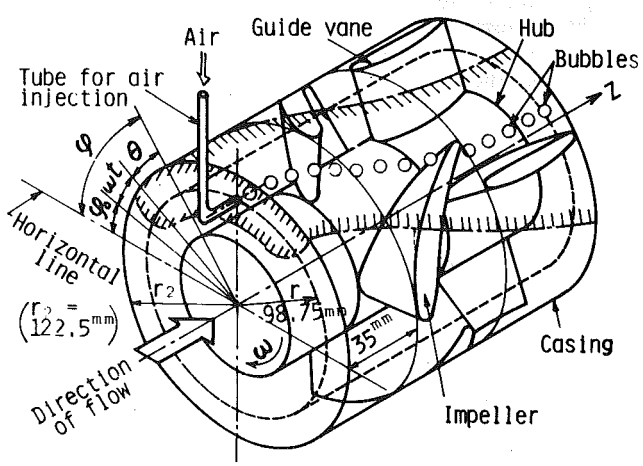

Fig. 1 Axial-flow pump employed

Contributed by the Fluids Engineering Division and presented at the ASME Applied Mechanics, Bioengineering, and Fluids Engineering Conference, Houston, Texas, June 20–22, 1983, of THE AMERICAN SOCIETY OF MECHANICAL ENGINEERS. Manuscript received by the Fluids Engineering Division, December 22, 1981. Paper No. 83-FE-9.

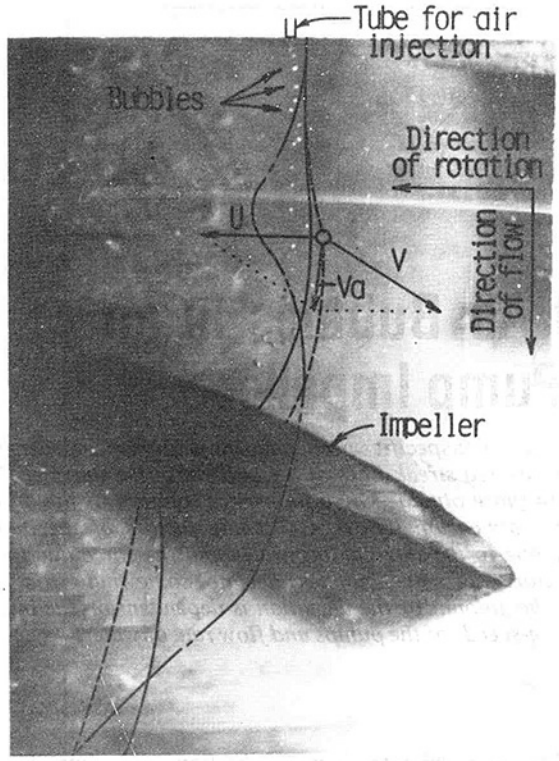

Fig. 2 Streak lines of bubbles in the impeller

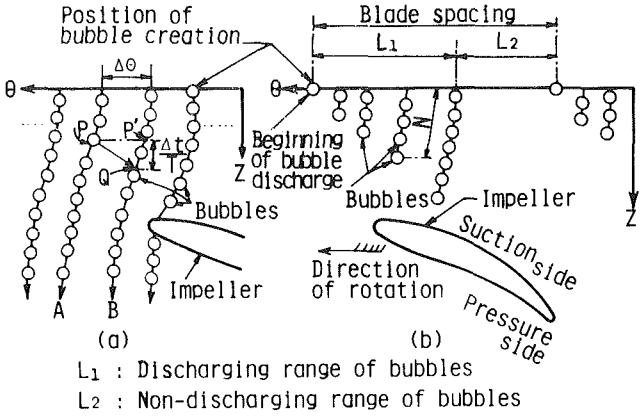

Fig. 3 Streak lines of bubble generated from the air tube located at the various positions relative to blades

slightly inside the impeller tip circle ($r_2 = 122.5$ mm). At this point the effects of the leakage flow and cavitation which might occur in the clearance between impeller blade and casing could be avoided.

Bubble trajectories were recorded at the normal capacity $\phi = 0.260$ of the pump, and at a speed of 1020 rpm. This speed, being considerably lower than the normal but it preserving the similarity low, was suitable for obtaining clear photographs of the bubble motion in the impeller.

Air bubbles entrained in the suction pipe are generally quite large, but they are crushed into finer spheres with nearly uniform size at the impeller entrance. The diameters of the spheres were measured to be of the order of 0.5 ~ 0.8 mm in the running condition mentioned above [2]. At the normal pump speed (1340 rpm) and with low air quantity (the volumetric ratio of air to water at the pump inlet being somewhat less than 2 percent), the diameter of the bubbles was measured to be about 0.5 mm. When an air pipe having an inside diameter of 0.2 mm was employed, the diameter of the bubbles ranged from 0.4 mm to 0.6 mm at the pump speed of 1020 rpm.

Experimental Procedure. The bubble flows were recorded photographically under stroboscopic lighting. When the pressure inside the pump was lowered beneath a certain critical value, $\{(p_s - p_a)/\rho g$ being equal to -0.54 m when expressed in the relative suction head$\}$, the detachment of air from the air pipe becomes periodical with a regular time interval, as shown in Fig. 1. An example of the photographs is shown in Fig. 2, in which a row of the bubbles exhibits a streak line of the flow in the impeller. The thick solid line in the figure shows an averaged locus of the streak line, as is mentioned later. The broken line indicates the streak line

Nomenclature

A = effective discharging area of impeller outlet
d = bubble diameter
$\mathbf{F}_B$ = Basset force vector
$\mathbf{F}_d$ = force vector due to flow resistance
$\mathbf{F}_p$ = force vector due to pressure gradient
$\mathbf{F}_v$ = force vector due to acceleration of apparent mass of a bubble
$\mathbf{F}_y$ = buoyancy vector due to the difference in densities between water and air
ΔH_i = pressure head difference between arbitrary position and pump inlet = $(p - p_i)/\rho g$
M = mass of a bubble
N = number of bubbles situating on a streak line
p = absolute pressure referred to pump centerline height
p_a = atmospheric pressure
p_i = total pressure of pump inlet measured on its centerline level
p_s = suction pressure of pump inlet
Q = pump discharge
r = radial distance
R = radial coordinate of a bubble
Re = Reynolds number based on a bubble velocity relative to water $= d|V - W|/\nu$
t = time
Δt = time required for shift of bubble between two neighboring streak lines
T = period of bubble discharge
u = peripheral speed of impeller
$\mathbf{V}$ = velocity vector of a bubble
V_w = velocity component of a bubble in the direction of water flow in a rotating flame
$\mathbf{W}$ = velocity vector of water
W = magnitude of water velocity in a rotating system
z = axial distance
Z = axial coordinate of a bubble
ρ = density of water
θ = angular coordinate
$\Delta\theta$ = circumferential distance of neighboring streak lines
Θ = angular coordinate of a bubble relative to impeller blade
ν = kinematic viscosity of water
ϕ = dimensionless expression of pump flow rate, $Q/A\,u_2$
ψ = angular coordinate of bubble referred to stationary coordinate system $= \Theta + \omega t + \psi_0$
ω = angular velocity of impeller

Subscripts

0 = initial condition of bubble
2 = impeller tip
a = absolute coordinate system

obtained by the numerical calculation described later, and the chain line exhibits a streamline of the absolute flow path. A considerable discrepancy between these lines is seen due to an unsteady flow nature in the impeller passage.

In this study, the flow analysis was made on the basis of the streak line with use of the pitch of each bubble on the line. The ascending velocity of the bubbles due to the buoyancy is negligibly small compared with the through flow velocity, and the bubbles can be assumed to move on a cylindrical surface. Since the locus of flow on the photographic plate receives some distortion caused by projection of the cylindrical surface against a plane, a correction is necessary. When the cylindrical surface is developed in a $\theta - z$ plane, rows of air bubbles corrected for the deformation can be obtained as is shown in Fig. 3(a).

If the pressure at the air tube opening exceeds a critical value, the tube does not continuously release the air bubbles in the downstream region as shown in Fig. 3(b), and there is a range where air is not discharged, expressed by the angle L_2. In the discharging range of bubbles, the number of bubbles on each streak line is not the same, but varies with the angle θ. This inequality is due to the effect of the impeller blade motion on the pressure at the air pipe opening.

An example of the pressure measured by a piezometric transducer is shown in the upper part of Fig. 5, in which the pressure difference $(p-p_a)/\rho g$ is plotted against θ, when the relative suction head $(p_s-p_a)/\rho g$ is -0.10 m. In this figure p is the air opening pressure and θ denotes the angular distance of the opening, measured from the leading edge of an impeller blade. The pressure is seen to change sinusoidally. In the lower part of the figure, the numbers of bubbles generated (N) are plotted against θ. The discharge of the bubbles can be observed only when the orifice pressure is lower than a critical value, namely, when the discharging orifice is not near the impeller blades. Since N increases linearly with θ, the period of bubble discharge T remains unaltered during the bubble discharge. Let the proportional constant between N and θ be k, the period T is given by the relation $T = 1/k\omega\,(=0.568$ ms). In Fig. 4 the relationship between N and θ for the different suction pressure head is also plotted. The proportionality between N and θ is seen to be established independently of the suction head. This relationship was used for determining the bubble trajectories from the observed data.

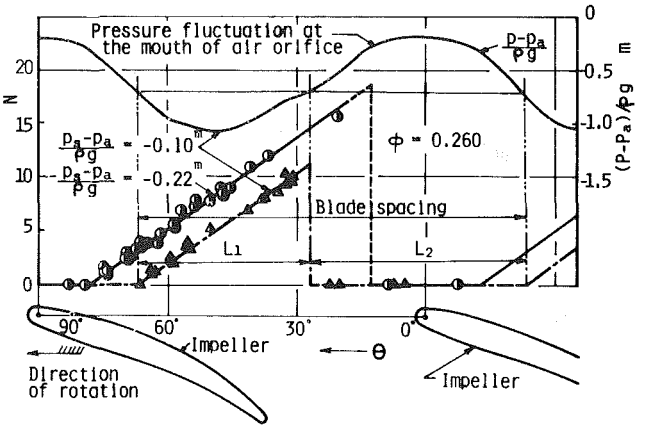

Fig. 4 Relationship between the location of air tube and the number of bubbles generated (Uncertainties for N, θ, and the relative suction head are ± 0.2, ± 0.2 deg, and ± 0.01 m, respectively)

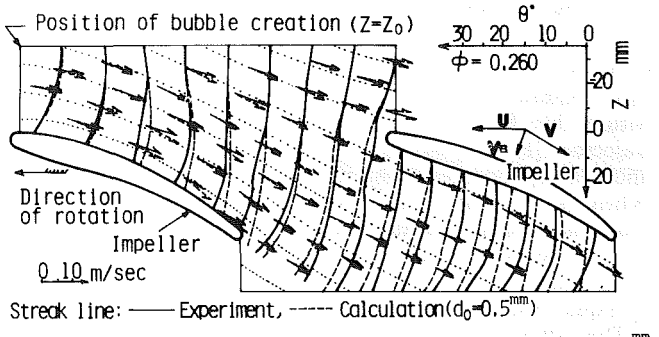

Fig. 5 Streak lines and relative velocity vectors of air bubbles (Uncertainties in θ and z for the streak lines are ±0.2 deg, and ±0.3 mm, respectively)

Method of Analyzing the Experimental Results. The successive locations of air bubble (by which the streak line of the bubble is decided) tend to scatter in the downstream region, and some treatment is necessary to make the data smooth enough for the further calculation. In this study, the mean streak lines were decided by use of multiexposure photographs. On a single flash photograph taken at the same location as the multiexposure photographs, each bubble position can be viewed as the endpoint of a perpendicular segment to the mean streak line obtained above.

If we let the bubbles be shifted from row A to row B by the impeller rotation in a small time $\Delta t\ (=\Delta\theta/\omega)$, as shown in Fig. 3($a$), then the point P on row A will move on the row to the point Q downstream of point P′. The distance between the two points P′ and Q is the pitch of the bubble, $\Delta t/T$. If the circumferential distance of neighboring streak lines, $\Delta\theta$, is sufficiently small, the relative velocity of the bubble at the point P can be graphically found by the relation of $\mathbf{V} = \overline{PQ}/\Delta t$. This calculation was carried out by use of a computer with the data recorded for each bubble row. The bubble position at each step ($\Delta t/T$) was estimated by use of cubic spline interpolation. The accuracy of the calculation depends on $\Delta\theta$. In this calculation, we selected thirty bubble rows for one impeller pitch and made the distance $\Delta\theta$ approximately equal to 3 deg. Uncertainties for the resulting velocity $\mathbf{V}$ and the relative flow direction are ± 1.3 m/s, and ± 5.5 deg, respectively.

Measured Values of Babble Velocities. Examples of the mean streak lines measured are shown by solid lines in Fig. 5. As the bubbles flow down the impeller, the streak lines tend to shift slightly toward the direction of impeller rotation. The bubble diameter in this case was measured to range from 0.4 mm to 0.6 mm. As an example of the numerical calculation which will be described later, the calculated streak lines of bubbles having a diameter of 0.5 mm at the initial section are shown by broken lines in Fig. 5. A slight discrepancy in the observed and calculated results is seen in the downstream sections. This is due to the integration error in the numerical calculation, but it may be considered that both results are generally in a good agreement in the available range. Also in Fig. 5, the relative bubble-velocity vectors obtained by observation are shown by solid lines, and those calculated by the numerical method are shown by broken lines. Throughout the impeller region, both the magnitudes and directions seem to coincide fairly well. Only in the negative side of impeller inlet can a slight discrepancy be seen. This is explained by the fact that the intervals of the bubbles on the streak line become incorrect in that region, due to the effect of the bubble break down, which is caused by some large external forces acting at the impeller entrance.

Numerical Procedures and Results

Numerical Procedure. In order to calculate the movement

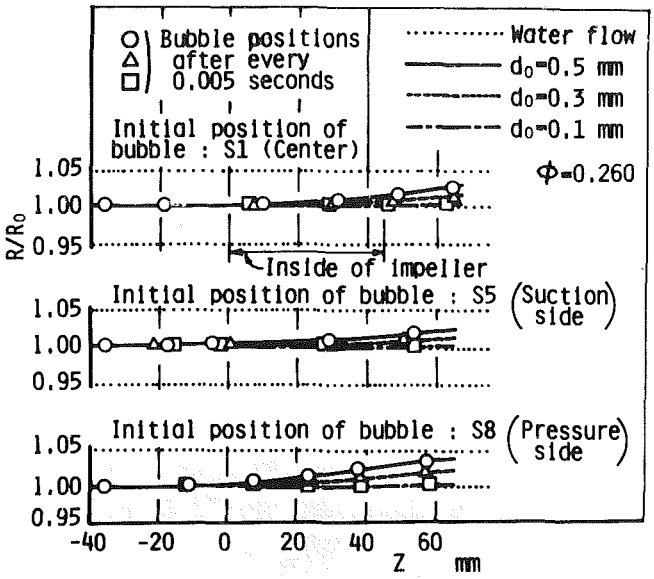

Fig. 6 Trajectories of air bubbles in a meridian section

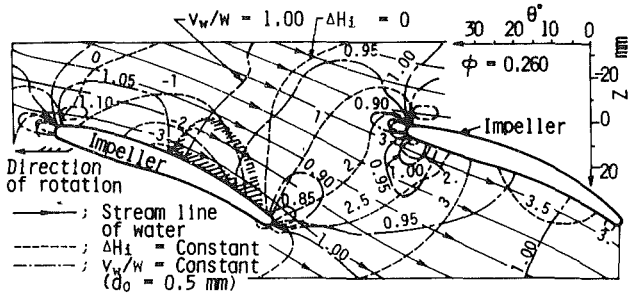

Fig. 7 Stream lines and isobaric lines of water in a stream surface of revolution

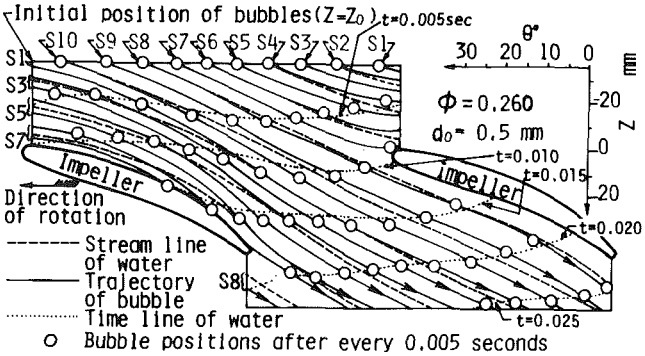

Fig. 8 Comparison of air bubbles trajectories with water stream lines

of air bubbles in an axial-flow pump, we first determine the flow condition of the water. Then we set an air bubble free within this flow field, and analyze the resulting bubble trajectory [1]. It is assumed that the bubbles are small in size and number and have no mutual interference in their motions. When the quantity of air admitted into the pump is small, these assumptions are satisfied well. If the flow of water in the pump is assumed to be inviscid and incompressible and has an axisymmetric stream surface, then the flow can be calculated by a quasi-three dimensional method [3, 4].

The equation of motion for a single air bubble in a stationary frame is given by

$$M(D_a\mathbf{V}/D_aT) = -\mathbf{F}_d + \mathbf{F}_p + \mathbf{F}_y + \mathbf{F}_v + \mathbf{F}_B \qquad (1)$$

The details of the further calculations are described in the paper in reference [1] {equation (5)}.

If it is assumed that the initial diameter d_0 of the bubble at the flow passage entrance is given and its initial velocity is same as the water velocity, then the three dimensional bubble accelerations are calculated by equation (17) in reference [1], and the bubble position and velocity, as well as forces acting on the bubble after every infinitely small time interval, can be obtained. This procedure is repeated until the bubble flows out of the region considered. The details of the further numerical procedures are described in reference [1].

Bubble Trajectories in Meridian Sections. As described before, a bubble essentially flows down on a stream surface of revolution ($z - \theta$ surface). We first discuss the bubble trajectory in a meridian section ($z - r$ surface) perpendicular to the $z - \theta$ surface. Figure 6 shows the change in the radial coordinate of a bubble R in the impeller passage, when the pump is operated at the best efficiency point discharge, $\phi = 0.260$. The top figure represents the results for a bubble starting at the position S1 (central zone of the impeller passage), and the middle and the bottom figures are the results for the point S5 (suction side of the blade) and the point S8 (pressure side), respectively (see Fig. 8). In the calculation, the initial position of the leading edge of the impeller was taken to be $\psi_0 = 0$, (see Fig. 1), and the flow of the bubble can be seen only in the region of $\theta > 0$, namely, in the upper half of pump passage (shaded region in Fig. 1). In this region the bubble is driven toward the impeller tip due to the buoyancy acting on it, and hence, $R/R_0 > 1$. The meridian streamlines of water are of course nearly horizontal, as is indicated by the dotted line, and $R/R_0 = 1$. The change in R/R_0 is greatest when the bubble is released from the point S8 and flows down along the pressure side of impeller. But the amount of the radial distance variation is extremely small and the change in R/R_0 can be neglected.

Bubble Trajectories on a Stream Surface of Revolution. The relative streamlines of water in a stream surface of revolution are shown in Fig. 7, when $\phi = 0.260$. The streamlines, shown by thin lines, lie almost parallel to the blade profile. In the same figure, the isobaric lines ($\Delta H_i = \text{const}$) are shown by broken lines which lie close together near the leading and trailing-edges of the impeller, at which the pressure gradient becomes high.

When bubbles having an initial diameter of $d_0 = 0.5$ mm are released from various points in the initial section 35 mm ahead of the impeller, the trajectories of the bubbles follow the loci as shown by solid lines in Fig. 8. In this figure the water streamlines are shown by broken lines. When the bubbles start from different positions S1,S2, . . . , S10 in the initial section, consequent positions of each bubble after every 0.005 seconds are denoted by circular marks, and the corresponding positions of water particles are indicated by the dotted line curves. The bubbles are seen to move nearly parallel to the water particles, and to leave the impeller in approximately the same time.

In the pressure side region the bubble trajectories lie nearly parallel to the water streamlines but in the suction side they are shifted a little towards the blade. The motion of a bubble in the impeller is governed substantially by the drag force $\mathbf{F}_d$ and the force due to the pressure gradient $\mathbf{F}_p$ as described in the latter section. The force $\mathbf{F}_p$ acts normally to the isobaric lines denoted by the broken lines in Fig. 7, and in the pressure side of the impeller $\mathbf{F}_p$ are in the direction of water flow, but in the negative side $\mathbf{F}_p$ makes approximately a right angle with the path of water. Hence, bubbles which flow through the central and suction side zones of the impeller passage (corresponding to the bubble motions started from the initial positions of S2 ~ S6) are driven toward the lower pressure side in the passages at the inlet and outlet of the impeller. This tendency differs somewhat from that of a radial-flow pump

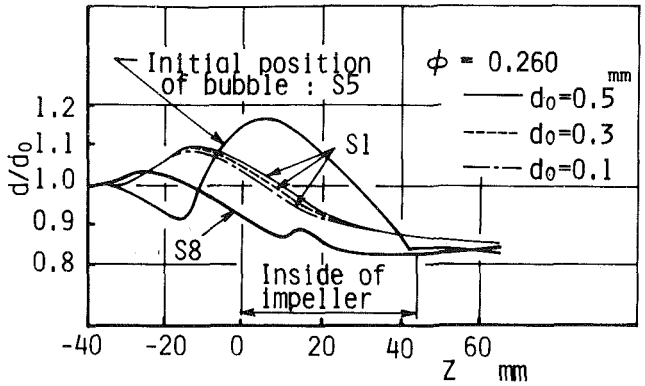

Fig. 9 Changes in bubble diameter in axial direction

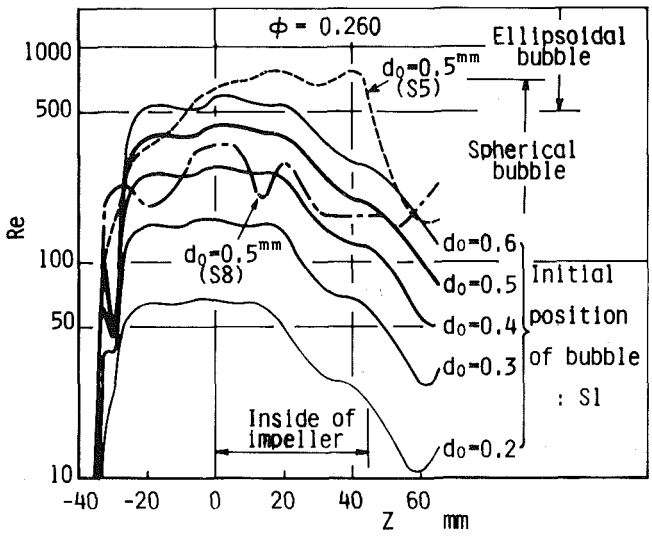

Fig. 10 Changes in Reynolds number of a bubble in axial direction

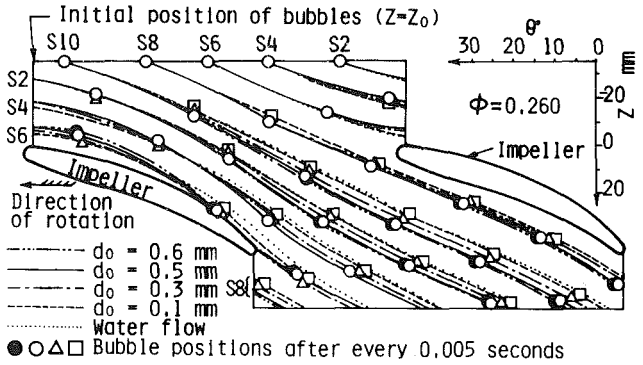

Fig. 11 Trajectories of bubbles with various initial diameter

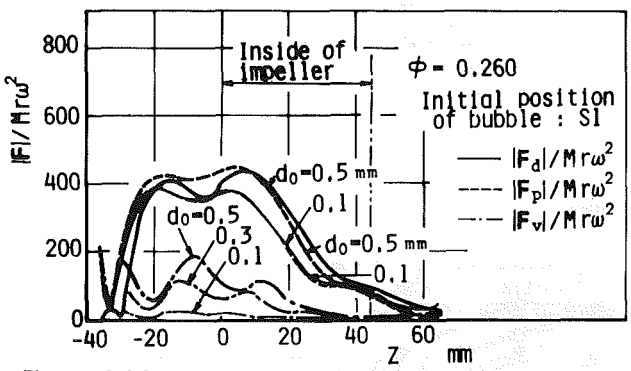

Fig. 12 Axial changes in magnitude of forces acting on a bubble

[1], in which the pressure changes mainly in the radial direction. Due to this pressure change the bubbles receive a pressure force toward the pressure side of the impeller blades, and the bubble trajectories are seen to be shifted to that side, the direction of this shift being opposite to that in the axial-flow pumps.

When the bubbles start from the points S6 and S7 in Fig. 8, they move toward the negative side of the passage in the latter half of the impeller, where a thick concentration of bubbles is seen.

In the region where a negative pressure gradient prevails, the bubbles move faster than water, and in the region in which an adverse pressure gradient is dominant they move slower. The equivelocity curves, $V_w/W = \text{const}$, are shown by broken lines in Fig. 7. Near the points where the values of V_w/W change from $V_w/W > 1$ to, $V_w/W < 1$, the bubbles gather closely and the chances for collision and unification of bubbles are increased. The shaded regions in the figure correspond to such regions when the amount of the admitted air is 2 percent. In a radial-flow pump, however, such regions are limited only to a narrow space near the impeller inlet. The effective area of the flow passage is throttled there and an increase in hydraulic loss is brought about, which constitutes the greater part of the pump performance degradation in an air-admitting condition [5].

Diameter and Reynolds Number of Air Bubbles. An air bubble in an impeller changes its diameter d according to the pressure in the flow field. When a bubble having an initial diameter of $d_0 = 0.5$ mm flows through the impeller, the diameter d changes as is shown in Fig. 9. The curves of the change in d/d_0 differ considerably when different initial bubble positions are selected, but the rate of the change is not so large. In Fig. 9 the results for different initial diameters are also plotted, when the bubbles start from the point S1. No noticeable difference can be seen in them.

In the course of flow in the impeller, the Reynolds number of the bubbles (Re) changes, as shown in Fig. 10. The results for different sizes of bubbles are plotted by solid lines, when the bubbles are released from the point S1. In the upstream region of the impeller, $z < 0$, and in the front half region of the impeller $0 < z < 20$ mm, Re has a nearly constant value for each bubble, but in the downstream region it decreases gradually. In the same figure, the results for different starting positions for $d_0 = 0.5$ mm are also plotted. In the path of a bubble flowing near the suction side of the impeller blades, a rise of Re is seen to occur.

Effect of Bubble Diameters. The results for bubbles having different initial diameters (d_0) are shown in Fig. 11. As d_0 increases, the paths of the bubbles are shifted toward the suction side of the impeller blades and the shift becomes significant when the bubbles move near the negative side. This shift of the path is lessened as d_0 decreases and a small bubble having a diameter of $d_0 = 0.1$ mm is considered to move essentially along on the water streamlines.

The flow velocity of a bubble changes with its size d_0, and the moving distances of different size bubbles for equal time intervals of 0.005 seconds are also plotted in Fig. 11. The time required for the bubbles to pass through the impeller passage is almost the same irrespective of the initial diameter d_0. In the radial-flow pump [1], however, the required time increases with d_0. This difference is attributable to the difference in the pressure gradient in both impellers.

The magnitudes of forces which act on a bubble flowing through the central zone of the impeller (S1) are plotted against the axial distance z in Fig. 12, where the forces are made dimensionless by use of the centrifugal force $Mr\omega^2$. The

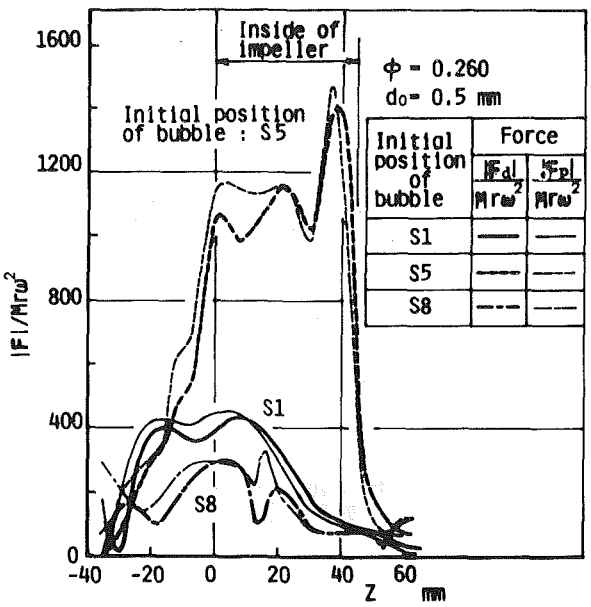

Fig. 13 Effects of the initial size of a bubble on the magnitude of forces

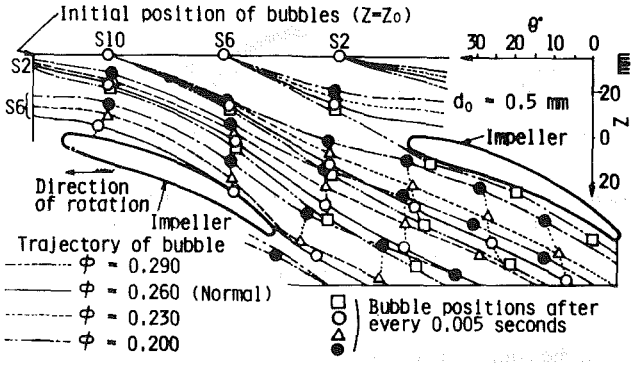

Fig. 14 Trajectories of air bubbles in various water capacities

buoyancy force due to the difference in fluid density $\mathbf{F}_y$, and inertia force together with Basset force $\mathbf{F}_B$ are found to be negligibly small, and their graphic expressions are omitted. The drag $|\mathbf{F}_d|/Mr\omega^2$ by the surrounding water and the resistance force due to the pressure gradient $|\mathbf{F}_p|/Mr\omega^2$ have nearly the same value and they change in a similar trend. The accelerating drag $|\mathbf{F}v|/Mr\omega^2$ decreases with a decrease in bubble diameter, and becomes substantially zero when $d_0 = 0.1$ mm. The same force relationships hold in the radial-flow pump. If bubbles are released from the respective points S1, S5, and S8, the forces $|\mathbf{F}_p|/Mr\omega^2$ and $|\mathbf{F}_d|/Mr\omega^2$ in the impeller vary as shown in Fig. 13. The two forces change similarly and with the same magnitude. The magnitude increases as the trajectories approach the suction side of the impeller.

Effect of the Water Flow Rate. If the water flow rate of the pump is altered, the meridian streamlines in the pump impeller will also change. But the bubble trajectories in a meridian section will always accord well with the streamlines of water as described before. Figure 14 exhibits the effect of the water flow rate ϕ on the bubble motion, when the bubbles with the initial bubble diameter of $d_0 = 0.5$ mm are released from the sections of S2, S6, and S10, respectively. As ϕ increases, the angle with which the water leaves the impeller is also increased. Correspondingly, the inclination of the water streamlines against the circumferential direction is raised, and the streamlines shift toward the low pressure side (see Fig. 14).

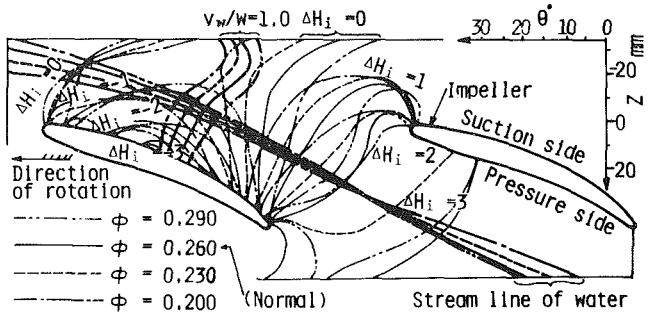

Fig. 15 Isobaric lines in the different water capacities

The bubble trajectories show similar changes. The locations of the bubbles after each elapsed time of 0.005 seconds are denoted by the marks, □, ○, △, and • in Fig. 14. The lines connecting the marked points are the path lines of the bubbles. In view of these results, it may be concluded that the flow speed of the bubbles changes to a great degree in accordance with the water flow rate ϕ.

As is seen in Fig. 7, the bubbles begin to accumulate in the downstream region from the line expressed by $V_w/W = 1$, which starts from the middle part of the suction side of the blade. The line $V_w/W = 1$ changes in accordance with the water capacity as is shown in Fig. 15, and approaches the leading edge of the blade as ϕ is reduced. In the figure, the isobaric lines, ΔH_i = const, are also plotted for different capacities. When ϕ decreases, a low pressure region, $\Delta H_i < -1$, approaches to the leading edge, and each iso-baric line lies close together in the suction side of the blade in the latter half of the impeller passage. In this downstream region the adverse pressure gradient is intensified and an accumulation of the bubbles will be promoted. When ϕ is increased over a certain critical value, a closed region near the impeller blade, expressed by $\Delta H_i < -1$, extends greatly, and the chance of the bubble accumulation in the impeller passage is greatly increased. From the above results it may be concluded that the least accumulation of air bubbles is expected in the impeller at a near-normal flow rate. The facts explained in Figs. 9 to 13 prove to hold for other water capacities.

Conclusions

Bubble motion in an axial-flow pump with a high-specific-speed was observed and the results were analyzed numerically. The following are the essentials of this study:

(1) Tracing of the air bubbles discharged from a small tube in front of the impeller provides an adequate means for investigation of the flow in a pump impeller working for a gas-liquid fluid.

(2) Air bubbles in an axial-flow pump move essentially on meridian streamlines. However, in the downstream region a small deviation is observed of the bubble trajectory from the liquid streamline. This deviation occurs in the direction from the pressure side of the blade towards the suction side. The amount of the deviation decreases as the bubble diameter reduces and a bubble of $d_0 = 0.1$ mm follows substantially the same path with the streamline of water.

(3) A bubble motion in an impeller is governed substantially by two forces: the drag due to the surrounding water and the force due to the pressure gradient in the impeller. The bubbles moving near the suction side of the blades experience greater forces and have larger flow velocities than those moving along the pressure side.

(4) On the suction side of blades there exists a region in which the pressure gradient changes its sign. In this vicinity the accumulation of air bubbles is promoted. The degree of this accumulation depends on the water capacity, and reduces to a minimum at a certain capacity near the normal.

Acknowledgment

The authors wish to express their thanks to Mr. K. Watanabe (M. Eng., Nagoya University) for his experimental work while carrying out this study.

References

1 Minemura, K., and Murakami, M., "A Theoretical Study on Air Bubble Motion in a Centrifugal Pump Impeller," ASME JOURNAL OF FLUIDS ENGINEERING, Vol. 102, No. 4, Dec. 1980, pp. 446–455.

2 Murakami, M., and Minemura, K., "Effects of Entrained Air on the Performance of a Horizontal-Axial Flow Pump," *Proc. of Symposium on Polyphase Flow in Turbomachinery*, ASME, Dec. 1978, pp. 171–184, (contributed to ASME JOURNAL OF FLUIDS ENGINEERING).

3 Katsanis, T., "Use of Arbitrary Quasi-Qrthogonals for Calculating Flow Distribution in a Turbomachine," ASME *Journal of Engineerig for Power*, Vol. 88, No. 2, Apr. 1966, pp. 197–202.

4 Katsanis, T., "Computer Program for Calculating Velocities and Streamlines on a Blade-to-Blade Stream Surface of a Turbomachine," NASA TN D-4525, 1968.

5 Murakami, M., Minemura, K., and Takimoto, M., "Effects of Entrained Air on the Performance of Centrifugal Pumps under Cavitating Conditions," *Bulletin of the Japan Society of Mechanical Engineers*, Vol. 23, No. 183, Sept. 1980, pp. 1435–1442.

Acknowledgment

The authors wish to express their thanks to Mr. K. Watanabe (M. Eng., Nagoya University) for his experimental work while carrying out this study.

References

1 Minemura, K., and Murakami, M., "A Theoretical Study on Air Bubble Motion in a Centrifugal Pump Impeller," ASME JOURNAL OF FLUIDS ENGINEERING, Vol. 102, No. 4, Dec. 1980, pp. 446-455.

2 Murakami, M., and Minemura, K., "Effects of Entrained Air on the Performance of a Horizontal-Axial Flow Pump," *Proc. of Symposium on Polyphase Flow in Turbomachinery*, ASME, Dec. 1978, pp. 171-184, (contributed to ASME JOURNAL OF FLUIDS ENGINEERING).

3 Katsanis, T., "Use of Arbitrary Quasi-Qrthogonals for Calculating Flow Distribution in a Turbomachine," ASME *Journal of Engineerig for Power*, Vol. 88, No. 2, Apr. 1966, pp. 197-202.

4 Katsanis, T., "Computer Program for Calculating Velocities and Streamlines on a Blade-to-Blade Stream Surface of a Turbomachine," NASA TN D-4525, 1968.

5 Murakami, M., Minemura, K., and Takimoto, M., "Effects of Entrained Air on the Performance of Centrifugal Pumps under Cavitating Conditions," *Bulletin of the Japan Society of Mechanical Engineers*, Vol. 23, No. 183, Sept. 1980, pp. 1435-1442.

DISCUSSION

R. B. Furst[2]

The authors are to be complimented for their carefully conducted test effort and the presented evaluation of the test results. The information is valuable in the analysis of cavitating flows as well as flow of liquids with entrained gases.

Selection of approximately the mean radius for the presented experimental results would be expected to provide the closest agreement with potential flow analytical procedures such as presented in references [3 and 4] of the paper. Comments on any of the authors experiences with the flow in regions of the impeller near the hub and the tip would be appreciated. Particularly of interest is the influence of deviation from potential flow in the region of the hub and tip in addition to the influence of the tip clearance flows mentioned by the authors.

The uncertainty of relative flow measurement of ± 5.5 degrees appears substantially greater than desirable. Measurements with a laser velocimeter could substantially reduce the uncertainty.

[2]Rockwell International, Canoga Park, Calif. 91304.

Author's Closure

This paper is an experimental confirmation of the calculated results of bubble motion in an impeller of an axial flow pump by the numerical method published in our previous paper. Mr. Furst refers to the effects of the secondary flows prevailing in the regions near the hub and the tip. The flows in these regions will be affected considerably by the secondary flow which does not obey the potential flow rule.

In the experiment, however, measurement of the secondary flow was not performed, but it may be assumed that its effects on the air bubble motion in the impeller channel are considered to be small, because the secondary flow velocity is generally much smaller than the through flow velocity within the region in which the bubbles move. In order to clarify the detailed effects of the secondary flow on the bubble motion a more precise method of flow measurement, for example, that by use of a laser velocity meter will be needed and also a three dimentional flow analysis may be required.

Further researches on these subjects will be indispensable.

The Effect of Free-Stream Turbulence on Turbulent Boundary Layers

P. E. Hancock[1]
Graduate Student.

P. Bradshaw
Professor.

Department of Aeronautics,
Imperial College,
London, England

Mean flow measurements, and some turbulence measurements, have been made in a two-dimensional incompressible constant-pressure ("flat plate") turbulent boundary layer beneath a nearly homogeneous nearly-isotropic (grid-generated) turbulent free stream. An appreciably nonlinear dependence of the skin-friction coefficient and other boundary layer parameters on rms free-stream turbulence intensity has been confirmed. A much wider range of free-stream length scales has been studied than in previous work, and the results (which agree well with previous data where they overlap) clearly indicate the large effect of free-stream length scale on the response of the boundary layer. The decrease of free-stream turbulence effect with increasing length scale is at least partly attributable to simple reduction of normal-component velocity fluctuations by the solid surface; this would not be the case in free shear layers.

1 Introduction

Except in external aerospace or marine flows, turbulent boundary layers or other shear layers generated in engineering generally lie beneath a significantly turbulent stream. A good example is the flow in a multistage axial turbomachine, in which the distubances felt by the blades of one of the later rows include (1) "ordered" – i.e., periodic – unsteadiness due to the rotating wakes of upstream stages, (2) periodic strong bursts of turbulence due to the wakes of the blades in the preceding few rows, (3) circumferentially homogeneous turbulence generated by the blade rows far upstream. In wind tunnel tests, possible disturbances include (1) large scale "unsteadiness," effectively-longitudinal pulsations of the tunnel flow, (2) genuine turbulence from corner vanes and other tunnel circuit components.

Most published work relates to the idealized nearly-homogeneous nearly-isotropic turbulence produced by a grid, and has mainly been restricted to boundary layers without pressure gradient. However, even in this simplest case basic uncertainties about the response exist. It has only recently been realized [1, 2] that the variation of skin-friction coefficient with free-stream, root-mean-square intensity is not even approximately linear, as assumed in most previous experiments. Also, the response to variations in the ratio of free-stream turbulence length scale to boundary layer thickness has been seriously underestimated in the past. The range of this ratio obtainable at a given value of the intensity is rather small unless special efforts are made (see Section 4), because the length-scale *ratio* and the intensity decrease together as x increases, and because the range of parameters easily available in conventional low-speed wind tunnels is limited. Previous work will not be reviewed in detail in the present paper, but results from the more reliable experiments will be presented for comparison with our own; a general review is given by Hancock [3].

The work presented in the paper formed a preliminary part of a longer study of turbulence structure, to be reported separately, in which the plate carrying the boundary layer was slightly heated so that boundary-layer turbulence and free-stream turbulence could be distinguished, using a fast-response resistance thermometer ("cold wire") to provide the conditioning function in conditional-sampling measurements. Results and preliminary discussion are given by Hancock [3]. During the early stages of the work, it was noticed that the ranges of intensity and length-scale ratio covered in previous experiments were quite well fitted by a *single line* in the intensity/length-scale plane (Fig. 1). The reasons are explained in Section 4. A prime object of the work reported here was, therefore, to cover a larger area in the intensity/length-scale plane. The response of the skin friction coefficient c_f will be used as a token of the response of the boundary layer in general, and a few mean-velocity profiles will be presented to show that the more sophisticated kinds of "log law plus wake" velocity profile family are still capable of representing velocity profiles, except perhaps at the highest free-stream intensities, so that c_f at given Reynolds number is indeed uniquely related to profile shape parameter. Turbulence measurements were taken at each test position, but only sample results are presented here: for details see [3].

2 Apparatus and Techniques

2.1 Configuration. The measurements were made in the

[1] Present address: Central Electricity Research Laboratory, Leatherhead, Surrey.

Contributed by the Fluids Engineering Division for publication in the JOURNAL OF FLUIDS ENGINEERING. Manuscript received by the Fluids Engineering Division, June 1, 1982.

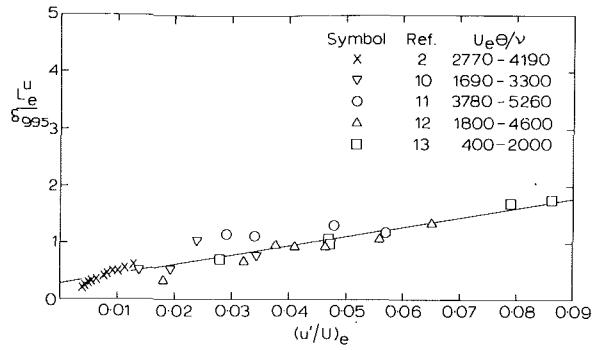

Fig. 1(*a*) Previous workers' parameters: range of momentum thickness Reynolds number, $U_e\theta/\nu$, shown

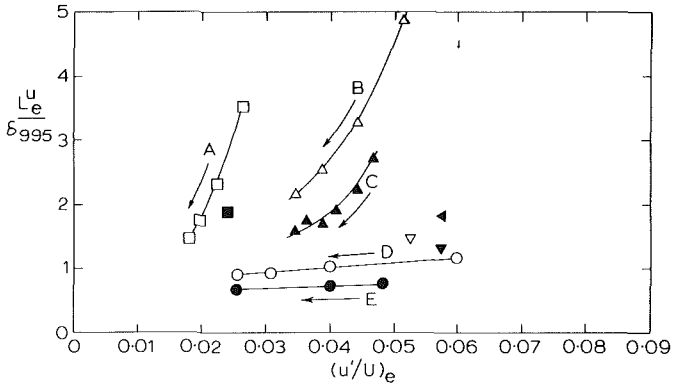

Fig. 1(*b*) Present measurements: $U_e\theta/\nu > 2000$. A, B, C, D, and E identify profile sets: points in each set correspond to different measuring stations along plate.

Fig. 1 Free-stream turbulence intensities and length-scale ratios used in experiments

Department's 0.91 × 0.91 m (3 ft × 3 ft) wind tunnel, at a speed of about 16.5 ms^{-1} (55 ft/s: unit Reynolds number 1080 per mm). Boundary layer measurements were made on a flat plate, 15 mm thick and 2.4 m long, supported horizontally midway between the working section floor and ceiling, with its leading edge set at several positions between 0.3 and 2.06 m from the working section entrance, where the turbulence grids were installed: the working section length was 4.9 m. The leading edge of the plate was ogive-shaped, 75 mm long with an included angle of 50 deg at the leading edge. This shape was chosen to reduce fluctuating separations at all likely instantaneous angles of incidence, but at the same time maintain a sharp leading edge. Limited flow-visualization tests showed no observable separation. Transition trip wires of diameter 0.8 mm were attached to the upper and lower surfaces at the end of the leading-edge section. Some of the tests reported here (see Table 1) were done with heating wires mounted just downstream of the trip, which thickened the boundary layer slightly. At the downstream end of the plate a symmetrically-tapered trailing edge unit (90 mm long) was fitted. Ten 89 mm dia. removable instrumentation disks were mounted along the centre line of the plate, flush with the upper (measuring) surface.

2.2 Turbulence Grids. Nearly all the measurements were made with square-mesh square-bar biplane grids, the results reported here being for grids with 76.2 mm mesh, 12.5 mm bar width and 152 mm mesh, 38.1 mm bar width. Biplane grids made of 2:1 rectangular bars with their larger dimension normal to the stream, and "monoplane grids," with horizontal and vertical bars in the same plane, were found to produce nonuniform unsteady flow, possibly because of the larger size of the separated region behind each intersection, and are not recommended for generating free-stream turbulence. Similar phenomena were observed by Cherry [4] in another of the Department's wind tunnels. Grids comprising a single row of parallel (square) bars were found to exhibit peculiar behaviour of the u-component spectra at low wave numbers. The straight line approximations to the measured decay of longitudinal-component intensity are, for the 76 mm grid,

$$[\overline{u^2}/U^2]_e^{-0.8} = 11.43\,(X/M - 4.81) \tag{1}$$

and for the 152 mm grid

$$[u^2/U^2]_e^{-0.8} = 8.39(X/M - 3.65) \tag{2}$$

the open-area ratios being 0.70 and 0.56, respectively. As usual for good-quality grid-generated turbulence the root-mean-square intensities of the lateral components were smaller, by roughly 5 percent, than the longitudinal component intensity.

For ease of comparison with other experiments in which only the u-component intensity was, or will be, measured, the length scale used in the presentation of our results is a form of dissipation length parameter, defined by the equation

$$U_e \frac{d(\overline{u^2})_e}{dX} = \frac{-(\overline{u^2})_e^{3/2}}{L_e^u} \tag{3}$$

where, *if* the turbulence were isotropic, the left-hand side would be two-thirds of the rate of turbulent energy dissipation. L_e^u can easily be deduced from the decay formulae, equations (1) and (2).

2.3 Test Conditions and Measurement Techniques. The maximum intensity allowed at the plate leading edge was 15 percent rms u-component, and the maximum intensity at any measurement station was 6 percent, the lowest being 1.8 percent. The lowest momentum-thickness Reynolds number at a measurement station was 1600: it is well known (see e.g., [5]) that the velocity-defect profile depends directly on Reynolds number at Reynolds numbers below about 5000, the effects being really significant only below about 2000. All our skin-friction increments and similar results are referred to the

Nomenclature

c_f = $\tau_w/(\frac{1}{2}\rho U_e^2)$, skin-friction coefficient
H = δ^*/θ, shape parameter
L_e^u = length scale of free-stream turbulence, defined in equation (3)
M = mesh width of turbulence-generating grid
U = mean velocity in x direction
u,v,w = velocity fluctuation in x,y, and z direction
u' = $(\overline{u^2})^{1/2}$
u_τ = $(\tau_w/\rho)^{1/2}$, friction velocity
V_E = entrainment velocity
X = distance from grid
x = distance from plate leading edge
y,z = normal and spanwise coordinates
$\Delta c_f, \Delta H$ = change in c_f, H from boundary layer in low-turbulence stream (no grid) at same $U_e\theta/\nu$
δ^* = displacement thickness
$\delta_{995} \equiv \delta$ = distance from surface at which $U/U_e = 0.995$
θ = momentum thickness
ν = kinematic viscosity
ρ = density
τ_w = surface shear stress

Suffixes

e = external-stream conditions
LE = leading edge
0 = no-grid conditions at same $U_e\theta/\nu$

Table 1 Details of profile sets (see Fig. 1(*b*))

Set A (76 mm grid, distance from grid to leading edge $X_{LE} = 2.06$m)

x,m	u'/U_e	L_e/δ	δ,mm	θ,mm	c_f	H
0.61	.0262	3.51	14.8	1.54	.00384	1.418
1.22	.0224	2.31	24.7	2.57	.00340	1.382
0.82	.0197	1.75	35.2	3.48	.00320	1.361
2.43	.0181	1.48	43.8	4.34	.00308	1.342

Set B (152 mm grid, $X_{LE} = 2.06$m)

x,m	u'/U_e	L_e/δ	δ,mm	θ,mm	c_f	H
0.61	.0514	4.94	19.1	1.63	.00403	1.366
1.22	.0442	3.28	31.5	2.62	.00360	1.334
1.82	.0387	2.53	44.3	3.62	.00340	1.307
2.43	.0345	2.15	55.9	4.30	.00330	1.291

Set C (152 mm grid, $X_{LE} = 2.06$m, heater wires near LE)

x,m	u'/U_e	L_e/δ	δ,mm	θ,mm	c_f	H
0.91	.0468	2.72	36.7	2.88	.00364	1.310
1.22	.0442	2.23	46.4	3.54	.00352	1.286
1.52	.0410	1.90	56.8	4.09	.00339	1.286
1.82	.0387	1.70	65.7	4.57	.00334	1.278
2.10	.0362	1.69	68.9	4.88	.00326	1.276

Set D (76 mm grid, $X_{LE} = 0.3$ m)

x,m	u'/U_e	L_e/δ	δ,mm	θ,mm	c_f	H
0.61	.0597	1.16	27.4	1.68	.00434	1.300
1.22	.0399	1.03	39.2	2.72	.00377	1.291
1.82	.0307	0.93	50.9	3.66	.00347	1.285
2.43	.0255	0.90	58.9	4.54	.00323	1.291

Set E (76 mm grid, $X_{LE} = 0.3$ m, heater wires near LE)

x,m	u'/U_e	L_e/δ	δ,mm	θ,mm	c_f	H
0.91	.0482	0.77	46.7	2.95	.00388	1.260
1.22	.0399	0.71	56.9	3.48	.00368	1.260
2.43	.0255	0.67	78.4	5.23	.00325	1.264

boundary layer below a turbulence-free stream at the same momentum-thickness Reynolds number.

2.4 Techniques and Accuracy Estimate. Skin-friction values were obtained from pitot velocity profile measurements in the logarithmic region, assuming that the constants in the "log" law are not disturbed by free-stream turbulence. The justification of this assumption is that the log law is extraordinarily insensitive to the variation of turbulence intensity in the outer part of ordinary turbulent boundary layers in various pressure gradients: direct evidence for its applicability is provided by the goodness of fit of the present profiles to the *slope* of the universal logarithmic law. Preston tube measurements of skin friction, which assume the logarithmic law is unaffected, were also made for several cases, using the calibration of Patel [6], and these agreed with the values from the velocity profiles.

Two-dimensionality of the flow was assessed from Preston-tube measurements off the plate center line, which showed spanwise variations of no more than ±2 percent, and by deducing skin friction (on the central line) from the two-dimensional momentum integral equation. Of the 22 values, of c_f so deduced, 15 were within ± 10 percent deviation from Preston-tube values – the bound considered by Coles [7] as classifying "normal" boundary layers – and all but one within ±20 percent.

Accuracy of the measured changes in c_f due to free-stream turbulence, the key result of the present paper, is controlled by the *repeatability* rather than the absolute accuracy, of measurements of c_f, which was found to be generally ±1 percent at 20:1 odds (see Fig. 2(*a*)).

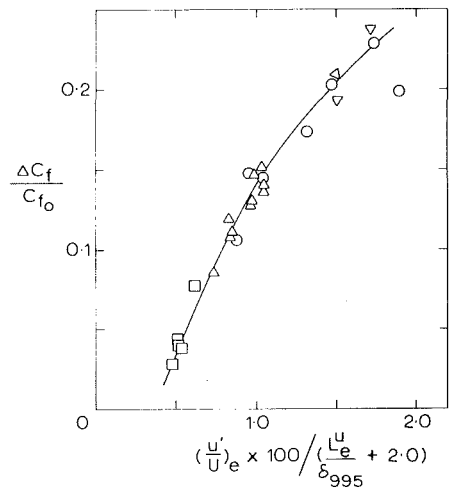

Fig. 2(*a*) Present measurements: parameter range and symbols as in Fig. 1(*b*)

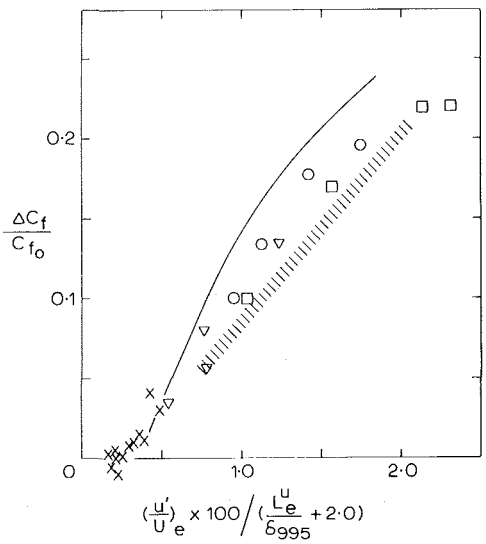

Fig. 2(*b*) Present and previous measurements: _____, fit to data of Fig. 2(*a*); symbols for other workers' data as in Fig. 1(*a*). . . . , Hatching as on dry present analysis of Charnay [12]. For data of Blair see [8].

Fig. 2 Correlation of fractional change in skin-friction coefficient as a function of free-stream intensity and length scale: c_{fo} is value in low-turbulence stream at same $U_e\theta/\nu$

3 Results

Figure 1 shows the area in the intensity/length-scale plane covered by previous workers (Fig. 1(*a*)), and by the present work (Fig. 1(*b*)). In the latter figure the curves are the trajectories of individual runs (i.e., sets of measurements at different positions downstream of the leading edge of the plate, for a fixed position of the plate downstream of a given grid). The reasons for the highly restricted coverage of previous work are discussed in Section 4. Details of test conditions are given in Table 1.

Figure 2 shows the response of the skin friction coefficient c_f at given $u_e\theta/\nu$, to the imposition of free-stream turbulence. The abscissa is a purely empirical parameter chosen by trial and error to collapse present and previous data as well as possible: individual variables are tabulated in Table 1. Figure 3 shows the one-to-one correspondence between changes in c_f, at given $u_e\theta/\nu$, and changes in the profile shape parameter H: as will appear below, the alternative shape parameter, the "wake strength" Π, is difficult to define in flows with high

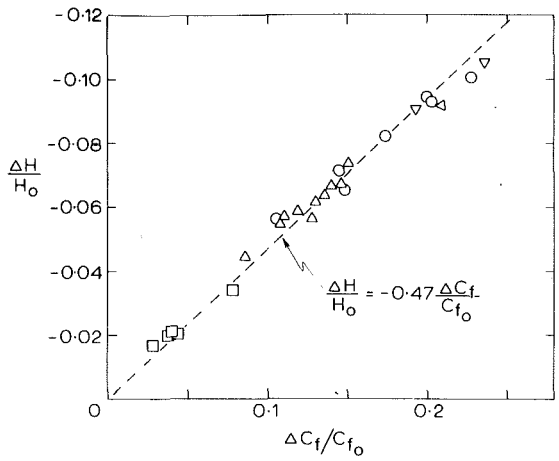

Fig. 3 Correlation between fractional increase in shape parameter $H \equiv \delta^*/\theta$ and c_f: present data; symbols as in Fig. 1(*b*)

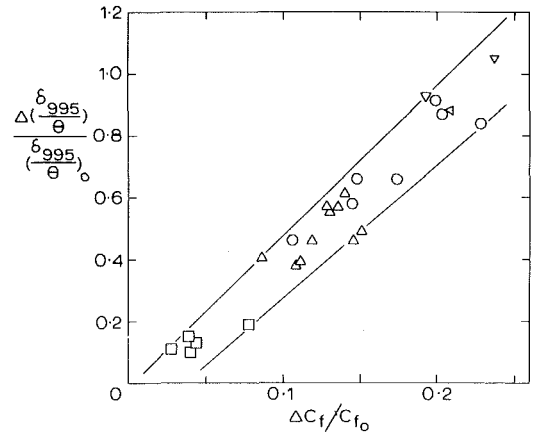

Fig. 4 Correlation between fractional increase in shape parameter δ_{995}/θ and c_f: symbols as in Fig. 1(*b*)

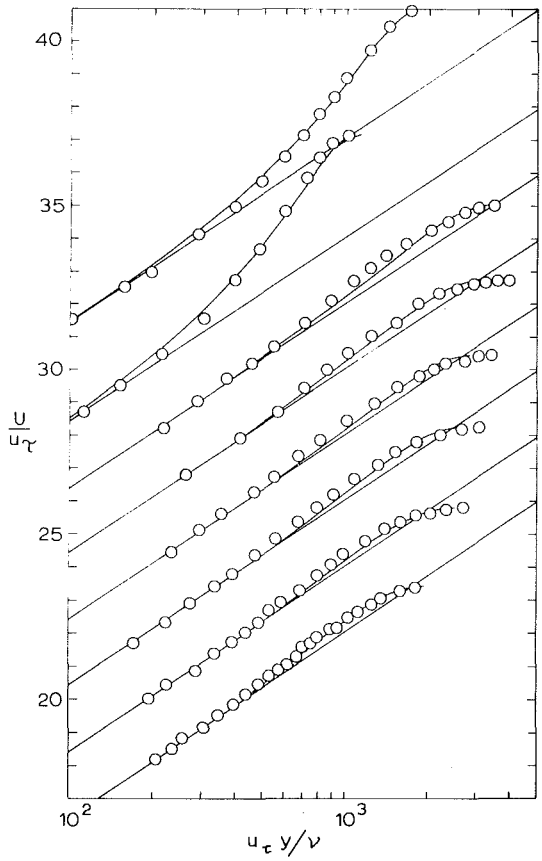

Fig. 5 Mean velocity profiles on "logarithmic law" plot. Top two profiles, low-turbulence stream: bottom six profiles 152 mm grid, plate leading edge 2.06 m from grid, profile set *C* in Fig. 1(*b*), *x* increasing upwards. Solid lines, equations (4) and (5). Ordinate scale refers to lowest profile.

free-stream turbulence, except in relation to a given empirical velocity profile "family." Figure 4 shows the somewhat less close correlation between the change in boundary layer thickness δ_{995}, at given θ, and the change in c_f. As the sample velocity profiles in Fig. 5 show, the velocity approaches the free-stream value very slowly if the free-stream turbulence intensity is high.

Detailed turbulence measurements will be presented in a separate paper, and are given by Hancock [3]. Figure 6 shows normal-component mean-square intensity profiles, corresponding to the first and last mean-velocity profiles of the group of 6 shown in Fig. 5. The measurements were made with *x*-array hot wire probes, and the u-component mean-square values are seen to agree well with check measurements made with a single-wire probe responding to u only. Figure 7 shows shear-stress profiles for the same conditions as Fig. 6. As expected, the shear stress tends to zero outside the boundary layer while the three mean-square intensities become nearly equal. The x z-plane shear stress, $-\rho\overline{uw}$, is nearly zero everywhere as it should be in two-dimensional flow.

4 Discussion

The region of the intensity/length-scale plane covered by previous reliable data is shown in Fig. 1(*a*), and the individual measurement points would be regarded, by an uninformed observer, as a tolerably good approximation to a single straight line! Obviously, the length scale L_e of the free-stream turbulence cannot be larger than a typical transverse dimension of the working section. Consequently if the measurements are to avoid low-Reynolds-number effects there must be an upper limit to the value of L_e/δ obtainable in a given facility, varying inversely as the lower limit set on the Reynolds number $U_e\delta/\nu$. *Small* values of L_e/δ can be obtained only at low intensities (i.e., far downstream where δ is large). Finally, the maximum permissible intensity is limited, almost independently of length scale, by the need to avoid excessive intensities at the plate leading edge, coupled with the need for a sufficient development length to avoid low-Reynolds-number effects. The effect of these various restrictions on the coverage of the present results is seen in Fig. 1(*b*), but, once the problems were realized, it was at least possible to cover a larger range than previous experiments. Our failure to reach the large intensities attained by Robertson and Holt [13] is explained by the lower limit we set on the momentum-thickness Reynolds number (their high-intensity results having being obtained at a momentum-thickness Reynolds number of only 400). The topic is discussed further in [3].

The simplest measure of free-stream turbulence effects is the response of the skin-friction coefficient c_f shown in Fig. 2(*a*); the abscissa is purely empirical and a more complicated parameter would probably be required to cover a larger range of length-scale ratio and intensity, even for closely isotropic free-stream turbulence. There are not enough data points at small intensity to verify that the correlation is applicable to naturally-occurring wind-tunnel turbulence. Meier and Kreplin [2] found a decrease in c_f with increasing L_e as implied by our correlation, but considered it to be within the likely experimental error. The nonlinearity of the curve in Fig.

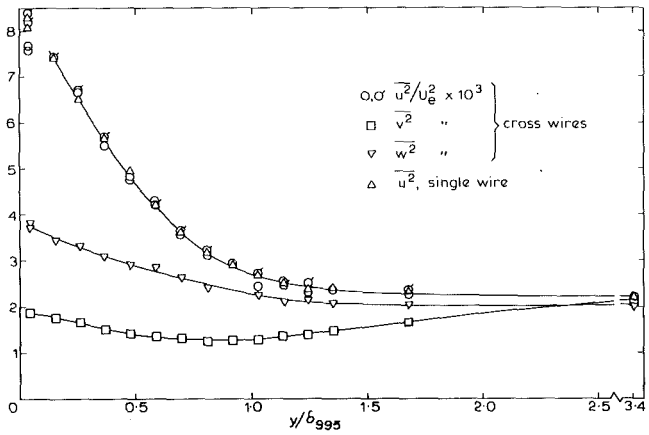

Fig. 6(*a*) $x = 0.912$ m, $(u'/U)_e = 0.0468$, $L^u_e/\delta_{995} = 2.72$

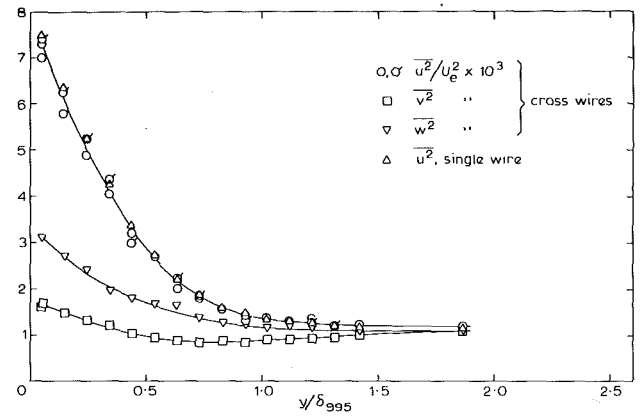

Fig. 6(*b*) $x = 2.432$ m, $(u'/U)_e = 0.0345$, $L^u_e/\delta_{995} = 1.55$

Fig. 6 Mean-square turbulence intensity profiles for same conditions as Fig. 5

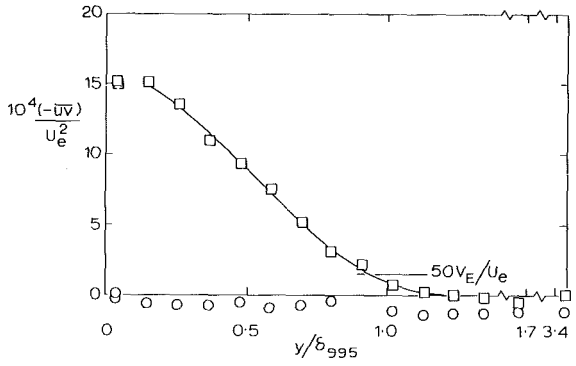

Fig. 7(*a*) $x = 0.912$ m, $(u'/U)_e = 0.0468$, $L^u_e/\delta_{995} = 2.72$

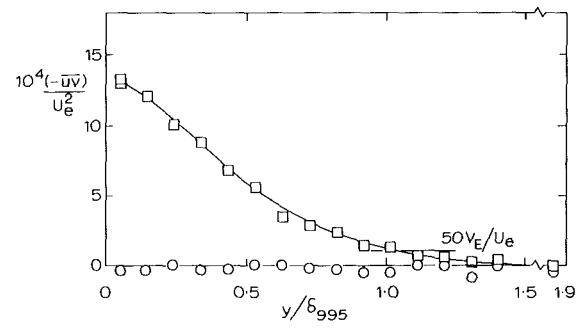

Fig. 7(*b*) $x = 2.432$ m, $(u'/U)_e = 0.0345$, $L^u_e/\delta_{995} = 1.55$

Fig. 7 Shear-stress profiles for same conditions as Fig. 5. Circles show $-\overline{uw}/U_e^2$ to same scale

2(*a*) is unmistakable, and borne out by previous results [2, 8, 10–13] as shown in Fig. 2(*b*). Meier and Kreplin [2] have clearly demonstrated that the variation of c_f with u' at small intensities is very much less rapid than at large intensities and it seems virtually certain that the response varies as the *mean square* rather than the rms intensity at small intensities, consistent with simple "superposition" arguments. The consensus of the other data suggests that the increase in skin-friction coefficient has a limiting value of little more than 0.2, but the present results suggest a stronger upward trend. The idea that further increase in c_f will be slow once the "wake" component of the velocity profile has been reduced to zero is probably a little too simplistic, although the postulated imperturbability of the logarithmic law does imply a lower limit on $U_e/u_\tau \cong \sqrt{(2/c_f)}$.

The decrease of free-stream turbulence effect variation with increasing length scale implied by Fig. 2(*a*) is to be expected, because of the effect of the wall in reducing the normal-component intensity, which is the component most likely to affect the boundary layer, below the free-stream value. The attenuation is a function of y/L_e, becoming insignificant for $y/L^u{}_e \gtrsim 1.3$ [9]. Being an effectively inviscid constraint it is not likely to depend on the properties of the boundary layer. (In the present work the free stream was defined as the region in which the mean velocity *and* the three turbulence intensities were independent of distance from the wall.) Values of $L^u{}_e/\delta_{995}$ larger than ours are likely to be of practical importance, but very small values are not, because unsheared turbulence with small scales decays rapidly as implied by equation (3). It is probable that c_f/c_{fo} decreases again at small length scales, because if the free-stream eddies are much smaller than the boundary layer eddies, "superposition" arguments, implying variation of Δc_f with $\overline{u^2}$ rather than – roughly – $\sqrt{(u^2)}$, are likely to apply again.

The Reynolds-number range of the data shown in Fig. 1(*b*) is $1600 < U_e\theta/\nu < 5000$ for the open symbols and $1600 < U_e\theta/\nu < 6000$ for the closed symbols. In the case of profile sets D and E, c_f/c_{fo} decreases with increasing distance from the leading edge and hence c_f/c_{fo} decreases with increasing Reynolds number, whereas for profile sets A, B and C, c_f/c_{fo} *increases* over the same distance and hence c_f/c_{fo} for these cases increases with Reynolds number. The success of a single correlation curve based upon intensity and length-scale ratio alone in correlating these different cases suggests that there is no significant Reynolds-number effect on the present data. Blair [8] shows that his data are well fitted by the present curve using a modified parameter $(u'/U)_e/(L^u_e/\delta_{995} + 2)\beta$, where $\beta \equiv (3e^{-\mathrm{Re}_\theta/400} + 1)$ is an additional empirical parameter to account for low Reynolds number effects. At $U_e\theta/\nu = 1600$, $\beta = 1.055$ which for $\Delta c_f/c_{fo} = 0.2$ is about equivalent to the estimated likely error in c_f of 1 percent. The single discrepant point in Fig. 2 differs from the trend more than this and would appear to be inaccurate.

Evidently, the relationship between $\Delta c_f/c_{fo}$ and $\Delta H/H_0$ in Fig. 3 is well fitted by a single curve, there being no evident trend with intensity length scale or Reynolds number. (Actually it is the behaviour of the Clauser shape parameter $G \equiv (1 - 1/\mathrm{H})\sqrt{(2/c_f)}$, rather than H, which is expected to be independent of Reynolds number, except at low Reynolds number). Figure 5 shows some sample velocity profiles, the solid lines being given by the logarithmic law and wake law,

$$\frac{U}{u_\tau} = \frac{1}{K}\ln\frac{u_\tau y}{\nu} + c + \frac{1}{K}\cdot g\left(\Pi, \frac{y}{\delta}\right) \tag{4}$$

with $K=0.41$, $c=5.2$, the "wake" component g being given by

$$g\left(\Pi, \frac{y}{\delta}\right) = (1+6\Pi)(y/\delta)^2 - (1+4\Pi)(y/\delta)^3 \quad (5)$$

This [14] is the simplest polynomial satisfying the boundary conditions, including the requirement that the slope of the velocity profile shall be zero at the outer edge of the boundary layer: the "cosine" formula frequently used for the wake does not satisfy the requirement, and is also unrealistic if Π is negative. Π and δ were evaluated in the usual way from U_e/u_τ and δ^*. Equation (5) provides a reasonable fit to the velocity profiles, except where $\Delta c_f/c_{fo}$ is large, that is where δ/θ is much larger and the "tail" of the velocity profile much longer than usual (Fig. 4). In any case, the velocity profile is a function of u_e'/u_τ, L_e/δ, and y/δ and so *any* wake function of the form $g(\Pi, y/\delta)$ is unlikely to be always adequate. The approximate similarity of the profiles in Fig. 5. is fortuitous because u_e'/u_τ and L_e/δ_{995} are by no means constant, and is due to the opposite effects of decreases in both intensity and length-scale ratio.

Figure 6 presents sample measurements of the three components of turbulence intensity for the first and last of the velocity profiles shown in Fig. 5. The decrease of the normal-component intensity below the free-stream value, as a result of the "inviscid" constraint applied to the solid surface, is particularly noticeable in Fig. 6(*a*) and it is seen that the intensities do not reach their free-stream values until $y \simeq 1.3\, L_e^u$. Figure 7 shows the corresponding shear-stress profiles (absolute values being apparently slightly too low) which show that the shear stress reaches zero well before the wall-constrained intensities reach their free-stream values, although the shear-stress profile at the smaller L/δ has a long "tail" corresponding to that in the velocity profile. No adjustment was applied to $-\overline{uv}$ to force it to zero in the free stream, although care was required in measuring the wire angles and probe alignment: for $u_e' = u_\tau$ a probe pitch error of 1 deg gives an error in $-\overline{uv}$ of $\sim 0.035\ u_\tau^2$. Some previous measurements [11] showed large shear stress at the edge of the mean velocity profile and well beyond, but must be regarded as doubtful. The shear stress at $y=\delta_{995}$, calculated from the entrainment rate $V_E \equiv d/dx\ (U_e(\delta_{995}-\delta^*))$ and the approximation $-\overline{uv}(y = \delta_{995}) = V_E U_e(1-0.995)$ compares well with the present hot-wire measurements as shown in Fig. 7.

4 Conclusions

The present results show that the strong nonlinear dependence of free-stream turbulence effects upon free-stream intensity, previously observed at low intensities by Meier [2], in fact occurs at all intensities. The results also show, apparently for the first time, that the free-stream length scale is also an important parameter. A purely empirical combination of intensity and length scale was found by trial and error to give a single-curve correlation for the skin-friction increase, as shown in Fig. 2. There is no reason to suppose the correlation will prove adequate over a much larger range of intensity and length-scale ratio than that from which it was deduced (Fig. 1(*b*)). In particular, the correlation is likely to break down at smaller values of L_e/δ_{995} where intuition suggests that the extra mixing due to free-stream turbulence will decrease. The variation of other integral parameters can be correlated linearly with the variation in c_f, and the velocity profiles can be fitted tolerably well, except when $\Delta c_f/c_{fo}$ is large, by the standard logarithmic law of the wall and cubic "wake" function. Intensity profiles clearly show that the "inviscid" constraint of the solid surface on the free-stream turbulence can be felt well outside the boundary layer, extending to a distance from the surface equal to about 1.3 times the length scale (L_e^u) of the free-stream turbulence.

References

1 Bradshaw, P., "Effects of Free-Stream Turbulence on Turbulent Shear Layers," Imperial College Aero Report 74-10, and ARC 35648, 1974.

2 Meier, H. U., and Kreplin, H. P., "Influence of Freestream Turbulence on Boundary Layer Development," *AIAA Journal*, Vol. 18, 1980, p. 11.

3 Hancock, P. E., "The Effect of Free-Stream Turbulence on Turbulent Boundary Layers," PhD thesis, Imperial College, London, 1980: available on microfiche from the author.

4 Cherry, N. J., "The Effect of Stream Turbulence on a Separated Flow With Reattachment," PhD thesis, Imperial College, London, 1982.

5 Murlis, J., Tsai, H. M., and Bradshaw, P., "The Structure of Turbulent Boundary Layers at Low Reynolds Numbers," *J. Fluid Mech.*, Vol. 122, 1982, p. 13.

6 Patel, V. C., "Calibration of the Preston Tube and Limitations on its Use in Pressure Gradients," *J. Fluid Mech.*, Vol. 23, 1965, p. 185.

7 Coles, D., "The Turbulent Boundary Layer in a Compressible Fluid," RAND Corp. Report R-403-PR, 1962.

8 Blair, M. F., "Influence of Free-Stream Turbulence on Turbulent Boundary Layer Heat Transfer and Mean Profile Development, Parts I and II," submitted for publication 1981.

9 Thomas, N. H., and Hancock, P. E., "Grid Turbulence Near a Moving Wall," *J. Fluid Mech.*, Vol. 82, 1977, p. 481.

10 Evans, R. L., "Free-Stream Turbulence Effects on the Turbulent Boundary Layer," Dept. of Engineering, University of Cambridge, Report CUED/A Turbo/TR41, 1972.

11 Huffaman, G. D., Zimmerman, D. R., and Bennett, W. A., "The Effect of Free-Stream Turbulence level on Turbulent Boundary Layer Behaviour," AGARD Proc. of Meeting on Boundary Layer Effects in Turbomachines, AGARDograph 164, 91 (Also, Detroit Diesel Allison Report), 1972.

12 Charnay, G., Comte-Bellot, G., and Mathieu, J., "Development of Turbulent Boundary Layer on a Flat Plate in an External Turbulent Flow," *AGARD Conference Proceedings*, No. 93, 1971.

13 Robertson, J. M., and Holt, C. F., "Stream Turbulence Effects on the Turbulent Boundary Layer," *Proc. ASCE*, Vol. 98, HY6, 1972, p. 1093.

14 Finley, P. J., Phoe, K. C., and Poh, C. J., "Velocity Measurements in a Thin Turbulent Water Layer," *Houille Blanche*, Vol. 21, 1966, p. 713: see also R. B. Dean, ASME JOURNAL OF FLUIDS ENGINEERING, Vol. 98, 1976, p. 723.

Laminar Flow in the Entrance Region of Elliptical Ducts

M. S. Bhatti
Owens-Corning Fiberglas Corporation,
Research and Development Division,
Technical Center,
Granville, Ohio 43023
Mem. ASME

A closed-form analytical solution is developed to hitherto unsolved problem of steady laminar flow of a Newtonian fluid in the entrance region of elliptical ducts. The analysis is based on the Karman-Pohlhausen integral method and entails solution of the integrated forms of the mass and the momentum balance equations. According to this analysis, the hydrodynamic entrance length based on 99 percent approach to the fully developed flow is equal to $0.5132\lambda/(1+\lambda^2)$ *where* λ *is the aspect ratio. Also, the fully developed incremental pressure defect is found to be 7/6 which is independent of the aspect ratio. In the limit when the flow becomes fully developed, the solution converges to the known exact asymptotic solution. Available, wide-ranging velocity measurements for a circular tube agree with the analytical predictions within 7 percent. Also, available pressure drop measurements near the inlet of a circular tube agree with the analytical predictions within 2 percent.*

Introduction

A survey of the literature on laminar duct flows revealed that the problem of flow development in elliptical ducts has not been solved [1]. Only two aspects of the problem have received some attention. Lundgren, et al. [2] predicted the fully developed incremental pressure defect for elliptical ducts without solving for the velocity development. Subsequently, McComas [3] extended the analysis of Lundgren, et al. [2] to predict the hydrodynamic entrance lengths for elliptical ducts. The problem of flow development in the limiting case of a circular tube, on the other hand, has been attacked by a number of investigators by a variety of methods. These solutions have been well reviewed and categorized by Shah and London [1]. In the present paper a compact and closed-form analytical solution is presented to the problem of flow development in elliptical ducts. The solution is based on the Karman-Pohlhausen integral method. The predictions of the present analysis are in remarkably close agreement with the available velocity [4, 5, 6] and pressure drop [7] measurements for the limiting case of a circular tube.

Analysis

The physical system under investigation is sketched in Fig. 1 which shows that the flow field is idealized as consisting of a viscous boundary layer along the duct wall and an essentially inviscid fluid core around the duct axis. At the duct inlet the flow velocity w_0 is uniform. The outer boundary of the viscous region is the duct wall represented by the ellipse $X^2+Y^2=1$. The inner boundary of the viscous region is another ellipse represented by $X^2+Y^2=\beta^2$ where β is a boundary layer parameter varying with the streamwise coordinate. The physical significance of β together with derivation of the equation $X^2+Y^2=\beta^2$ is provided in the Appendix.

Basic Equations. With the usual boundary layer theory simplifications, the steady laminar flow of a Newtonian fluid in the hydrodynamic entrance region of an elliptical duct can be described by the axial momentum balance equation

$$\rho\left(u\frac{\partial w}{\partial x}+v\frac{\partial w}{\partial y}+w\frac{\partial w}{\partial z}\right)=-\frac{dp}{dz}+\mu\left(\frac{\partial^2 w}{\partial x^2}+\frac{\partial^2 w}{\partial y^2}\right) \tag{1}$$

and the continuity equation

$$\frac{\partial u}{\partial x}+\frac{\partial v}{\partial y}+\frac{\partial w}{\partial z}=0 \tag{2}$$

Introducing the dimensionless variables, equations (1) and (2) transform to

$$\lambda U\frac{\partial W}{\partial X}+V\frac{\partial W}{\partial Y}+\frac{\sqrt{\lambda}}{\mathrm{Re}}W\frac{\partial W}{\partial Z}=\frac{\sqrt{\lambda}}{2\mathrm{Re}}\frac{dP}{dZ}+\frac{1}{\sqrt{\lambda}\mathrm{Re}}\left(\lambda^2\frac{\partial^2 W}{\partial X^2}+\frac{\partial^2 W}{\partial Y^2}\right) \tag{3}$$

$$\lambda\frac{\partial U}{\partial X}+\frac{\partial V}{\partial Y}+\frac{\sqrt{\lambda}}{\mathrm{Re}}\frac{\partial W}{\partial Z}=0 \tag{4}$$

Integrating equation (3) across the duct cross section by utilizing equation (4), we obtain the integrated form of the momentum balance equation

$$\frac{d}{dZ}\int_{X=0}^{1}\int_{Y=0}^{\sqrt{1-X^2}}W^2\,dX\,dY=\frac{\pi}{8}\frac{dP}{dZ}$$

Contributed by the Fluids Engineering Division and presented at the ASME Applied Mechanics, Bioengineering, and Fluids Engineering Conference, Houston, Texas, June 20-22, 1983 of THE AMERICAN SOCIETY OF MECHANICAL ENGINEERS. Manuscript received by the Fluids Engineering Division, June 11, 1982. Paper No. 83-FE-1.

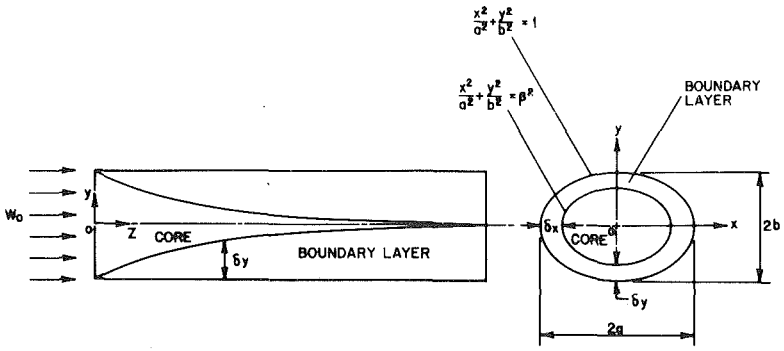

Fig. 1 Physical system

$$+\frac{1}{\lambda}\left[\lambda^2\int_{Y=0}^{1}\left(\frac{\partial W}{\partial X}\right)_{X=\sqrt{1-Y^2}}dY + \int_{X=0}^{1}\left(\frac{\partial W}{\partial Y}\right)_{Y=\sqrt{1-X^2}}dX\right] \quad (5)$$

In arriving at equation (5), the no-slip condition along the duct wall and the symmetry conditions along the duct axes have been utilized. Imposition of these conditions causes the transverse velocity components U and V to drop out from equation (5) without any assumptions regarding their magnitudes. This means that in equation (5) attention need be confined to the axial velocity W and the axial pressure P which are the principal momentum transfer quantities of interest. An additional relation is required to determine W and P. Such a relation is provided by the integrated form of the mass balance equation which can be obtained simply by equating the mass flow rate at the duct inlet to that at an arbitrary axial location. Thus,

$$\int_{X=0}^{1}\int_{Y=0}^{\sqrt{1-X^2}} WdXdY = \frac{\pi}{4} \quad (6)$$

Axial Velocity Profile. In order to solve the system of equations (5) and (6), we shall assume the following velocity profile within the boundary layer

$$W_b = \frac{W_c(1-X^2-Y^2)}{(1-\eta)} \quad (7)$$

where $W_c = W_c(Z)$ is the axial velocity in the inviscid core. Equation (7) is obtained by a generalization of the following velocity profile

$$W = W_c(1-X^2-Y^2) \quad (8)$$

prevailing in the fully developed region. In equation (8), W_c denotes the axial velocity along the duct axis. For the fully developed flow $W_c = 2$. When the flow becomes hydrodynamically developed (i.e., $\eta = 0$), equation (7) becomes identical with equation (8). Likewise at the duct inlet where the flow is all inviscid equation (7) becomes identically zero. Furthermore, equation (7) shows that at the duct wall represented by $X^2 + Y^2 = 1$, $W_b = 0$. Thus the no-slip condition is satisfied. Finally, at the inner boundary of the viscous region represented by $X^2 + Y^2 = \eta$, equation (7) shows that $W_b = W_c$. Thus equation (7) is satisfied at all the boundaries of the flow field and as such constitutes an appropriate velocity profile.

Relationship Between W_c and η. Equation (7) represents the axial velocity W_b within the boundary layer in terms of the fluid core velocity W_c and the boundary layer parameter η both of which are functions of the streamwise coordinate Z. Before concerning ourselves with the streamwise variation of W_c and η, we will first establish one-to-one correspondence between them via the use of the mass balance equation (6). Introducing equation (7) into equation (6) and remembering that within the boundary layer $W = W_b(X,Y,Z)$ and within the fluid core $W = W_c(Z)$, we obtain after evaluating the appropriate surface integrals.

$$W_c = \frac{2}{(1+\eta)} \quad (9)$$

Equation (9) predicts that when $\eta = 1$, $W_c = 1$ which is the correct limit at the duct inlet where the flow is uniform. Equation (9) also predicts that when $\eta = 0$, $W_c = 2$ which is also the correct limit for the fully developed flow.

Relationship Between η and Z. As a part of the velocity

Nomenclature

a = semimajor axis of the duct wall
b = semiminor axis of the duct wall
f = local friction coefficient
$\bar{f}$ = average friction coefficient
K = dimensionless incremental pressure defect
p = static pressure within the duct
p_0 = static pressure at the duct inlet
P = $[(p_0 - p)/\frac{1}{2}\rho w_0^2]$, dimensionless axial pressure drop
Re = $(w_0\sqrt{ab}/\nu)$, Reynolds number
u,v,w = velocity components parallel to x,y,z axes, respectively
U,V,W = (u/w_0), (v/w_0), (w/w_0) dimensionless velocity components
w_0 = uniform velocity at the duct inlet
x,y,z = cartesian coordinates
X,Y = (x/a), (y/b), dimensionless spanwise coordinates
Z = $[(z/\sqrt{ab})/\mathrm{Re}]$, dimensionless streamwise coordinate
β = $(1-\delta_x/a)$ or $(1-\delta_y/b)$, dimensionless boundary layer thickness parameter
δ_x,δ_y = boundary layer thickness along the semimajor and semiminor axis, respectively
η = β^2, dimensionless boundary layer thickness parameter
λ = (b/a), duct aspect ratio
μ = dynamic viscosity
ν = (μ/ρ), kinematic viscosity
ρ = fluid density

profile assumption we shall now assume the streamwise variation of the boundary layer parameter η entering equations (7) and (9) in the form

$$Z = A(1 + B\eta^2 + C\ln\eta^2) \tag{10}$$

where A, B, C are constants to be determined from the appropriate boundary conditions. The first of these conditions is that at the duct inlet the boundary layer thickness is zero which translates to $\eta = 1$ at $Z = 0$. The second boundary condition expresses the fact that at the duct inlet the streamwise growth of the boundary layer is identical to that on a flat plate at zero incidence. From Blasius' solution [8] it is known that for a flat plate at zero incidence the boundary layer thickness $\delta \sim \sqrt{z}$ whence using the definition of η it follows that at $Z = 0$, $d\eta/dZ = -\infty$, i.e., $dZ/d\eta = 0$. Using these two boundary conditions in conjunction with equation (10), we obtain $B = -1$ and $C = 1$. The constant A can now be determined from the process of matching the axial pressure predicted by Bernoulli's equation to that predicted by equation (7) at the duct inlet where the flow is inviscid. Combining Bernoulli's equation $P = W_c^2 - 1$ with equation (9), we obtain

$$P = \frac{4}{(1+\eta)^2} - 1 \tag{11}$$

Next, the pressure drop predicted by equation (7) at the duct inlet is governed by

$$\frac{dP}{dZ} = \frac{4W_c}{(1-\eta)} \frac{(1+\lambda^2)}{\lambda}$$

which is obtained from equation (3) by setting $U = V = W = 0$ and $(\partial^2 W/\partial X^2) = (\partial^2 W/\partial Y^2) = -4/(1-\eta^2)$ as obtained from equations (7) and (9). Combining the foregoing equation with equation (10) with $B = -1$ and $C = 1$, we obtain

$$\frac{dP}{d\eta} = \frac{16A}{\eta}\left(\frac{1+\lambda^2}{\lambda}\right)$$

The solution of this equation subject to the boundary condition that at $\eta = 1$, $P = 0$ is

$$P = 16A\left(\frac{1+\lambda^2}{\lambda}\right)\ln\eta \tag{12}$$

Equating the pressures given by equations (11) and (12), we get

$$16\left(\frac{1+\lambda^2}{\lambda}\right)A = \lim_{\eta \to 1}\left[\frac{4-(1+\eta)^2}{(1+\eta)^2 \ln\eta}\right]$$

By the application of l'Hospital's rule, the limit of the quantity on the right-hand side is seen to be -1. Thus the constant A is found to be equal to $[-\lambda/16(1+\lambda^2)]$. Having determined the three constants, equation (10) can finally be written as

$$16\left(\frac{1+\lambda^2}{\lambda}\right)Z = (\eta^2 - 1 - 2\ln\eta) \tag{13}$$

Equation (13) shows that at $\eta = 0$, $Z = \infty$ and $(d\eta/dZ) = 0$. This means that the flow becomes hydrodynamically developed asymptotically at $Z = \infty$. Thus the present analysis does not suffer from the drawback of McComas' analysis [3] according to which the flow becomes developed abruptly at a finite distance from the duct inlet. When the flow becomes developed abruptly, the condition $(d\eta/dZ) = 0$ is not satisfied. The physical meaning of this condition is that once the flow becomes fully developed, the streamwise variation of the boundary layer thickness ceases due to the fact that the viscous boundary layer now spans the entire duct cross section.

Hydrodynamic Entrance Length (Z_∞). The hydrodynamic entrance length Z_∞ is the dimensionless axial distance required for the viscous flow to cover the entire duct cross section. This happens when $\eta = 0$. As pointed out above, equation (13) predicts that $\eta = 0$ at $Z = \infty$. This being the case for practical purposes we shall define Z_∞ as that axial distance at which the center line velocity W_c is within 1 percent of its ultimate fully developed value 2, i.e., $W_c = 1.98$. Introducing $W_c = 1.98$ into equation (9), we notice that when $W_c = 1.98$, $\eta = 0.01$. Introducing $\eta = 0.01$ into equation (13), we obtain

$$Z_\infty = 0.5132\left(\frac{\lambda}{1+\lambda^2}\right) \tag{14}$$

Axial Pressure Drop (P). All the ingredients for the determination of the axial pressure drop P from the momentum equation are now in hand and we proceed to determine it by introducing equations (7) and (9) into equation (5). When the indicated surface integrals are evaluated with due regard to the limits of applicability of equations (7) and (9), we obtain after considerable algebraic manipulation

$$\frac{dP}{dZ} = \frac{8}{(1-\eta^2)}\left(\frac{1+\lambda^2}{\lambda}\right) - \frac{16}{3}\frac{\eta}{(1+\eta)^3}\frac{d\eta}{dZ} \tag{15}$$

Determining $(d\eta/dZ)$ from equation (13) and introducing it into equation (15), we have

$$\frac{dP}{dZ} = \frac{8}{(1-\eta^2)}\left[\frac{3\eta^3 + 9\eta^2 + 25\eta + 3}{3(1+\eta)^3}\right]\left(\frac{1+\lambda^2}{\lambda}\right) \tag{16}$$

Setting $\eta = 0$ in equation (16), we get $dP/dZ = [8(1+\lambda^2)/\lambda]$ which is the correct fully developed limit for dP/dZ. Setting $\eta = 1$ in equation (16) it is seen that $dP/dZ = \infty$. This simply means that at the duct inlet pressure changes very rapidly.

Next, to determine the axial pressure drop P from equation (15), we eliminate Z between equations (13) and (15) and solve the resulting differential equation subject to the boundary condition that at $\eta = 1$, $P = 0$. This leads to

$$P = \frac{2(1-\eta)(1+3\eta) - 3(1+\eta)^2\ln\eta}{3(1+\eta)^2} \tag{17}$$

which is the desired pressure distribution in the entrance region of elliptical ducts. Since one-to-one correspondence between η and Z is established by equation (13), the use of equation (17) in conjunction with equation (13) gives the required axial variation of P.

Incremental Pressure Defect (K). In duct flows, it is customary to represent the axial pressure drop as a difference between the actual pressure and an ideal pressure which is considered hydrodynamically developed right from the duct inlet. We shall call this pressure difference as the incremental pressure defect K. According to the present analysis the actual pressure is given by equation (17) and the ideal pressure can be determined from $dP/dZ = [8(1+\lambda^2)/\lambda]$ as $P = 8[(1+\lambda^2/\lambda]Z$. Combining this relation with equation (13), we can express the ideal pressure as

$$P = \tfrac{1}{2}(\eta^2 - 1 - 2\ln\eta) \tag{18}$$

Recalling the definition of K in conjunction with equations (17) and (18), we have

$$K = \frac{(3\eta^3 + 9\eta^2 + 21\eta + 7)(1-\eta)}{6(1+\eta)^2} \tag{19}$$

The fully developed value of K is obtained simply by setting $\eta = 0$ in equation (19). Thus, according to the present analysis $K_\infty = 7/6$ which is independent of the duct aspect ratio.

Friction Coefficients (f,$\bar{f}$). In engineering applications, it is customary to represent the relation between the pressure gradient (dp/dz) and the mean velocity of flow w_0 by introducing a friction coefficient f by setting the pressure gradient proportional to the dynamic head $\rho w_0^2/2$ according

to the relation $(dp/dz) = -(f\rho w_0^2)/(2\sqrt{ab})$. Introducing the dimensionless variables this can be written as $f\mathrm{Re} = (dP/dZ)$. Recalling equation (16), we have

$$\left(\frac{\lambda}{1+\lambda^2}\right) f\mathrm{Re} = \frac{8(3\eta^3+9\eta^2+25\eta+3)}{3(1-\eta^2)(1+\eta)^3} \tag{20}$$

When the flow becomes fully developed $\eta = 0$ and equation (20) predicts that $[\lambda/(1+\lambda^2)]f_\infty \mathrm{Re} = 8$ which is the correct fully developed limit of $f\mathrm{Re}$. In actual practice it is more useful to know the average value $\bar{f}$ of the friction coefficient. By definition

$$\bar{f}\mathrm{Re} = \frac{1}{Z}\int_0^Z f\mathrm{Re}\, dZ \tag{21}$$

Introducing equation (20) into equation (21) and evaluating the indicated integral via equation (13), we obtain

$$\left(\frac{\lambda}{1+\lambda^2}\right)\bar{f}\mathrm{Re} = \frac{16}{3}\left[\frac{2(1-\eta)(3+\eta)-3(1+\eta)^2\ln\eta}{(1+\eta)^2(\eta^2-1-2\ln\eta)}\right] \tag{22}$$

By the repeated application of l'Hospital's rule it can be shown that the limiting value of the quantity on the right-hand side of equation (22) as $\eta \to 0$ is 8 which means $\bar{f}$ eventually converges to the same limit as f. Equations (20) and (22) also show that at the duct inlet, i.e., at $\eta = 1$, both f and $\bar{f}$ possess infinite values.

Results and Discussion

Using the analytical results derived in the preceding section, a number of momentum transfer quantities of practical interest are computed and presented in this section. Presentation of the results is vastly simplified as the duct aspect ratio λ is effectively absorbed in the streamwise coordinate Z. This eliminates the need for presenting separate sets of curves for ducts with different aspect ratios.

Axial Velocity Distribution in Elliptical Ducts. The axial velocity at any point in the flow field can be calculated by the use of equations (7), (9), and (13). The manner in which the results depicted in Fig. 2 were calculated consisted in assigning a value to X^2+Y^2 and computing the values of the axial velocity W for a series of values of η ranging between 0 and 1. For $X^2+Y^2 \le \eta$, W was calculated using equation (9) and for $X^2+Y^2 > \eta$, W was calculated using equation (7). For each value of η, the corresponding value of the stretched streamwise coordinate $[(1+\lambda^2)/\lambda]Z$ was calculated using equation (13).

One way to view the curves in Fig. 2 is to imagine that the duct cross section is divided into a number of zones by the concentric ellipses $X^2+Y^2 = C$ where $0 \le C \le 1$. Let each of these ellipses represent the cross section of the bounding surface of a stream tube extending from $Z=0$ to $Z=\infty$. Then the curves in Fig. 2 represent the velocity of the fluid particles on the surface of each of the stream tubes. For example, the curve corresponding to $X^2+Y^2=0$ represents the velocity along the duct axis which may be viewed as a stream tube of zero radius. Likewise the curve corresponding to $X^2+Y^2=1$ represents the velocity along the duct wall which is the outermost stream tube in a set of eleven stream tubes imagined to be constructed. It is seen from Fig. 2 that all the curves originate at $W=1$ and asymptotically approach the fully developed values of W given by equation (8).

Axial Velocity Distribution in Circular Tubes. The solution to the problem of flow development in a circular tube is obtained as a limiting case of the general solution to the problem of flow development in elliptical ducts. Figure 3 contains a set of nine curves representing the axial velocity distribution in the entrance region of circular tubes. These curves are obtained from equations (7), (9), and (13) in a manner analogous to the one used in deriving the curves in Fig. 2.

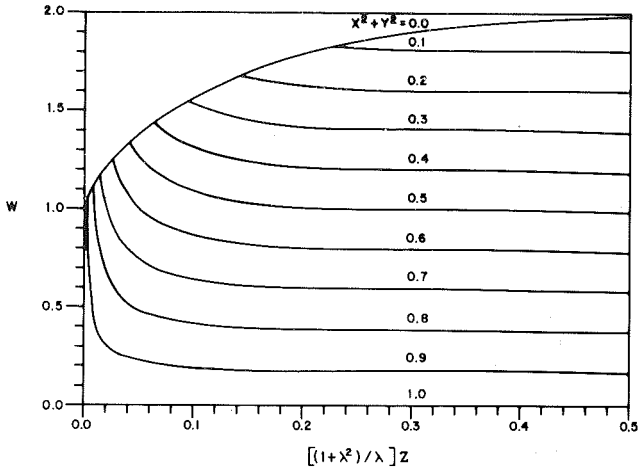

Fig. 2 Axial velocity distribution in the entrance region of elliptical ducts

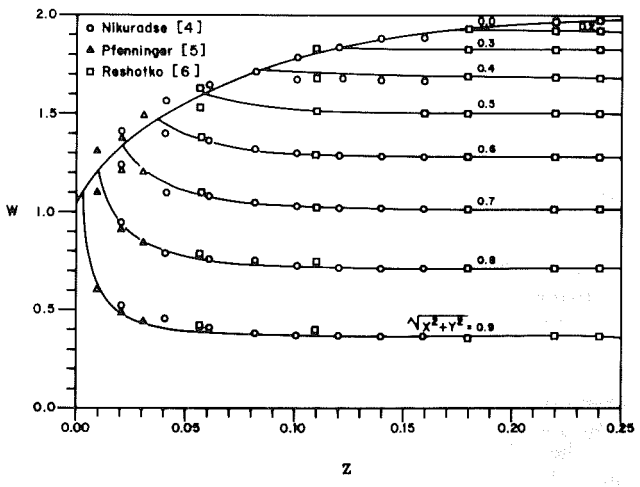

Fig. 3 Comparison of the predicted axial velocity distribution with the experimental measurements for a circular tube

The experimental data points shown in Fig. 3 are due to three independent investigators: Pfenninger [5], Nikuradse [4], and Reshotko [6]. The maximum deviation of the present analysis predictions from the experimental measurements is seen to be near the duct inlet section $Z<0.04$. This deviation is no more than 7 percent with the present analysis predictions generally lower than the measurements. Part of the reason for this deviation is attributable to the practical difficulties encountered in experimental setups to simulate the uniform flow condition at the duct inlet section. Farther down the duct $Z>0.04$, the present analytical predictions are practically indistinguishable from the experimental measurements.

Hydrodynamic Entrance Length. The hydrodynamic entrance length Z_∞ prediction of the present analysis based on 99 percent approach to the fully developed flow is given by equation (14). The only other analytical investigation with which to compare the prediction of equation (14) is that due to McComas [3]. The Z_∞ predictions of McComas appear to be in serious error not only due to their finiteness as already discussed but also due to their improper dependence on the aspect ratio λ. This can be best illustrated for the case of a duct with $\lambda = 0$. Physically $\lambda = 0$ represents a duct whose

semiminor axis is compressed to zero. Intuitively it is apparent that in such a duct no fluid flow can occur and as such Z_∞ of such a duct should be zero. According to reference [3], Z_∞ of duct with $\lambda=0$ is nonzero being 81 percent of the value for a circular tube. This latter value is predicted to be 0.1040. According to the present analysis for a duct with $\lambda=0$, $Z_\infty=0$ and for a duct with $\lambda=1$, i.e., circular tube, $Z_\infty=0.2566$ based on 99 percent approach to the fully developed flow.

Christensen and Lemmon [9] as well as Friedmann, et al. [10] have compared the predictions of Z_∞ for circular tube by various investigators. The predicted values range between 0.1040 and 0.2700. The values on the lower side are based on the analyses which predict abrupt approach to the fully developed flow and as such are inherently in error. The present analysis value of 0.2566 is on the higher side of the predicted values and compares favorably with the predictions of the analyses which are regarded as accurate. For example, in the above-cited references the values 0.2700, 0.2600, 0.2500, and 0.2440 are attributed to Campbell and Slattery, Boussinesq, Nikuradse, and Langhaar, respectively. The value of 0.2500 due to Nikaradse is an experimental value and compares particularly well with the present analysis value.

Axial Pressure Drop. The axial pressure drop at any cross section in the entrance region of elliptical ducts can be calculated from equations (17) and (13). The upper curve in Fig. 4 represents the axial pressure drop computed from these equations. Figure 4 also contains a straight line passing through the origin and sloping upward to the right. This line represents the ideal pressure drop given by equation (18) for a flow which is hydrodynamically developed right from $Z=0$. The vertical displacement of the actual pressure drop represented by the upper curve from the ideal pressure drop represented by the straight line is the incremental pressure defect K given by equation (19).

In the limit when the flow becomes hydrodynamically developed asymptotically at $Z=\infty$, K attains its fully developed value K_∞ which according to equation (19) is seen to be 7/6. This value is independent of the duct aspect ratio λ as is the value of 4/3 predicted by Lundgren, et al. [2] for elliptical ducts. The present analysis prediction of 7/6 is 12.5 percent lower than the prediction of Lundgren, et al. [2]. No experimental measurements of K_∞ for elliptical ducts are available to assess the relative accuracy of the two predictions. It appears that the analysis of [2] overestimates K_∞. This is inferred from the experimental measurements of K_∞ by Sparrow, et al. [11] for rectangular ducts vis-a-vis the predictions of Lundgren, et al. [2]. The K_∞ values measured by Sparrow, et al. [11] for ducts with aspect ratios 5 and 2, respectively, are 0.89 and 0.99 compared with the values 1.00 and 1.38 computed by Lundgren, et al. [2]. Thus for rectangular ducts the analysis of reference [2] overestimates K_∞ by 11 to 28 percent.

In ducts with discontinuities, K_∞ is a function of the aspect ratio. However, in elliptical duct K_∞ turns out to be independent of the aspect ratio. The explanation of this somewhat surprising result can be given in terms of the inertia force and the corner effect. Within the inviscid core of the entrance region there is a balance between the inertia and the pressure forces. Since the inertia force is proportional to the fluid acceleration and to the fluid core cross-sectional area, viz., $\pi(a-\delta_x)(b-\delta_y)$, it is apparent that the inertia force and hence the pressure force including its dimensionless measure K must depend on the aspect ratio b/a. The aspect ratio dependence of K in the entrance regions of ducts with discontinuities is more pronounced because the viscous effects in the neighborhood of the discontinuities are accentuated due to interaction among the viscous influence lines emanating normally from the adjoining surfaces. This is the so-called corner effect which is strongly dependent on the aspect ratio.

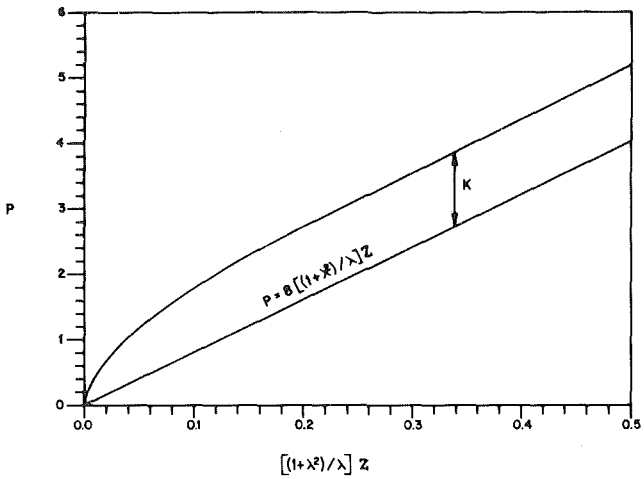

Fig. 4 Axial pressure drop in the entrance region of elliptical ducts

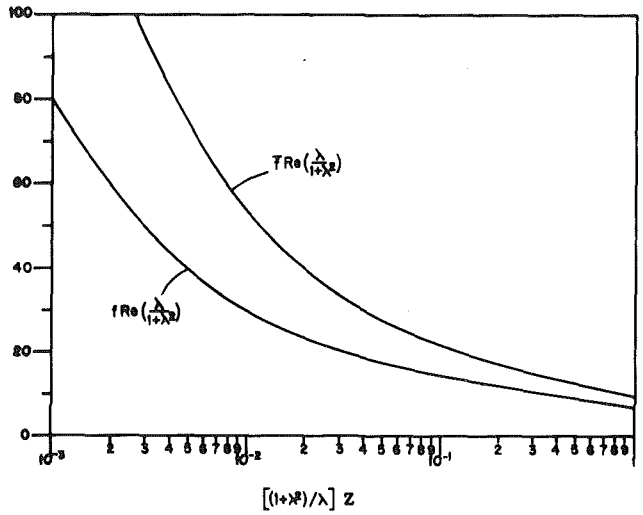

Fig. 5 Friction coefficients in the entrance region of elliptical ducts

When the flow becomes fully developed the inertia forces vanish thereby eliminating one source of aspect ratio dependence of K. Since in ducts with smooth continuous walls (e.g., circular and elliptical ducts), this is the only source of aspect ratio dependence, K_∞ for such ducts becomes independent of the aspect ratio. In ducts with discontinuities (e.g., rectangular and triangular ducts) the additional source of aspect ratio dependence, viz., the corner effect persists in the fully developed region. This renders K_∞ for such ducts a function of the aspect ratio.

According to the present analysis as well as the analysis of Lundgren, et al. [2], the predicted K_∞ values for elliptical ducts should apply to circular tubes since K_∞ is independent of the aspect ratio. Schmidt and Zeldin [12] have given rather extensive comparison of the predicted and the measured K_∞ values for circular tubes. The analytically predicted values range between 1.08 and 1.41 while experimentally measured values range between 1.00 and 1.45. The present analysis prediction of 7/6 falls on the lower side and the prediction of 4/3 by Lundgren, et al. [2] on the higher side of the spectrum of K_∞ values referred to above.

Some accurate measurements of the axial pressure drop in the entrance region of a circular tube were made by Shapiro, et al. [7]. Their experimental data in the range $0.00004<Z<0.004$ is correlated by the equation $P=6.87\sqrt{Z}$.

Within the range of applicability of this correlation, the predictions of the present analysis agree with the values computed from the correlation within 2 percent. Even beyond the range of applicability of the correlation, the analytical predictions agree fairly well with the values computed from the correlation. In the range $0.004 < Z < 0.02$, the agreement is within 10 percent. Thus it appears that the correlation can be extrapolated considerably beyond the range of the experimental measurements.

Friction Coefficients. The local friction coefficients f and the average friction coefficient $\bar{f}$ at any duct cross section can be calculated from equations (13), (20), and (22). The calculated results are displayed in Fig. 5. In constructing Fig. 5, the duct aspect ratio λ had to be incorporated in the abscissa as well as in the ordinate so as to obtain universal curves applicable to elliptical ducts with any value of λ.

At the duct inlet both f and $\bar{f}$ possess infinite values. This is due to the fact that f and $\bar{f}$ are derived from the pressure gradient given by equation (16) which has an infinite value at the duct inlet. The only physical significance to be attached to this infinite value is that at the duct inlet the axial pressure changes very rapidly due to the contribution of the viscous forces to the overall force balance.

Concluding Remarks

The problem of flow development in elliptical ducts is solved in closed-form by the Karman-Pohlhausen integral method. The resulting solution is extremely compact and readily amenable to practical use. The compact nature of the solution is attributable to the simplifying assumption that in the entrance region the inner boundary of the viscous region is elliptical. This assumption is justified in the Appendix. The available velocity and pressure drop measurements for a circular tube are in excellent accord with the analytical predictions. Also when the flow becomes hydrodynamically developed, the solution converges smoothly with the known exact asymptotic solution. Both these facts provide a certain degree of confidence in the present analysis.

References

1 Shah, R. K., and London, A. L., *Laminar Flow Forced Convection in Ducts*, Academic Press, New York, 1978.

2 Lundgren, T. S., Sparrow, E. M., and Starr, J. B., "Pressure Drop Due to the Entrance Region in Ducts of Arbitrary Cross-Section," ASME *Journal of Basic Engineering*, Vol. 86, 1964, pp. 620–626.

3 McComas, S. T., "Hydrodynamic Entrance Lengths for Ducts of Arbitrary Cross Section," ASME *Journal of Basic Engineering*, Vol. 89, 1967, pp. 847–850.

4 Prandtl, L., and Tietjens, O. G., *Applied Hydro- and Aero-mechanics*, Dover Publications, Inc., New York, 1957.

5 Pfenninger, W., "Experiments With Laminar Flow in the Inlet Length of a Tube at High Reynolds Numbers With and Without Suction," Technical Report, Northrop Aircraft Inc., Hawthorne, Calif., 1952.

6 Reshotko, E., "Experimental Study of the Stability of Pipe Flow," Progress Report No. 20-364, Jet Propulsion Laboratory, California Institute of Technology, Pasadena, Calif., 1958.

7 Shapiro, A. H., Siegel, R., and Kline, S. J., "Friction Factor in the Laminar Entry Region of a Smooth Tube," *Proc. U.S. Natl. Congr. Appl. Mech.*, 2nd Am. Soc. Mech. Eng., New York, 1954, pp. 733–741.

8 Schlicting, H., *Boundary Layer Theory*, McGraw-Hill, New York, 6th edition, 1968.

9 Christiansen, E. G., and Lemmon, H. E., "Entrance Region Flow," *AIChE Journal*, Vol. II, 1965, pp. 995–999.

10 Friedmann, M., Gillis, J., and Liron, N., "Laminar Flow in a Pipe at Low and Moderate Reynolds Numbers," *Applied Scientific Research*, Vol. 19, 1968, pp. 426–438.

11 Sparrow, E. M., Hixon, C. W., and Shavit, G., "Experiments on Laminar Flow Development in Rectangular Ducts," ASME *Journal of Basic Engineering*, Vol. 89, No. 1, Mar. 1967, pp. 116–124.

12 Schmidt, F. W., and Zeldin, B., "Laminar Flow in Inlet Sections of Tubes and Ducts," *AIChE Journal*, Vol. 15, 1969, pp. 612–614.

APPENDIX

It is a well-recognized fact that the viscous effects in a flowing fluid confined in a duct diffuse normally from the duct wall. The obvious reason for this is that at the duct wall there is a balance between the pressure and the viscous forces. Since the pressure force is impressed normally upon the duct wall, the viscous force must be directed normally away from it. The second fact to be recognized is that if there are no discontinuities such as sharp corners in the duct wall, the viscous influence lines emanating normally from the wall remain normal to all equal velocity curves. In other words, the influence lines and the equal velocity curves constitute a set of orthogonal trajectories. This is easy to visualize when it is remembered that the equal velocity curves are analogous to the isotherms and the influence lines are analogous to the flux lines in the related problem of heat flow in a duct with heated wall and flowing fluid. Now the normal diffusion of the viscous effects is possible if and only if the equal velocity curves have the same slope at the corresponding points. Since the duct wall itself is an equal velocity curve connecting zero velocity (no slip) points this is tantamount to saying that all equal velocity curves have the same shape as the duct wall and are concentric with it. Recognizing that the inner boundary of the viscous region is an equal velocity curve connecting inviscid core velocity points, it follows that the inner boundary of the viscous region in the present instance must be elliptical. Thus the inner boundary of the viscous region can be represented by

$$\frac{x^2}{(a-\delta_x)^2} + \frac{y^2}{(b-\delta_y)^2} = 1 \tag{A}$$

where δ_x and δ_y are the boundary layer thicknesses along the semimajor and semiminor axes, respectively, of the elliptical duct wall represented by

$$\frac{x^2}{a^2} + \frac{y^2}{b^2} = 1 \tag{B}$$

By differentiating equation (B) the slope of the duct wall at a general point (x_w, y_w) can be written as

$$\frac{dy}{dx} = -\left(\frac{b^2}{a^2}\right)\left(\frac{x_w}{y_w}\right) \tag{C}$$

Since the viscous influence lines are normal to the duct wall, their slope at a general point (x,y) must be negative reciprocal of the slope given by equation (C), i.e.,

$$\frac{dy}{dx} = \left(\frac{a^2}{b^2}\right)\left(\frac{y}{x}\right) \tag{D}$$

The influence lines themselves are the solution curves of the simple separable differential equation (D) which can be solved at once to yield

$$y = \gamma x^{a^2/b^2} \tag{E}$$

where γ is the integration constant. Equation (E) shows that the shape of the influence lines is a function of the aspect ratio $\lambda = b/a$. For example, for a circular duct with $\lambda = 1$, the influence lines are seen to be a family of straight lines $y = \gamma x$ which are readily recognized as the radial influence lines.

Now the normal diffusion of the viscous effects requires that the influence lines represented by equation (E) also be normal to the inner boundary of the viscous region at a general point (x_c, y_c). From equation (D) then slope of the inner boundary must be

$$\frac{dy}{dx} = -\left(\frac{b^2}{a^2}\right)\left(\frac{x_c}{y_c}\right) \tag{F}$$

By differentiating equation (A), the slope of the inner boundary at the general point (x_c, y_c) is also seen to be

$$\frac{dy}{dx} = -\frac{(b-\delta_y)^2}{(a-\delta_x)^2}\left(\frac{x_c}{y_c}\right) \tag{G}$$

Equating the slopes given by equations (F) and (G), we have

$$\frac{(b-\delta_y)}{(a-\delta_x)} = \frac{b}{a} \tag{H}$$

whence it follows that $(a-\delta_x)=\beta a$ and $(b-\delta_x)=\beta b$ where β is the proportionality constant. Introducing these relations into equation (A), the inner boundary of the viscous region can be represented by $X^2+Y^2=\beta^2$.

The physical significance of β can now be brought out with the help of Fig. 1 which shows that $(a-\delta_x)$ and $(b-\delta_y)$ are, respectively, the semimajor and semiminor axes of the elliptical inviscid core whereas a and b are the corresponding axes of the elliptical duct wall. From the relations $(a-\delta_x)=\beta a$ and $(b-\delta_y)=\beta b$ it is then seen that β is the ratio of the semimajor (or semiminor) axis of the inviscid core to the semimajor (or semiminor) axis of the duct. A more meaningful interpretation of β can be given in terms of η which equals β^2. The cross-sectional area of the duct is πab whereas the cross-sectional area of the inviscid core is $\pi ab\beta^2$. Thus β^2, i.e., η represents a fraction of the cross-sectional area carrying the inviscid flow. From this reasoning it is clear that at the duct inlet $\eta=1$ and at the end of the entrance region where the flow is completely viscous $\eta=0$.

Before concluding this Appendix, it behooves us to check reasonableness of equation (H) which can be recast for this purpose in the form

$$\frac{\delta_x}{\delta_y} = \frac{a}{b} \tag{I}$$

At the duct inlet $\delta_x=\delta_y=0$ and the equation (I) is identically satisfied. In the fully developed region $\delta_x=a$, $\delta_y=b$ and the condition (I) is again satisfied. Also for a circular duct with $a=b$, equation (I) predicts that $\delta_x=\delta_y$ which is physically correct. Thus condition (I) correctly predicts all known limiting values.

R. C. Hendricks

T. T. Stetz

National Aeronautics and Space Administration,
Lewis Research Center,
Cleveland, Ohio 44135

Studies of Flows Through N-Sequential Orifices

Critical mass flux and axial pressure profile data for fluid nitrogen are presented for $N = 20, 15, 10$, and 7 N-sequential-orifice-inlet configurations uniformly spaced at 15.5 cm. These data correlate well over a wide range in reduced temperature ($0.7 < Tr, 0 <$ ambient) and reduced pressure (to $Pr = 2$) and are in general agreement with previous studies of one to four inlets. Experimental and theoretical agreement is good for liquid and gas critical mass flux, but inconclusive in the near-thermodynamic critical regions.

Introduction

The inlets to many flow devices are not the smooth entrances often researched. Frequently they contain a series of constrictions which may not act independently of one another. This class of flows is categorized as having sequential inlets. Compressors, pin-finned heat exchangers, separators, and labyrinth and step seals are examples of inlet configurations consisting of two or more such constrictions or, in a stricter sense, sequential inlets. The details of the flow dynamics and heat transfer in these configurations are in many cases not well understood.

Similarity principles can often be applied to assist the designer in cases where the theory is incomplete or no data are available. In reference [1], the principle of similarity as applied to thermophysical properties and fluid mechanics (with emphasis on the thermodynamic critical region) is shown to qualitatively group the experimental results for several physical processes, including heat transfer and two-phase choked flows.

In other work [2–5] it was assumed that some form of similarity relationship between mass flux and reduced pressure was valid. It was then shown analytically and experimentally that critical mass flux through well-separated sequential inlets for $N < 4$ could be related to flow through a single inlet. The statement appears valid even for such diverse inlets as those of the orifice and Borda types [6].

These results also show that a similarity exists between the flow losses in a rough tube and those in sequential inlets. For example, consider a tube of length L that is artificially subdivided into N connected segments each of length L/N and an N-sequential inlet configuration. When the values of the friction parameter $4fL/D$ are of order one or more for each tube segment, the flow losses through these N connected tubes can be made equivalent to the flow losses through the N sequential inlets [6, 7].

The primary purpose of this paper is to extend the range of available critical (choked) flow and pressure profile data of N sequential orifice inlets with $N > 4$ for a large range of inlet stagnation conditions. As a secondary purpose, existing similarity principles will be used and others developed as required to enable designers to predict the critical mass flow through N sequential inlets and to provide assessments of the pressure profiles.

Apparatus and Instrumentation

The basic components and operations of the blowdown-type facility described in references [7] and [8] were modified to accommodate the various sequential-orifice-inlet configurations (Fig. 1).

A photograph illustrating the N-inlet test configurations, as installed in the facility, for $N = 7, 10, 15$, and 20, is shown in Fig. 2.

The orifice-type inlets with l/D of 0.5, similar to those of references [6] and [7], were designed with spacers of 15.24 cm (6.0 in.). These provided fixed spacings of 32 orifice diameters between apertures, or approximately 15.5 cm aperture to aperture. A schematic of a segment of an N-sequential-orifice-inlet configuration illustrating the pressure tap locations and the inlet geometry is presented in Fig. 3; a photograph of the orifice proper is shown in Fig. 4.

These sequential-inlet configurations were fitted between inlet and outlet flange adapters to accommodate the multiple lengths. Six threaded rods and two plastic spacers per segment were required to assemble and provide rigidity to the configuration. In principle there should be no problem with the assembly of N-inlet segments, but in practice small variations in rod tension and combined machining tolerances causes the system to behave like the connected linkages of a snake. The configurations were assembled on a flat bench and hoisted into position. The multiple surfaces were satisfactorily sealed by vacuum-greased mylar gaskets between the flat faces. Pressure and flow data were recorded using automatic digital equipment [7, 8].

In general, the agreement in mass flow rates as metered by the tank venturi and the exhaust orifice is ± 5 percent. The pressures and temperatures are within ± 1 percent, and systematic deviations between pressure transducers are less than ± 0.5 percent. The working fluid is nitrogen, and the

Contributed by the Fluids Engineering Division and presented at the ASME Applied Mechanics, Bioengineering, and Fluids Engineering Conference, Houston, Texas, June 20–22, 1983. Manuscript received by the Fluids Engineering Division, January 26, 1982. Paper No. 83-FE-22.

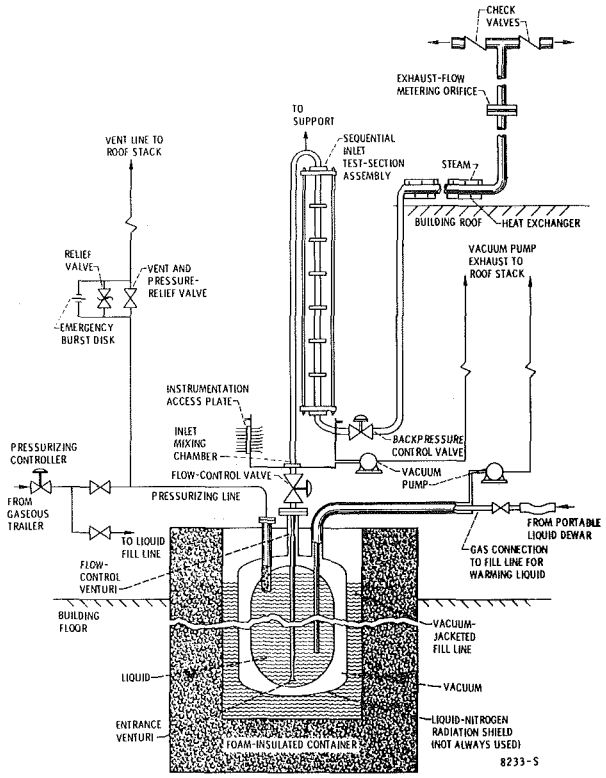

Fig. 1 Schematic of flow facility modified for operations with *N* sequential inlets

reduced inlet stagnation temperature ranges from 0.7 $T_{r,0}$ to ambient gas with the reduced inlet stagnation pressure to $P_{r,0} < 2.5$.

Results and Analysis

The theory for flows through sequential apertures (e.g., orifices) is not well developed. Previous success using a combined thermodynamic and choked-flow analysis will be applied here [6, 7, 9]. The governing equations are given in the Appendix and a description of the theoretical iterative approach used in solving the *N*-sequential-inlet problem follows.

The process at the *i*th inlet (Fig. 5) is assumed to expand isentropically through that inlet, followed by isobaric recovery in the spacer reservoir with (or without) heat addition. The solution is complicated by the fact that the pressure ratios across each inlet, $\zeta_i = P_{r,i}/P_{r,i-1}$, are unknown, and stability of the solution is not guaranteed. Thus, to solve the problem of flow through *N* inlets (Fig. 5), one must first determine the inlet properties for the first inlet at the given stagnation conditions. Next assume a pressure ratio across the first inlet, $\zeta_1 = P_{r,1}/P_{r,0}$; then calculate the conditions of the expansion and determine the stagnation

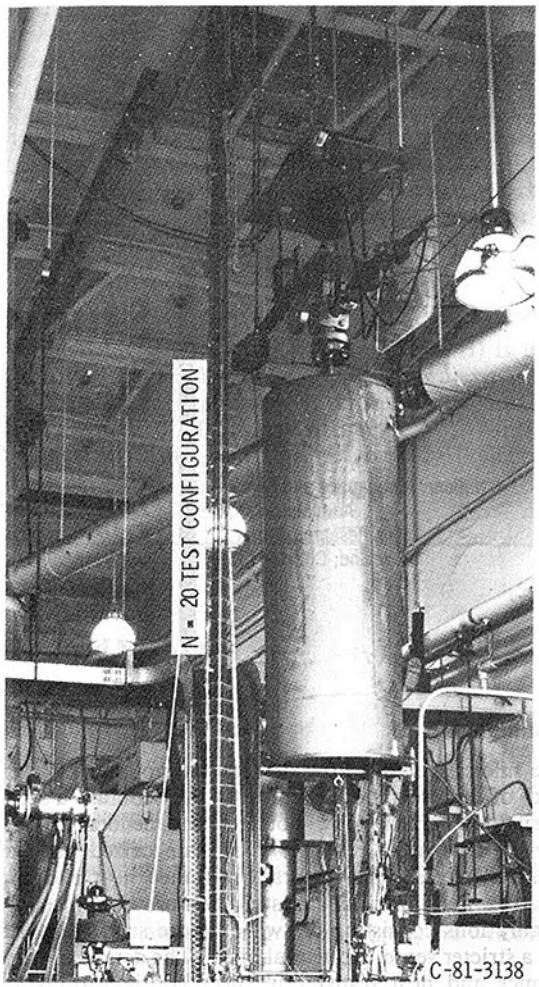

Fig. 2 Photograph of *N* = 7, 10, 15, and 20 sequential inlet installations

conditions for the next inlet (including heat addition or extraction in the reservoir spacers). Repeat for the next $N-1$ inlets. At the *N*th inlet, determine the expansion conditions and compare to those calculated from the choked flow constraint, including the effects of two-phase flows; if the flow rates and the pressure ratios are within a convergence range, they are said to be computed for the prescribed configuration of apertures (e.g., orifices) and any addition or reduction of heat in the spacer reservoirs.

In essence, the constraints form the basis of a variational approach in which a solution with the least increase in entropy is formulated with real fluid properties determined using the GASP code [10].

Choked Flow Rate. In theory, similarity exists via the

Nomenclature

C_f = flow coefficient
D = diameter of orifice or tube
f = function defined in equation (1)
G = mass flux
$G^* = \sqrt{\frac{\rho_c P_c}{Z_c}}$ = flow normalizing parameter, 6010 g/cm^2-s for nitrogen
g = function defined in equation (1)
L = tube length
l = orifice length
N = number of inlets
P = pressure
T = temperature
X = axial location
Z = compressibility
$1/V$ = density
ζ = pressure ratio

Subscripts

c = thermodynamic critical
i,j,M,N = ith, jth, Mth, Nth sequential inlet
0 = stagnation
r = reduced by normalizing parameter
v = venturi
1 = case for $N = 1$, the single inlet, or unit

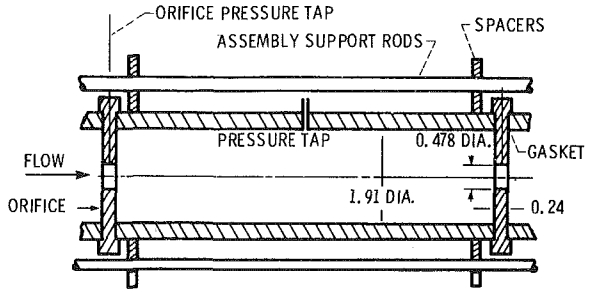

Fig. 3 Schematic of a segment of an *N*-sequential-orifice-inlet configuration

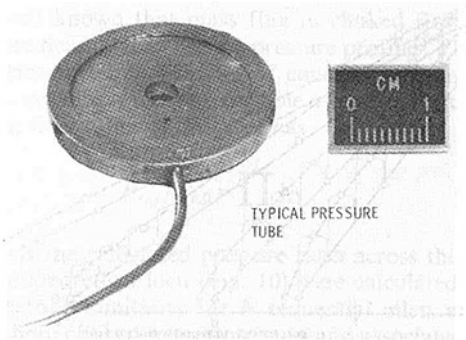

Fig. 4 Photograph of a typical orifice

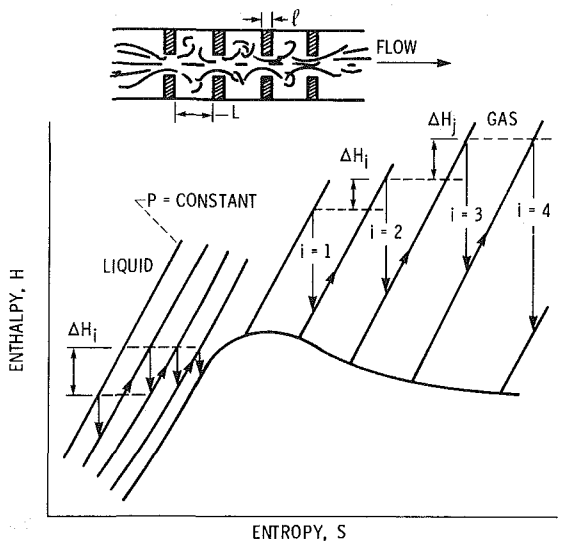

Fig. 5 Schematic H-S diagram of the *N*-sequential-inlet flow process

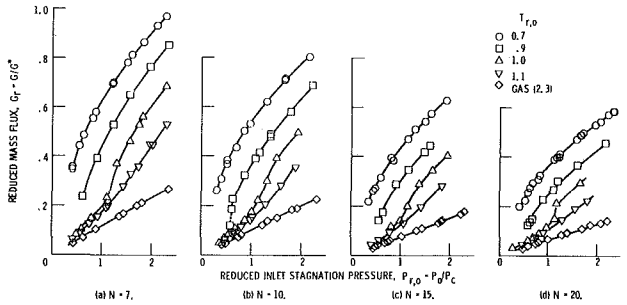

Fig. 6 Reduced mass flux as a function of reduced inlet stagnation pressure at selected reduced inlet stagnation temperatures, $T_{r,0}$ for *N* sequential orifice inlets with 15.2-cm spacer reservoirs

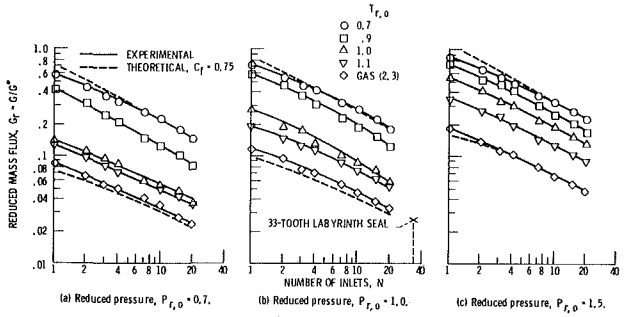

Fig. 7 Reduced mass flux versus number of orifice inlets at three reduced inlet stagnation pressures $P_{r,0}$ for selected reduced inlet stagnation temperatures $T_{r,0}$

$$G_{r,N}/G_{r,v} = g(C_f, N, T_{r,0} P_{r,0}) \tag{1}$$

$$G_{r,N}/G_{r,1} = f(N, T_{r,0}, P_{r,0}) \tag{2}$$

where

$$G_{r,1} = C_f G_{r,v}$$

The function g represents a loss coefficient for the configuration, and if the combined flow coefficient and friction factor losses for each inlet reservoir are similar, f applies. Even though much theoretical work has been done on flows through apertures, $G_{r,1}$ (the flow through the first inlet) usually results from a calibration facility where it is related in terms of flow through the classic venturi $G_{r,v}$ using a flow coefficient C_f. For the venturi $G_{r,v}$ can be predicted using the two-phase choked-flow theory [9] and with the similarity theory using corresponding states [1–5]. Consequently if the function f were known and $G_{r,1}$ was either estimated from theory or obtained by calibration or through other sources, then one could predict the mass flux through N sequential inlets over a wide range of temperatures and pressures for a variety of fluids.

These observations lead to the formulation of Fig. 7, which illustrates the similarity between reduced mass flux with the number of inlets for reduced inlet stagnation pressures of 0.7, 1.0, and 1.5 at selected values of reduced inlet stagnation temperature. Although the levels change with pressure, the locii are form similar at these pressures.

The function f is nearly exponential with N and is weakly dependent on inlet conditions ($P_{r,0}$, $T_{r,0}$). For many cases, the exponent may be considered a constant ranging from 0.35 for $N < 3$ to 0.45 for $N > 15$. Thus one may write:

$$f(N) = N^{-.4} \tag{3}$$

A slight improvement comes from a more complex quadratic relation. However, one can use the data figures directly.

Superimposed on the data of Fig. 7 are the theoretical locii calculated using the iterative procedures of the appendix and outlined previously. As can be seen, the data and the analysis are, in most cases, in reasonably good agreement. Moreover,

conservation equations (see also [1–5]). For the *N*-sequential-inlet problem, nonsimilar terms are lumped into the flow coefficients. Losses are also lumped into the flow coefficients, with the assumption that they remain nearly constant for all stages. This makes the problem tractable, but masks the complexity.

As pointed out earlier, similarity relationships between mass flux and reduced pressure have been demonstrated for $N < 4$. We must now establish form similarity for $N > 4$; this can be done as follows. As seen from Fig. 6 by comparing data for $N = 7$, 10, 15, and 20, the reduced mass flux locii are form similar with reduced inlet stagnation pressure $P_{r,0}$ for selected variations in the parameter, reduced inlet stagnation temperature $T_{r,0}$. This leads to normalizing the flow rates with respect to that of the first inlet as a function of N and the inlet stagnation conditions upstream of the first inlet ($T_{r,0}$, $P_{r,0}$).

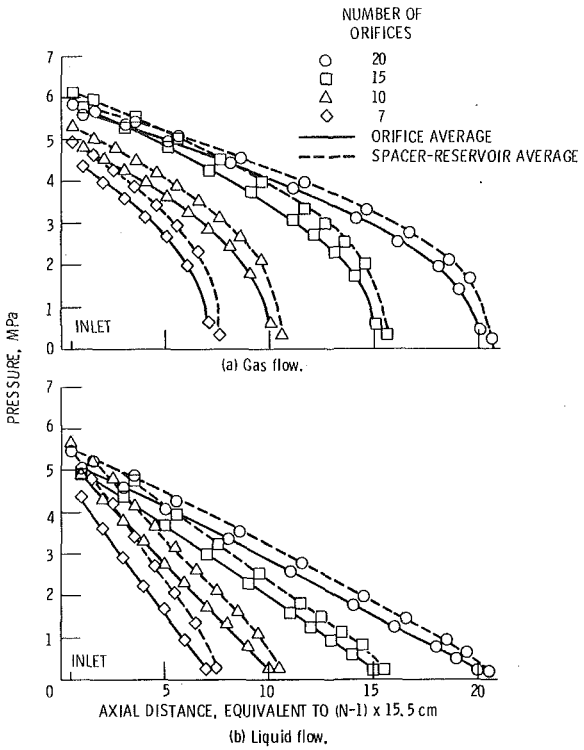

Fig. 8 Average connected-orifice and spacer-reservoir axial pressure profiles for 7, 10, 15, and 20 sequential orifice inlets for gas and liquid flows

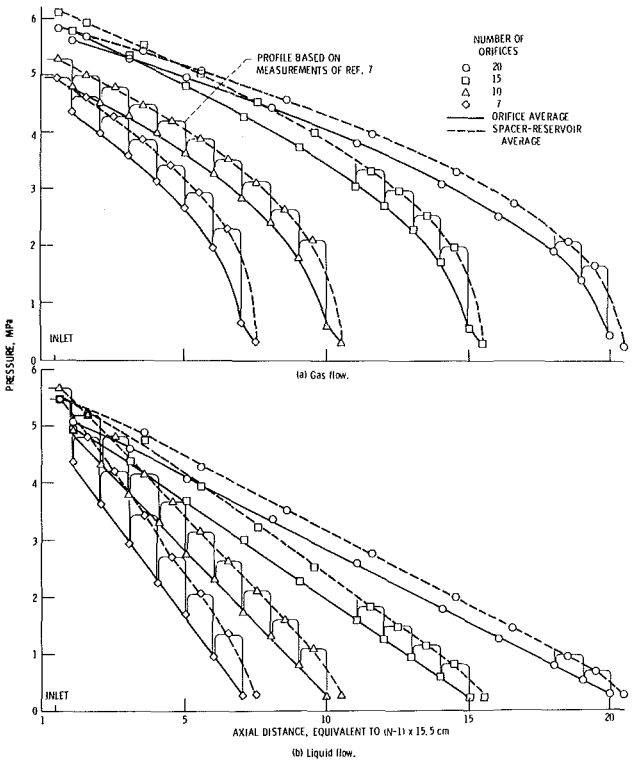

Fig. 9 A comparison of axial pressure profiles based on detailed measurements of reference [7] and average connected-orifice and spacer-reservoir profiles for 7, 10, 15, and 20 sequential orifice inlets for gas and liquid flows

the change of slope corresponding to the exponent variation (equation (3)) is also predicted by theory. As the results of the analysis have previously been shown to possess form similarity (valid for even such diverse apertures as the orifice and Borda types), it appears that extending the similarity hypothesis to the case of N sequential inlets is justified.

With equations (1) to (3), one can predict the mass flux for N sequential inlets over a large range in inlet temperature and pressure and possibly for a variety of fluids when either $G_{r,1}$ or C_f is known.

Pressure Profiles. Typical axial pressure profiles for the N-sequential-orifice-inlet configurations with inlet stagnation conditions ($T_{r,0}$, $P_{r,0}$) are given in Figs. 8 and 9. In both figures, part (a) represents gas flow and part (b) represents liquid flows. The abscissa represents the number of orifices in the configuration or the axial distance (e.g., 155 cm for N = 10). In Fig. 8 the spacer-reservoir pressures are connected by dashed lines and the orifice pressures are connected by solid lines. The pressure profiles between the orifice and the spacer reservoir (Fig. 9) can be inferred from the more detailed experimental work of references [6 and 7], and although such detail is not part of this experiment, the profiles can be represented by a series of 'horse-shoes' (Fig. 9). It should be immediately apparent that the locii of Figs. 8 and 9 for the gas and liquid cases differ significantly. In Figs. 8(*b*) and 9(*b*), the orifice locii vary almost linearly (slightly-concave) with axial position for each value of N tested, whereas in Figs. 8(*a*) and 9(*a*), they are convex or parabolic and are typical friction loss characteristics. The spacer-reservoir locii appear parabolic in either case, but are essentially linear for liquid flows. Such pressure profiles are not only characteristic of N sequential apertures, but also of flows through high L/D tubes [12] and shaft seals of high-performance turbomachines [13, 14].

The axial pressure profiles for inlet stagnation conditions ($T_{r,0}$, $P_{r,0}$) appear to be similar for large N when normalized

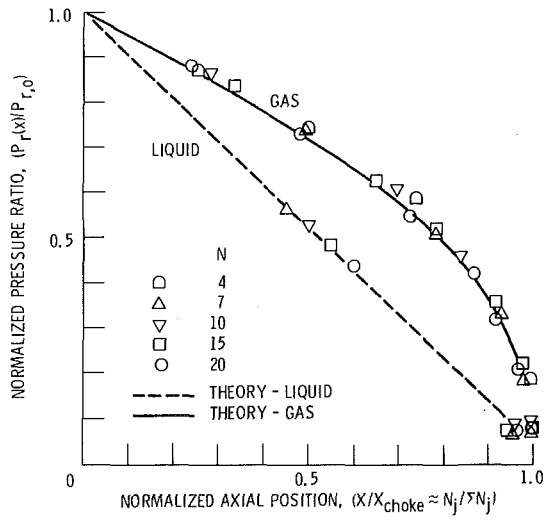

Fig. 10 Normalized axial pressure profiles for N sequential orifice inlets for gas and liquid flows

in terms of the number of sequential inlets and the inlet stagnation pressure.

$$\langle P_r \rangle_0 = P_r(x)/P_r(x=0) \tag{4}$$

$$\frac{X}{X_{\text{choke}}} = \frac{N_j}{\sum_{i=1}^{k} N_i} \tag{5}$$

where $P_r = P/P_c$, X the axial distance, X choke the distance to the point of choked flow (assumed to be in the exit orifice), and N_j represents a segment of an N-sequential-orifice-inlet configuration (Fig. 3). Applying equations (4) and (5) to the data of Fig. 8 produces the two distinct locii for all values of

N shown in Fig. 10. At this time, the limitations of equation (5) are not clear; e.g., the limits of N and that all the distances between N_j and $N_j - 1$ need be the same.

Since the liquid and gas profiles represent $T_{r,0} = 0.7$ and $T_{r,0} = 2.3$, respectively, it is quite apparent that the shapes of the locii of Fig. 10 depend on $T_{r,0}$. From earlier work, [13-15] it is known that these locii are nearly linear for $T_{r,0} < 1$; parabolic for $T_{r,0} > 1$; and experience a transition from linear to the parabolic near $T_{r,0} = 1$. However, at 16,200 L/D [13], the pressure locii are a little more concave than either here or for the shaft seals [13-14]. Such evidence indicates that for very large N, the liquid profiles will also be more concave. Such corroborating evidence also extends the hypothesis of the similarity relationship between N segmented rough tubes and N sequential inlets.

It is well known that mass flux in choked flows is more readily predictable than are the pressure profiles. Yet in terms of the normalized coordinates of equations (4) and (5), the pressures do appear to be predictable directly from the data or within the limitations of the theory as

$$P_{r,j}/P_{r,0} = \prod_{i=1}^{j} \zeta_i \tag{6}$$

where ζ_i is the calculated pressure ratio across the ith aperture. The theoretical locii (Fig. 10) were calculated for $N = 10$. Thus form similarity for N sequential inlets appears to exist for both choked-mass flow rates and associated pressure profiles.

Summary

We have presented critical mass flux and pressure profile data for N-sequential-orifice-inlet configurations where $N = 20$, 15, 10, or 7. The orifices were uniformly spaced at 15.5 cm, and the working fluid was nitrogen.

The data correlated well over a large range of reduced inlet temperatures from 0.7 $T_{r,0}$ to ambient and reduced pressures from near saturation conditions to $P_{r,0} = 2$. Data are also in good agreement with previous studies of one to four inlets.

The agreement between experiment and analysis is good for the liquid and gas critical mass flux cases, but inconclusive for the near-thermodynamic critical regions.

Pressure profiles normalized in terms of inlet stagnation pressure and axial distance to choke appear independent of the number of inlets. The pressure profile shape changes from slightly concave to convex (parabolic friction loss form) with increased inlet stagnation temperature.

It does appear that a form similarity hypothesis can be extended to the case of N sequential inlets and used by the designer to determine both the chocked-mass flow rates and a description of the associated pressure profiles.

Pressure profiles normalized in terms of inlet stagnation pressure and axial distance to choke appear independent of the number of inlets. The pressure profile shape changes from slightly concave to convex (parabolic friction loss form) with increased inlet stagnation temperature.

It does appear that a form similarity hypothesis can be extended to the case of N sequential inlets and used by the designer to determine both the choked-mass flow rates and a description of the associated pressure profiles.

References

1 Hendricks, R. C., and Sengers, J. V., "Application of the Principle of Similarity to Fluid Mechanics," *Water and Steam: Their Properties and Current Industrial Application*, J. Straub and K. Scheffler, eds., Pergamon Press, New York, 1980, pp. 322-335 (unabridged version as NASA TMX 79258, 1979).

2 Hendricks, R. C., "Normalizing Parameters for the Critical Flow Rate of Simple Fluids Through Nozzles," *International Cryogenic Engineering Conference*, 5th, IPC Sci. and Tech. Press, England, 1974, pp. 278-281.

3 Hendricks, R. C., Simoneau, R. J., and Barrows, R. F., "Two-Phase Choked Flow of Subcooled Oxygen and Nitrogen, NASA TN D-8169, 1976.

4 Simoneau, R. J., and Hendricks, R. C., "Generalized Charts for Computation of Two-Phase Choked Flow of Simple Cryogenic Liquids," *Cryogenics*, Vol. 17, No. 1, Jan. 1977, pp. 73-76.

5 Hendricks, R. C., Sengers, J. V., and Simoneau, R. J., "Toward the Use of Similarity in Two-Phase Choked Flows," ASME HTD, Vol. 14, *Scaling in Two-Phase Choked Flows*, ASME Winter Annual Meeting-1980, Chicago, Ill. pp. 45-53.

6 Hendricks, R. C., and Stetz, T. T., "Experiments on Flow Through One to Four Inlets of he Orifice and Borda Type," Presented at the Cryogenic Engineering Conference and the International Cryogenic Materials Conference, paper JB-7, San Diego, Calif., Aug. 1981.

7 Hendricks, R. C., and Stetz, T. Trent, "Some Flow Phenomena Associated with Aligned Sequential Apertures with Orifice Type Inlets," NASA TP-1967, 1982.

8 Hendricks, R. C., Graham, R. W., Hsu, Y. Y., and Freidman, R., "Experimental Heat-Transfer Results for Cryogenic Hydrogen Flowing in Tubes at Sub-Critical and Supercritical Pressures to 800 Pounds Per Square Inch Absolute," NASA TN D-3095, 1965.

9 Simoneau, R. J., and Hendricks, R. C., "Two-Phase Choked Flow of Cryogenic Fluids in Converging Diverging Nozzles," NASA TP-1484, 1979.

10 Hendricks, R. C., Baron, A. K., and Peller, I. C., "GASP—A Computer Code for Calculating the Thermodynamic and Transport Properties for Ten Fluids: Parahydrogen, Helium, Neon, Methane, Nitrogen, Carbon Monoxide, Oxygen, Fluorine, Argon, and Carbon Dioxide," NASA TN D-7808, 1975.

11 Hendricks, R. C., "Investigation of a Three Step Labyrinth Seal for High Performance Turbomachines," NASA TP-1850, 1981.

12 Hendricks, R. C., and Simoneau, R. J., "Two Phase Choked Flow in Tubes with Very Large L/D," *Advances in Cryogenic Engineering*, Vol. 23, Plenum Press, New York, 1978, pp. 265-275.

13 Hendricks, R. C., "Investigation of a Straight Cylindrical Seal for High Performance Turbomachines," NASA TP-1850, 1981.

14 Hendricks, R. C., "Investigation of a Three Step Cylindrical Seal for High Performance Turbomachines," NASA TP-1849, 1981.

APPENDIX

Example of Analysis – An Analysis of Sequential Inlet Flow[1]

The flow process is neither steady, adiabatic, nor frictionless, as described in the text. However, if we simply ignore these problems, the governing equations for the i[th] inlet, see sketch and Fig. 10, can be written as (reference [7]):

Continuity

$$\frac{\partial \rho u_l}{\partial x_l} = 0 \tag{A1}$$

Momentum

$$\frac{\partial \rho u_l u_j}{\partial x_j} - \frac{\partial p}{\partial x_l} = 0 \tag{A2}$$

Energy

$$\frac{\partial}{\partial x_l} \rho u_l H_0 = 0 \tag{A3}$$

where

$$H_0 = H + \frac{1}{2} u_l u_l \tag{A4}$$

State

$$p = p(\rho, H, x_\alpha) \tag{A5}$$

Similarity (extended van der Waals one-fluid model for corresponding states)

$$Z_m(T,V,x_\alpha) = Z_0\left(\frac{V}{h}, \frac{T}{f}\right)$$

$$g_m(V,T,x_\alpha) = f g_0\left(\frac{V}{h}, \frac{T}{f}\right)$$

$$+ RT\left(\sum_{x_\alpha} x_\alpha \ln x_\alpha - \ln h\right) \tag{A6}$$

[1] Reprinted from NASA TP-1792, May 1981.

where

$$\left.\begin{aligned} h &= \sum_{\alpha}\sum_{\beta} x_\alpha x_\beta h_{\alpha\beta,0} \\ fh &= \sum_{\alpha}\sum_{\beta} x_\alpha x_\beta f_{\alpha\beta,0} h_{\alpha\beta,0} \end{aligned}\right\} \quad \text{(A7)}$$

$$\left.\begin{aligned} f_{\alpha\alpha,0} &= \left(\frac{T^c_{\alpha\alpha}}{T^c_0}\right)\theta_{\alpha\alpha,0} \\ h_{\alpha\alpha,0} &= \left(\frac{V^c_{\alpha\alpha}}{T^c_0}\right)\phi_{\alpha\alpha,0} \end{aligned}\right\} \quad \text{(A8)}$$

Isentropic restraint

$$TdS_i = dH - \frac{dp}{\rho} = 0 \quad i=1,n \quad \text{(A9)}$$

Isobaric restraint

$$S_{i+1} = S(p_i, H_0) \quad i=1,n \quad \text{(A10)}$$

Choking constraint

$$G^2_{\max} = \rho^2\left(\frac{dp}{dp}\right)_e = \frac{2}{V^2}\int_{p_e}^{p_0} V dp \quad \text{(A11)}$$

It appears that at the 30-diameter separation choking can occur at the entrance or exit of the last ($i=n$) of the sequential inlets. At the 0.8-diameter separation choking can occur at the inlet of the first ($i=1$) inlet of the sequential inlets or at the exit of the last ($i=n$) inlet. The details of the choking constraint, at a fixed position, for flows with change of phase are quite complex and, although used herein, will not be repeated at this time; see reference [9] for further details.

Furthermore, if one isolates an inlet (one section of Fig. 4 or 7) and forms it into a blackbox, the conservation equations yield the isentropic expansion restraint

$$\left.\begin{aligned} dH_0 &= dH + d\frac{u^2}{2} \\ dp &+ \rho d\frac{u^2}{2} = 0 \end{aligned}\right\} \quad \text{(A12)}$$

or

$$\frac{dp}{\rho} - dH = 0$$

Thus we need only consider an isentropic process, and from the momentum equation we find

$$u^2_{i+1} - u^2_i = 2\int_{p_{i+1}}^{p_o} \frac{dp}{\rho} \quad \text{(A13)}$$

Consider now the following cases:

(1) When $u_{i+1} >> u_i$ or $u_i \to 0$, the mass flux across the ith inlet becomes

$$G^2 = (\rho_{i+1}u_{i+1})^2 = 2\rho^2_{i+1}\int_{p_{i+1}}^{p_i} \frac{dp}{\rho} \quad \text{(A14)}$$

(2) When $u_{i+1} \sim u_i$ or $u_i \to u_{i+1}$, $p_{i+1} \to p_i$ and jetting can occur, provided the jet has been established elsewhere in the system and

$$G^2 - G^2_{\max} = \rho^2\left(\frac{dp}{d\rho}\right)_e \quad \text{(A15)}$$

(3) For plug flow continuity, $\dot{w} = \rho_i u_i A_i = \rho_{i+1} u_{i+1} A_{i+1}$, the mass flux becomes

$$G^2 = \frac{2\rho^2_{i+}}{[1-(\rho_{i+1}A_{i+1}/\rho_i A_i)^2]}\int_{p_{i+1}}^{p_i} \frac{dp}{\rho} \quad \text{(A16)}$$

Again, consider two cases: (*a*) when $A_i >> A_{i+1}$, case (1) above results; and (*b*) when $(A_{i+1}\rho_{i+1} \to \rho_i A_i)$, it leads to case (2).

(4) In jetting data (references [3, 4, and 13]) $p_{i+1} > p_i$, and it follows that $u_{i+1} < u_i$ and that the system functions as a diffuser.

The same results are achieved with enthalpy as the independent variable; from the energy equation it follows that

$$u^2_{i+1} - u^2_i = 2(H_0 - H_{i+1}) = 2\int_{p_{i+1}}^{p_i} \frac{dp}{\rho} \quad \text{(A17)}$$

The enthalpy relation is used for the preliminary calculations herein.

In this report we use the simplified form of van der Waals corresponding-states principle since we only have data for fluid nitrogen.

$$\left.\begin{aligned} \theta_{\alpha\alpha,0} &= 1 \\ \phi_{\alpha\alpha,0} &= 1 \\ f = T_R &= \frac{T}{T_c} \\ P_R &= \frac{P}{P_c} \\ h = V_R &= \frac{V}{V_c} \end{aligned}\right\} \quad \text{(A18)}$$

and

$$G_R = \frac{G}{G^*}$$

All thermophysical properties were calculated by using the computer code GASP (reference [10]).

R.M. Terrill
Reader,
Department of Applied Mathematics
& Theoretical Physics,
The University of Liverpool,
Liverpool, England

Laminar Flow in a Porous Tube

It is shown that an axisymmetric solution of the Navier-Stokes equations can be obtained for potential flow superimposed on Poiseuille flow. The result is used here to obtain a fully developed solution for flow in a porous pipe with variable suction or injection and to show how to obtain the suction distribution needed to change a specified axial velocity distribution at one cross-section to a specified axial velocity distribution at another cross-section.

1 Introduction

Fluid flow through cylindrical pipes with mass transfer at the wall has received much attention in recent years because of its many practical applications, for example, in transpiration cooling, gaseous diffusion technology, control of fluids in nuclear reactors. The experimental and theoretical investigations have been mainly concerned with steady, incompressible, laminar flow with either constant injection or suction.

All the previous research, to the best of the author's knowledge, has been confined to *constant* suction or injection. The solutions have either dealt with the fully developed profile in which the axial velocity profile is taken to be similar at all cross-sections (see, for example, references [1–8]) or with the inlet length region which has been solved numerically (see, for example, references [10–12]). One difficulty with these solutions (see [15–17]) is that sometimes the fluid has a "long memory of the inlet velocity profile" and the fully developed profile is never reached. Another difficulty is that the fully developed solution is irrelevant when the axial velocity profile changes shape. The prime purpose of this paper is to introduce solutions with variable suction at the wall which will overcome these difficulties.

In Section 2 it is shown that an axisymmetric solution of the Navier-Stokes equations can be obtained for potential flow superimposed on the Poiseuille flow. It is shown that the corresponding solution for parallel plates or for an annulus can only exist provided one of the walls moves, that is, for Couette flow. The solution developed in this section proves to be useful in other problems besides the flow in porous channels; for example, the author has used it to find solutions to some flows in pipes with varying cross-sections. The application to fully developed flows in a porous pipe is made in Section 3. Here it is shown how analytic solutions for variable suction or injection can be developed; these could be extended to a variety of heat transfer problems.

An enlightening question is posed in Section 4. Given the axial velocity profile at one cross-section (probably the inlet) what distribution of suction or injection is required to produce a specified velocity distribution at another cross-section? An analytic answer follows which could be used to calculate the suction distribution required in the inlet length to produce the fully developed constant suction profile or the fully developed variable suction profile. Corresponding to each inlet axial velocity profile there are many possible distributions and these will be discussed in later papers.

The pressure distribution is obtained in Section 5 where it pointed out that another class of problems could be tackled by assuming that pressure at the inside wall of the pipe is related to the outside pressure by a suitable law—such as Darcy's law for porous media—and finding the resulting suction distribution.

Some particular examples of variable suctions are chosen to illustrate the flows in Section 6 and then applied to a specific problem in Section 7. Unfortunately there are no experimental results for variable suction and these are now desirable. Consequently in Section 7 the experiment by Quaile and Levy [12] was chosen in which fluid with a parabolic axial velocity profile enters a closed pipe with constant suction at the walls. Surprisingly good agreement between the theory in the present paper and the experimental and numerical results is obtained. It is also demonstrated that the failure of the inlet profile to develop into a fully developed *constant* suction profile is not unexpected and that indeed variable suction in the inlet length would be the best way of achieving such a profile.

It is clear that work in this paper leaves many questions to be answered and numerous extensions, for example, to heat transfer.

2 The Equations

Consider the steady laminar axisymmetric motion of an incompressible fluid in a semi-infinite or in a finite circular cylinder of radius a. Choose a cylindrical polar coordinate system (r, θ, z) where the axis $0z$ lies along the center of the tube, r is the distance measured radially and θ is the azimuthal angle. Let u and v be the velocity components in the directions of z and r increasing, respectively. Then, for axisymmetric flow, the equation of continuity is

$$\frac{\partial}{\partial r}(rv) + r\frac{\partial u}{\partial z} = 0 \tag{1}$$

and the Navier-Stokes equations are

$$u\frac{\partial u}{\partial z} + v\frac{\partial u}{\partial r} = -\frac{1}{\rho}\frac{\partial p}{\partial z} + \nu \nabla^2 u, \tag{2}$$

Contributed by the Fluids Engineering Division and presented at the ASME Applied Mechanics, Bioengineering, and Fluids Engineering Conference, Houston, Texas, June 20–22, 1983. Manuscript received by the Fluids Engineering Division, May 24, 1982. Paper No. 83-FE-5.

$$u\frac{\partial v}{\partial z}+v\frac{\partial v}{\partial r}=-\frac{1}{\rho}\frac{\partial p}{\partial r}+\nu\left(\nabla^2 v-\frac{v}{r^2}\right), \tag{3}$$

where

$$\nabla^2=\frac{\partial^2}{\partial r^2}+\frac{1}{r}\frac{\partial}{\partial r}+\frac{\partial^2}{\partial z^2},$$

and where p is the pressure, ρ the density and ν the kinematic viscosity of the fluid.

The boundary conditions at the pipe wall are

$$u=0 \text{ at } r=a, \tag{4}$$

together with the speed of injection or suction which is

$$v=V(z) \text{ at } r=a. \tag{5}$$

In addition, symmetry implies that

$$v=0 \text{ at } r=0 \tag{6}$$

The boundary conditions (4)–(6) will be applied later. For the present, suppose that there is a solution of equations (1)–(3) of the form

$$u=u_0(r)+\frac{\partial}{\partial z}\phi(r,z), \quad v=\frac{\partial \phi}{\partial r}(r,z) \tag{7}$$

For example, the velocity component $u_0(r)$ could represent the Poiseuille flow in a pipe or annulus. The equation of continuity is immediately satisfied provided

$$\nabla^2\phi=0, \tag{8}$$

that is, ϕ is an harmonic function.

The Navier-Stokes equations (2) and (3) become

$$(u_0+\phi_z)\phi_{zz}+(u_0'+\phi_{zr})\phi_r=-\frac{1}{\rho}p_z+\nu\nabla^2 u_0, \tag{9}$$

$$(u_0+\phi_z)\phi_{rz}+\phi_r\phi_{rr}=-\frac{1}{\rho}p_r. \tag{10}$$

Elimination of the pressure p gives

$$u_0'(\phi_{zz}+\phi_{rr})+\phi_r u_0''=\nu\frac{\partial}{\partial r}(\nabla^2 u_0)$$

or, using (8),

$$(ru_0''-u_0')\phi_r=r\nu\frac{\partial}{\partial r}(\nabla^2 u_0). \tag{11}$$

To satisfy (11) exactly, $u_0(r)$ must be of the form

$$u_0(r)=\beta-\lambda r^2, \tag{12}$$

where λ and β are constants.

It follows that an exact solution of the Navier-Stokes equations for axisymmetric flow is

$$u=\beta-\lambda r^2+\phi_z, \quad v=\phi_r,$$

where ϕ is an harmonic function. This surprising result may have several useful applications; here it will be used to provide a deeper understanding of flows in porous channels.

It is immediately seen that $u_0(r)=\lambda(a^2-r^2)$ is of the form (12) and satisfies the no-slip condition (4) so that Poiseuille flow in a circular pipe has this exact perturbation. Clearly the flow in an annulus with outer wall $r=a$ and inner wall $r=b$ is not of the form (12). However if one wall is allowed to move, say the inner wall $r=b$ has the appropriate velocity $\lambda(a^2-b^2)$, then $u_0(r)=\lambda(a^2-r^2)$ is a possible solution. This is, of course, Couette flow. Now it is known that the flow between parallel plates can be obtained from the flow in an annulus (see Terrill [13]). This can be seen by writing $b=a(1+\epsilon)$, $r=b+\epsilon a y$, where ϵ is small, and letting $\epsilon\to 0$. The walls of the annulus become the parallel plates $y=0$ and $y=1$. Thus in plane flow, the potential flow can only be superimposed on Couette flow.

The conclusion reached is that while potential flow can be superimposed on Poiseuille flow in a pipe, it is not possible to do this for the annulus or for parallel plates. This superimposition can only be made in the latter cases when one of the walls is allowed to move with the appropriate speed, that is for Couette flow.

3 The Solution for Fully Developed Flow

For flow in a porous pipe, the solution from (4), (7), and (12) is

$$u=\lambda(a^2-r^2)+\phi_z, \quad v=\phi_r, \tag{13}$$

where λ is an arbitrary constant and ϕ is a solution of Laplace's equation (8) satisfying the boundary conditions

$$\begin{aligned} &\text{at} \quad r=0, \quad \phi_r=0 \\ &\text{at} \quad r=a, \quad \phi_z=0, \quad \phi_r=V(z). \end{aligned} \tag{14}$$

It is readily seen that typical solutions of (8) are of the form

$$\phi=[A\cosh\alpha z+B\sinh\alpha z][J_0(\alpha r)+DY_0(\alpha r)]$$

where A, B, D, and α are arbitrary constants and where $J_0(\alpha r)$ and $Y_0(\alpha r)$ are Bessel functions of the first and second kind, respectively. Now $Y_0(\alpha r)$ is infinite at $r=0$ so that $D\equiv 0$ and since $J_0'(\alpha r)$ is zero at $r=0$, the condition $\phi_r=0$ at $r=0$ is automatically satisfied. The boundary condition $\phi_z=0$ at $r=a$ necessitates $J_0(\alpha a)\equiv 0$, that is αa are the zeros of the Bessel function J_0. Let these zeros be $\alpha_n a (n=0,1,2,\ldots)$, then the appropriate solution is

$$\phi=\sum_{n=1}^{\infty}(A_n\cosh\alpha_n z+B_n\sinh\alpha_n z)J_0(\alpha_n r) \tag{15}$$

where $J_0(\alpha_n a)=0$. This solution corresponds to the prescribed speed of suction

$$V(z)=-\sum_{n=1}^{\infty}\alpha_n[A_n\cosh\alpha_n z+B_n\sinh\alpha_n z]J_1(\alpha_n a). \tag{16}$$

It follows that injection or suction with speed (14) should result in the fully developed profiles given by (13). In contrast to all the previous analytic solutions which have necessitated constant suction or injection and which have produced similar velocity profiles for u, the above work shows that analytic solutions for variable suction or injection are now feasible and, in general, their resulting velocity profiles for u will be changing shapes. A fascinating feature is that to any particular solution it should be possible to add a multiple of (a^2-r^2) to u.

These fully developed flows are discussed more fully in Terrill [14] using a completely different approach to the problem. An altogether new method of tackling these problems will now be proposed which will provide further insight into the flow through porous pipes.

4 An Analytic Solution for Developing Flow

The object of all previous papers has been to specify V and to find the resulting velocity distribution either analytically for the fully developed flow or numerically for the developing flow. Instead of this method, the axial velocity distribution at one cross-section will now be assumed and the question will be asked "What velocity of suction is required to produce a specified axial velocity distribution at another cross-section?" The problem of finding ϕ is analogous to a heat conduction problem in which either ϕ or ϕ_z is taken to be the temperature and it simply remains to solve Laplace's equation subject to the temperature distribution given on a circular cylinder.

Suppose that the axial velocity component at $z=0$ is $u(r)=\lambda(a^2-r^2)+f(r)$ and that this profile gradually changes

until at $z = l$, say, it becomes $u(r) = \lambda(a^2 - r^2) + g(r)$. It may be noted that λ is arbitrary and could be zero while $f(r)$ and $g(r)$ are assumed to be reasonably well behaved functions that must satisfy $f(a) = g(a) = 0$. Then it only remains to solve

$$\nabla^2 \phi_z = 0 \tag{17}$$

subject to the boundary conditions

$$\begin{aligned} &\text{at} \quad z=0, \qquad \phi_z = f(r) \\ &\text{at} \quad z=l, \qquad \phi_z = g(r) \\ &\text{and} \quad 0 \le z \le l, \; r=a, \qquad \phi_z = 0. \end{aligned} \tag{18}$$

This is a typical heat conduction problem whose solution can be readily constructed from those given in Carslaw and Jaeger [18] or Moon and Spencer [19]. It immediately follows that

$$\phi_z = \sum_{n=1}^{\infty} \left\{ \frac{A_n \sinh\alpha_n (l-z) + B_n \sinh\alpha_n z}{\sinh\alpha_n l} \right\} J_0(\alpha_n r) \tag{19}$$

$$\left.\begin{aligned} \text{where} \quad A_n &= \frac{2}{a^2 [J_1(\alpha_n a)]^2} \int_0^a r f(r)\, J_0(\alpha_n r)\, dr \\ \text{and} \quad B_n &= \frac{2}{a^2 [J_1(\alpha_n a)]^2} \int_0^a r g(r)\, J_0(\alpha_n r)\, dr \end{aligned}\right\} \tag{20}$$

and $\alpha_n a$ are the zeros of the Bessel function J_0, that is, $J_0(\alpha_n a) = 0$.

Integration of (19) gives, taking $\phi = 0$ at $r = a$,

$$\phi = \sum_{n=1}^{\infty} \frac{1}{\alpha_n} \left\{ \frac{B_n \cosh\alpha_n z - A_n \cosh\alpha_n (l-z)}{\sinh\alpha_n l} \right\} J_0(\alpha_n r)$$

so that the radial velocity component is

$$v = \phi_r = \sum_{n=1}^{\infty} \left\{ \frac{A_n \cosh\alpha_n (l-z) - B_n \cosh\alpha_n z}{\sinh\alpha_n l} \right\} J_1(\alpha_n r). \tag{21}$$

Hence the required velocity of suction needed to change the given axial velocity distribution is

$$V(z) = \sum_{n=1}^{\infty} \left\{ \frac{A_n \cosh\alpha_n (l-z) - B_n \cosh\alpha_n z}{\sinh\alpha_n l} \right\} J_1(\alpha_n a) \tag{22}$$

where the A_n and B_n are given by (20).

Although the problem is now solved, it is instructive to study some particular features of the solution. Given an inlet velocity profile $f(r)$ at $z = 0$, it can be used to calculate the suction distribution $V(z)$ that is required to produce at the end of an entry length l the desired fully developed profile $g(z)$. This fully developed profile could be either one of constant suction flows given in references [1-8] or one of the variable suction flows outlined in Section 3. However, should this suction distribution $V(z)$ be unsuitable for experiments, other distributions can be found by dividing the inlet length into a number of subdivisions; an example of this will be given later. Alternatively the solution could be regarded as fully developed with a constantly changing velocity profile. Before looking at a few specific examples, the pressure distribution for the flow will be calculated.

5 Pressure Distribution

For the velocity components (13), equations (9) and (10) can be readily integrated to yield

$$p + \rho\left\{ \frac{1}{2} (\phi_r^2 + \phi_z^2) + u_0 \phi_z + u_0' \int \phi_r dz \right\} = H(r) - 4\lambda\mu z \tag{23}$$

where $u_0 = \lambda (a^2 - r^2)$, ϕ_r and ϕ_z are given by (21) and (19), respectively and $H(r)$ is an arbitrary function of r.

Previous research workers on flows with constant suction or injection have usually given the pressure variations along the center line or along the wall for analytical, numerical or experimental results. From (23) it is immediately seen that at $r = 0$

$$(p)_{r=0} + \rho\left(\frac{1}{2} \phi_z^2 + \lambda a^2 \phi_z \right)_{r=0} = H(0) - 4\lambda\mu z \tag{24}$$

where, from (19),

$$(\phi_z)_{r=0} = \sum_{n=1}^{\infty} \left\{ \frac{A_n \sinh\alpha_n (l-z) + B_n \sinh\alpha_n z}{\sinh\alpha_n l} \right\}.$$

An even simpler result is obtained for the pressure variation along the wall, namely,

$$(p)_{r=a} + \frac{1}{2} \rho V^2 - 2\lambda a \rho \int V\, dz = H(a) - 4\lambda\mu z, \tag{25}$$

where V is the velocity of suction. The latter form is particularly interesting as it shows that between two cross-sections $z = z_1$ and $z = z_2$, say, the change in $(p)_{r=a} + 1/2\, \rho V^2$ is simply

$$2\lambda\rho \left[a \int_{z_1}^{z_2} V\, dz - 2\nu(z_2 - z_1) \right]. \tag{26}$$

The axial pressure distribution at the walls can be used to provide a different set of solutions which will be the subject of a future paper. The difference between the pressure inside the pipe wall (25) and a given pressure distribution outside the pipe wall can be assumed to be proportional to a power of V (see Taylor [20]) or can be related to Darcy's law for porous media. The resulting equation can then be solved for $V(z)$ to give sets of fully developed solutions corresponding to the assumptions made at the wall.

6 Some Particular Cases

To investigate further the links between the axial velocity profile and the suction or injection distribution at the wall, some particular cases will be shown.

Case 1 $f(r) = g(r)$. It immediately follows from (20) that when the inlet axial velocity profile and the final axial velocity profile are identical then $A_n = B_n$ and (19) becomes

$$\phi_z = \sum_{n=1}^{\infty} \frac{A_n \cosh\alpha_n \left(\frac{l}{2} - z \right)}{\cosh \frac{\alpha_n l}{2}} J_0(\alpha_n r)$$

and the appropriate suction is, from (21),

$$V(z) = \sum_{n=1}^{\infty} \frac{A_n \sinh\alpha_n \left(\frac{l}{2} - z \right)}{\cosh \frac{\alpha_n l}{2}} J_1(\alpha_n a).$$

A parabolic profile can be maintained without suction—which is obvious since it is Poiseuille flow in an impermeable pipe. For any other flow it is necessary to have suction and injection; the suction in $0 \le z \le l/2$, say, balanced exactly by the injection in $l/2 \le z \le l$. From the conservation of mass, this result is to be expected. It may be noted that for l very small, $V(z)$ is linearly proportional to $(l/2 - z)$ while $f(r) - \phi_z$ is proportional to $(l - z)z$.

Case 2 $g(g) = -f(r)$. gives

$$\phi_z = \sum_{n=1}^{\infty} \frac{A_n \sinh\alpha_n\left(\frac{l}{2} - z\right)}{\sinh\alpha_n l/2} J_0(\alpha_n r)$$

where A_n is given in (20) while the suction distribution is

$$V(z) = \sum_{n=1}^{\infty} \frac{A_n \cosh\alpha_n\left(\frac{l}{2} - z\right)}{\sinh\alpha_n l/2} J_1(\alpha_n a).$$

Although for $f(r) \geq 0$ it is clear that $g(r) \leq 0$, the axial velocity given by (13) may still be positive as there is also the arbitrary term $\lambda(a^2 - r^2)$. For l small, the value of ϕ_z changes linearly while $V(z)$ is approximately constant.

Case 3 $g(r) \to 0$ as $z \to \infty$. This is a particular simple example with

$$\phi_z = \sum_{n=1}^{\infty} A_n e^{-\alpha_n z} J_0(\alpha_n r) \text{ and } V(z) = \sum_{n=1}^{\infty} A_n e^{-\alpha_n z} J_1(\alpha_n a)$$

as the solution. This shows the effect of a sudden burst of injection or suction near to $z = 0$. For example, write $u(r) = (\lambda + \epsilon)(a^2 - r^2) + f(r)$ where $f(r) = -\epsilon(a^2 - r^2)$. Then the solution could be used to show how a Poiseuille flow could be increased from $\lambda(a^2 - r^2)$ to $(\lambda + \epsilon)(a^2 - r^2)$ by a suitable injection of fluid in the neighborhood of $z = 0$. This could be repeated at further cross-sections downstream.

Case 4 $g(r) = -f(r) = -C(a^2 - r^2)$. The constant C is arbitrary here. Theoretical workers and experimenters have chosen a variety of inlet profiles of which the parabolic has been one of the most popular.

Then, from (20), the A_n in Case 2 are given by

$$A_n = \frac{2}{a^2 J_1(\alpha_n a)^2} \int_0^a C(a^2 r - r^3) J_0(\alpha_n r)\, dr$$

Now

$$\int_0^a r\, J_0(\alpha_n r)\, dr = \frac{a J_1(\alpha_n a)}{\alpha_n}$$

and

$$\int_0^a r^3 J_0(\alpha_n r)\, dr = \frac{a^3}{\alpha_n} J_1(\alpha_n a) - \frac{2a^2}{\alpha_n} J_2(\alpha_n a).$$

Further using $J_0(\alpha_n a) \equiv 0$ and $(2/a\alpha_n)\, J_1(\alpha_n a) = J_0(\alpha_n a) + J_2(\alpha_n a)$ the expression for A_n simplifies to

$$A_n = \frac{8aC}{\alpha_n^3 [J_1(\alpha_n a)]}$$

Hence, from Case 2, the suction distribution

$$V(z) = \sum_{n=1}^{\infty} \frac{8aC}{\alpha_n^3} \frac{\cosh\alpha_n\left(\frac{l}{2} - z\right)}{\sinh\frac{\alpha_n l}{2}} \tag{27}$$

produces a change in the axial velocity u given by

$$\phi_z = \sum_{n=1}^{\infty} \frac{8aC}{\alpha_n^3} \frac{\sinh\alpha_n\left(\frac{l}{2} - z\right)}{\sinh\frac{a_n l}{2}} \frac{J_0(\alpha_n r)}{J_1(\alpha_n a)}. \tag{28}$$

These results will now be used in considering a particular problem.

7 A Theoretical and Experimental Comparison

It is difficult to compare the theory in the present paper with previous research papers since they have all involved constant suction or injection. However, as an example, the problem considered by Quaile and Levy [12] will be studied. They took the tube to be closed at the downstream end, $z = L$ say, so that the fluid which enters at $z = 0$ is extracted with constant radial velocity uniformly over the length L. The inlet profile was chosen to be parabolic and the transverse (i.e., radial) pressure variations were neglected. Experimental and numerical results were presented representing an inlet length problem, that is, an axial velocity profile that was not similar at all cross-sections.

An interesting attempt to produce comparable flows could be made by dividing the pipe into n equal sections, each of length L/n, such that the inlet axial velocity $K(a^2 - r^2)$ is reduced by an amount $2C(a^2 - r^2)$ across each section. For the fluid to be completely extracted by $x = L$, it follows that $2nC = K$. Now consider the m'th section. The axial velocity at the start of the section is $u = u_{m-1} + C(a^2 - r^2)$ and at the end of the section it is $u = u_{m-1} - C(a^2 - r^2)$ where

$$u_{m-1} = [K - (2m-1)C](a^2 - r^2)$$
$$= K\left[1 - \frac{(2m-1)}{2n}\right](a^2 - r^2).$$

The suction distribution in the m'th section is given by (27) and the axial velocity $u = u_{m-1} + \phi_z$ by (28). [Note that in (27) and (28) the z should be replaced by $z_{m-1} = z - (m-1)L/n$ and $0 \leq z_{m-1} \leq l$.] The experimental and numerical results presented by Quaile and Levy include several curves of the axial pressure variations along the pipe. The axial pressure increase Δp_{m-1} across the m'th section is, from (24),

$$\Delta p_{m-1} = \rho K\left[1 - \frac{(2m-1)}{2n}\right]\left\{\frac{Ka^4 - 4\nu L}{n}\right\}, \tag{29}$$

To conform with the notation of Quaile and Levy it is necessary to introduce

(i) an average inlet axial velocity component $\bar{u}_0$; it is readily shown that $\bar{u}_0 = \frac{1}{2}Ka^2$,

(ii) a typical suction Reynolds number, $\mathrm{Re}_r = [a\int_0^L V dz]/L\nu$, say; this becomes identical with the usual suction Reynold's number when V is a constant. From continuity, it follows for this particular problem that $2\pi a \int_0^L V\, dz = \pi a^2 \bar{u}_0$ so that $\mathrm{Re}_r = (a^2\bar{u}_0)/2L\nu$.

Hence the pressure increase across the m'th section is given by

$$\frac{\Delta p_{m-1}}{\frac{1}{2}\rho\bar{u}_0^2} = \frac{8}{n}\left[1 - \frac{(2m-1)}{2n}\right]\left[1 - \frac{1}{\mathrm{Re}_r}\right], \mathrm{Re}_r > 0. \tag{30}$$

Thus the total dimensional pressure increase from $z = 0$ to $z = L$ along the axis is readily shown to be

$$\frac{p_L - p_0}{\frac{1}{2}\rho\bar{u}_0^2} = 4\left[1 - \frac{1}{\mathrm{Re}_r}\right] \tag{31}$$

irrespective of the number of sections. It should be noted that the theory can easily be applied when the sections are not equal in length but the results (29), (30), and (31) are modified slightly.

In comparing these expressions with experimental results it should be remembered that this theory is based on *variable suction* at the wall whereas the experimental results are for constant suction. However (31) follows closely the shape of the curve of the experimental results throughout the range of Re_r and has the correct asymptotic form as $\mathrm{Re}_r \to \infty$. Formula (31) suggests that the pressure increases for $\mathrm{Re}_r > 1$ and decreases for $\mathrm{Re}_r < 1$. Quaile and Levy observe "according to the (inlet region/numerical) theory, the pressure gradient increases for $\mathrm{Re}_r > 1.25$; adverse pressure gradients we observed experimentally for $\mathrm{Re}_r > 1$." Such an exact agreement between experimental data and (31) is indeed

fortuitous. It is worth noting that as the number of sections n increases, the velocity of suction becomes closer and closer to being constant although it is essential that the suction decreases and increases in any section in the way described earlier so that the shape of the parabolic profile is maintained. This explains the excellent correlation between the experimental and theoretical results—whereas the similarity solutions yield completely different answers for $\mathrm{Re}_r > 2$. Another feature of the analytic solution is that the axial pressure increase across the m'th section is linear. When $n = 1$ the pressure increase is a linear function of z but it is readily shown that as $n \to \infty$ the pressure increase is a quadratic function of z. (Any intermediate number of sections, N say, give N line segments of this curve.) The quadratic function of z, corresponding to almost constant suction, is precisely the shape one expects to obtain for the constant suction inlet length (see Quaile and Levy).

8 Conclusions

In the introduction it was mentioned that the similarity solution for constant suction was often not reached in some experiments and that experimenters had concluded that sometimes the fluid had a "long memory of the inlet velocity profile." In the previous section it has been shown that for some suction distributions, the inlet parabolic profile can be preserved, even for suction that is almost constant. [For injection the arguments of the previous section can be repeated with $C < 0$ and although this yields a doubling of the axial velocity profile and a different pressure distribution, the inlet parabolic profile can again be preserved for almost constant injection]. Now in any experimental apparatus in which fluid has to be extracted by a finite number of holes, the variable suction distribution in (7) may even by a better approximation than constant suction. This observation helps to explain why some flows have long memories of the inlet profile and the fully developed flow cannot be achieved. However experimental results for variable suction would be the most useful test of the theories in this paper. For example, an experimental study of the solution in Section 7 with a suction distribution given by equation (27) would be most instructive.

To obtain a fully developed constant suction profile or a fully developed variable suction profile of the type given in Section 3, from any given inlet profile, the desirable suction in the inlet length is given in Section 4. Indeeed there are many possible suction distributions that can achieve this.

References

1 Yuan, S. W., and Finkelstein, A. B., "Laminar Pipe Flow With Injection and Suction Through a Porous Wall, *Trans. ASME*, Vol. 78, 1956, p. 719.

2 White, F. M., Jr., "Laminar Flow in a Uniformly Porous Tube," ASME *Journal of Applied Mechanics*, Vol. 29, 1962, p. 203.

3 Terrill, R. M., and Thomas, P. W., "On Laminar Flow Through a Uniformly Porous Pipe," *Appl. Sci. Res.*, Vol. 21, 1969, p. 31.

4 Raithby, G. D., "Laminar Heat Transfer in the Thermal Entrance Region of Circular Tubes and Two-Dimensional Rectangular Ducts With Wall Suction and Injection," *Int. J. Heat and Mass Transfer*, Vol. 14, 1971, p. 223.

5 Zinchenko, V. I., and Fedorova, O. P., "Analysis of Flow in an Annula Duct with Large Injection at the Walls," *Izv. Aka. Nauk SSR, Mekhaniki Zhidosti*, Vol. 3, 1976, p. 135.

6 Morel, J., Lavan, Z., and Bernstein, B., "Flow Through Rotating Porous Annuli," *Phys. Fluids*, Vol. 20, 1977, p. 726.

7 Terrill, R. M., and Thomas, P. W., "Spiral Flow in a Porous Pipe," *Phys. Fluids*, Vol. 16, 1973, p. 356.

8 Morel, J., Bernstein, B., and Lavan, Z., *Angew, Math. Phys.*, Vol. 27, 1976, p. 289.

9 Weissberg, H., "Laminar Flow in the Entrance Region of a Porous Pipe," *Phys. Fluids*, Vol. 5, 1959, p. 510.

10 Hornbeck, R., Routeau, W. T., and Osterle, F., "Laminar Entry Problem in Porous Tubes," *Phys. Fluids*, Vol. 6, 1963, p. 1649.

11 Friedman, M., and Gillis, J., "Viscous Flow in a Pipe with Absorbing Walls," ASME *Journal of Applied Mechanics*, Vol. 34, 1967, p. 819.

12 Quaile, J. P., and Levy, E. K., "Laminar Flow in a Porous Tube with Suction," ASME *Journal of Heat Transfer*, Vol. 97, 1975, p. 66.

13 Terrill, R. M., "Flow Through a Porous Annulus," *Appl. Sci. Res.*, Vol. 17, 1966, p. 204.

14 Terrill, R. M., "An Exact Solution for Flow in a Porous Pipe," *Z. Angew, Math. Phys.*, Vol. 33, 1982, p. 547.

15 Raithby, G. D., and Knudsen, D. C., "Hydrodynamical Development in a Duct With Suction and Blowing," ASME *Journal of Applied Mechanics*, Vol. 41, 1974, p. 896.

16 Gupta, B. K., and Levy, E. K., "Symmetric Laminar Channel Flow With Wall Suction," ASME JOURNAL OF FLUIDS ENGINEERING, Vol. 98, 1976, p. 469.

17 Aggarwala, B. D., and Gangal, M. K., "Fully Developed Laminar Flow in Porous Ducts," *Journal of Maths. & Physical Sciences*, Vol. 11, 1977, p. 37.

18 Carslaw, H. S., and Jaegar, J. C., *Conduction of Heat in Solids*, Oxford, 1947.

19 Moon, P., and Spencer, D. E., *Field Theory for Engineers*, Van Nostrand 1960.

20 Taylor, G. I., Fluid Flow in Regions Bounded by Porous Surfaces, Theoretical and Experimental Considerations," *Proc. Roy. Soc.*, Vol. 234, 1956, p. 456.

The Effect of Transverse Curvature on the Drag and Vortex Shedding of Elongated Bluff Bodies at Low Reynolds Number

D. R. Monson
Principal Scientist,
Donaldson Co., Inc.,
Minneapolis, Minn. 55440

This paper establishes the drag characteristics of finite cylinders of aspect ratio 1, 4, 10 and 100 for Reynolds numbers less than 1000 including the viscous regime. The effect of the drag and vortex shedding characteristics of curving a finite cylinder into a toroidal shape is investigated. The curvature reduces drag by as much as 13 percent over its linear counterpart in the viscous regime. Vortex shedding characteristics of tori include all the features of cylinders in addition to a solidity range that behaves like solid bodies and an intermediate range where two vortex flow patterns can exist. These patterns can occur either as alternating ring vortices or a less common but more stable counterrotating helical vortex pair.

Introduction

The problem of determining the drag and understanding the flow around bluff bodies at low Reynolds numbers has been studied by numerous investigators. The infinite circular cylinder and the sphere have received the most attention for two reasons; first because of their simple geometrical description, and second, because of the wide variety of practical applications. Between these two extremes of length to diameter ratio ($L/c=A$) fall an infinite variety of elongated bluff bodies. Much less work has been done on determining drag of these intermediate families of elongated shapes.

Consider the drag coefficient of a right circular cylinder over the range A^{-1} from zero to one with the major axis normal to the flow. We are interested in the viscous, transitional and low subcritical inertial flow regimes. No unified solution exists to cover these regimes. The data tend to fall between the C_D versus Re curves for the sphere and the infinite cylinder.

In the viscous regime, the most promising solution is one by Batchelor which was empirically improved to fourth order in Batchelor's aspect ratio function ϵ by Stalnaker and Hussey [1], yielding a drag equation that is valid for $A > 20$. The latter also presented an empirical relation (in Reynolds number) which is valid in the transitional regime.

At a Reynolds number of approximately 44, the drag curves for the sphere and the infinite cylinder cross. Above this value, the sphere has a lower drag coefficient than an infinite cylinder. This suggests that for this family of elongated bodies, all have approximately the same drag coefficient (1.65) at Re = 44. This drag coincidence Reynolds number matches that where vortex shedding in the wake of bluff bodies begins. In the range of Reynolds number from 44 to approximately 2000, the author is not aware of any data or analysis for the drag of the cylinder family.

There is currently interest in predicting the drag of elongated bodies having curvature in the transverse plane. Applications include the biological study of macromolecules and micro-organisms, the fluid mechanics of particle agglomerates and micelles, and the drag on curved fibers found in filter media.

If our cylinder family is given the smallest constant radius of curvature for a given A without overlapping, we end up with a family of tori as the limiting geometry. It is the purpose of this paper to:

1. Compare the drag characteristics of this limiting geometry with that of its linear counterpart.
2. To document limited experimental drag characteristics for the torus family in the vortex shedding regime and to compare the effect on vortex shedding of this transverse curvature with that for circular cylinders.

A recent paper by Amarakoon et al. [2] also provides experimental measurements of the viscous drag of tori and provides a detailed study of a number of boundary conditions which affect the drag. Portions of the present paper are covered in more detail in reference [3].

Experimental Equipment

Test Models. To fill in gaps in the cylinder drag data, four cylinders of A = 1, 4, 10, and 100 were constructed. The cylinder of A = 1 was a composite structure machined from half acrylic and half aluminum with the interface along its axis to prevent uncontrollable oscillations in the vortex

Contributed by the Fluids Engineering Division of THE AMERICAN SOCIETY OF MECHANICAL ENGINEERS at the Winter Annual Meeting, November 15-20, 1981, Washington, D.C. Manuscript received by the Fluids Engineering Division, March 15, 1982. Paper No. 81-WA/FE-4.

shedding regime. The remaining cylinders were precision cut from steel piano wire.

The bulk of the data for tori is taken from a thesis written by the author [4], hereafter referred to as 4.

A new set of tori was assembled. They were classified according to their projected area solidities, S. The following solidities were used (compatible with those tested in 4): 1.0, 0.803, 0.602, 0.395, 0.200, and 0.036.

The torus of $S = 1.0$ was machined from acrylic. The next three were precision silicone rubber O-rings. The $S = 0.2$ and 0.036 tori were formed from brass wire and steel piano wire respectively. The joint on the $S = 0.2$ torus was butt-soldered and filed smooth, while that for $S = 0.036$ had a small overlap which was soldered and blended.

A systematic investigation to determine the drag of curved shapes for constant radius of curvature between these extremes was planned by using segments of tori. However, the settling experiments of 4 showed that in the viscous regime a segment of a torus, e.g., a half torus, assumed a stable attitude with the axis of revolution normal to the flow direction (with the U up); whereas, in the inertial regime, the same body fell with the U in the desired horizontal position. It was not practical to fabricate variably weighted segments for such a test. This negated a comparison of the broadside viscous drag on a segment of a torus with the theories of Tschen [5] and Johnson [6].

In these tests, drag is inferred from measurements of the terminal velocity as they fall through a viscous liquid in a cylindrical container. Under these conditions, the drag is equal to the difference between the gravitational force and the buoyancy force, i.e., the net weight in the fluid. Attempts to measure the apparent mass in the test fluids directly on an analytical balance as was done by Stalnaker and Hussey [1] and Amarakoon et al. [2] were abandoned for the following reasons. First, a surface tension force on the single 0.0025 cm wire suspending the model caused an unreliable increase in the apparent mass reading, especially with water. The net result, however was a *reduction* in the apparent mass readings.

Test model volumes were calculated by dividing the difference between the mass in air and the apparent value in the liquid by the density of the fluid. These values were higher by 1 to 2 percent than the volumes calculated directly from the measured test model dimensions. These discrepancies have also been noted in reference [1], however Amarakoon et al. [2] have noted both reductions and increases in the apparent mass readings compared to subtracting $\rho_f V_m$ from the measured particle mass in air. The source of this discrepancy has not been satisfactorily explained. Thus, for the present experiments the net weight in the fluid was determined from

$$W_n = (\rho_m - \rho_f) g\ V_m \cdot \tag{1}$$

For the cylinders, V_m was calculated directly from the measured dimensions, and ρ_m was determined by dividing the measured mass m by V_m. For the tori made from acrylic, steel, or brass, ρ_m was derived from the mass and volume of a cylindrical sample of the material from which the part was made. The value V_m was determined from the ratio m/ρ_m. For the silicone rubber O-rings, V_m was calculated from average dimensions determined on an optical comparator and ρ_m was found from m/V_m.

The physical parameters of the test models are summarized in Table 1. Cylinder dimensions are length L and diameter c, while those for tori are given by maximum ring diameter d and cross-section diameter c.

Test Fluids and Containers. Four liquids were used which allowed coverage of six orders of magnitude in Reynolds number in the range of interest. The lowest viscosity liquid was distilled water. The next three of higher viscosity were water-soluble polyalkylene glycols made by Union Carbide.

Viscosities were measured with a Cannon-Fenske viscometer which was immersed in a temperature-controlled water bath except for the highest viscosity liquid which was measured in 4 by means of the falling sphere method.

Fluid densities were measured with ASTM float hydrometers which read sp. gr. to 0.0005 except for the most viscous fluid which was measured with a pycnometer in 4.

Tests were conducted in an environmentally conditioned room held at a temperature of 23°C ± 1°C. Temporal fluid temperatures were stable within ± 0.5°C. Fluid spacial temperatures were generally within 0.1°C throughout the container. Within the range of interest, the temperature dependence of the fluid density and kinematic viscosity can be expressed as follows:

Distilled water:	$\rho_f = 1.0039\text{-}0.002T$ g/cm^3
	$\nu = 0.0143\text{-}0.0002T$ cm^2/s
UCON 50-HB-55:	$\rho_f = 0.09655@23.00°C$ g/cm^3
	$\nu = 0.2606\text{-}0.0052T$ cm^2/s
UCON 50-HB-170:	$\rho_f = 1.0722\text{-}0.0013T$ g/cm^3
	$\nu = 1.5910\text{-}0.0358T$ cm^2/s
UCON 50-HB-5100:	$\rho_f = 1.0713\text{-}0.0009T$ g/cm^3
	$\nu = 50.469\text{-}1.1917T$ cm^2/s

where T is temperature in °C.

For tests in the two highest viscosity liquids, two container

Nomenclature

A = aspect ratio, L/c
A_f = projected frontal area, cm^2
C_D = drag coefficient
D = test cylinder inside dia. or dia, cm
K_b = boundary correction factor to drag, $K_b = K_b\ (\lambda)$
K_∞ = dynamic shape factor
L = major axis length (mean circum. for torus), cm
R = drag, (g cm/s^2)
Re_i = Reynolds number based on $i = c, d_s, d$ or L
S = projected area solidity $[4(1 - c/d)c/d]$
T = temperature, °C
U = velocity, cm/s
V = volume, cm^3
W_n = net weight in fluid, g cm/s^2
b = half length of rectangular container, cm
c = minor axis length, cm
d = outside diameter of torus or diameter, cm
g = acceleration of gravity (980.57 cm/s^2, local value)
h = half width of rectangular container, cm
m = mass, g
α = $\alpha(A)$
β = constant
γ = Euler's const (0.577216)
ϵ = $[\ln(2A)]^{-1}$
λ = boundary proximity parameter, d_s/D
λ' = boundary proximity parameter, d/D
μ = dynamic viscosity, g/cm s
ν = kinematic viscosity, cm^2/s
ρ = density, g/cm^3
$\sigma_c\sigma_t$ = ratio of ellipsoid aspect ratio to that of a cylinder or torus of equal drag

Subscripts

c = cylinder
e = ellipsoid of equal drag
f = fluid
h = hydraulic diameter
m = test model
0 = infinite A cylinder in infinite fluid
s = sphere of equal volume
t = torus
v = viscous regime
∞ = infinite fluid

Table 1 Physical parameters

Cylinders	L/c	L (cm)	c (cm)	m (g)	V_m (cm^3)	ρ_m (g/cm^3)	
	1.002	0.3167	0.3160	0.0496	0.0248	1.999	
	4.000	0.6401	0.1600	0.1006	0.0129	7.822	
	9.998	1.1938	0.1194	0.1039	0.0134	7.781	
	100.078	8.1864	0.0818	0.3381	0.0430	7.863	Results of Tests in Water
Tori	S	d	c	m	V_m	ρ_m	Re	C_D
	1.000	0.5065	0.2533	0.0483	0.0409	1.182	232	0.72
	0.803	0.6348	0.1751	0.0514	0.0348	1.477	242	0.75
	0.602	0.9524	0.1740	0.0843	0.0582	1.499	204	0.99
	0.395	1.5776	0.1765	0.1582	0.1077	1.469	199	1.13
	0.200	1.5403	0.0817	0.2045	0.0238	8.579	244	1.27
	0.036	4.194	0.0381	0.1182	0.0151	7.848	71.3	1.32

diameters were used with diameters of 29.253 cm and 14.00 cm, respectively. This allowed extrapolation to zero d_s/D ($\equiv \lambda$), the infinite fluid condition. Here, d_s is the equivalent spherical diameter of the particle, and D is the tube inside diameter.

The large tube was sized so that λ was about 0.01 for most test models. Since boundary effects become much less severe at higher Reynolds numbers, tests in the two lowest viscosity liquids were done only in the largest tube. The maximum area blockage of the present models was less than 0.001. Liquid column heights were 102 cm for the three lowest viscosity tests and 71 cm for the highest viscosity tests.

Apparatus and Procedure. Settling velocities were measured by the time of flight between two laser beams as described in Stalnaker and Hussey [1].

The main differences in the method are as follows. The 2 mw He-Ne laser beam was introduced into a TSI Model 915-2 beam splitter which produced two parallel beams nominally 50 mm apart. These beams were aligned to the tube center line and leveled by adjusting the reflected beam from the opposite side of the tube to coincide with the incident beam.

The beams were intercepted by two photocells (United Detector PIN 10 DP). Acceptable beam attenuation was achieved with white paper diffusers in front of the diodes. The signals from the photocells were fed to a crystal-based, two-channel event timer (Hewlett-Packard 5315A). For a given sensitivity setting, the beam spacing, as indicated by the trigger lights on the timer, was measured by moving the tail of a vernier micrometer mounted on the side of the tube through the two beams. The beam spacing was equal on both sides of the tube to within 0.0025 cm.

The beams were located approximately 40 cm above the bottom of the container. This provided sufficient acceleration length above for the high Reynolds number tests and sufficient distance between the top and bottom boundaries to produce a negligible effect on the settling velocity.

Solutions to many operational problems too numerous to mention here were all overcome. These include problems with bubbles on the models, tilting of the models in the viscous regime, launch techniques, hitting the beam with the small models, gliding, and oscillations of the cylindrical test models in the vortex shedding regime. The later problem was not overcome for the aspect ratio 4 and 10 cylinders. They oscillated about their minor axis but did not drift substantially. In some cases, the solution was to practice.

Data Reduction

Viscous Regime. In the viscous or Stokes regime, it is convenient to work with the dynamic shape factor defined as $K_\infty = U_\infty/U_s$, where U_∞ is the settling velocity of an arbitrary finite particle in an infinite fluid. U_s is the settling velocity of a sphere of equal drag and volume in an infinite fluid. K_∞ depends only on particle shape.

When boundaries are present, the arbitrary particle takes on a new velocity U. The ratio of this value to that which the particle has in an infinite fluid is known as the boundary correction factor $K_b = U/U_\infty$.

With these definitions, the drag R_m on an arbitrary particle in the Stokes regime is given by

$$R_m = \frac{3\ \pi\ \mu U\ d_s}{K_\infty K_b} \tag{2}$$

where d_s is the diameter of a sphere of equal volume to that of the particle and μ is the fluid viscosity.

Brenner [7] derived a general first-order theory for K_b which for cylindrical containers is

$$K_b = 1 - \frac{2.1044}{K_\infty}\lambda \cdot (\lambda << 1) \tag{3}$$

This equation shows that K_b depends on the shape of the particle via K_∞, the shape of the container (2.1044 for cylinders), and the proximity of the container walls via λ. Brenner specifically mentioned that this form is more accurate than a less general form

$$K_b = \left[1 + \frac{2.1044}{K_\infty}\lambda\right]^{-1}. \tag{3a}$$

For all possible geometries under consideration, the full range that the parameters λ, K_∞, and K_b can take is $0 < \lambda, K_\infty, K_b < 1$.

For terminal velocity conditions, the net weight given by equation (1) is equal to the drag R_m of equation (2). Combining these results in a relation for the product $K_\infty K_b$ in terms of experimentally-measurable variables, i.e.,

$$(K_\infty K_b)_{\text{exp}} = \frac{3\ \pi\ \mu\ U d_s}{(\rho_m - \rho_f) g\ V_m}. \tag{4}$$

One method of extracting K_∞ from data of this type is to plot $(K_\infty K_b)_{\text{exp}}$ against several values of λ and extrapolate the curve back to zero λ. Under this condition as $\lambda \to 0$, $U \to U_\infty$, therefore $K_b \to 1$, and thus $(K_\infty K_b) \to K_\infty$. The accuracy of this procedure depends in part on how close the smallest value of λ is to zero. In the present derivation d_s is the characteristic model dimension. Amarakoon et al. [2] chose d for the characteristic dimension of tori and of course the choice is arbitrary, however they have shown that the drag can be substantially affected if $\lambda' \equiv d/D$ is large even though d_s/D may be small. Thus, for best accuracy in obtaining K_∞ by extrapolation we must require that

$$\lambda < \lambda' << 1 \tag{5}$$

for the smallest values tested. Amarakoon et al. [2] empirically derived a boundary correction factor for tori which is

of the form of equation (3*a*) but contains terms involving λ' and aspect ratio A rather than λ and K_∞.

For cylindrical models one must also require $L/D << 1$ although the requirement isn't as critical as it is for the torus. When this condition is violated, Stalnaker and Hussey [1] derived an approximate empirical correction to the drag on a cylinder due to endwall boundaries in a rectangular container. Although the "endwall" correction for a cylindrical container does not exist, one might as a first order approximation use the Stalnaker and Hussey relation for the case of a square container. Under this condition, their equation (25) becomes for the present nomenclature

$$K_{be} = 1 - \frac{0.011(D_h/L)^{1/4}}{(D_h/L) - 1}, \tag{6}$$

where K_{be} represents the endwall boundary correction factor and D_h is the hydraulic diameter of the square and is taken to be approximately equal to the diameter of a cylindrical container D.

If Brenner's theory is valid, we can also predict K_∞ from $(K_\infty K_b)_{\exp}$ and K_b given by equation (3) as follows

$$K_\infty = \frac{(K_\infty K_b)_{\exp}}{K_b} = \frac{(K_\infty K_b)_{\exp}}{1 - (2.1044/K_\infty)\lambda}. \tag{7}$$

Solving for K_∞ results in

$$K_\infty = (K_\infty K_b)_{\exp} + 2.1044\,\lambda. \tag{8}$$

Brenner's theory will be compared to the extensive data for tori over a wide range of particle elongation (decreasing S).

Inertial Regime. If during the model tests the Reynolds number is not sufficiently small, K_∞ may contain some inertial terms that cannot be neglected. Chwang and Wu [8] have shown that for elongated bodies (spheroids) two Reynolds numbers are relevant. One based on the minor axis and one based on the major axis length. For other elongated bodies such as the torus, one may presume that the maximum dimension of the body may be an appropriate characteristic dimension. Thus, to ensure a viscous or Stokes result for the drag on tori or cylinders we require that

$$\mathrm{Re}_c < \mathrm{Re}_{d_s}, \mathrm{Re}_d, \mathrm{Re}_L << 1 \tag{9}$$

for the lowest values tested. Reynolds number is given as the product of U/ν and any one of the characteristic dimensions c, d_s, d, or L.

A general first order drag theory for arbitrary particle shapes in the Oseen regime has been developed by Brenner [9]. Amarakoon et al. [2] tentatively used this relation to correct Oseen drag on a torus to the Stokes drag. This correction will be evaluated for the present test models.

For the unbounded fluid, equation (2) becomes

$$R_m = \frac{3\pi\mu U_\infty d_s}{K_\infty}. \tag{10}$$

In terms of this definition for the drag, Brenner's relation can be written as

$$\frac{K_{\infty_v}}{K_\infty} = 1 + \frac{3}{16}\frac{\mathrm{Re}_{d_s}}{K_{\infty_v}}, \tag{11}$$

where the v subscript represents the Stokes condition. Solving for K_{∞_v} yields the viscous regime shape factor. Brenner mentioned that this result can be deduced from any of the known solutions of the Oseen equation. The recent first order solution for the Oseen drag on the prolate spheroid family by Chwang and Wu [8] can also be used to deduce equation (11). This includes the case where $\mathrm{Re}_L/\mathrm{Re}_c = A$ is large but $\mathrm{Re}_L << 1$. Note that the Reynolds number in equation (11) can be expressed in terms of any other characteristic dimension since

$$\mathrm{Re}_{d_s} = \frac{d_s}{d}\mathrm{Re}_d = \frac{d_s}{L}\mathrm{Re}_L, \text{ etc.}$$

It should be noted that equation (11) gives an overestimate of the inertial correction since Brenner and Cox [10] have shown that the second order term is negative for $\mathrm{Re}_L < 1$. This was pointed out by Amarakoon et al. [2].

For the case of a finite cylinder, Stalnaker and Hussey [1] have given the following empirical relation between the Stokes and Oseen shape factors

$$\frac{K_{\infty v}}{K_\infty} = 1 + 0.062\,\mathrm{Re}_L^{1/2} = 1 + 0.062(A\,\mathrm{Re}_c)^{1/2}. \tag{12}$$

This correction will be compared with that of equation (11), where appropriate, for cylinders.

The presence of boundaries has diminishing importance as Reynolds number is increased. For the Oseen or transitional regime, Stalnaker and Hussey [1] developed an empirical relation for the boundary correction to the drag on finite cylinders falling within rectangular containers. The width is $2h$ and the length is $2b$ (parallel to the major axis of the cylinder). In terms of K_b and K_∞, it becomes

$$K_b = 1 - \frac{B}{K_\infty}\left(\frac{3}{4}\right)\left(\frac{d_s}{2h}\right), \tag{13}$$

where for cylinders and tori

$$d_s = c\left(\frac{3}{2}A\right)^{1/3} \tag{14}$$

and B is a slope parameter defined in Fig. 10 of reference [1]. When considering a square container, such that $2h = 2b$ and expressing the width in terms of the hydraulic diameter D_h of the container, the following relation is obtained

$$2h = \frac{D_h}{2}\left[1 + \frac{2h}{2b}\right] = D_h = D. \tag{15}$$

The last equality is valid since the hydraulic diameter of a circle and a square are the same.

If equation (15) is substituted into equation (13) which in turn is combined with the first part of equation (7) we obtain

$$K_\infty = (K_\infty K_b)_{\exp} + \frac{3}{4}B\,\lambda. \tag{16}$$

Stalnaker and Hussey obtained

$$B = 0.886 \qquad \text{for } \mathrm{Re}_L \leqslant 3 \tag{17a}$$

and

$$B \cong 2.66\,\mathrm{Re}_L^{-1} \qquad \text{for } \mathrm{Re}_L > 3. \tag{17b}$$

The latter relation is based on cylinder data taken by Huner (see Fig. 10 of reference 1).

At high Reynolds numbers shapes having equal hydraulic diameters usually yield similar results, however for the Stokes regime Happle and Bart [11] have shown approximately a 10 percent reduction in the container shape constant of equation (3) when the container is changed from a cylinder to a square container whose sides are equal to the cylinder diameter, i.e., equal hydraulic diameter. The present test results using UCON 50-HB-170 will be compared to the results of equations (17) which cover a similar range of Reynolds number.

In the inertial regime, it is more conventional to use the drag coefficient C_D rather than a shape factor. The following relations express the drag coefficient in terms of experimentally measurable quantities for the terminal velocity condition as well as its relation to shape factor

$$C_D = \frac{W_n}{0.5\rho U_\infty^2 A_f} = \frac{6\pi c d_s}{K_\infty \mathrm{Re}_c A_f} = \frac{21.5773}{K_\infty \mathrm{Re}_c}A^{-1/3}. \tag{18}$$

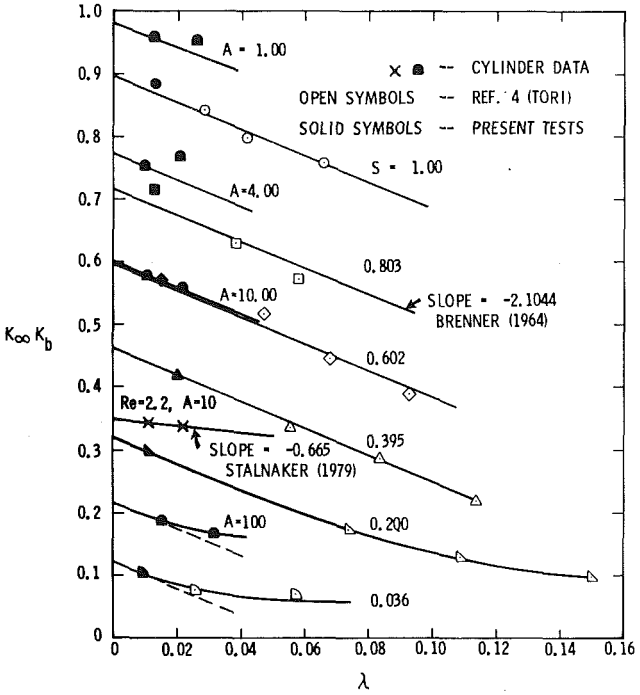

Fig. 1 The effect of boundaries on shape factor for tori and finite cylinders

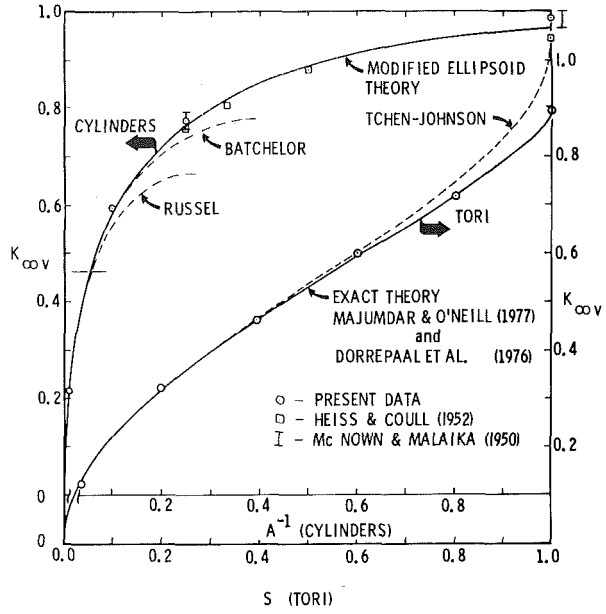

Fig. 2 Dynamic shape factor for the cylinder and torus family (viscous regime)

Here, A_f is the projected frontal area of the body. The second expression is general. The third relation was obtained using equation (14) and $A_f = c^2 A$. It applies to tori and cylinders.

Drag coefficients derived from the tests in UCON 50-HB-55 and water were not corrected for blockage due to the negligible magnitude and sufficiently high Reynolds numbers. The basis for this is discussed in Roos and Willmarth [12].

Statement of Experimental Uncertainty. The uncertainty estimate of the experimentally derived parameter $K_\infty K_b$ is ± 1.4 percent, and for λ, ± 0.2 percent. It is believed that there is a systematic error in $K_\infty K_b$ on the order of 4 to 5 percent maximum in some of the small tube tests and 1 to 2 percent maximum in some of the large tube data. The reason was occasional excessive exposure of the fluid to the laser beam. The resultant heating created a sheet of lower viscosity fluid above the beams and some general heating of the fluid, which was dependent on the mass of fluid in the tube. The effect would be to cause higher settling velocities for the less elongated test models and those in the small tube.

The estimated uncertainty of C_D and Re are ± 3 percent and ± 1.5 percent, respectively. Variation in the velocity measurement (an average of three for each data point) is the largest contributor to the uncertainty in all parameters involving velocity.

Results and Discussion

Viscous Regime. The values of $(K_\infty K_b)_{\exp}$ for cylinders and tori, including data from 4, are shown in Fig. 1. The slope of the data for tori of $S \geq 0.395$ for the most part supports that predicted by Brenner's general boundary correction theory, equation (8). For these data, we obtained $\mathrm{Re}_d \leq 0.01$ and $\lambda' \leq 0.05$ for the smallest values of λ tested and $\mathrm{Re}_d = 0.034$ and $\lambda' = 0.315$ for the largest λ tested. The inertial correction, equation (11), was applied using Re_d at the smallest values of λ tested. For this group it did not exceed 0.2 percent and thus was neglected. For each value of solidity, K_{∞_v} was determined for each λ using equation (8) and then averaged.

For the $S = 0.2$ and the $S = 0.036$ tori the data reduction was done two ways. In the extrapolation method shown in Fig. 1, a curve was drawn through the data points which was made to match Brenner's slope at $\lambda = 0$. Then inertial effects were accounted for by using equation (11) at the smallest test λ to obtain K_{∞_v}.

The second method used the more elaborate empirical boundary correction relation developed by Amarakoon et al. [2]. First, equation (11) was assumed to apply at each λ′ to correct $(K_\infty K_b)_{\exp}$ to $(K_\infty K_b)_v$[1].

Then the Amarakoon et al. relation was used to correct $(K_\infty K_b)_v$ to K_{∞_v}. It can be expressed as

$$K_{\infty_v} = (K_\infty K_b)_v \left[1 + \frac{2.09\,\lambda'(1+s_0)s_0^{-0.05}}{1+s_0-\pi\lambda'\sqrt{s_0}}\right], \qquad (19)$$

where $s_0 = A/\pi$. The resulting K_{∞_v} were averaged.

These results are compared to the exact theory of Majumdar and O'Neill [15] for the open torus ($S<1.0$) and Dorrepaal et al. [16] who first solved for the viscous drag on the closed torus ($S=1.0$). The exact theory has been evaluated over a wide range of aspect ratio by Goren and O'Neill [17]. Figure 2 shows the results for cylinders and tori. The torus data is plotted against solidity for convenience.

For $S \leqslant 0.395$, there was no advantage of the method two correction scheme over Brenner's relation for the range of λ tested. For $S=0.200$, the extrapolation scheme using Brenner's slope at $\lambda = 0$ yielded a K_{∞_v} 1.6 percent higher than the exact theory while method two predicted 2.3 percent low for the present data. For $S=0.036$, the extrapolation method predicted 3 percent below the exact theory. This point was erroneously stated to be 6.1 percent low in reference [3] due to an error in estimating the exact theory. Herein the exact theory values were obtained by linear interpolation of the values given in reference [17]. The second method experiences trouble when the $\lambda=0.057$ data point was included in the

[1] This is an approximation. McNown et al. [13] have shown that for spheres, transition to the inertial regime is delayed to higher Reynolds number when λ is not zero. McNown and Malaika [14] have suggested that the results for spheres can be applied, approximately, to other shapes if the square root of the projected area of the particle is substituted for d_s in the definition of λ.

average. As seen in Fig. 1, this data point appears to be excessively large. In addition, Re_d was 0.803 which may be out of bounds for the first order inertial correction term, equation (11). Using only the two lowest λ data points, method two predicted a K_{∞_v} 2.7 percent below the exact theory.

Applying Brenner's relation to the torus data of Amarakoon et al. [2] showed that it fit well for the high to medium solidity data as long as λ' was less than 0.1 to 0.2 depending upon solidity. At the lowest value of solidity, the slope of the curve predicted by Brenner's theory did not match the empirical relation of Amarakoon et al. It should be noted that for low solidity tori there is insufficient data below $\lambda' = 0.1$ to support either the Amarakoon et al. or the Brenner relation. The average normalized error between the six data points and the exact theory is 0.998 with a normalized standard deviation of $\pm$ 0.015.

The exact theory is difficult to use because of the complex mathematical relations involved. A closed-form relation for the drag on a torus of low solidity was obtained by Tchen [5] and later by Johnson and Wu [18]. It can be written as

$$K_{\infty_v} = \frac{3}{4}\left(\frac{3}{2}\right)^{1/3} A^{-1/3}\left[\ln\left(\frac{8A}{\pi}\right) + \frac{1}{2}\right]. \tag{20}$$

This relation fits the exact theory within 0.5 percent for $S<0.3$ as shown in Fig. 2. Note that for tori, aspect ratio is related to solidity by

$$A = \pi\left[\frac{2}{1-\sqrt{1-S}} - 1\right]. \tag{21}$$

Another approximation can be made by a modification of ellipsoid theory. The viscous drag for transverse flow past a prolate spheroid can be expressed in terms of shape factor as follows

$$K_{\infty_v} = \frac{3}{8} A_e^{1/3}\left[\frac{(2A_e^2-3)\operatorname{arccosh} A_e}{(A_e^2-1)^{3/2}} + \frac{A_e}{A_e^2-1}\right]. \tag{22}$$

This relation is due to Oberbeck (1876), see e.g., Chwang and Wu [8]. Here we have written A_e rather than A for reasons that will now be explained. It seemed that for any torus having aspect ratio A, one could find a spheroid of some other aspect ratio A_e that would have the same drag as the torus. Thus, if A_e was the aspect ratio of a spheroid of equal drag to that of a torus of aspect ratio A, there is some function $\sigma_t = \sigma_t(A)$, where

$$A_e = \sigma_t A. \tag{23}$$

It was found that σ_t could be expressed empirically by

$$\sigma_t = 0.774 \exp[-0.4692/A^{\zeta}], \tag{24a}$$

where

$$\zeta = 0.3236 + 51.41\, A^{-3.424}. \tag{24b}$$

This relation matches the exact theory within 0.5 percent for all values of S.

For the cylinder data of Fig. 1, the suspected systematic error in the small tube data for cylinders of $A = 1$ and 4 is apparent. The large tube data were thought to be more reliable for these models. Therefore, Brenner's theory was applied only to the large tube data for these test cylinders. The same method was applied to the $A = 10$ cylinder even though the slope (-1.25) did not match that predicted by Brenner's relation. With only two values of λ quite close together, the slope is rather sensitive to experimental error in the measured values of $(K_\infty K_b)$. The average K_∞, using equation (8), was then corrected for inertial effects using equation (11). For all of the above data points, the inertial correction did not exceed 0.3 percent and the "endwall" correction, equation (6), was less than 0.1 percent.

The $A = 100$ cylinder data was reduced using the extrapolation method as illustrated in Fig. 1 and then corrected for inertial and endwall effects as previously described. These corrections increased K_∞ by 0.95 percent and 0.6 percent, respectively.

The data for cylinders are also shown in Fig. 2 along with some other data for low aspect ratio cylinders found in the literature; Heiss and Coull [19] tested cylinders of $A = 1, 2, 3$, and 4. The latter was also tested by McNown and Maliaka [14]. The exact theory of Batchelor [20], valid for large A, and a numerical solution by Russel et al. [21], also valid for large A, have been combined into a single expression by Stalnaker and Hussey [1]. It can be written as

$$K_{\infty_v} = \frac{3}{4}\left(\frac{3}{2}\right)^{1/3} A^{-1/3} [\epsilon - 0.193\,\epsilon^2 + 0.215\,\epsilon^3 + 0.97\,\epsilon^4]^{-1}, \tag{25}$$

where

$$\epsilon = [\ln(2A)]^{-1}. \tag{26}$$

Terms through ϵ^3 represent the Batchelor solution, while the entire relation represents the Russel numerical solution. This function was verified by Stalnaker and Hussey [1] and by others for aspect ratios $A > 20$. These functions are plotted in Fig. 2. The tic mark indicates the upper limit of validity for A^{-1} according to Stalnaker and Hussey [1].

The present data for $A = 10$ and 100 falls 3.1 percent and 1.3 percent above the Batchelor theory, respectively. If we had used equation (12) rather than equation (11) for the inertial correction, the above discrepancies would increase by an additional 1.0 percent and 1.9 percent, respectively.

By a second method, if we simply use the slope determined by the two values of λ, to find the zero λ intercept K_∞ then correct for endwall effect and the equation (11) inertial effect, the resulting K_{∞_v} for the above mentioned A fall 1.7 percent above and 2.5 percent below the Batchelor theory, respectively. Using the second method in combination with the equation (12) inertial correction results in K_{∞_v} 2.5 percent above and 0.7 percent below the Batchelor theory for the same respective A. Considering the previously mentioned sensitivity of the slope to experimental error, the second method is thought to be less reliable for the present data which covers only two values of λ.

The Stalnaker-Hussey empirical inertial correction, equation (12), predicts a considerably higher inertial effect than Brenner's relation, equation (11). The former appears to be based on a curve fit to data having considerable scatter. This relation will be discussed further in the inertial section.

When one considers the whole regime of A, and the additional data plotted for small A, it seems that the original Batchelor relation fits the data over a wider range than does the Russel relation. Both relations fail at lower aspect ratios, however.

We desire a relation that covers the whole range of A. This was accomplished by again using a modification of the ellipsoid relation, equation (22). For cylinders the aspect ratio A_e of a spheroid of equal drag to that of the cylinder of aspect ratio A is given by

$$A_e = \sigma_c A. \tag{27}$$

Using the exact theory of Batchelor, where applicable, and a smooth curve through the data for the low aspect ratio range, the following relation was found for σ_c,

$$\sigma_c = 0.835 \exp[0.527 A^{-0.69}]. \tag{28}$$

The set of equations (22), (27), and (28) are plotted in Fig. 2 and denoted as modified ellipsoid theory. At large A, this relation fits the Batchelor exact theory for cylinders within 0.5 percent. It provides a good mean curve through the data at low A. Most of the data falls within $\pm$ 2 percent of this curve, thus it is felt that this may predict within 2 percent or better for the full range of A.

At low aspect ratios, prolate spheroids of the same A as that of a cylinder have less drag (higher K_∞). At large aspect ratios, where we are comparing the drag predicted by two exact theories, a prolate spheroid of the same aspect ratio as a cylinder has higher drag (lower K_∞) than the cylinder. For equal drag it must have an aspect ratio 83.5 percent as large as the cylinder. All but 5 percent of this discrepancy can be accounted for if the average diameter $c\pi/4$ is taken as the characteristic diameter rather than the minor diameter c.

We are now ready to examine the effect of transverse curvature on the drag of elongated particles. This is presented in Fig. 3 as a ratio of K_∞ for any curved particle to that of a cylinder of the same aspect ratio, K_{∞_c}. The curve shown is for the exact torus theory, and the abscissa represents the cylinder given by equations (22), (27), and (28). Drag curves for segments of a torus will fall between these boundaries. The theory of Tchen [5] was evaluated for segments of a torus and it was found to predict a rather rapid increase in drag (decreasing K_{∞_v}) as the torus was opened up. However Tchen's geometry did not maintain a constant cross sectional diameter during this process but rather changed steadily to a prolate spheroid in the limit rather than a cylinder. Since we have shown that a spheroid of the same aspect ratio as that of a cylinder has higher drag, it is not clear what fraction of Tchen's drag change is due to change in shape and what fraction is due to changing the curvature of the torus. One can see in Fig. 3 that the maximum correction to shape factor due to transverse curvature is 15.1 percent at $A^{-1} = 0.09$.

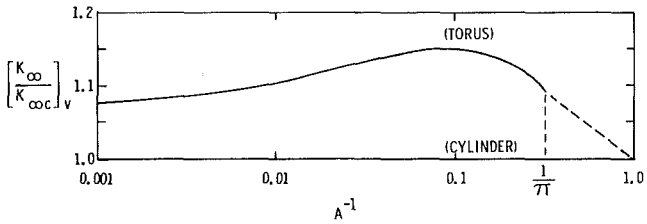

Fig. 3 Effect of transverse constant radius of curvature on shape factor of finite elongated bodies.

Inertial Regime

Cylinders. In Fig. 1 we show a typical result for the cylinders tested in UCON 50-HB-170, $A = 10$, $\mathrm{Re}_c = 2.2$. These tests covered a Reynolds number range $0.004 < \mathrm{Re}_L \leqslant 99$. This was stated incorrectly in reference [3] due to mistaking Re_c for Re_L. The boundary effects were found to be weaker at the higher Reynolds numbers, however the slope which was obtained by connecting the data points at the two values of λ described previously gave quite different results than the values expressed by Stalnaker and Hussey in the form of equations (17). For the present data we obtained that $B = 3.55\ \mathrm{Re}_L^{-0.54}$ for $\mathrm{Re}_L > 6$; at $\mathrm{Re}_L = 2.9$, $B = 1.37$, which is in substantial agreement with de Mestre's result of 1.337 (see Fig. 10 of reference [1]); as Reynolds number further decreased, B continued to increase toward the value of 2.8059 predicted by Brenner's theory. These slope results must be regarded as preliminary, keeping in mind the sensitivity of the slope to experimental error in $K_\infty K_b$ as discussed previously. The intercept values of K_∞ at $\lambda = 0$ were converted to C_D by means of equation (18) as was the data for the other fluids.

The drag results for cylinders are shown in Fig. 4 plotted two ways. In Fig. 4(*a*), the data are presented as the conventional drag coefficient as a function of Reynolds number for the various aspect ratios. Curves drawn through the data show the crossing-over effect around $\mathrm{Re}_c = 44$, as discussed in the introduction.

Supporting data or interpolations from data is shown where available. This includes data from Heise and Coull [19], McNown and Malaika [14], and Huner and Hussey [22]. These data support the present results within a few percent. The curves stop at a Reynolds number of about 1000 for lack of data. They must join another set of curves based on the drag coefficients taken at high Reynolds numbers. An approximate relation for the drag curves shown in Fig. 4(*a*) for Reynolds numbers greater than 5000 was given in reference [3].

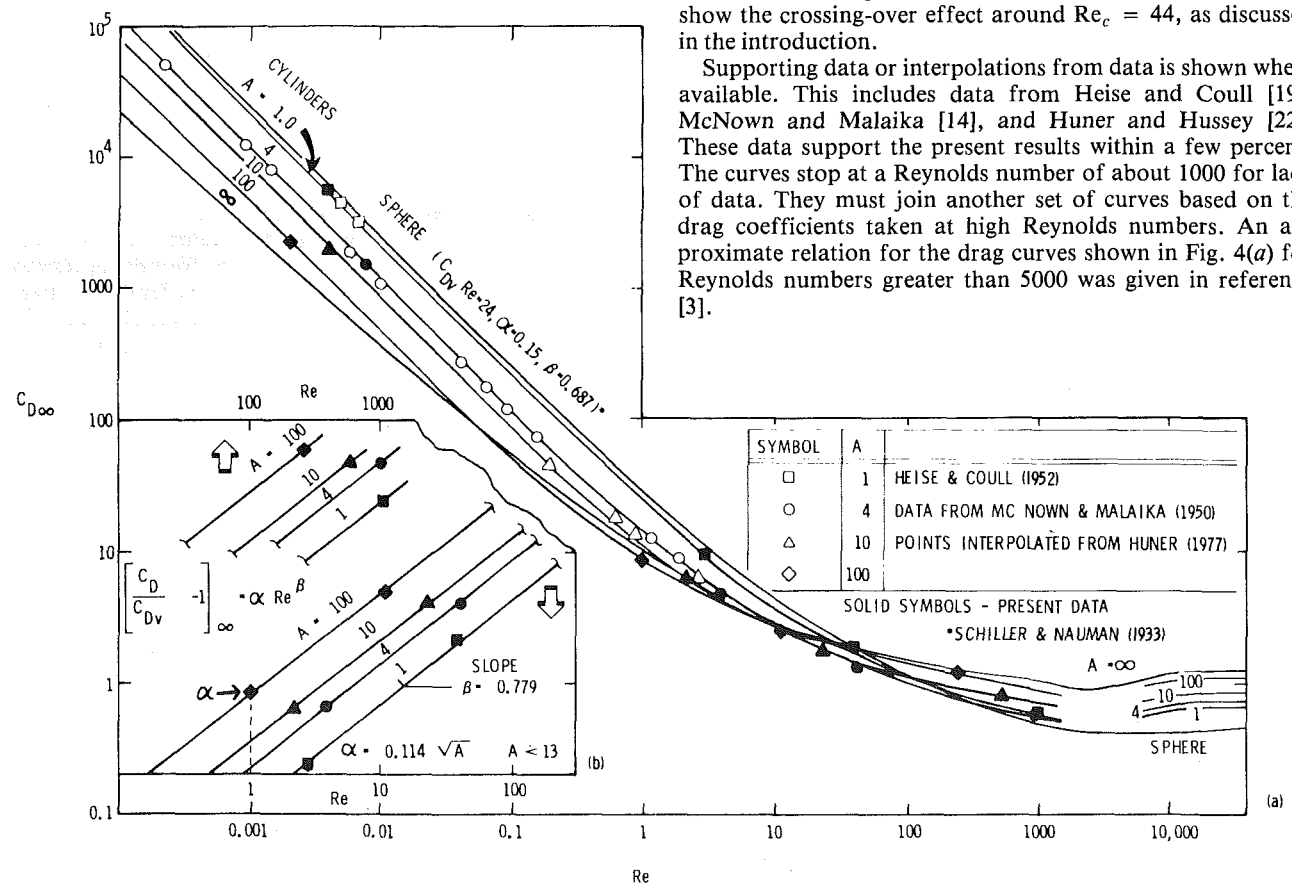

Fig. 4(*a*) Variation of the drag coefficient with Reynolds number for selected cylinder aspect ratios; (*b*) Variation of $[(C_D/C_D)-1]_\infty$ with Reynolds number for the cylinder data of Fig. 4(*a*)

Actually, the curves drawn through the data in the conventional plot, Fig. 4(*a*), could not have been drawn through the present limited set of data were it not for the curves of Fig. 4(*b*).

In this inset, we have plotted the parameter $[C_D/C_{Dv} - 1]_\infty$ against Reynolds number for the four aspect ratio cylinders that were tested. C_{Dv} is the Stokes drag coefficient at the same Reynolds number. On this type of plot, the curves are nearly linear and can be fit by an average curve of the form

$$[C_D/C_{Dv} - 1]_\infty = \alpha \, \mathrm{Re}_c^\beta. \tag{29}$$

The slopes are all the same, $\beta = 0.779$, and the intercepts can be read at the intersection of the curves with the ordinate passing through $\mathrm{Re}_c = 1.0$, Fig. 4(*b*). There is a hint in the fit of these curves to the data near $\mathrm{Re}_c = 40$ that there may be subtle shifts in the slope and drag of the type described by Pruppacher et al. [23], but there is an insufficient quantity of precise data to discern these details. Roos and Wilmarth [12] noted that oscillating discs in free fall had higher drag coefficients than those that were held rigidly. The oscillations of the $A = 4$ and 10 cylinders did not seem to significantly affect the drag data since the data fit the relation of equation (29). The value α as found to follow the relation

$$\alpha = 0.114\sqrt{A}. \quad (A < 13) \tag{30}$$

At aspect ratios greater than 13, there is a significant departure from this relation. The line through the $A = 100$ data is the only data point above $A = 13$ for the present tests, thus there is insufficient data to predict the drag characteristics for larger aspect ratio cylinders. Examination of the data on finite length cylinders by Tritton [24] over the range $150 < A < 876$ had too much scatter and an insufficient range of Reynolds number to resolve the issue.

At Reynolds numbers below 1.0, the empirical relation of Stalnaker and Hussey, equation (12), predicts a different relation when converted to the form of equation (29), with $\alpha = 0.062\sqrt{A}$ and $\beta = 0.5$. These relations are valid for $\mathrm{Re}_c < 10/A$ and, presumably $19.6 < A < 388$, the range of their test parameters. The general theory of Brenner and Cox [10], given by equation (11) to first order, can be written in terms of equation (29) by making use of equations (14) and (18) with the result

$$[C_D/C_{Dv} - 1]_\infty = \frac{3}{16}\left(\frac{3}{2}A\right)^{1/3} \mathrm{Re}_c/K_{\infty_{vc}} + 0[\mathrm{Re}_c^2 \ln \mathrm{Re}_c], \tag{31}$$

where $K_{\infty_{vc}}$ for cylinders is given by equations (22), (27), and (28).

The present relation with $\beta = 0.779$ and the measured α or the relation of equation (30), in addition to fitting the data well at higher Reynolds numbers, is in much closer agreement with equation (31) than is the Stalnaker-Hussey relation for Reynolds numbers less than 1.0.

The exact nature of transition as aspect ratio is increased is still lacking unified relations up to large Reynolds number, however, equation (31) and the analysis of Chwang and Wu [8] for ellipsoids give some ideas about the beginnings of transition to first order in Reynolds number. Equation (31) shows that α follows some function of A and that β is a function of Reynolds number. At low values of Reynolds number equation (31) suggests $\beta \to 1.0$. At high values Pruppacher et al. have shown that β can shift abruptly as flow patterns change as a function of Reynolds number.

Prior to this investigation, this author had the impression that the drag coefficient curves for elongated bodies would blend or coalesce with the drag curve for an infinite cylinder as Reynolds number increased. For example, the ellipsoid equations of Shi [25] which are valid for large A show all the drag coefficient curves for various aspect ratio ellipsoids converging to a single curve as Reynolds number increases. In another example, the average drag curve drawn by Tritton [24] through data for large but finite aspect ratio cylinders is often averaged in with similar data from other investigators. These results are then used to represent the drag coefficient curve for infinite aspect ratio cylinders. Others such as Huner [22], take data in a narrow Reynolds number range and develop empirical relations as a function of A which allow one to extrapolate to the inifinte aspect ratio case. Huner's correction to the drag coefficient for infinite aspect ratio was based on data from cylinders of $10 < A < 50$. Stalnaker and Hussey [1] suggest that the Huner relation may be valid from $0.0079 < \mathrm{Re}_c < 2.5$

With the present curve for $A = 100$ in Fig. 4(*a*), one would have some difficulty utilizing the Huner relation to predict the infinite cylinder drag coefficient from the data at $\mathrm{Re} = 1.0$. The transition curve (defined by equation (29) with $\alpha = 0.825$, $\beta = 0.779$) goes below the $A = \infty$ drag curve. Thus, a different relation would be needed for this case. The functional form of Huner's relation would need a negative sign in front of his aspect ratio function rather than a positive value (equation (24) of reference [1]).

The reference drag coefficient curve for infinite cylinders is useful in its own right for many studies. Presently, its representation is a collection of theories, curve fits and data sets for various ranges of Reynolds number. Using selected data and theory described in reference [3], the following curve fit resulted, which is valid for $\mathrm{Re}_c < 1000$:

$$C_{D0} = \frac{8\pi}{\mathrm{Re}_c}\epsilon_e, \tag{32a}$$

where

$$\epsilon_e = \left[\frac{1}{2} - \gamma - \ln\frac{\mathrm{Re}_c}{8} + f_1(\mathrm{Re}_c) + f_2(\mathrm{Re}_c)\right]^{-1} \tag{32b}$$

$$f_1(\mathrm{Re}_c) = 0.30851\,\mathrm{Re}_c^{0.17834} \tag{32c}$$

$$f_2(\mathrm{Re}_c) = [9.12640^{\mathrm{Re}_c^{-0.450605}} - 0.83139 - 0.00245\,\mathrm{Re}_c^{0.25}]^{-1}. \tag{32d}$$

The error is $\leqslant 0.7$ percent for $\mathrm{Re}_c < 0.1$, $\leqslant 0.8$ percent for $0.1 \leqslant \mathrm{Re}_c \leqslant 2.5$, and $\leqslant 2.0$ percent for $2.5 < \mathrm{Re}_c \leqslant 1000$, except for a small region around $\mathrm{Re}_c = 4$ where the error is +4.5 percent. The 5 place precision is necessary around $\mathrm{Re}_c = 1000$.

Tori. The limited drag coefficient measurements made for tori of solidity $0.036 \leqslant S \leqslant 1$ in the Reynolds number range $70 < \mathrm{Re}_c < 270$ are given in Table 1 to avoid confusion in adding the data to the many curves of Fig. 4(*a*). When these data are plotted in Fig. 4(*a*), we find that the trends are similar to the trends for cylinders of the same aspect ratio.

For the data of $S = 1$, 0.803, and 0.602, one can compare the measured torus drag coefficient with that of a cylinder of the same A by means of equations (18), (22), (27), (28), (29), and (30). The solidities are related to A by means of equation (21). The results are $C_{D\mathrm{torus}}/C_{D\mathrm{cylinder}} = 0.93$, 0.87, and 0.99, respectively. Thus, these tori are running up to 13 percent lower than a cylinder of the same A with considerable scatter in the data evident. The cylinder data is not well enough defined to make a comparison with the lower solidity torus data.

A tentative conclusion for this section (pending more data at large A) is that the transition curves (C_D versus Re_c) for elongated bodies of finite aspect ratio follow curves of the general form given by equation (29).

Subtle shifts in the slope with increasing Reynolds numbers when encountering new flow patterns are anticipated. These transition curves fall close to the curve for an infinite cylinder but are not necessarily related. They do not coalesce with the

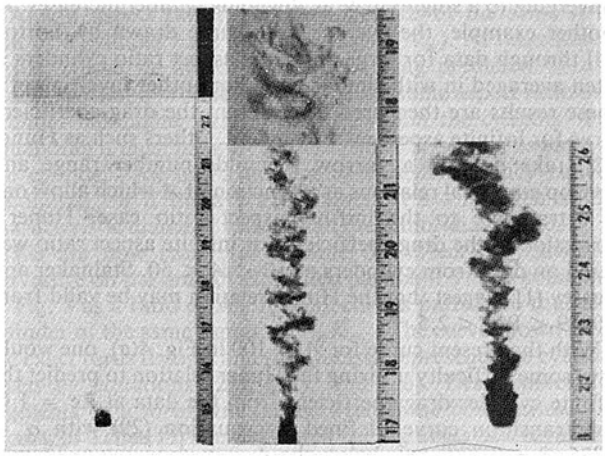

(a) $Re_c = 274$ (b) $Re_c = 1770$ (c) $Re_c = 2940$

Fig. 5 Tori $S = 1.000$

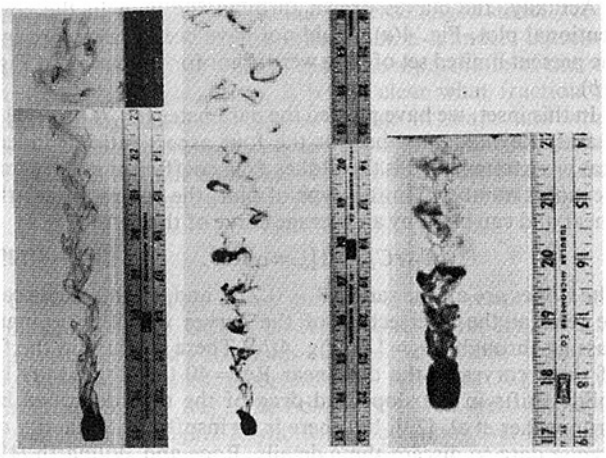

(a) $Re_c = 115$ (b) $Re_c = 182$ (c) $Re_c = 347$

Fig. 6 Tori $S = 0.803$

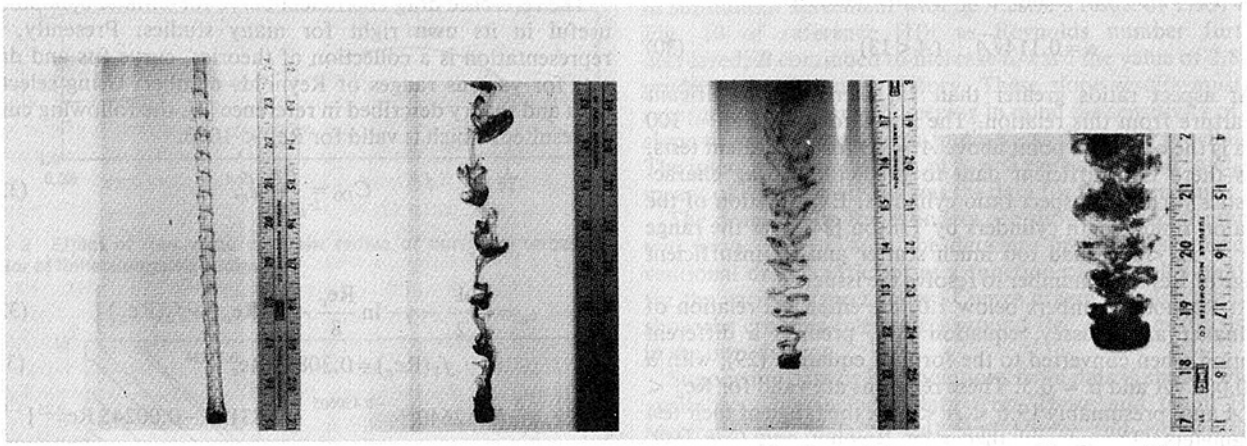

(a) $Re_c = 78$ (b) $Re_c = 94$ (c) $Re_c = 97$ (d) $Re_c = 464$

Fig. 7 Tori $S = 0.602$

infinite cylinder drag curve with increasing Reynolds number; but, each constant aspect ratio curve crosses the infinite cylinder curve and goes below it at a particular Reynolds number.

Vortex Shedding Regime—Tori. The results of this section are a brief summary of the more extensive systematic flow visualization studies done in 4. The effect of transverse curvature on the vortex shedding characteristics of the torus family of shapes was studied by means of flow visualization using falling bodies dipped in a dye solution. Reynolds number was varied by mixing various combinations of water and glycerine. Figures 5 through 10 show the results of visualizations for seven decreasing solidities from 1 to 0.036. For each case, visualizations of several progressively increasing Reynolds numbers are shown.

Three general flow regimes are classified according to the solidity S of the torus as follows:

1. In the high solidity range, $0.45 \leqslant S \leqslant 1$, tori behave similar to solid bodies, producing rows of oblique vortex loops which change, at a given Reynolds number, to regular but distorted rows of counterrotating ring vortices. This is accompanied by a sudden increase in the Strouhal number. This change can be seen in Figs. 7(*b*) and (*c*), respectively. Roshko [27] correctly speculated on this phenomenon based entirely on wake frequency measurements using a hot wire anemometer. Takamoto and Izumi [28] recently reported observing the counterrotating ring wake behind a flat annular washer of solidity $S = 0.556$, but did not report observing the oblique loop wake.

These results suggest that there may be three subcategories of wake patterns within this general solidity range; a solidity range (say > 0.7) where only the oblique loop wake exists, a range $0.55 < S < 0.7$ where either the oblique loop or the counterrotating ring wake can exist depending on Reynolds number (some hysteresis has been noted in this critical Reynolds number), and a range $0.45 < S < 0.55$ where only the counterrotating ring wake exists. It can be seen that higher Reynolds numbers produce periodic turbulent "puffs" in the wake. Refer to Figs. 5–7.

2. In the medium solidity range, $0.15 < S < 0.45$, two possible vortex patterns exist: one consists of rows of counterrotating ring vortex pairs; the second is a surprising pattern which appears at random, namely, a counterrotating helical vortex pair. With increasing Reynolds numbers, three-dimensional circumferential disturbances become more predominant and the wake pattern gradually reduces to periodic turbulent annular puffs. Refer to Figs. 8 and 9.

Studies of the helix angle as a function of Reynolds number in 4 for the helical wake mode show a decreasing angle (measured perpendicular to the axis of revolution) with increasing Reynolds number. Apparently when the Reynolds

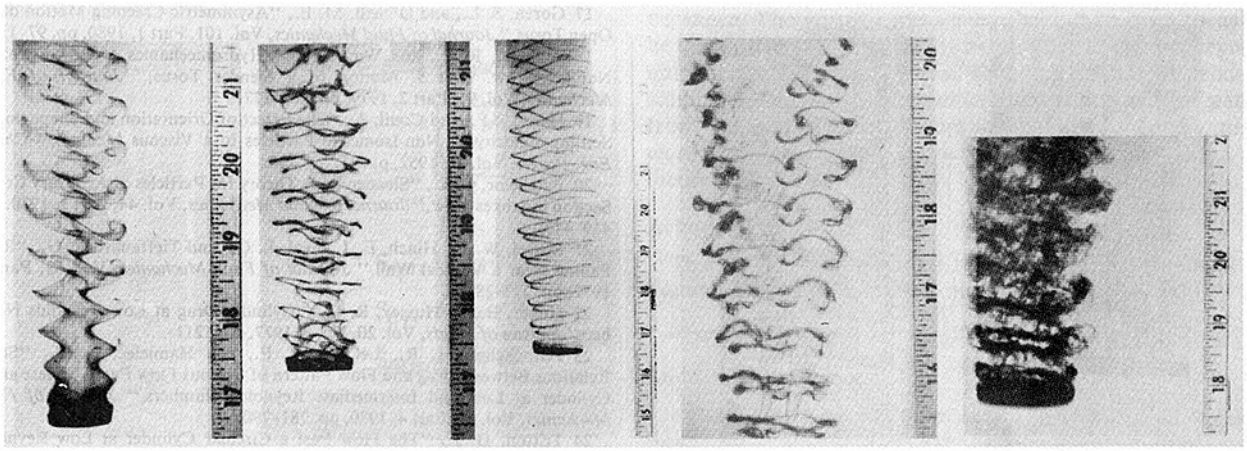

(a) $Re_c = 55$ (b) $Re_c = 84$ (c) $Re_c = 100$ (d) $Re_c = 150$ (e) $Re_c = 459$

Fig. 8 Tori $S = 0.395$

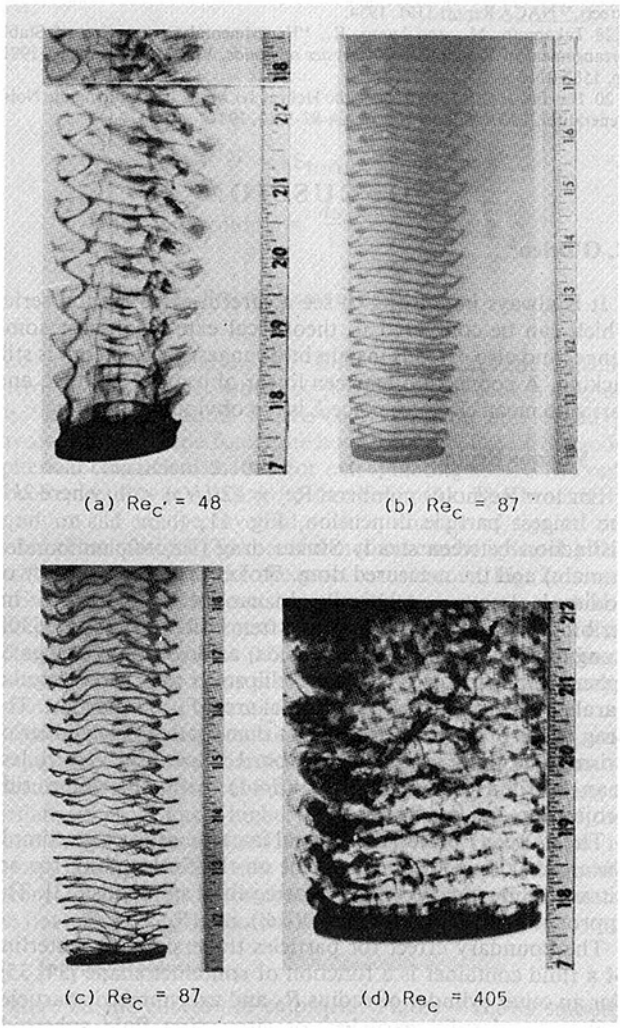

Fig. 9 Tori $S = 0.200$

number exceeds some critical value (or range of values), the helix angle becomes too low for the helical mode to exist and the system reverts to the ring wake mode. One of the annular bodies visualized in 4 was caught in the act of switching from one mode to the other.

The flow past a torus is not unlike the flow from a thick lip nozzle with an external flow superimposed. Axisymmetric and helical modes and the switching phenomenon have been observed in both low and high Reynolds number turbulent jets with no external flow field. This phenomenon is currently under investigation as it pertains to jet noise, see, e.g., Hardin [29]. The isolated jet produces a much larger helix angle in the helical mode than does the torus at low Reynolds number. This suggests that the helical wake of the torus may reappear with somewhat different characteristics at higher Reynolds numbers than were tested herein depending on the relative stability of the modes and whether or not the flow field is perturbed by external sources.

3. In the low solidity range, $0 < S < 0.15$, only the ring vortex street is observed. Refer to Fig. 10. As solidity is decreased toward zero, the vortex shedding characteristics steadily approach those observed for the infinite cylinder.

Reference [3] contains a more detailed discussion of the wake structure, stability and dimensionless shedding frequencies.

Conclusions

For tori, the drag data closely support the exact theory of Majumdar and O'Neill and Dorrepaal et al. in the viscous regime. In the Reynolds number range $70 < Re_c < 270$, the drag coefficients for tori are about the same as a finite cylinder of the same aspect ratio. In the vortex shedding regime, a wide variety of flow patterns are observed.

In the high solidity range, $0.45 \leqslant S \leqslant 1.0$, there is a critical Reynolds number at a solidity of ~ 0.6 where the flow pattern suddenly shifts from the oblique loop wake structure typically generated by solid bodies to a ring-type counterrotating vortex pair. In the medium solidity range $0.15 \leqslant S \leqslant 0.45$, two annular vortex patterns can exist, either the counterrotating ring vortex pair or as a helical counterrotating vortex pair. The latter is less common but more stable and occurs in the approximate Reynolds number range of $100 < Re_c < 300$. In the low solidity range $0 < S \leqslant 0.15$, only the ring-type vortex structure was observed. The wake properties approach that of a circular cylinder as $S \to 0$.

The viscous drag of a family of finite circular cylinders is predicted by Batchelor's relation at high aspect ratio. The drag of low aspect ratio cylinders is predicted within ± 2 percent by a modified ellipsoid theory. The transition regime is predicted by relations of the form $[(C_D/C_{Dv}) - 1]_\infty = \alpha Re^\beta$.

The effect of transverse curvature reduces the drag by a maximum of 13 percent in the viscous regime.

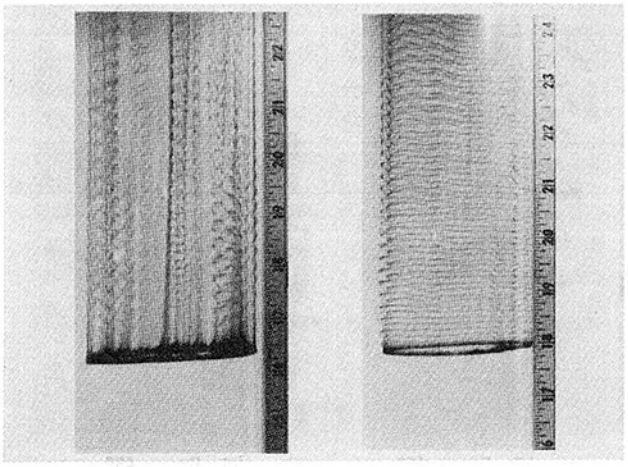

(a) $Re_c = 41$ (b) $Re_c = 53$

Fig. 10 Tori $S = 0.036$

Acknowledgments

The author wishes to acknowledge the consultation and assistance of B. N. McDonald of the Donaldson Co. in the design and setting up of the experimental timing system. The assistance of Jayne Enthoven and Judy Neufeld, work-study students, during testing and data reduction is gratefully acknowledged.

References

1 Stalnaker, J. F., and Hussey, R. G., "Wall Effects on Cylinder Drag at Low Reynolds Number," *Physics of Fluids*, Vol. 22, No. 4, Apr. 1979, pp. 603-613.

2 Amarakoon, A. M. D., Hussey, R. G., Good, B. J., and Grimsal, E. G., "Drag Measurements for Axisymmetric Motion of a Torus at Low Reynolds Number," *Physics of Fluids*, Vol. 25, No. 9, Sept. 1982, pp. 1495-1501.

3 Monson, D. R., "The Effect of Transverse Curvature on the Drag and Vortex Shedding of Elongated Bluff Bodies at Low Reynolds Number," ASME Paper 81/WA/FE-4, 1981.

4 Monson, D. R., "Experimental Drag Characteristics of Tori, Ducted-Spheres, and Other Shapes at Low Reynolds Numbers," Masters thesis, Department of Aerospace and Engineering Mechanics, University of Minnesota, 1965.

5 Tchen, C. M., "Motion of Small Particles in Skew Shape Suspended in a Viscous Liquid," *Journal of Applied Physics*, Vol. 25, No. 4, Apr. 1954, pp. 463-473.

6 Johnson, R. E., "An Improved Slender-Body Theory for Stokes Flow," *Journal of Fluid Mechanics*, Vol. 99, Part 2, 1980, pp. 411-431.

7 Brenner, H., "Effect of Finite Boundaries on the Stokes Resistance of an Arbitrary Particle, Part 1," *Journal of Fluid Mechanics*, Vol. 12, Jan. 1962, pp. 35-48.

8 Chwang, A. T., and Wu, T. Y., "Hydromechanics of Low-Reynolds-Number Flow. Part 4. Translation of Spheroids," *Journal of Fluid Mechanics*, Vol. 75, Part 4, 1976, pp. 677-689.

9 Brenner, H., "The Oseen Resistance of a Particle of Arbitrary Shape," *Journal of Fluid Mechanics*, Vol. 11, 1961, pp. 604-610.

10 Brenner, H., and Cox, R. G., "The Resistance to a Particle of Arbitrary Shape in Translational Motion at Small Reynolds Numbers," *Journal of Fluid Mechanics*, Vol. 17, 1963, pp. 561-595.

11 Happle, J., and Bart, E., "The Settling of A Sphere Along the Axis of a Long Square Duct at Low Reynolds Number," *Applied Scientific Research*, Vol. 29, 1974, pp. 241-258.

12 Roos, F. W., and Willmarth, W. W., "Some Experimental Results on Sphere and Disk Drag," *AIAA Journal*, Vol. 9, No. 2, Feb. 1971, pp. 285-291.

13 McNown, J. S., Lee, H. M., McPherson, M. B., and Engez, S. M., "Influence of Boundary Proximity on the Drag of Spheres," *Proc. VII Intern. Cong. of Appl. Mech.*, London, 1948, pp. 17-27.

14 McNown, J. S., and Malaika, J., "Effects of Particle Shape on Setting Velocity at Low Reynolds Numbers," *Trans. of Am. Geophys. Union*, Vol. 31, 1950, pp. 74-82.

15 Majumdar, S. R., and O'Neill, M. E., "On Axisymmetric Stokes Flow Past a Torus," *Journal of Applied Mathematics and Physics (ZAMP)*, Vol. 28, 1977, pp. 541-550.

16 Dorrepaal, J. M., Majumdar, S. R., O'Neill, M. E., and Ranger, K. B., "A Closed Torus in Stokes Flow," *Q. J. Mech. Appl. Math.*, Vol. 29, 1976, pp. 381-397.

17 Goren, S. L., and O'Neill, M. E., "Asymmetric Creeping Motion of an Open Torus," *Journal of Fluid Mechanics*, Vol. 101, Part 1, 1980, pp. 97-110.

18 Johnson, R. E., and Wu, T. Y., "Hydromechanics of Low-Reynolds Number Flow. Part 5. Motion of a Slender Torus," *Journal of Fluid Mechanics*, Vol. 95, Part 2, 1979, pp. 263-277.

19 Heiss, J. F., and Coull, J., "The Effect of Orientation and Shape on the Settling Velocity of Non-Isometric Particles in a Viscous Medium," *Chem. Eng. Progr.*, Vol. 48, 1952, p. 133.

20 Batchelor, G. K., "Slender-Body Theory for Particles of Arbitrary Cross-Section in Stokes Flow," *Journal of Fluid Mechanics*, Vol. 44, Part 3, 1970, pp. 419-440.

21 Russel, W. B., Hinch, E. J., Leal, L. G., and Tieffenbruck, G., "Rods Falling Near a Vertical Wall," *Journal of Fluid Mechanics*, Vol. 83, Part 2, 1977, pp. 273-287.

22 Huner, B., an Hussey, R. G., "Cylinder Drag at Low Reynolds Number," *Physics of Fluids*, Vol. 20, No. 8, 1977, pp. 1211-

23 Pruppacher, H. R., LeClair, B. P., and Hamielec, A. E., "Some Relations Between Drag and Flow Pattern of Viscous Flow Past a Sphere and a Cylinder at Low and Intermediate Reynolds Numbers," *Journal of Fluid Mechanics*, Vol. 44, Part 4, 1970, pp. 781-790.

24 Tritton, D. J., "The Flow Past a Circular Cylinder at Low Reynolds Numbers," *Journal of Fluid Mechanics*, Vol. 6, 1959, pp. 547-567.

25 Shi, Y., "Low Reynolds Numbers Flow Past An Ellipsoid of Revolution of Large Aspect Ratio," *Journal of Fluid Mechanics*, Vol. 23, Part 4, 1965, pp. 657-671.

26 Schiller, and Nauman, *Ver. Deut. Ing.*, Vol. 77, 1933, pp. 318-320.

27 Roshko, A., "On the Development of Turbulent Wakes from Vortex Streets," NACA Report 1191, 1954.

28 Takamoto, M., and Izumi, K., "Experimental Observation of Stable Arrangement of Vortex Rings," *Physics of Fluids*, Vol. 24, No. 8, Aug. 1981, pp. 1582-1583.

20 Hardin, J. C., "The Role of the Helical Jet Mode in Aerodynamic Noise Generation," AIAA Paper No. AIAA-82-1963, 1981.

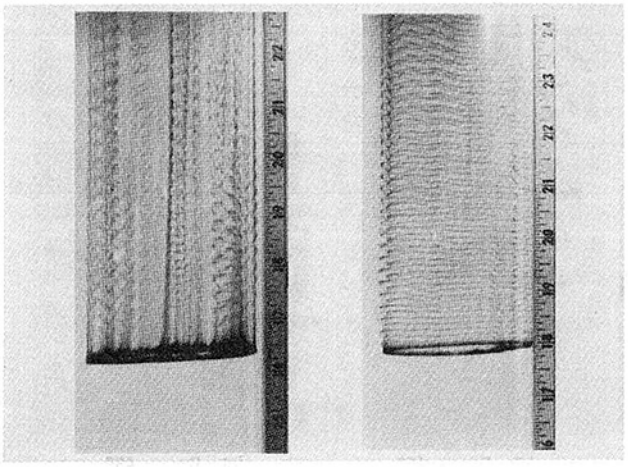

(a) $Re_c = 41$ (b) $Re_c = 53$

Fig. 10 Tori $S = 0.036$

Acknowledgments

The author wishes to acknowledge the consultation and assistance of B. N. McDonald of the Donaldson Co. in the design and setting up of the experimental timing system. The assistance of Jayne Enthoven and Judy Neufeld, work-study students, during testing and data reduction is gratefully acknowledged.

References

1 Stalnaker, J. F., and Hussey, R. G., "Wall Effects on Cylinder Drag at Low Reynolds Number," *Physics of Fluids*, Vol. 22, No. 4, Apr. 1979, pp. 603-613.

2 Amarakoon, A. M. D., Hussey, R. G., Good, B. J., and Grimsal, E. G., "Drag Measurements for Axisymmetric Motion of a Torus at Low Reynolds Number," *Physics of Fluids*, Vol. 25, No. 9, Sept. 1982, pp. 1495-1501.

3 Monson, D. R., "The Effect of Transverse Curvature on the Drag and Vortex Shedding of Elongated Bluff Bodies at Low Reynolds Number," ASME Paper 81/WA/FE-4, 1981.

4 Monson, D. R., "Experimental Drag Characteristics of Tori, Ducted-Spheres, and Other Shapes at Low Reynolds Numbers," Masters thesis, Department of Aerospace and Engineering Mechanics, University of Minnesota, 1965.

5 Tchen, C. M., "Motion of Small Particles in Skew Shape Suspended in a Viscous Liquid," *Journal of Applied Physics*, Vol. 25, No. 4, Apr. 1954, pp. 463-473.

6 Johnson, R. E., "An Improved Slender-Body Theory for Stokes Flow," *Journal of Fluid Mechanics*, Vol. 99, Part 2, 1980, pp. 411-431.

7 Brenner, H., "Effect of Finite Boundaries on the Stokes Resistance of an Arbitrary Particle, Part 1," *Journal of Fluid Mechanics*, Vol. 12, Jan. 1962, pp. 35-48.

8 Chwang, A. T., and Wu, T. Y., "Hydromechanics of Low-Reynolds-Number Flow. Part 4. Translation of Spheroids," *Journal of Fluid Mechanics*, Vol. 75, Part 4, 1976, pp. 677-689.

9 Brenner, H., "The Oseen Resistance of a Particle of Arbitrary Shape," *Journal of Fluid Mechanics*, Vol. 11, 1961, pp. 604-610.

10 Brenner, H., and Cox, R. G., "The Resistance to a Particle of Arbitrary Shape in Translational Motion at Small Reynolds Numbers," *Journal of Fluid Mechanics*, Vol. 17, 1963, pp. 561-595.

11 Happle, J., and Bart, E., "The Settling of A Sphere Along the Axis of a Long Square Duct at Low Reynolds Number," *Applied Scientific Research*, Vol. 29, 1974, pp. 241-258.

12 Roos, F. W., and Willmarth, W. W., "Some Experimental Results on Sphere and Disk Drag," *AIAA Journal*, Vol. 9, No. 2, Feb. 1971, pp. 285-291.

13 McNown, J. S., Lee, H. M., McPherson, M. B., and Engez, S. M., "Influence of Boundary Proximity on the Drag of Spheres," *Proc. VII Intern. Cong. of Appl. Mech.*, London, 1948, pp. 17-27.

14 McNown, J. S., and Malaika, J., "Effects of Particle Shape on Setting Velocity at Low Reynolds Numbers," *Trans. of Am. Geophys. Union*, Vol. 31, 1950, pp. 74-82.

15 Majumdar, S. R., and O'Neill, M. E., "On Axisymmetric Stokes Flow Past a Torus," *Journal of Applied Mathematics and Physics (ZAMP)*, Vol. 28, 1977, pp. 541-550.

16 Dorrepaal, J. M., Majumdar, S. R., O'Neill, M. E., and Ranger, K. B., "A Closed Torus in Stokes Flow," *Q. J. Mech. Appl. Math.*, Vol. 29, 1976, pp. 381-397.

17 Goren, S. L., and O'Neill, M. E., "Asymmetric Creeping Motion of an Open Torus," *Journal of Fluid Mechanics*, Vol. 101, Part 1, 1980, pp. 97-110.

18 Johnson, R. E., and Wu, T. Y., "Hydromechanics of Low-Reynolds Number Flow. Part 5. Motion of a Slender Torus," *Journal of Fluid Mechanics*, Vol. 95, Part 2, 1979, pp. 263-277.

19 Heiss, J. F., and Coull, J., "The Effect of Orientation and Shape on the Settling Velocity of Non-Isometric Particles in a Viscous Medium," *Chem. Eng. Progr.*, Vol. 48, 1952, p. 133.

20 Batchelor, G. K., "Slender-Body Theory for Particles of Arbitrary Cross-Section in Stokes Flow," *Journal of Fluid Mechanics*, Vol. 44, Part 3, 1970, pp. 419-440.

21 Russel, W. B., Hinch, E. J., Leal, L. G., and Tieffenbruck, G., "Rods Falling Near a Vertical Wall," *Journal of Fluid Mechanics*, Vol. 83, Part 2, 1977, pp. 273-287.

22 Huner, B., an Hussey, R. G., "Cylinder Drag at Low Reynolds Number," *Physics of Fluids*, Vol. 20, No. 8, 1977, pp. 1211-

23 Pruppacher, H. R., LeClair, B. P., and Hamielec, A. E., "Some Relations Between Drag and Flow Pattern of Viscous Flow Past a Sphere and a Cylinder at Low and Intermediate Reynolds Numbers," *Journal of Fluid Mechanics*, Vol. 44, Part 4, 1970, pp. 781-790.

24 Tritton, D. J., "The Flow Past a Circular Cylinder at Low Reynolds Numbers," *Journal of Fluid Mechanics*, Vol. 6, 1959, pp. 547-567.

25 Shi, Y., "Low Reynolds Numbers Flow Past An Ellipsoid of Revolution of Large Aspect Ratio," *Journal of Fluid Mechanics*, Vol. 23, Part 4, 1965, pp. 657-671.

26 Schiller, and Nauman, *Ver. Deut. Ing.*, Vol. 77, 1933, pp. 318-320.

27 Roshko, A., "On the Development of Turbulent Wakes from Vortex Streets," NACA Report 1191, 1954.

28 Takamoto, M., and Izumi, K., "Experimental Observation of Stable Arrangement of Vortex Rings," *Physics of Fluids*, Vol. 24, No. 8, Aug. 1981, pp. 1582-1583.

20 Hardin, J. C., "The Role of the Helical Jet Mode in Aerodynamic Noise Generation," AIAA Paper No. AIAA-82-1963, 1981.

DISCUSSION

V. O'Brien[2]

It is always interesting to see a careful experimental series which can be compared to theoretical expressions for some range, and also extends insight into ranges where theory is still lacking. A connection between linear objects of length L and tori with mean circumference L is not obvious.

I. Viscous Regime

For low Reynolds numbers, $Re_l = (2lU/\nu) < 1$, where $2l$ is the longest particle dimension, Fig. 11, there has to be a distinction between steady Stokes drag ($Re_l \to 0$, unbounded domain) and the measured drag. Stokes drag for a variety of bodies is known analytically or can be estimated by inscribing/circumscribing bodies after Hill and Power [30]. Long cylinders fall stably broadside, as do straight strings of spherical particles [31], prolate ellipsoids and a rectangular parallelpiped, Fig. 1(*a*). The frontal area, F, is important. The drag of the prolate spheriod is less than that of the cylinder or prism. The open tori, solidity $S < 1$, have $F = S \cdot \pi l^2$, less than a solid closed particle ($S = 1$) with the same side projection, and less Stokes drag.

The "Oseen" effect, the inertial increase of drag is a simple linear function of Re_l dependent on the Stokes drag for arbitrary solid particles[3] or circulating fluid spheroids [33]. The approximation is only valid to $0(Re_l)$, i.e., $Re_l << 1$.

The boundary effect for particles traversing the centerline of a fluid container is a function of container shape [34, 35]. For an outer cylinder of radius R_0 and axisymmetric particles [36], general solid particles[5] or circulating fluid spheroids [33], it is a linear function of $\lambda = l/R_0$, to $0(\lambda^2)$, where the coefficient multiplying λ is also a function of Stokes drag.

In the *linear* perturbation range then for all test particles

$$\text{Drag} = \text{Stokes drag}\,[1 + k_1\,Re_l + k_2\lambda] \qquad [1]$$

where the constants k_1 and k_2 are functions of particle shape

[2]M. S. Eisenhower Research Center, Applied Physics Laboratory, The Johns Hopkins University, Laurel, Md. 20707.

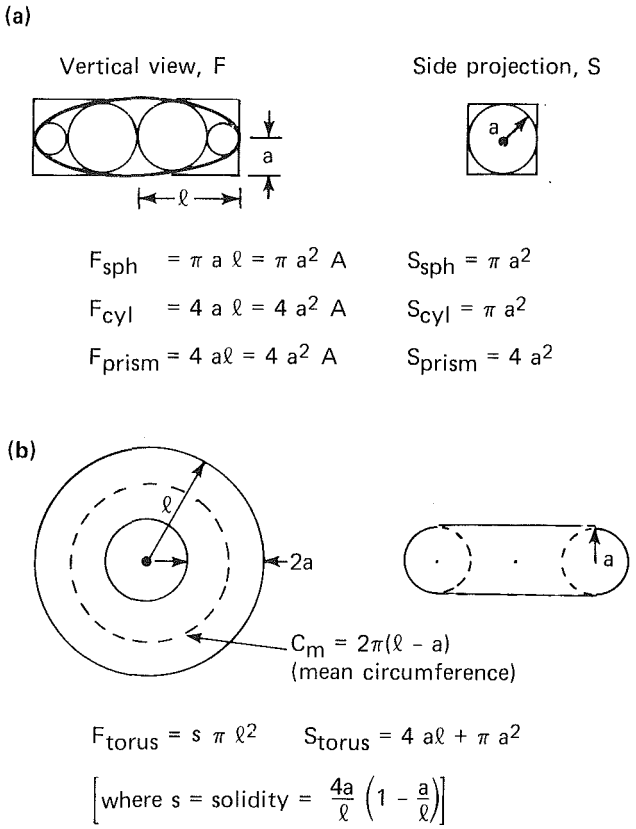

Fig. 11 Projected area of particles.

and internal circulation for fluid spheroids. The settling factor $K_\infty = U_\infty / U_s$, where U_s pertains to the Stokes drag on an "equivalent" solid sphere (same volume and density), involves other shape functions but allows the use of the solid spherical coefficient 2.1044 for extrapolating $\lambda \to 0$ for very low Re_l results at small λ (author's Fig. 1). The bracket in equation (1) can be inverted with k_i change of sign to the order of estimation. (The second method can be ignored.) The results are consistent with the exact torus theory, Fig. 2.

Extrapolations are sensitive to data accuracy and the percentages quoted seem to be in terms of $K_b = 1$ not K_∞. (The data point for $S = 0.036$, $Re_d = 0.803$ should not have been included. The *value* is large because of Re_d.) An average *error* of 0.998 must be a mistake.

Since all shape factors can be related, one could use A_e, an "equivalent prolate spheroid" instead of a sphere. However, I doubt the statement, about two "exact" theories showing a prolate spheroid has a higher drag than the a cylinder of the same (large) aspect ratio. The frontal area of the spheroid is always less by a factor $\pi/4$ for all values of A. Slender-body theory, all singularities on the axis, does not take into account the flat ends of a cylinder. See references [37, 38].

II. Inertial Regime

Here all the curves are empirical. Figure 4 shows smooth curves for the cylinder data, each A value represented by a linear C_D versus log Re_c relationship at small Re_c (less C_D for greater A), curving up as $Re_c \to 1000$ (inverse order for A). The equation (29), for the deviation of measured C_D from the linear (Stokes) C_D, obviously cannot be used for $1 > Re_c \to 0$. The "transition region" where standing vortices develop, become unstable and detach themselves as $Re_c \to \infty$ is dependent on boundary proximity even if the measured drag is not. The attached vortex behind a finite cylinder moving broadside must be three-dimensional from its initial appearance. The vortex arrangement behind an open torus will be quite different, but initially axisymmetric. As the Reynolds number increases, the vortex shedding pattern depends on solidity S. The critical Reynolds number for shift of pattern from the solid spheroidal loops to ring-pairs is a phenomenon worth pursuing in more depth experimentally and theoretically.

Acknowledgment

This work was supported by the U. S. Navy (Naval Sea Systems Command) under Contract N00024-83-C-5301.

Additional References

30 Hill, R., and Power, G., *Quart. J. Mech. Appl. Math.*. Vol. 9, 1956, p. 313.

31 Gluckman, M. J., Weinbaum, S., Pfeffer, R., *J. Fl. Mech.*, Vol. 55, 1972, p. 677.

32 Brenner, H., *J. Fl. Mech.*, Vol. 11, 1961, p. 604.

33 O'Brien, V., APL/JHU Rpt. CM-1003, "'Axisymmetric Viscous Flows Correct to First-Order in Reynolds Number," Oct. 1961.

34 Brenner, H., *J. Fl. Mech.*, Vol. 12, 1962, p. 35.

35 Happel, J., and Bart, E., *Appl. Sci. Res.*, Vol. 29, 1974, p. 241.

36 I-D. Chang, *ZAMP*, Vol. 12, 1961, p. 6.

37 Amarakoon, A. M. D., Hussey, R. G., Good, B. J., and Gremsal, E. G., *Phys. Fl.*. Vol. 25, 1982, p. 1495.

38 O'Brien, V., *Can. J. Chem. Engr'g.*, Vol. 51, 1973, p. 793.

R. E. Johnson[3]

Although the title of this paper emphasizes that it will study the effects of curvature on the drag and vortex shedding of elongated bodies, this paper seems to concentrate its effort on determining which theoretical or empirical equation best describes the drag on cylinders and tori. Consequently, the paper gives the reader a fairly good overview of our ability to predict the drag on cylinders and tori for Reynolds numbers below 1000.

I found the observations and photographs of vortex shedding from tori to be the most interesting part of the paper. Some of the interesting features observed, however, may be due to the unique body symmetry and absence of body ends. One must question whether a cylinder bent into a segment of a torus would produce any of the same vortex shedding patterns. The existence of two possible vortex patterns, a counterrotating ring vortex pair and a helical counterrotating vortex pair, in the medium solidity range is an intriguing observation. Unfortunately the present study gave little indication of why these two patterns exist.

R. G. Hussey[4]

The paper by D. R. Monson is interesting and well done. His drag results and his striking photographs of vortex shedding from tori are valuable contributions. Some of his results for cylinders are different from those found by me and my co-workers, so I welcome the opportunity to comment on these differences. The author points out that his boundary effect observations for cylinders in the inertial regime are different from those of Huner, and for $Re_L = 2.9$, his coefficient of 1.37 is closer to de Mestre's 1.339 than to Stalnaker's 0.886. Huner, de Mestre, and Stalnaker treated the case of a cylinder moving midway between parallel walls, whereas a circular outer boundary is used in Monson's experiment. The author obtains a relation between the two

[3] Assistant Professor, Department of Theoretical and Applied Mechanics, University of Illinois at Urbana-Champaign, Urbana-Champaign, Ill.

Professor of Physics, Dept. of Physics and Astronomy, Louisiana State Univ., Baton Rouge, La. 70803.

geometries by using the concept of hydraulic diameter. He correctly points out that the solution of Happel and Bart for a square outer boundary indicates that the use of the hydraulic diameter concept in that instance gives a boundary coefficent that is too large by 10 percent. Another example is the sphere moving midway between infinite parallel plane walls, where use of the hydraulic diameter gives a coefficient of 1.052, which is larger than the correct value of 1.004. It is possible that when the object is a slender cylinder moving broadside rather than a sphere, the difference in the coefficient may be larger. Therefore, in the absence of a more complete justification for the use of the hydraulic diameter concept in the Stokes flow region and the interial region, I am inclined to attribute our different experimental results to differences in the geometry of the outer boundary. The author may wish to compare his results to those of C. M. White [39], who also used a circular outer boundary.

The author is correct in stating that Stalnaker's empirical inertial correction is based on a curve fit to experimental points that have considerable scatter. In a subsequent paper, Yang-Jen Chen [40] obtained a better correlation that extends to higher Reynolds number, but is consistent with Stalnaker's results. However, I think that the difference between these empirical correlations and Brenner's first order theory is not as large as the author indicates. In order to use Brenner's theory, it is necessary to know the Stokes drag. For long cylinders ($A \geq 20$), the slender body calculations of Russel (or Batchelor) can be used for the Stokes drag. Then at $\mathrm{Re}_L = 1$, Brenner's theory gives a correction factor of 1.046 for $A = 100$ and 1.067 for $A = 20$, while Stalnaker's expression gives 1.062 (independent of A) and Chen's expression gives 1.051 for $A = 100$ and 1.068 for $A = 20$. It is true for $\mathrm{Re}_L < 1$, both Chen's and Stalnaker's empirical functions give larger values for the correction factor than Brenner's formula, but the correction is small in this region (less than 0.7 percent at $\mathrm{Re}_L = 0.1$). At values of Re_L larger than 1, Brenner's theory is not valid. Finally, since Stalnaker's and Chen's correlations were obtained with cylinders of large aspect ratio, they should not be expected to apply to short cylinders ($A = 1$ or $A = 4$).

Huner found that over the range of Reynolds number of his experiment ($0.22 < Re_c < 2.6$), the dimensionless drag ($\mathrm{drag}/4\pi\mu UL$) consistently decreased with increasing cylinder length, and he used this observation to devise a means of extrapolating to infinite cylinder length. The author's results at $\mathrm{Re}_c = 1$ imply that the dimensionless drag increases with increasing cylinder length for $A \geq 100$. I am unable to explain the difference between our results. I think it is unlikely that the difference is due to the larger aspect ratio used by the author, because (at fixed Re_c) larger aspect ratio implies larger Re_L and the larger Re_L the more valid is the physical model (small end effects) proposed by Huner to explain his observations.

Additional References

39 White, C. M., "The Drag of Cylinders in Fluids at Slow Speeds," *Proc. Royal Soc. London*, Series A, Vol. 186, 1946, pp. 472–479

40 Chen, Yang-Jen, and Hussey, R. G., "Effect of a Horizontal Plane Boundary on a Falling Horizontal Cylinder at Low Reynolds Number," *Phys. Fluids*, Vol. 23, No. 5, 1980, pp. 853–857.

Author's Closure

I would like to thank Professors Hussey and Johnson and Dr. O'Brien for their interest in and comments on this paper. Their discussions and additional references add further insight to the subject of this paper. I will comment on a few of their points.

In order to detect the effect of transverse curvature on the drag and vortex shedding of elongated bodies, one must have a reliable noncurved body data base with which to compare. Even for the simple straight cylinder family, such needed information was lacking, and thus considerable effort focused on establishing this reference baseline. The study of transverse curvature effects in planes other than normal to the flow direction was beyond the stated scope of the paper. There are no doubt many further discoveries to be made in this area of study.

Viscous Regime

Dr. O'Brien seems to be implying that in the viscous regime study, comparisons were made between measured drag and various theoretical Stokes drag solutions which apply only for $\mathrm{Re}_L \to 0$ and an unbounded fluid. This is not the case. Every effort was made to eliminate boundary and inertial terms from the measured drag values. With the present definition of shape factor, the Stokes drag on a sphere of the same volume as any arbitrary elongated body is used as a reference geometry. Then e.g., for a cylinder falling broadside within a container, equation (2) will give the measured drag as

$$\text{Meas. Drag} = \begin{bmatrix}\text{Stokes drag on}\\ \text{sphere of equal}\\ \text{vol. at same velocity}\end{bmatrix}\left(\frac{1}{K_\infty}\right)\left(\frac{1}{K_b}\right)\left(\frac{1}{K_{be}}\right). \tag{33}$$

The shape factor K_∞ may contain some inertial terms which may be estimated by Brenner's relation, equation (11). For the linear perturbation range, we solve equation (11) for $K_{\infty v}$, then use series expansions of the solution and retain only the first term. The result can be expressed in the form $K_\infty = K_{\infty v}/(1 + k_1\ \mathrm{Re}_L)$. Note that if Re_L (or Re_d for the case of the torus) is significant, K_∞ will be *smaller* than $K_{\infty v}$ not larger as supposed by Dr. O'Brien. K_b is approximated by equation (3*a*) which can be expressed as $K_b = (1 + k_2\ \lambda)^{-1}$. Equation (3) can be converted to the same form as discussed by Dr. O'Brien, however, I find equation (3) to be accurate over a broader range of λ than is equation (3*a*). Similarly, the approximate "endwall" correction factor K_{be}, equation (6), can be expressed as $K_{be} = 1.0$.

I agree with Prof. Hussey that the constant in equation (6) may be a little low for the cylindrical boundary application, however, even in the $A = 100$ case, which had the largest endwall correction, if we increase the constant 0.011, say as much as 20 percent, the endwall correction $1 - K_{be}$ would only change from 0.6 to 0.7 percent. The question remains whether Brenner's equation (3) remains accurate for greatly elognated particles. I believe this requires further verification.

When these linearized expressions are substituted into equation (33), we obtain

$$\text{Meas. Drag} = \left[\frac{\text{Stokes drag . . .}}{K_{\infty v}}\right](1 + k_1\ \mathrm{Re}_L + k_2\ \lambda), \tag{34}$$

which is the same as Dr. O'Brien's linearized equation. For solid particles, k_1 is a function of the particle shape and k_2 and is a function of the particle shape and the boundry shape. The original relations from which equation (34) was derived are accurate over a somewhat wider range of Re_L, λ, and D_h/L than would be this linearized version.

The value $K_{\infty v}$, the Stokes regime shape factor for an unbounded fluid, is then extracted from equation (33), hopefully with a minimum of error if we have met all the conditions on the various relations. In the alternate graphical extrapolation method, to eliminate the boundary effect K_b,

the experimental measured quantity ($K_\infty\ K_b\ K_{be}$) obtained from equation (33) is plotted for various values of λ and extrapolated back to zero λ using the slope predicted by Brenner's theory as a guide at the intercept if the curve is not linear. The intercept value yields the quantity ($K_\infty\ K_{be}$) since when $\lambda = 0$, $K_b = 1$. then ($K_\infty\ K_{be}$) was divided by K_{be} as estimated by equation (6) and corrected to the Stokes regime utilizing Brenner's equation (11) evaluated at the Reynolds number of the lowest value of λ tested. Be advised that in 4, the test container diameter was fixed and the model size (and hence Re) was varied. This yields an estimate for $K_{\infty v}$ which is compared to theoretical values. It is the error $1 - (K_{\infty v}/K_{\infty v\,\text{theory}})$ in percent that is being quoted.

C. M. White measured the drag on cylinders having aspect ratios from 4.9 to 158. He used a combined empirical extrapolation relation to simultaneously correct to infinite aspect ratio and an unbounded fluid. Only in his Table 2 tests did he give uncorrected drag coefficients which could be corrected to finite aspect ratio. Choosing two values close to the present tests, $A = 4.9$ and 11, I reduced the data to $K_{\infty v}$ as was done for the cylinders of $A < 10$ in the present paper. The results are $K_{\infty v} = 0.697$ and 0.559, respectively, compared to 0.727 and 0.570, respectively, for the semiempirical cylinder relation, equations (22), (27), and (28).

Dr. O'Brien's discussion of the "equivalent prolate spheriod" has pointed out a misleading statement in the paper. As long as we are comparing bodies of equal volume but different shapes at a given velocity, equal shape factors will ensure equal drag. The ad hoc modification of prolate spheriod theory adjusts its shape factor to be equal to that of a cylinder or torus of a given aspect ratio. The drag on the two bodies will be different at a given velocity since the volumes of the two bodies are not the same. The ratio of the volume of the prolate spheriod of equal shape factor to that of the geometry of interest is given by $V_e/V_i = 2/(3\ \sigma_i^2)$. The ratio of equivalent spherical diameters would be the cube root of this ratio. Thus, the subscript e and the definition of σ in the paper should be taken to represent an ellipsoid of equal shape factor rather than drag. d_s for the geometry of interest is to be used in equations (2) and (10) to estimate the drag. Comparisons on the basis of equal frontal areas are equally valid but would require a redefinition of the drag equation to reflect this change of reference.

Dr. O'Brien has reminded us that the cylinder drag theories become increasingly inaccurate with decreasing aspect ratio since they neglect the drag of the ends. Oddly, inclusion of this term would increase the differences between experimental data and, e.g., the Batchelor theory at the low aspect ratio end of its range of validity.

Dr. O'Brien has cited references which lead to a multitude of alternate a priori analyses which attempt to predict the Stokes drag of arbitrary bodies, especially elongated bodies. Except for the Hill and Power extremum principles method, all the other analysis are oriented toward estimating drag for the case of fall along the major axis rather than broadside. Although some of the methods have been suggested to be applicable for the broadside fall case as well, their accuracy and range of validity has not been demonstrated. They all appear to lose accuracy and/or become unwieldy for large aspect ratios and thus would not be useful over the full range of aspect ratio. I find the ad hoc modification of the prolate spheriod equation to be a relatively easy procedure which allows approximations to data or other theories over the full range of aspect ratio since it has the correct asymptotic form for both large and small aspect ratios.

For the torus, $K_{be} = 1$ in equation (33) since it has no ends. The $S = 0.036$ data point had little influence on how the curve was extrapolated back to zero λ, Fig. 11. As can be seen in the paper, when this data point was not included in the second method, results were comparable to the first method. The "error" of 0.998 should be corrected to read "correlation."

Inertial Regime

From a theoretical standpoint, Dr. O'Brien is correct in that transitional expressions developed for $\text{Re}_c > 1$ which fit the form of equation (29) are not necessarily correct for $1 > \text{Re}_c \to 0$. This is especially true for large A since we know β is a function of Reynolds number even though it may be constant over a limited range of Reynolds number. The status of transitional relations for the cylinder family is as follows:

$[C_D/C_{Dv} - 1]_\infty$	Range of Study	Author
$0.062\ \text{Re}_L^{1/2}$	$20 < A < 380$ $0.02 < \text{Re}_L < 10$	Stalnaker and Hussey [1]
$0.12\ A^{-1/4}\text{Re}_L^{0.75}$	$11 < A < 49$ $0.01\ A^{1/4} < \text{Re}_L < 30\ A^{1/4}$	Chen and Hussey (Hussey's references [40])
$0.114\ A^{-0.279}\text{Re}_L^{0.779}$ $0.825\ A^{-0.779}\text{Re}_L^{0.779}$	$A < 13$ $A = 100$ $\dfrac{3}{1+\log A} < \text{Re}_L < \dfrac{1200}{1+\log A}$	Present
$\dfrac{0.215}{K_{\infty vc}} A^{-0.67}\ \text{Re}_L$	Theory $\text{Re}_L < 0.05$	Brenner and Cox [10]

For the purpose of making engineering estimates, the overlaps in aspect ratio and Reynolds number of these studies and the similarities in form and values of the constants in these relations suggest that Chen's relation may be acceptable for $A < 11$ and the present relation for $A < 13$ may be usable for $\text{Re}_L < 3/(1 + \log A)$. Stalnaker's relation appears to be most accurate in the $A = 10$-20 range and the present relation

for $A = 100$ may be acceptable for $Re_L < 1$. In the range $0.05 < Re_L < 1$ most of these relations agree within a percent or two. For $Re_L < 0.1$, Prof. Hussey has shown that the difference between these relations are small and Brenner's theory suggests that the drag will be less than one percent greater than the Stokes drag for $Re_L < 0.05$ for all A.

At $Re_c = 1$, the $A = 100$ drag coefficient is 17 percent less than the drag projected by Huner [22] for $A = \infty$. There would have to be an error in this data point several times the stated accuracy for this point to fall above the curve for infinite aspect ratio. Presently, I have no reason to suspect such an error in the data. This result points out the need for more data at large aspect ratios over a range of Reynolds number spanning this point.

Dr. O'Brien suggests, without documentation, that the vortex shedding patterns may be sensititive to boundary proximity. If this is correct, it points out the need for test containers which are large compared to the largest dimension for greatly elongated bluff bodies. This need was also made clear for obtaining accurate viscous drag data as well. The reasons for the dual vortex patterns in the medium solidity range will no doubt be revealed in a stability analysis of coannular shear layers of opposite vorticity. To my knowledge, such a study has never been done.

M. J. Davies
Research Engineer,
Research & Technology Centre,
John Lysaght (Aust.) Ltd.,
Port Kembla, 2505, Australia

D. H. Wood
Lecturer,
Department of Mechanical Engineering,
University of Newcastle, N.S.W.,
2308, Australia

The Basic Aerodynamics of Floatation

The original derivation of the basic theory governing the aerodynamics of both hovercraft and modern floatation ovens, requires the validity of some extremely crude assumptions. However, the basic theory is surprisingly accurate. It is shown that this accuracy occurs because the final expression of the basic theory can be derived by approximating the full Navier-Stokes equations in a manner that clearly shows the limitations of the theory. These limitations are used in discussing the relatively small discrepancies between the theory and experiment, which may not be significant for practical purposes.

Introduction

Sheet metal strip that is painted or coated simultaneously on both sides is widely used in the construction of domestic refrigerators, washing machines, and many other products. The basic aerodynamics of modern floatation ovens, in which the continuous, freshly painted metal strip is floated, dried, and cured, is the two-dimensional analog of that of hovercraft [1-3]. The continuous strip, represented, in side view, by FF′ in Fig. 1, passes through a series of ovens containing floatation nozzles arranged in pairs above and below the strip; only the upper nozzle is shown in Fig. 1. The centerline shown in Fig. 1 is also the centerline for the lower nozzle of the pair. Each nozzle is symmetrical about the centerline and consists of two jets, each emerging at an angle θ. In practice the jets are effectively two-dimensional and are aligned at right angles to the direction of strip movement. We show below that the force acting on FF′ is proportional to the momentum flux of the jets, but varies roughly as the inverse of the floatation height, h. With the upper nozzle delivering a smaller momentum flux than the lower, strips of varying thickness and hence weight, and with different surface coatings can be supported without varying the momentum flux of either nozzle. The reason is that a static strip will float at a height where the combination of its weight and the force due to the upper nozzle just balances the upward force due to the lower nozzle. In general, this balance could not be achieved if the nozzle consisted of a single jet only, because then the force acting on FF′ would be independent of h. In practice, the ratio of strip speed to jet exit speed is usually much less than one, so that a static analysis, in which the strip is assumed stationary, is justified.

When we surveyed the literature on hovercraft, we were amazed by both the extreme crudity of the basic theory for the static lift, analogous to the force acting on FF′ [2, 3] and by its spectacular success in describing the experimental results [3]. This paper is an attempt to explore the reasons for this success. In the next section we outline the basic theory and then show how the resulting expressions for the lift can be derived from the full Navier-Stokes equations in a manner that clearly shows the limitations on the validity of the expressions. We then show the generally good agreement between the theory and the axisymmetric (about the centerline) results of [3] and our results in a simulated two-dimensional geometry. Finally we discuss briefly some of the experimental departures from the theory in terms of the limitations of our analysis.

Theoretical Aspects

We briefly describe the basic theory, which is treated more fully by Jaumotte and Kiedrzynski [3]. To save space, the left side of Fig. 1 shows the assumptions and definitions for the basic theory and those for our alternative analysis (given below) are on the right. On the left side of Fig. 1, fluid of uniform density emerges from a slot of thickness t at an angle θ and then impinges on CF as shown. The basic theory assumes:

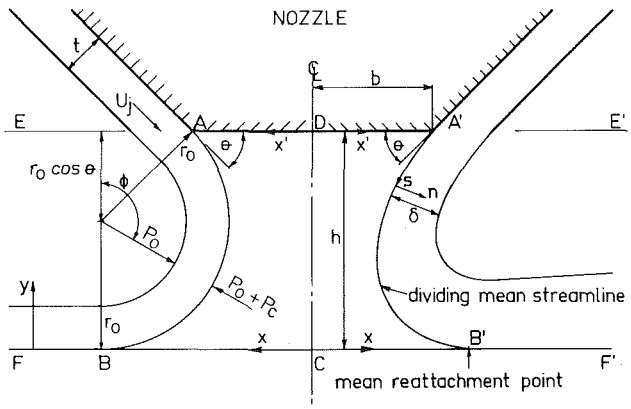

Fig. 1 Schematic of nozzle and plate. The assumptions and definitions for the basic theory are shown on the left side, those for our alternative analysis on the right. The metal strip, or the pressure tapped plate for the experiments, is represented by FF′.

Contributed by the Fluids Engineering Division for publication in the JOURNAL OF FLUIDS ENGINEERING. Manuscript received by the Fluids Engineering Division, May 26, 1982.

(i) the jet always remains at thickness t;

(ii) the jet velocity always remains at U_j, the value at exit;

(iii) the jet follows a path tangential to the direction of the slot at exit and to CF at the impingement point B in Fig. 1 and that the radius of curvature remains constant; and

(iv) P_c, the gage cushion pressure, is constant everywhere in the region bounded by the jets, the nozzle and CB.

Note that assumptions (i) and (ii) imply that the flow is inviscid. Under assumptions (i) - (iv), the momentum flux through an elemental slice of the jet of thickness t and width $d\phi$, where ϕ is defined in Fig. 1, must be balanced by the force due to the pressure difference across the jet. Provided that $r_0 >> t$, it is easy to show that this balance requires

$$\rho U_j^2 t = P_c r_0. \tag{1}$$

Since $r_0 = h/(1 + \cos\theta)$, from assumption (iii) and the geometry, then

$$J(1 + \cos\theta) = P_c h \tag{2}$$

where J is the jet momentum flux of one jet. The force acting on the nozzle or craft is given by a y-direction momentum balance. For a circular model it is

$$L = P_c S + J l \sin\theta \tag{3a}$$

where S is the area of the base of the model. For a two-dimensional nozzle the lift per unit width, L', is

$$L'/2 = P_c b + J \sin\theta. \tag{3b}$$

Equations (3a) and (3b) show that the effect of opposing the two jets, each at an angle θ, is to introduce an extra term containing P_c into the equation for the lift. This effect can be described conveniently by defining a theoretical coefficient of ground effect, A_T, as the ratio of L or L' from (3) to F or F', the force generated by a single vertical jet having the same momentum flux as the opposing jets [3]. Since $F = Jl$, and $F' = 2J$, and using equations (2) and (3), we have

$$A_T = S(1 + \cos\theta)/(hl) + \sin\theta \tag{4a}$$

for circular models, and

$$A_T = b(1 + \cos\theta)/h + \sin\theta \tag{4b}$$

for two-dimensional geometries. Equations (4a) and (4b), the final expressions of the basic theory, are shown below to be in surprisingly good agreement with the available experimental results. We suggest that the reason for this agreement is that equation (2) and hence (4), can be derived from the Reynolds-averaged Navier-Stokes equations for turbulent flow at sufficiently high Reynolds number.

The fundamental equation we need is the x-component momentum balance for the control volume CDE′F′, on the right side of Fig. 1, chosen so that the flow out of face E′F′ is nearly parallel to CF′. Apart from the obvious necessity that it has to lie to the right of the mean reattachment point, B′, we make no further restrictions on the position of F′. By symmetry there can be no mean flow across the centerline, so we assume that the centerline pressure, P_{cc}, remains constant with y. After neglecting the contributions from the entrained fluid and the turbulent fluctuations to the momentum flux, we have

$$\rho\int_0^\infty U_{x'}^2(x')\,dx' + \rho\int_0^\infty U_x^2(y)\,dy = P_{cc}h + \int_0^b \tau_w(x')\,dx' + \int \tau_w(x)\,dx \tag{5}$$

where $U_{x'}$ is the component of the exit velocity in the x' direction and the second shear stress integral is evaluated from C to F′. In words, equation (5) represents the balance between the net efflux of x-direction momentum from the control volume and the sum of the x-direction forces acting on the surface of the control volume. The two shear stress integrals along DA′ and CB′ will be small and of opposite sign. Furthermore, the flow out of the face E′F′ will be a wall jet, with a local velocity U_x, so the contribution to the second integral of τ_w from B′F′ is likely to be small [4], and we later present experimental results that support this assumption. Thus, equation (5) can be rewritten as

$$J\cos\theta + J_w \simeq P_{cc}h. \tag{6}$$

The only additional assumption made is that the streamlines are tangential to the slot direction at exit; uniformity of the exit profile has *not* been assumed. To obtain a useful expression for the lift from equation (6), we have to relate J to J_w. To do this in the most general manner, we write the Reynolds-averaged Navier-Stokes equations for turbulent flow in the orthogonal s,n-coordinates shown on the right-hand side of Fig. 1. These equations were derived by Bradshaw [5] and Mahgoub [6], and have been used in several calculations of curved turbulent shear layers, e.g., [7–9]. We arbitrarily choose the s-axis, and origin for the n-coordinate, as the dividing mean streamline separating the jet from the interior flow. The normal direction, n, is at right angles to s, with a local radius of curvature, R, which need not be con-

Nomenclature

A_E = experimental coefficient of ground effect
A_T = theoretical coefficient of ground effect, equation (4)
b = distance of slot from centerline, Fig. 1
h = floatation height, Fig. 1
J = jet momentum flux per unit width
J_w = wall jet momentum flux per unit width
L = force acting on circular model
L' = force per unit width acting on two-dimensional model
l = length of jet in azimuthal direction
n = normal coordinate for s,n-system, Fig. 1
P = pressure
P_c = cushion gage pressure
P_{cc} = centerline gage pressure
$P_{cs}(s)$ = gage pressure along dividing mean streamline
P_0 = ambient pressure
R = local radius of curvature in s,n-system
r_0 = assumed radius of curvature, Fig. 1
S = area of circular model
s = streamwise co-ordinate for s,n-system, Fig. 1
t = slot (and jet) thickness at exit, Fig. 1
U = mean velocity in s-direction
U_j = exit velocity for uniform jet
u = fluctuating velocitiy in s-direction
V = mean velocity in n-direction
v = fluctuating velocity in n-direction
x,x',y = coordinates defined in Fig. 1
z = spanwise coordinate, into page in Fig. 1
δ = jet thickness at any s, Fig. 1
θ = angle at exit of jet, Fig. 1
ρ = density
τ_w = wall shear stress

Overbars

denote time averages

stant. We define the local jet thickness, δ, as the distance from the dividing mean streamline, where $V = 0$ (as there can be no mean flow across any mean streamline), to the position where U is effectively zero on the atmospheric side of the jet. Although we make an order of magnitude restriction on δ later, δ need not remain constant. We will assume that the turbulence quantities like $\overline{uv}$ and $\overline{u^2}$ are effectively zero at the edges of the jet. The continuity equation is

$$\frac{\partial U}{\partial s} + \frac{\partial}{\partial n}\left(1+\frac{n}{R}\right)V = 0$$

$$\frac{U''}{s} \quad \frac{V}{\delta} \quad \frac{V}{r_0} \tag{7}$$

where the order of magnitude of each term is given underneath. Here U'' is the maximum velocity in the jet at any s, and r_0 has been used as a convenient estimate for R. Thus

$$V = 0\left(\frac{U''\delta}{s}\right) \tag{8}$$

where 0 denotes order of magnitude, as R must be greater than δ. The n-momentum equation is

$$\frac{\partial UV}{\partial s} + \frac{\partial}{\partial n}\left(1+\frac{n}{R}\right)V^2 - \frac{U^2}{R} = -\frac{1}{\rho}\frac{\partial P}{\partial n} - \frac{\partial \overline{uv}}{\partial s}$$

$$-\left(1+\frac{n}{R}\right)\frac{\partial \overline{v^2}}{\partial n} - \frac{\overline{v^2}-\overline{u^2}}{R}. \tag{9}$$

The continuity equation has been used to modify the mean velocity terms. To obtain an expression for the momentum flux, equation (9) has to be integrated across the jet. We anticipate the need to neglect the integrals of the first two terms in comparison to that of U^2/R. Using equation (8) to obtain the orders of magnitude of the integrals shows that this neglect is justified if

$$s^2/(r_0\delta) >> 1 \quad \text{or} \quad h/s \leq 0(10) \tag{10}$$

assuming that $s/\delta = 0(10)$. The restriction on h/s is likely to be satisfied except at very small s. With the assumed end-point behavior of the turbulence terms, the integral of equation (9) is

$$\frac{1}{R}\int_0^\delta (U^2+\overline{u^2})\,dn \simeq \frac{P_{cs}(s)}{\rho} - \frac{\partial}{\partial s}\int_0^\delta \overline{uv}\,dn \tag{11}$$

where $P_{cs}(s)$ is the static (gage) pressure along the dividing streamline. Given the large effects of mean streamline curvature on turbulence structure, e.g., [5], it is not safe to assign an order of magnitude to the last term in equation (11). If it is negligible (the integral must be zero if the jet was symmetrical about the position of U'') then we arrive at the approximation of which equation (1) is a special case. Equation (11), with the $\overline{u^2}$ and $\overline{uv}$ terms ignored, was used in the calculations of [8, 9]. Finally we require the s-dependence of the momentum flux which can be obtained from the s-momentum equation. It is

$$\frac{\partial U^2}{\partial s} + \frac{\partial}{\partial n}\left(1+\frac{n}{R}\right)UV + \frac{UV}{R} = -\frac{1}{\rho}\frac{\partial P}{\partial s} - \frac{\partial \overline{u^2}}{\partial s}$$

$$-\left(1+\frac{n}{R}\right)\frac{\partial \overline{uv}}{\partial n} - \frac{2\overline{uv}}{R}. \tag{12}$$

Although the second mean velocity term will integrate to zero across the jet, we again anticipate the need for the U^2 term to dominate, in this equation over UV/R. Using equation (8) this dominance occurs when

$$\delta/r_0 << 1 \quad \text{or} \quad h/t >> 1 \tag{13}$$

taking $\delta \sim t$, $r_0 \sim h$, and s not too small. We discuss the effect of the limitations (10) and (13) later. Since P_0 is obviously constant we can write the approximate integral of equation (12) as

$$\frac{\partial}{\partial s}\int_0^\delta (U^2+\overline{u^2})\,dn \simeq -\frac{1}{\rho}\frac{\partial}{\partial s}\int_0^\delta (P-P_0)\,dn - \frac{2}{R}\int_0^\delta \overline{uv}\,dn.$$

Again we cannot assess the importance of the turbulence term. If the last integral is nearly zero (as it would be in a symmetrical jet), then

$$\int_0^\delta (U^2+\overline{u^2})\,dn + \frac{1}{\rho}\int_0^\delta (P-P_0)\,dn \simeq \text{constant}.$$

$$\frac{P_{cs}(s)\,r_0}{\rho} \qquad \frac{P_{cs}(s)\,\delta}{2\rho}$$

The orders of the two integrals are given underneath. The order of the first comes from equation (11), that of the second should be obvious. Thus, by limitation (13)

$$\int_0^\delta (U^2+\overline{u^2})\,dn \simeq \text{constant} = J = \rho U_j^2\, t \tag{14}$$

if the exit profile is uniform and of low turbulence intensity. In contrast to equation (5), which is valid only for the control volume CDE′F′, equation (14) applies at any point along the jet from the exit to the mean reattachment point B′. At reattachment however, there is no guarantee that the mean streamlines lie totally in the x-direction, as required by equation (5). If the momentum flux out of face E′F′ in Fig. 1 is equal to the left hand side of equation (14), which seems likely but cannot be proved easily, then the unknown J_w in equation (6) is given by

$$J_w \simeq J = \rho\, U_j^2\, t \tag{15}$$

for a uniform exit profile. Thus, equation (6) becomes

$$J(1+\cos\theta) \simeq P_{cc}h. \tag{16}$$

From equation (11), $P_{cs}(s) \sim R^{-1}$ so that a nearly constant R is associated with a nearly constant $P_{cs}(s)$, and hence with $P_{cc} \simeq P_c$ everywhere[1]. Equation (16) then reduces to equation (2). Since equation (3) is valid if the cushion pressure is constant, the final expression of the basic theory, equation (4), is also an approximate solution to the Navier-Stokes equations.

The present derivation of equation (2) clearly shows two important restrictions on the validity of the basic theory. Firstly, limitations (10) and (13) require that the inequalities $s^2/(r_0\delta) >> 1$ and $r_0/\delta >> 1$, are valid together. Since s/r_0 is of order one at most, the first inequality requires $s/\delta >> 1$, in other words the jet must obey the classical thin shear layer approximation. The restriction on r_0/δ, which is likely to be satisfied if h/t is sufficiently large, then reduces to the requirement that $r_0/t >> 1$ needed to obtain the simple form of equation (1). Secondly, R must remain nearly constant, but there are no further restrictions on, say, the position of the mean reattachment point. Apart from these restrictions, equations (2) and (4) are almost independent of the detailed mean velocity and turbulence profiles of the jet and of its path. Thus it is not surprising that equation (4) remains substantially unaltered by the many ad hoc modifications to the basic theory, such as those described in [3] and [10], or by the inclusion of compressibility effects, e.g., [11].

Comparison With Experiments

The only previous measurements we could find were those of Jaumotte and Kiedrzynski [3] which were not sufficiently detailed to test the limitations of the present derivation. Our

[1] Note that under these conditions $U \simeq 0$ along the dividing streamline. In this paper we have tried to avoid the vexing, but peripheral, question of whether the cushion pressure determines R or vice versa.

experiments were performed on a nozzle box fitted to the contraction of the wind tunnel described by Subramanian and Antonia [12]. The nozzle box dimensions were: b = 75mm; t = 5 mm; and width = 375 mm. The slot was constructed as a slightly convergent nozzle with an average θ of 30 deg. The width was constrained by the wind tunnel dimensions and so the aspect ratio was significantly smaller than in an actual floatation oven. To simulate a two-dimensionality geometry, end plates were installed to force all the flow to exhaust in the x-direction of Fig. 1. The two-dimensionality of each jet was checked by traversing a 1.2 mm total head tube along the surface, just upstream of each of the four lips. No detectable variation of surface total head was found over the central 300 mm or between the two jets.

The lift per unit width was measured using a plate with eighteen 1 mm wall pressure tappings installed along the centerline (z = 0). Several other tappings, placed symmetrically about either z = 0 or x = 0, were used to set up the plate at each h by zeroing the pressure differences across the centerline. All pressures were measured by a Betz projection manometer with a resolution of 0.02 mm H_2O. Using the same total head tube, the wall jet velocity profiles were measured at a position where the wall pressure had fallen to (and stayed at) atmospheric; all the present results were obtained at x/b = 1.87. At this x/b, the two-dimensionality of the wall jet flow was checked using the total head tube. Over the central 200 mm, the surface total head varied by less than 5 and 10 percent at h/t = 2 and 15, respectively. The negligible difference between the wall and ambient pressures implies the validity of the boundary layer approximation and hence that the streamlines were nearly parallel to the plate. Thus our fundamental equation, (6), applies at x/b = 1.87 and can be used to check the accuracy of measurement.

Because of the uncertain behavior of the static pressure across the jet, and the consequent difficulty of measuring it accurately, the jet profiles at exit were measured using a home-made 5 μm single hot wire probe and a DISA 55D01 main unit. The probe was calibrated before and after measurement in the potential core of an adjacent plane jet rig. There was no detectable drift in the calibrations for the results presented. The jet exit velocity was around 25 ms^{-1}, Fig. 2. To simulate an actual floatation oven, the fan speed was held constant, so the momentum fluxes varied with h. We estimate the accuracy of measurement as: L', 4 percent; $U_{x'}$, 4 percent; U_x, 2 percent; J and J_w, 10 percent; and A_E, 14 percent where $A_E = L'/2J$ is the experimental coefficient of ground effect. The important experimental results are given in Table 1.

The jet profiles, measured about 0.5 mm downstream of the exit, are shown in Fig. 2; x_n' is parallel to x', but with an arbitrary origin that was constant for all h/t. The jet profiles become more uniform as h/t increases and the magnitude of the velocities of the entrained air, on both sides of the jet, is small but non-zero. Note that a single hot wire measures the magnitude of velocity only, but that the entrained air is likely to enter the jet predominantly in the n-direction and so will not contribute to the s-direction momentum flux. This causes a small uncertainty in calculating J from

$$J/\sin\theta = \rho\int U^2(x_n')\,dx_n'. \tag{17}$$

The integral was evaluated only over the region where $U > 10$ ms^{-1}.

The measured wall pressure distributions with the fitted cubic spline curves used to obtain L' are shown in Fig. 3. P_{cc} decreases rapidly with increasing h/t. The position of maximum pressure, x_{max}, and x_{min}, the position of the local minimum between x = 0 and x_{max}, both move inward with increasing h/t. This movement is shown more clearly in Fig. 4. As in other reattaching flows, such as over a backward facing step, e.g., [13], the mean reattachment point is likely to lie between x_{min} and x_{max}. Because of the extremely small logarithmic region in our wall jet profiles, we could not measure any wall shear stresses with sufficient accuracy to obtain a better estimate for the reattachment point. However Fig. 4 strongly suggests that the reattachment point moves inward as h/t increases.

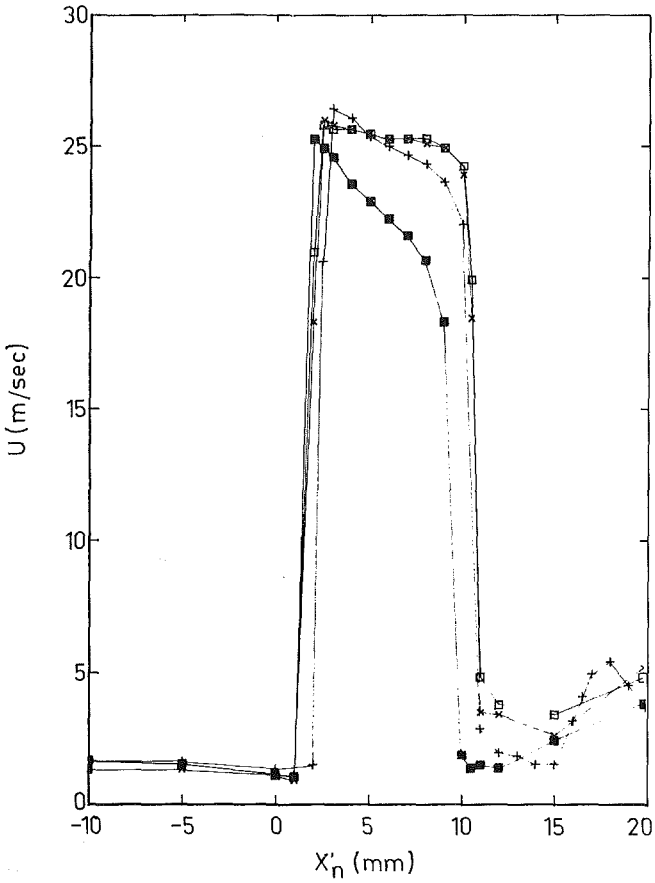

Fig. 2 Jet exit velocity profiles. Symbols given in Table 1.

Table 1 shows r, the ratio of the left hand and right-hand sides of equation (6). The magnitude of the ignored contribution from the wall shear stress to the right hand side was estimated using the approximate relation between the wall jet Reynolds number and skin friction given by Launder and Rodi [4]. Although this relation is valid only for fully developed wall jets, the maximum contribution was less than 2 percent justifying the neglect of the term. The maximum measured imbalance in equation (6) is 20 percent at h/t = 6, which is just inside the sum of the estimated errors in J and J_w. Although this discrepancy may appear to be large, it is no worse than typical errors incurred in applying a much simplified form of equation (6) to a wall jet issuing from a slot parallel to the x-axis. Launder and Rodi [4] list fourteen such experiments and indicate an average of the maximum imbalance in the individual experiments of 26 percent. Thus it is reasonable to conclude that equation (6) is valid at all h/t.

Table 1 shows that the equality between J and J_w required by equation (15), breaks down for $h/t \gtrsim 8.0$. This breakdown is associated with increasing non-uniformity of the cushion pressure, as evidenced by the behavior of P_{min}/P_{cc} in Fig. 4. As J_w/J decreases, equation (6) causes the measured P_{cc} to increase relative to the value calculated from equation (16) and given in Table 1. The table also shows P_{cc} calculated from equation (3b) with the assumption that $P_c = P_{cc}$. Comparison

with the measured P_{cc} shows a discrepancy that increases slightly between $h/t = 2$ and 15.

Figure 5 compares the theoretical coefficients of ground effect with the present measurements and those of [3] who used a circular "hovercraft" model of 352 mm diameter with $t = 3.8$ mm and $\theta = 45$ deg. They measured the lift directly by mounting a pressure tapped plate on a force balance. For different balance forces the mass flow to the model was adjusted until a specified h was obtained. The jet momentum flux was obtained from the measured mass flux by assuming that U_j was constant across the exit.

The discrepancy between equation (4*b*) and the present results becomes significant for $h/t \gtrsim 8.0$, while the axisymmetric results of [3] show excellent agreement everywhere with (4*a*). However, they did not report any independent measurements of either J or J_w, nor did they mention any consistency checks between the measured plate pressure distribution and the balance force. Therefore it is difficult to assess the reasons for the excellent agreement; it is possible that there may be smaller changes in R if θ is increased from 30 to 45 deg.

Discussion and Conclusions

The most important results from the last section are firstly, the experimental support for equation (6) at all h/t and secondly, the breakdown of the basic theory, equation (4*b*), for $h/t \gtrsim 8.0$, in the present study. The second result is somewhat surprising because the limitation of (13), taken at face value, suggests that the basic theory should become more

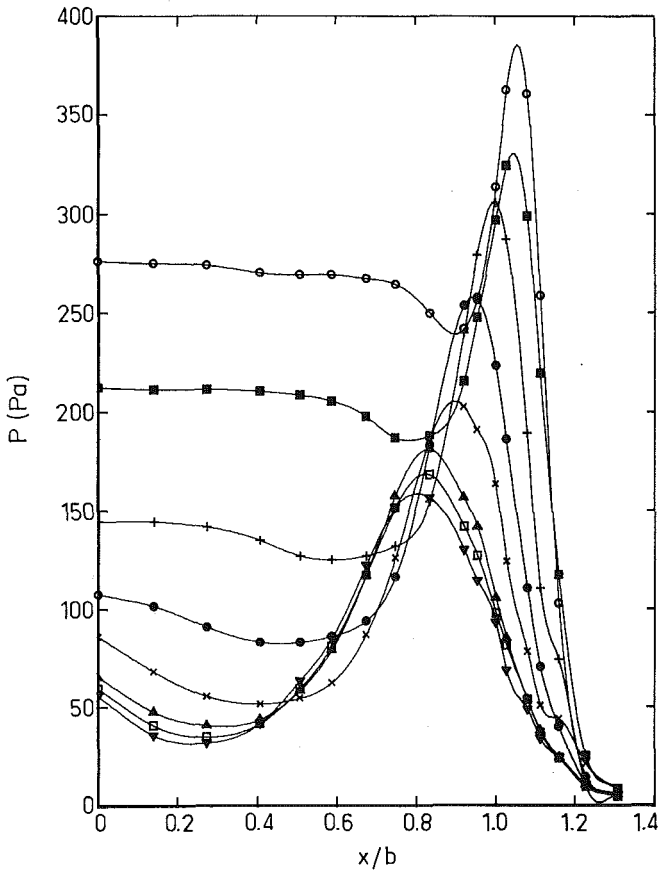

Fig. 3 Plate pressure distribution. Symbols given in Table 1. Pressure in Pascals (Pa).

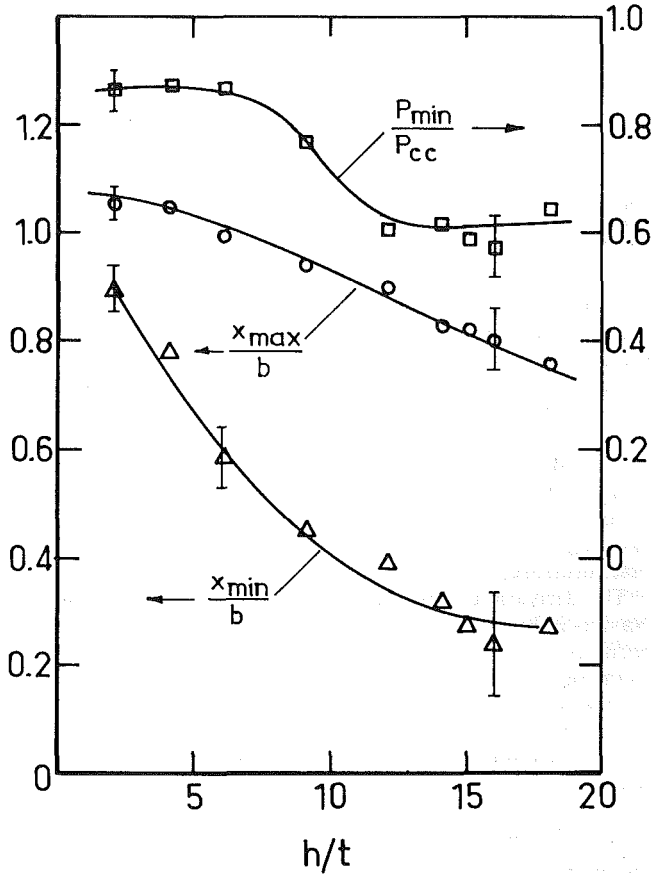

Fig. 4 Dependence of P_{min}, x_{min}, and x_{max} on h/t. □, P_{min}/P_{cc}, ○, x_{max}/b; △, x_{min}/b.

Table 1 Main experimental results

h/t	Symbol	J (N/m)	J_w (N/m)	L' (N/m)	r	P_{cc} (Pa) (*a*)	(*b*)	(*c*)
2	○		2.02	47.90		276.3		
4	■	2.18		38.44	1.03	212.6	203.4	241.7
6	+	2.80	2.53	27.93	1.21	145.0	174.16	167.5
9	•	3.10*		21.38		107.8		
12	x	3.23	2.13	16.93	1.03	86.21	100.45	91.33
14	▲	3.25*	1.77	14.99		65.63		
15	□	3.26	1.72	14.12	1.10	59.76	81.11	72.40
16	▼	3.27*	1.61	13.60		55.84		
18		3.27*	1.55	13.11		68.57		

*denotes interpolated or extrapolated value
(*a*) P_{cc} measured
(*b*) P_{cc} from equation (16)
(*c*) P_{cc} from equation (3b) and assuming $P_c = P_{cc}$.

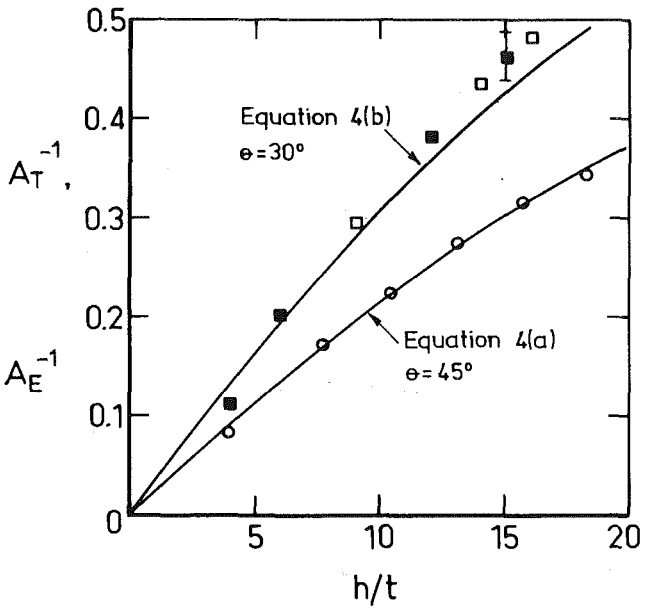

Fig. 5 Theoretical and experimental coefficient of ground effect. ■, present results; □, present results with J interpolated or extrapolated (see Table 1); ○, [3], Solid lines are from equation (4).

accurate as h/t increases. Our extended analysis shows that the breakdown is most likely associated with the failure of the local radius of curvature to remain constant near the mean reattachment point. Figure 4 shows that the reattachment point moves inward (x decreases) with increasing h/t. If altering h does not influence the trajectory at small s, as suggested by Fig. 2, then the significant changes in R occur close to the reattachment point. This would be associated with a considerable variation in the pressure acting along the dividing mean streamline, causing the non-uniformity of the plate pressure, as measured by P_{min}/P_{cc}.

The derivation of the basic theory, equation (4), from the Navier-Stokes equations shows that the former contains or requires the least amount of information possible. For example, it is independent of the detailed mean velocity profile of the jet. A more detailed theory would either have to be given, or be able to calculate, the path of the dividing mean streamline. However, for engineering purposes, the discrepancy between the theoretical and experimental coefficients of ground effect may not be important, and could be reduced by an empirical, geometry-dependent modification to equation (4). Therefore, the basic theory, originally derived using extremely crude assumptions, has a generality that is not obvious in the restrictiveness of those assumptions.

One of the referees suggested that we comment on the applicability of our analysis to other "flows with constant pressure cavities." The only relevant flow known to us is a turbulent jet discharging parallel to, but offset from, a solid wall. The resulting velocity and temperature fields cannot be described adequately by assuming a constant cavity pressure according to Hoch and Jiji [14].

Although not important for hovercraft, there is a need to understand the heat transfer characteristics of floatation oven nozzles. Such an investigation is currently underway.

Acknowledgments

Many people helped us in this work in many ways. In particular we thank Dr. L. W. B. Browne, C. H. Ellen and A. E. Perry and Professor R. A. Antonia. The work was supported by John Lysaght (Australia) Limited and the authorship is alphabetical. The referees provided several valuable comments.

References

1 Beggs, D., and Thome, W. L., "Stabilizing System for Strip Work," U.S. Patent No. 3,328,997, 1967.

2 Mair, W. A., "The Physical Principles of the Hovercraft," *Hovering Craft and Hydrofoil*, Vol. 4, 1964, pp. 5-13.

3 Jaumotte, A., and Kiedrzynski, A., "Theory and Experiments on Air Cushion Vehicles at Zero Speed," *Hovering Craft and Hydrofoil*, Vol. 4, 1965, pp. 4-25.

4 Launder, B. E., and Rodi, W., "The Turbulent Wall Jet," *Prog. Aerospace Sci.*, Vol. 19, 1981, pp. 81-128.

5 Bradshaw, P., "The Effects of Mean Streamline Curvature on Turbulent Flow," *AGARDograph 169*, 1973.

6 Mahgoub, H. E. H., "Calculation of the Interaction Between a Complex Turbulent Shear Layer and an External Inviscid Stream," Ph.D. thesis, University of London, 1978.

7 Mahgoub, H. E. H., and Bradshaw, P., "Calculation of Turbulent-Inviscid Flow Interactions with Large Normal Pressure Gradients," *AIAA Journal*, Vol. 17, 1979, pp. 1025-1029.

8 Gibson, M. M., and Rodi, W., "A Reynolds-Stress Closure Model of Turbulence Applied to the Calculation of a Highly Curved Shear Layer," *J. Fluid Mech.*, Vol. 103, 1981, pp. 161-182.

9 Gibson, M. M., Jones, W. P., and Younis, B. A., "Calculation of Turbulent Boundary Layers on Curved Surfaces," *Phys. Fluids*, Vol. 24, 1981, pp. 386-395.

10 Bradbury, L. J. S., "A Mixing Theory for the Hovering of Peripheral-Jet Air Cushion Vehicles," *J. Roy. Aero. Soc.*, Vol. 71, 1967, pp. 53-54.

11 Hope-Gill, C. D., "Analysis of High-Speed Peripheral Jet for ACV Applications,'" *J. Hydronautics*, Vol. 4, 1970, pp. 80-85.

12 Subramanian, C. S., and Antonia, R. A., "Effect of Reynolds Number on a Slightly Heated Turbulent Boundary Layer," *Int. J. Heat Mass Transfer*, Vol. 24, 1981, pp. 1833-1846.

13 Chandrsuda, C., and Bradshaw, P., "Turbulence Structure of a Reattaching Mixing Layer," *J. Fluid Mech.*, Vol. 110, 1981, pp. 171-194.

14 Hoch, J., and Jiji, L. M., "Theoretical and Experimental Temperature Distribution in Two-Dimensional Turbulent Jet-Boundary Interaction," ASME *Journal of Heat Transfer*, Vol. 103, 1981, pp. 331-336.

Analysis of Turbulent Gas-Solid Suspension Flow in a Pipe

Young Don Choi
Assistant Professor,
Department of Mechanical Engineering,
Korea University, Seoul, Korea

Myung Kyoon Chung
Assistant Professor,
Department of Mechanical Engineering,
Korea Advanced Institute of
Science and Technology,
Seoul, Korea

The mixing length theory is extended to close the relevant momentum equations for two-phase turbulent flow at a first-order closure level. It is assumed that the mass fraction of the particles is on the order of unity, that the particle size is so small that the particles are fully suspended in the primary fluid, and that the relaxation time scale of the particles is sufficiently small compared with the time scale of the energy containing eddies so that the suspended particles are fully responsive to the fluctuating turbulent field. Bulk motion of the particles is treated as a secondary fluid flow with its own virtual viscosity. The proposed closure is applied to a fully developed gas-solid pipe flow in which the particles are assumed to be uniformly distributed across the pipe section. Predicted velocity profiles and the friction factors are in good agreement with available experimental data.

1 Introduction

Basic knowledge on flow of suspended solids in a gas through pipes has become increasingly important in the design of energy-related systems since the friction factor and heat transfer through the pipe wall may be significantly different from those of single-phase fluid flow in the pipe. Engineering applications include the pneumatic transportation of pulverized coal, flow of combustion products in heat exchanger tubes and feeding of fine chemical powders into a chemical reactor. There have been a number of experimental investigations on two-phase pipe flow and on two-phase flow through a nozzle or a Venturi, however, there have been relatively few analytical studies.

Abramovich [1] assumed that the fluid element is retarded by a total drag force due to the suspended particles which results in a decrease of turbulent fluctuating velocity. Using an approximate mixing length theory, he found that finer particles had a stronger effect in decreasing turbulence levels than coarse particles. This is compatible with Sharma and Crowe's [2] computational result using a one-dimensional physical model, which states that the pressure drop in a Venturi tube is mostly due to finer particles suspended in the flow.

Owen [3] estimated that rate of turbulent energy dissipation in a fluid containing small particles is higher than in a particle free fluid by the ratio $(1 + \bar{\rho}_p/\rho)$ where $\bar{\rho}_p$ is the mass of the particles per unit volume. By assuming that the turbulence energy is produced by the fluid only, he further proposed that the intensity of turbulence is decreased by the particles in the ratio $(1 + \bar{\rho}_p/\rho_f)^{-1/2}$.

Melville and Bray [4] applied Owen's theory to analyse a gas-solid turbulent round jet, in which the bulk motion of the particles was treated as a hypothetically continuous fluid which is mixed with the suspending primary fluid (they called this hypothetical fluid a secondary fluid). Their results were in good agreement with Laats and Frishman's [5] experimental data.

The present study is essentially a further extension and modification of Melville and Bray's model to a typical wall bounded two-phase turbulent flow in pipes. We derived virtual laminar and eddy viscosity models of the secondary fluid which are different from previous models. Using the proposed models, the appropriate momentum equations for fully developed pipe flow were integrated numerically to obtain the velocity profile and the skin friction factor and the results were compared with Boothroyd's [6] experimental data.

2 Analysis of Gas-Solid Suspension Flows

2.1 Momentum Equation. If the particle size is very small and the velocity of the primary fluid is high enough for the particles to be fully suspended [3], if $\bar{\rho}_p/\rho_f$ is of the order of unity and the Stokesian relaxation time scale is of the order of the eddy life time of the primary fluid, the mean velocity of the secondary fluid can be assumed approximately equal to that of the primary fluid [4]. Under these assumptions, the Reynolds averaged equations for thin shear flows become, after Melville [7].

$$\frac{\partial U}{\partial x} + \frac{1}{r}\frac{\partial}{\partial r}(rV) = 0 \tag{1}$$

$$U\frac{\partial \bar{\rho}_p}{\partial x} + V\frac{\partial \bar{\rho}_p}{\partial r} = -\frac{1}{r}\frac{\partial}{\partial r}(\overline{r\rho_p' v_p'}) \tag{2}$$

$$U\frac{\partial U}{\partial x} + V\frac{\partial U}{\partial r} = -\frac{1}{\rho_f + \bar{\rho}_p}\frac{\partial p}{\partial x} - \frac{\rho_f}{\rho_f + \bar{\rho}_p}\frac{1}{r}\frac{\partial}{\partial r}\left[r\left(\overline{u'v'} - \nu_{fl}\frac{\partial U}{\partial r}\right)\right]$$

Contributed by the Fluids Engineering Division and presented at the ASME Applied Mechanics, Bioengineering, and Fluids Engineering Conference, Houston, Texas, June 20–22, 1983, of The American Society of Mechanical Engineers. Manuscript received by the Fluids Engineering Division, December 16, 1980. Paper No. 83-FE-6.

$$-\frac{1}{\rho_f+\bar{\rho}_p}\left[\overline{\rho_p' v_p'}\frac{\partial U}{\partial r}+\frac{1}{r}\frac{\partial}{\partial r}\left\{r\bar{\rho}_p\left(\overline{u_p' v_p'}-\nu_{pl}\frac{\partial U}{\partial r}\right)\right\}\right]. \quad (3)$$

Here, the laminar kinematic viscosity of the primary fluid, ν_{fl}, and the virtual laminar kinematic viscosity of the secondary fluid, ν_{pl}, have been added to the equations in Melville [7] due to the low Reynolds number region near the pipe wall.

Upper casses U and V are the mean velocity components in the axial and the radial directions, respectively. Primed lower cases u' and v' are the fluctuating turbulent velocity components of the primary fluid and u_p' and v_p' stand for those of the secondary fluid. The mean density of the secondary fluid is denoted by $\bar{\rho}_p$ and its fluctuating component by ρ_p'. An overbar is used to indicate the appropriate average of a variable.

In order to close the system of equations at the first-order closure level, the following Boussinesq eddy viscosity models are assumed.

$$\overline{u'v'}=-\epsilon_f\frac{\partial U}{\partial r} \quad (4)$$

$$\overline{u_p' v_p'}=-\epsilon_p\frac{\partial U}{\partial r} \quad (5)$$

and

$$\overline{\rho_p' v_p'}=-\kappa_p\frac{\partial \bar{\rho}_p}{\partial r} \quad (6)$$

where, ϵ_f is the scalar eddy viscosity of the primary fluid, ϵ_p is that of the secondary fluid, and κ_p is an eddy diffusivity of the secondary fluid. The model (6) was proposed by Melville and Bray [4].

In general, the density of the secondary fluid is not uniform. It is well known that the variation of this density in a radial direction increases when the solid-gas loading ratio increases [8]. This is mainly due to the deposition of particles and gravity for horizontal flows. It is well known that the deposition may be due to turbulence in the core region. The particles may also be re-entrained back into the core flow due to the magnus lift and impact from other particles. It is not certain when the deposition becomes more pronounced in the pipe flows compared with the re-entrainment of particles. If the deposition of particles needs to be accounted for, the governing equations should be time-dependent, three-dimensional and a realistic deposition model is necessary. Since our main objective is to devise simple turbulence models and a numerical methodology to compute wall-bounded suspension flow, consideration of such a complex situation mentioned above is not helpful to isolate the modeling problems from more complex phenomena. Thus it was assumed that the density of the secondary fluid is uniform over the cross-sectional area in a pipe [8]. Then, the momentum equation (3) is simplified to the following form.

$$U\frac{\partial U}{\partial x}+V\frac{\partial U}{\partial r}=-\frac{1}{\rho_f+\bar{\rho}_p}\frac{\partial p}{\partial x}+\frac{\rho_f}{\rho_f+\bar{\rho}_p}\frac{1}{r}\frac{\partial}{\partial r}\left[(\epsilon_{et}+\nu_{el})r\frac{\partial U}{\partial r}\right] \quad (7)$$

where ϵ_{et} is an effective eddy viscosity and is defined by

$$\epsilon_{et}=\epsilon_f+\frac{\bar{\rho}_p}{\rho_f}\epsilon_p \quad (8)$$

and ν_{el} is an effective laminar kinematic viscosity defined by,

$$\nu_{el}=\nu_{fl}+\frac{\bar{\rho}_p}{\rho_f}\nu_{pl}, \quad (9)$$

where $\bar{\rho}_p/\rho_f$ is the solid-gas loading ratio. (More detailed discussion about ν_{pl} is presented in Section 2.4)

2.2 Eddy Viscosity of Primary Fluid. Our model for the eddy viscosity of the primary fluid is based on Owen's [3] theory, which states that the presence of solid particles decreases the eddy viscosity of the primary fluid due to dissipation of turbulence energy at the interface between solid particles and the fluid. Assuming that the turbulence is in an equilibrium in which the rate of turbulence energy production is balanced by the rate of energy dissipation,

Nomenclature

a, b, c = model constants
D = Van Driest damping function ($D = 1-\exp(-y^+/26)$)
d_p = particle diameter
D_p = pipe diameter
f_0 = friction factor in clean fluid flow
f_{f+p} = friction factor in gas-solid suspension flow
f_p = increment of friction factor due to particles
$\mathrm{F_r}$ = Froude number ($\mathrm{F_r} = U_m/\sqrt{gD_p}$)
l_f = characteristic length scale for primary fluid flow
l_p = characteristic length scale for secondary fluid flow
P = static pressure
r = radial distance from the pipe axis
$\mathrm{R_e}$ = Reynolds number based on pipe diameter
R = pipe radius
t^* = Stokesian relaxation time ($t^* = \rho_s d_p^2/18\mu$)
t_e = eddy life time
t_l = Lagrangian integral time scale
u', v' = fluctuating velocity components in axial and radial directions of primary fluid
u_p', v_p' = fluctuating velocity components in axial and radial directions of secondary fluid
U, V = ensemble averaged mean velocity components in axial and radial directions
u_f = characteristic velocity scale for primary fluid flow
u_p = characteristic velocity scale for secondary fluid flow
U_m = axial mean velocity
U^+ = non-dimensional axial velocity ($U^+ = U/U_\tau$)
U_τ = friction speed ($U_\tau = \sqrt{\tau_w/\rho_f}$)
x = axial coordinate
y = distance from the pipe wall
y^+ = non-dimensional distance from the pipe wall ($y^+ = y\,U_\tau/\nu_{fl}$)
$\delta_{.99}$ = boundary layer thickness
$\epsilon_f, \epsilon_{f_0}, \epsilon_p$ = kinematic eddy viscosity
$\nu_{fl}\ \nu_{pl}$ = kinematic laminar viscosity
ν_{el} = effective kinematic laminar viscosity
ν_{et} = effective kinematic eddy viscosity
Λ = Eulerian integral length scale
ρ = density
τ_w = shear stress at the wall
$\alpha, \beta, \kappa, \lambda$ = model constants
$\bar{\rho}_p$ = average density of secondary fluid defined by average mass of particles per unit volume

Subscripts

e = effective, or eddy
f = primary fluid
l = laminar
0 = of clean fluid
p = particle laden, or secondary fluid
s = solid

$$\rho_f u_f l_f \left(\frac{dU}{dr}\right)^2 = c(\rho_f + \bar{\rho}_p)\frac{u_f^3}{l_f}, \tag{10}$$

where c is a model constant, he proposed the following model for the eddy viscosity of the primary fluid.

$$\frac{\epsilon_f}{\epsilon_{f_0}} = \frac{1}{\left(1+\frac{\bar{\rho}_p}{\rho_f}\right)^{1/2}} \tag{11}$$

Here, u_f is some turbulent velocity scale and l_f is its length scale and ϵ_{f_0} is the kinematic eddy viscosity of clean fluid flow which is without suspension of solid particles. The validity of the above equations were restricted to a case when the Stokesian relaxation time t^* is much shorter than that of an eddy life time t_e.

The implicit assumption of the balance equation (10) is that the turbulence energy in the composite fluid is generated only by the primary fluid. However, Boothroyd [9] found by an experiment that the turbulence energy is substantially generated by the presence of the fluctuating solid particles and he explained that this is due to the extraction of large scale turbulence energy by solid particles from mean motion of the primary fluid. Denoting the rate of production of turbulence energy by the secondary fluid by $\bar{\rho}_p u_p l_p (dU/dr)^2$ where u_p is a velocity scale and l_p is a length scale of the secondary fluid, the following balance equation may be more appropriate.

$$\bar{\rho}_p u_p l_p \left(\frac{dU}{dr}\right)^2 + \rho_f u_f l_f \left(\frac{dU}{dr}\right)^2 = c(\rho_f + \bar{\rho}_p)\frac{u_f^3}{l_f} \tag{12}$$

where the model constant $c = 0.145$ was taken from Crawford and Kays [10]. Using this equation, equation (11) is modified to

$$\frac{\epsilon_f}{\epsilon_{f_0}} = \left(\frac{\left(1+\frac{\bar{\rho}_p}{\rho_f}\frac{\epsilon_p}{\epsilon_f}\right)}{1+\frac{\bar{\rho}_p}{\rho_f}}\right)^{1/2} \tag{13}$$

As for the eddy viscosity model of the clean fluid flow without suspension of solid particles, we used the conventional mixing length model with a damping function,

$$\epsilon_{f_0} = \kappa^2 (R-r)^2 D^2 \left|\frac{dU}{dr}\right| \quad \text{for} \quad (R-r) \le \frac{\lambda\delta_{.99}}{\kappa} \tag{14}$$

and

$$\epsilon_{f_0} = \nu_{fl} a\, \mathrm{Re}^b \quad \text{for} \quad (R-r) > \frac{\lambda\delta_{.99}}{\kappa} \tag{15}$$

where, D is the van Driest damping function and $a = 0.005$, $b = 0.9$, and $\kappa = 0.41$ [10].

The boundary layer thickness $\delta_{.99}$ is the distance from the wall at which mean velocity is 99 percent of the velocity on the axis. A model constant λ is selected in such a way that an estimate by equation (14) is continuously matched with an estimate by equation (15) at their interface.

2.3 Eddy Viscosity of Secondary Fluid. A difficult problem in the analysis of gas-solid suspension flow is to model the eddy viscosity of the secondary fluid. Frequently, it is assumed that the eddy viscosity of the secondary fluid is proportional to the eddy viscosity of the primary fluid and that this proportionality coefficient is a function of a ratio of the Stokesian relaxation time scale to Lagrangian integral time scale.

According to Meek and Jones [11] the ratio between these eddy viscosities is given by,

$$\frac{\epsilon_p}{\epsilon_f} = \frac{1}{1+\frac{t^*}{t_l}} \tag{16}$$

where t_l is the Lagrangian integral time scale. Hinze [12], Soo [13], O'Brien [14], and Peskin [15], have suggested more complex eddy viscosity models for the secondary fluid, theoretically or empirically. However, most of these models can be converted into a form,

$$\frac{\epsilon_p}{\epsilon_f} = \frac{1}{1+\alpha\left(\frac{t^*}{t_l}\right)^\beta} \tag{17}$$

where α and β are model constants. From the above models, α is found to be about unity and β has a value between $1 \sim 2$. In this study, we fixed $\alpha = 1$, and the value $\beta = 2$ was selected such that predicted pipe frictions are in best agreement with experiments.

Corrsin [16] suggested that t_l may be estimated by,

$$t_l = \frac{\Lambda}{u_f} \tag{18}$$

where Λ is an Eulerian integral length scale. Assuming that $\Lambda \sim l_f$, Melville and Bray [4] obtained,

$$t_l = \frac{l_f^2}{\epsilon_f} \tag{19}$$

Since, in the core region of the pipe, $l_f (\approx \lambda\delta_{.99})$ and ϵ_f are assumed to be constant for a given flow, the eddy viscosity of the secondary fluid is also taken to be constant there according to equation (17). Near the wall, however, equations (17), (19) and the Prandtl's mixing length theory together predict that ϵ_p/ϵ_f would decrease as the wall comes closer. But, this is in contradiction to Soo's [17] theoretical and experimental result which states that ϵ_p/ϵ_f is nearly constant across the stream and is not significantly affected by the solid boundary. Accordingly, we assumed that ϵ_p/ϵ_f in the inner region has a constant value which is the same as that in the outer region.

Substitution of equation (11) into equation (8) yields

$$\epsilon_{et} = \epsilon_{f_0} \frac{1+\frac{\epsilon_p}{\epsilon_f}\frac{\bar{\rho}_p}{\rho_f}}{\left(1+\frac{\bar{\rho}_p}{\rho_f}\right)^{1/2}} \tag{20}$$

and substitution of equation (13) into equation (8) gives

$$\epsilon_{et} = \epsilon_{f_0} \frac{\left(1+\frac{\epsilon_p}{\epsilon_f}\frac{\bar{\rho}_p}{\rho_f}\right)^{3/2}}{\left(1+\frac{\bar{\rho}_p}{\rho_f}\right)^{1/2}} \tag{21}$$

Thus, equation (20) or (21) gives an estimate for effective eddy viscosity as a function of solid-gas loading ratio and relative particle size.

2.4 Laminar Kinematic Viscosity of Secondary Fluid. When a particle is suspended in a shear layer, the particle rotates due to a velocity difference between its upper surface and its lower surface. The fluid parcel over the upper surface moves down and that below the bottom surface goes up, each with its respective momentum. As a result, momentum transfer takes place between adjacent layers. The augmentation of the laminar momentum transfer, usually called the laminar viscosity of the secondary fluid, has been investigated by Happel [18], Frankel and Acrivos [19], Sather and Lee [20], and many others.

Most of them have discussed the Einstein formula, $\nu_{pl} \propto \nu_{fl}$ Φ where Φ is the volume fraction, which is now well conceived as a relatively good model for homogeneous shear flows with particles moving in the same direction and at the same speed

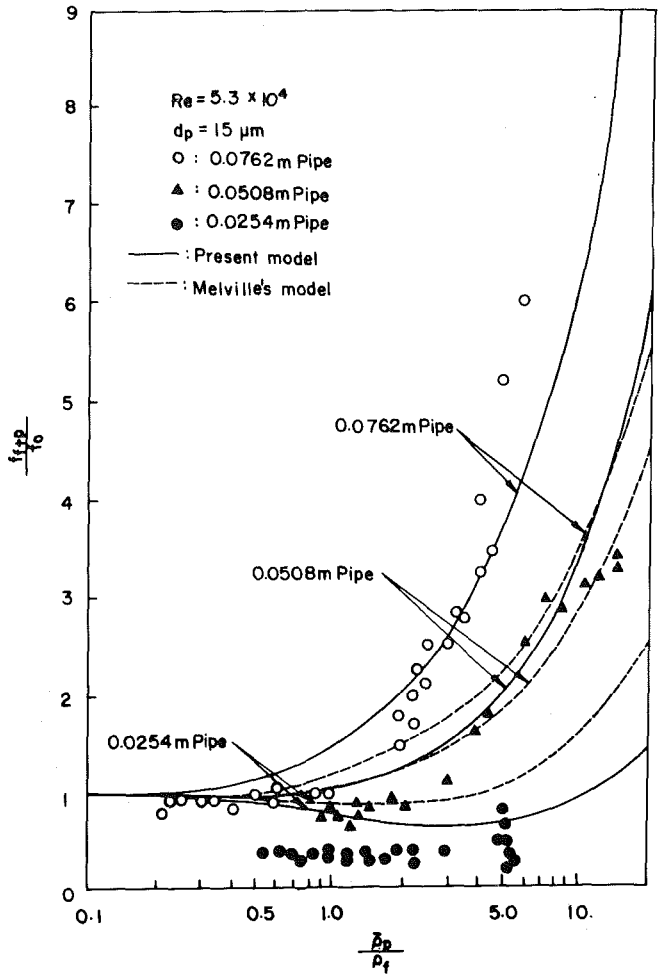

Fig. 1 Comparison of predicted friction factors with experimental data by Boothroyd [6]

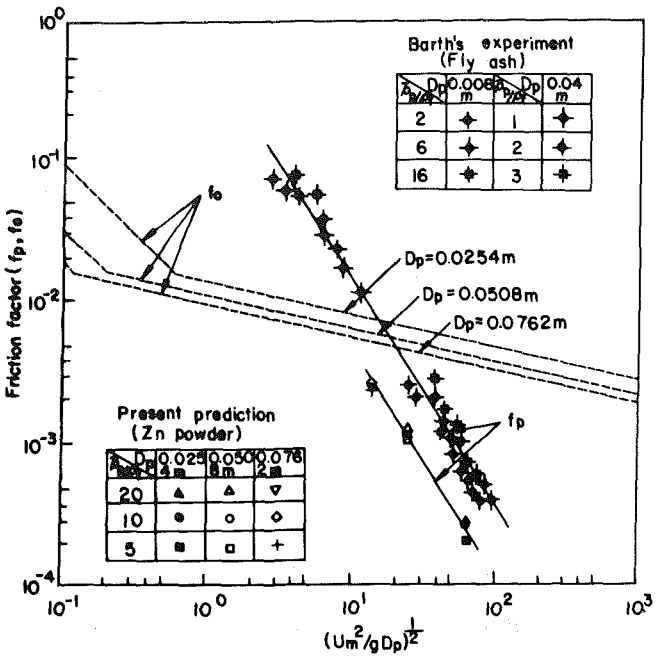

Fig. 2 Predicted variation of friction factor in pipe with Zn Powder of 15 μm diameter as a function of Froude number (experimental data for fly ash of 1 μm are taken from Barth [21])

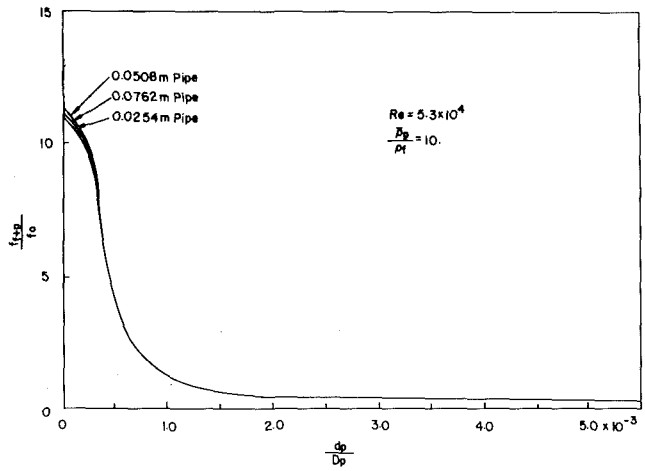

Fig. 3 Prediction of friction factors as a function of relative particle size

as that of the suspending fluid. Now, in our case, the situation is very different from such assumptions for the Einstein formula. We are interested in the momentum transfer mechanism mostly in the near wall region, where the mean rate of shear is very high and the particles cross the laminar sublayer region up and down due to the magnus lift, re-entrainment mechanism and deposition of particles on the wall. These activity crossings of the particles must, of course, contribute to the momentum transfer more strongly than the particles in homogeneous parallel motion with the suspending fluid. Therefore it may not be expected that the Einstein formula has any reasonable validity in this intermittently turbulent region. Since the crossing motions are indirectly due to the turbulence process, ν_{pl} may depend on the surrounding turbulence. A first rough assumption to approximately estimate ν_{pl} is that the ratio ν_{pl}/ϵ_p of the secondary fluid is similar to that of the primary suspending fluid, i.e.,

$$\frac{\nu_{pl}}{\epsilon_p} \sim \frac{\nu_{fl}}{\epsilon_f} \tag{22}$$

Then, equation (9) becomes,

$$\nu_{el} = \nu_{fl}\left(1 + \frac{\epsilon_p}{\epsilon_f}\frac{\bar{\rho}_p}{\rho_f}\right) \tag{23}$$

The resulting model (23) is more inclusive than other models [18–20] in that ν_{el} is implicitly a function of the Reynolds number, the relative particle size and the solid-gas loading ratio, whereas in other models it is a function of the solid-gas loading ratio only.

3 Computational Results and Discussion

In order to examine the applicability of the above extended mixing length model to two-phase wall turbulence, computations were compared with Boothroyd's [6] experiments. He measured friction factors of air flows in smooth pipes which carry spherical zinc powders. Pipe diameters were 0.0254m, 0.0508m, and 0.0762m and the particle sizes distributed over $0 \sim 40\mu$m with an average size of 15μm. Solid-gas loading ratios were between 0 to 10, and the Reynolds number based on the pipe diameter and the average velocity of the air was fixed to 53000 for all cases.

Figure 1 compares predicted friction factors with these experimental data whose uncertainty is estimated to be within 10 percent. The dotted curves were obtained by Melville and Bray's eddy viscosity model, i.e., equation (16) and (20), whereas, the solid curves were obtained by equations (17) and (21). In the computations, we assumed that the particle size is uniformly fixed to 15μm and that the secondary fluid has

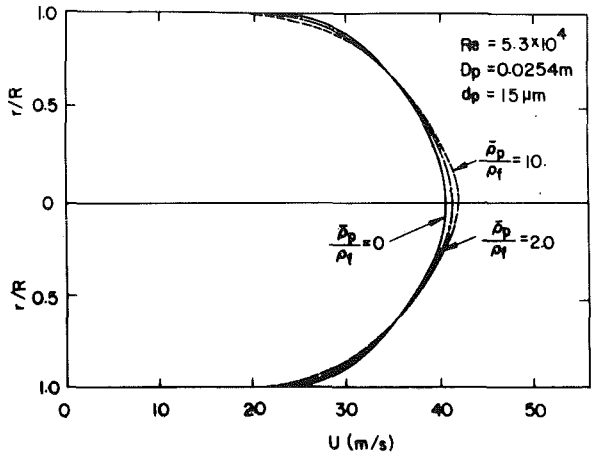

Fig. 4 Velocity profiles for various solid-gas loading ratios in 1 in. pipe

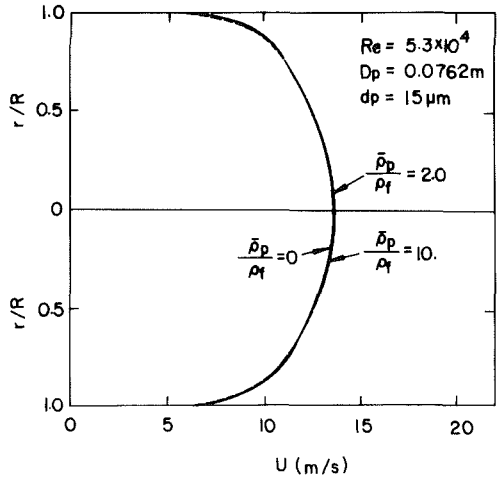

Fig. 5 Velocity profiles for various solid-gas loading ratios in 3 in. pipe

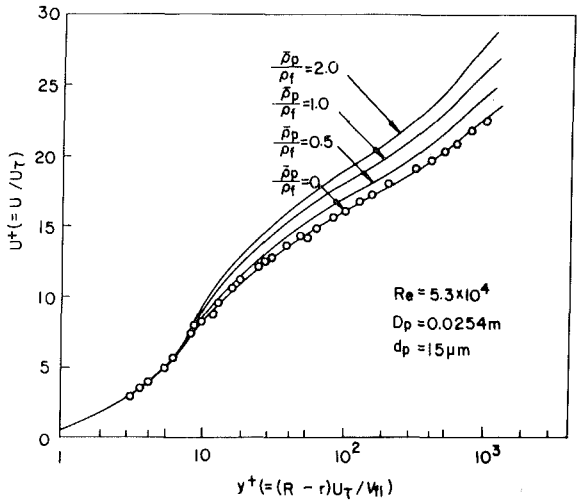

Fig. 6 Velocity profiles in wall coordinates in 1 in. pipe (o; experimental data taken from Laufer [23])

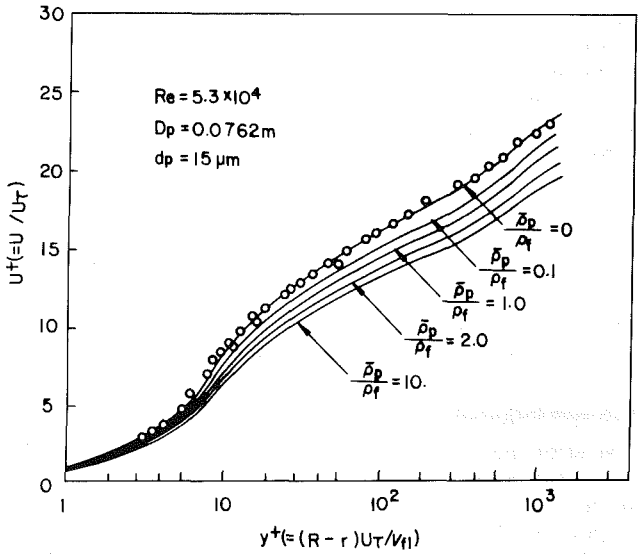

Fig. 7 Velocity profiles in wall coordinates in 3 in. pipe (o; experimental data taken from Laufer [23])

constant density over all regions. In spite of these assumptions, the predictions by our model agree well with the experimental data. For more accurate calculation, we need to take into account the particle size distribution. In this case, the friction factor may be calculated by $f = \int_0^\infty P(d_p) f(d_p, \bar{\rho}_p/\rho_f) d(d_p)$ where $P(d_p)$ is the particle size distribution function and $f(d_p, \bar{\rho}_p/\rho_f)$ is from Fig. 3, for example. Using this method, we found that our result reported here for 0.0762m pipe is over-predicted by about 3 percent and that for 0.0254m pipe is under-predicted by about 5 percent. Since we do not expect that our turbulence model and many assumptions we made can give any better accuracy than the above figures, we simply assumed the monodispersity of the particles for convenience to show the validity of our approach. It is interesting to note from both the experiments and the predictions that, for the 0.0254m pipe, the friction factor first decreases and then increases with increasing $\bar{\rho}_p/\rho_f$. Boothroyd [6] reasoned that the presence of the solid particles interferes with the primary fluid in the transport process at low solid-gas loading.

The predictions of friction factors in Fig. 1 are replotted in Fig. 2 in a different coordinate system proposed by Barth [21]. He measured friction factors in pipes carrying flying ash of uniform size of 1 μm. He observed that the friction factor due to the particles is logarithmically linear with its Froude number as shown by a straight line fit to his experimental data in Fig. 2. The same dependence can be clearly seen in our predicted friction factors.

Figure 3 shows the friction factors plotted as a function of relative particle size, which indicates that for a given Reynolds number and solid-gas loading ratio most of wall friction is predominantly caused by the presence of smaller particles. It is noted that an increase of pipe diameter (with the same particle size) has a similar effect on the friction factor as a decrease of particle size (in a pipe of same diameter). In other words, the ratio of particle size to pipe diameter instead of pipe diameter itself may be a more appropriate variable to represent the variation of friction factor.

Time mean velocity profiles in 0.0254m and 0.0762m pipes are shown in Figs. 4 and 5 with the solid-gas loading ratio as a parameter. When this ratio increases, the velocity profiles become more rounded in the core region. The variation of the velocity profile is more significant for larger relative particle size as can be seen by comparing the two figures. This increase of the maximum velocity at the pipe center for higher solid-gas loading ratio has been observed in Gill et al. [22] experiment.

The above velocity profiles are nondimensionalized and plotted in $U^+ - y^+$ coordinates in Figs. 6 and 7. For reference, the velocity profile in a turbulent clean air flow was computed and compared with Laufer's [23] experimental data as shown in these figures. For 0.0254m pipe (i.e., for larger

relative particle size), dimensionless velocity increases with increasing loading ratio. On the other hand, for 0.0762m pipe (i.e., for smaller relative particle size), the dimensionless velocity decreases with increasing loading ratio. The opposite variation is the very reason for the different signs of slopes of the friction factors in 0.0254m and 0.0762m pipes for low solid-gas loading (Fig. 1).

4 Conclusion

The mixing length theory has been extended to calculate the turbulent pipe flow suspended with solid particles for low solid-gas loading ratios and small relative particle size. It was assumed that motion of the suspended particles as a whole could be considered to be that of the secondary fluid mixed with the primary fluid. Augmentation of turbulent transport of momentum due to the presence of the particles was modeled by assuming that the turbulent kinetic energy is generated by particle fluctuations as well as by the shear of the primary fluid. The resulting eddy viscosity model gave us satisfactory prediction of friction factors in the pipes. The virtual laminar kinematic viscosity of the secondary fluid is implicitly taken to be a function of the Reynolds number and the relative particle size as well as the solid-gas loading ratio, which differs from conventional models which are functions of only the solid-gas loading ratio.

The following conclusions may be drawn about the two-phase turbulent pipe flows, which are in agreement with experimental observations by previous workers.

(*i*) Friction factor increases as the ratio of particle size to pipe diameter decreases.

(*ii*) If the relative particle size is large and the solid-gas loading ratio is low, the friction factor can be smaller than that of particle-free flow.

(*iii*) Augmentation of the friction factor due to the particles is logarithmically linear with its Froude number.

Acknowledgment

Most of the computations were supported by the Department of Mechanical Engineering and Computer Center of Korea Advanced Institute of Science Technology. Partial support of this work by Korea Science and Engineering Foundation is also acknowledged.

References

1 Abramovich, G. N., "The Effect of Admixture of Solid Particles or Droplets on the Structure of a Turbulent Gas Jet," *Int. J. Heat and Mass Transfer*, Vol. 14, 1971, p. 1039.

2 Sharma, M. P., and Crowe, C. T., "A Novel Physico-Computational Model for Quasi One-Dimensional Gas-Particle Flows," ASME JOURNAL OF FLUIDS ENGINEERING, Vol. 100, Sept. 1978, p. 343.

3 Owen, P. R., "Pneumatic Transport," *J. Fluid Mech.*, Vol. 39, 1969, p. 407.

4 Melville, W. K., and Bray, K. N. C., "A Model of the Two Phase Turbulent Jet," *Int. J. of Heat and Mass Transfer*, Vol. 22, 1979, p. 647.

5 Laats, M. K., and Frishman, F. A., "Scattering of an Inert Admixture of Different Grain Size in a Two-Phase Axisymmetric Jet," *Heat Transfer-Soviet Res.*, Vol. 2, 1970, p. 7.

6 Boothroyd, R. G., "Pressure Drop in Duct Flow of Gaseous Suspensions of Fine Particles," *Trans. Instu. Chem. Engrs.*, Vol. 44, 1966, p. 306.

7 Melville, W. K., "Two Phase Turbulent Jet," Ph.D. thesis, Southampton University, 1974.

8 Govier, G. W., and Aziz, K., *The Flow of Complex Mixtures in Pipes*, Van Nostrand Reinhold Company, 1972, p. 623.

9 Boothroyd, R. G., "Turbulence Characteristics of the Gaseous Phase in Duct Flow of a Suspension of Fine Particles," *Trans. Instn. Chem. Engrs.*, Vol. 45, 1967, p. T297.

10 Crawford, M. E., and Kays, W. E., *A Program for Numerical Computation of Two Dimensional Internal/External Boundary Layer Flows*, Rept. HMT-23, Stanford University, California, 1975.

11 Meek, C. C., and Jones, B. G., "Studies of the Behaviour of Heavy Particles in a Turbulent Fluid Flow," *J. Atmos. Sci.*, Vol. 30, 1973, p. 239.

12 Hinze, J. D., *Turbulence*, McGraw-Hill, New York, 1975, p. 467.

13 Soo, S. L., "Statistical Properties of Momentum Transfer in Two Phase Flow," *Chem. Engr. Sci.*, Vol. 5, Apr. 1956, p. 57.

14 O'Brien, R. W., "A Method for the Calculation of Effective Transport Properties of Suspensions of Interacting Particles," *J. Fluid Mech.*, Vol. 91, Part 1, 1979, p. 17.

15 Peskin, R. L., "Some Fundamental Research Problems in Gas-Solid Flows," AICHE Symposium, Vol. 71, No. 147, 1975, p. 52.

16 Corrsin, S., "Estimates of the Relations Between Eulerian and Lagrangian Scales in Large Reynolds Number Turbulence," *J. Atmos. Sci.*, Vol. 20, 1963, p. 115.

17 Soo, S. L., and Tien, C. L., "Effect of the Wall on Two-Phase Turbulence Motion," ASME *Journal of Applied Mechanics*, Mar. 1960, p. 5.

18 Happel, J., "Viscosity of Suspensions of Uniform Spheres," *J. of Appl. Phy.*, Vol. 28, Nov. 1957, p. 1288.

19 Frankel, N. A., and Acrivos, A., "On the Viscosity of a Concentrated Suspension of Solid Spheres," *Chem. Engr. Sci.*, Vol. 22, 1967, p. 847.

20 Sather, N. F., and Lee, K. J., "Viscosity of Concentrated Suspensions of Spheres," Vol. 6, 1972, p. 575.

21 Barth, W., "Flow Problems With Mixtures of Gaseous and Entrained Solid Particles," *Engr. Digest*, Vol. 23, 1962, p. 81.

22 Gill, L. E., Hewitt, C. F., and Lacey, M. C., "Sampling Probe Studies of the Gas Core in Annular Two-Phase Flow-II," *Chem. Engr. Sci.*, Vol. 19, 1964, p. 665.

23 Laufer, J., "The Structure of Turbulence in Fully Developed Pipe Flow," N.A.C.A. Rep. No. 1174, 1954.

H. Karadogan[1]
Visiting Assistant Professor.

D. Rockwell
Professor.

Department of Mechanical Engineering
and Mechanics,
Lehigh University,
Bethlehem, Pa. 18015

Toward Attenuation of Self-Sustained Oscillations of a Turbulent Jet Through a Cavity

Several attenuation configurations are assessed, involving the following concepts: generating streamwise vorticity, dephasing the azimuthal coherence of the jet, and reducing rigidity of the jet separation edge. By proper design, effective attenuation of the discrete frequency components of the oscillation can be achieved. For cases where there is not complete attenuation, the phase condition corresponding to maximum relative amplitude of the oscillation is maintained, the disturbance phase speed is essentially unaltered, and there is a proportional reduction in amplitude along the jet, including the initial fluctuation level at separation.

Introduction

Self-sustained oscillations of wakes, mixing layers, and jets are well-known for both nonimpinging and impinging flow configurations having laminar or turbulent boundary layers at separation. The coherence of such oscillations can be substantially enhanced by interaction of the inherent instability of the separated shear layer with a resonant acoustic or free-surface mode of the flow system (Rockwell 1982 [9]). Although much effort has been devoted to characterizing the nature of these oscillatory flows, their attenuation deserves in-depth consideration (Naudascher and Rockwell 1980 [7]). The primary objective of this investigation is to assess several attenuation concepts for a basic type of separated flow occurring in a variety of internal flow systems: turbulent flow through a cavity enhanced by resonant modes of the approach flow pipe(s) (Rockwell and Schachenmann 1980, 1982). In practice, the separated flow zone occurs at a tee or bend in the duct/pipe, at a valve, etc.. There have been few investigations related to mitigation of these oscillations at their source, namely the process of flow separation; those techniques that have been employed will be discussed below in the appropriate category of attenuation.

Experimental System

The experimental apparatus involved a long pipe of length l and diameter D terminated by an axisymmetric cavity of length L (see Fig. 1 and Rockwell and Schachenmann 1982 [10]). For the experiments described here, the Reynolds number of the flow at the end of the pipe was $2061 \leq \mathrm{Re}_{\theta_0} = U_0\theta_0/\nu \leq 3805$ ($U_0 \equiv$ centerline velocity $\theta_0 =$ momentum thickness). Since $l/D = 82.3$, the flow was fully turbulent at the cavity inlet; mean and fluctuating velocity distributions agreed well with previous studies of fully-developed turbulent flow (Laufer 1953 [5]). All experiments were run at a cavity length $L/\theta_0 = 36.03$, corresponding to $L/D = 1.8$.

As described by Rockwell and Schachenmann (1980, 1982 [10, 11]), the inherent instability of the separated shear layer through the cavity is enhanced by the acoustic modes of the upstream pipe, yielding strongly coherent oscillations. When U_0 or L is varied, there are variations in frequency and amplitude of the oscillation, with jumps in frequency occurring at minimum oscillation amplitude; consequently a number of "modes" of oscillation are negotiated, with maximum amplitude occurring at about the middle of each mode. The mode number corresponds to the acoustic mode of the organ-pipe resonance. In this investigation, two typical modes of oscillation (III, IV) will be considered, allowing examination of attenuator effectiveness over a range of velocity.

In characterizing oscillation frequency and amplitude, hot wire measurements were taken along the centerline of the cavity ($\tilde{u}_e$) and pressure measurements were acquired within the cavity ($\tilde{P}_b$). Since the acoustic wavelength (λ_a) was much longer than the cavity length (L), the pressure amplitude $\tilde{P}_b$ was representative of that throughout the cavity.

In order to determine the spectral content of the oscillation, an Ortec lock-in amplifier (with a vector computer module) was driven by a frequency ramp generator through its reference channel, while the pressure or velocity fluctuation of interest was fed into the signal channel. The resultant spectral peak(s) gave the amplitude(s) of the organized oscillation.

To provide a reference case for all attenuators, experiments were run without the attenuator insert, indicated by the dashed lines in Fig. 1. Then various attenuators were examined, continuously checking the no-attenuator reference conditions.

[1] On leave from Faculty of Mechanical Engineering, Istanbul Technical University, Istanbul, Turkey.

Contributed by the Fluids Engineering Division for publication in the JOURNAL OF FLUIDS ENGINEERING. Manuscript received by the Fluids Engineering Division, May 7, 1982.

Types of Attenuators

Figure 2 depicts the various categories of attenuators, classified as vortex generators, azimuthal dephasors, and compliant boundaries.[2]

The principle of the vortex generators involves production of streamwise vorticity, having a vector orientation orthogonal to the mean vorticity of the separating boundary layer, thereby destroying the spanwise or azimuthal coherence of the primary vortices. As discussed by Kuethe (1972 [4]), in a study of generators at the trailing edge of an airfoil, it is possible to distinguish counter-and corotating regions of streamwise vorticity, depending upon the spacing between generators, all of which are parallel to each other and inclined at the same angle of attack. Keller and Escudier (1979 [3]) show a strong influence of incidence angle of a row of generators (all having the same inclination) in attenuating cavity oscillations. Bradbury and Khadem (1975 [1]) and Pannu and Johannesen (1976 [8]) have demonstrated that protruding tabs at the exit of, and notches at the lip of, an axisymmetric jet nozzle can significantly affect the time mean and total turbulence intensity distributions of the jet. To date, there has been no systematic investigation of the effect of vortex generator configuration, spacing, inclination angle, and height, all *relative* to the characteristic boundary layer momentum thickness (θ_0) at separation.

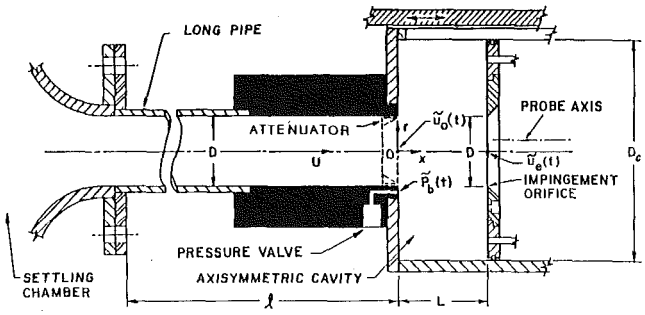

Fig. 1 Schematic of pipeline-cavity system showing location of typical attenuator at entrance of cavity

With regard to the classes of slotted and asymmetric boundaries depicted in Fig. 2, the basic concept involves decreasing the azimuthal, or spanwise, coherence of the separating shear layer, as well as dephasing the coherence of the pressure perturbations incident upon the separation edge (Rockwell 1982 [9]). To be sure, there will be generation of streamwise vorticity as well, evident in the notched trailing edge leading to formation of a mixing layer (Breidenthal 1980 [2]); this vorticity arises from spanwise dephasing of the separation process.

In respect of the compliant boundary configuration, the mechanism involves decreasing the rigidity of the separation edge and mitigating the conversion process (most effective at a *rigid* trailing edge) between disturbances incident upon the edge and vorticity fluctuations in the shear layer (Rockwell 1982 [9]). If the compliant boundary has streamwise slits (Fig. 2), the mechanism of azimuthal dephasing can also be expected to play a significant role.

Vortex generators and azimuthal dephasors were manufactured from 0.05 mm thick tin sheets, while the compliant boundaries were cut from highly flexible, 0.05 mm thick, plastic (used for manufacture of "GLAD" lunch bags). For purposes of illustrating the technique of mounting the attenuators at the exit of the long pipe, photographs of typical attenuators inserted in a plexiglas duct are shown in Fig. 3.

[2] Configuration II of the vortex generators, as well as the general concepts of the slotted and asymmetric boundaries, were suggested and designed by Prof. *M. V. Morkovin*, who stimulated this research program.

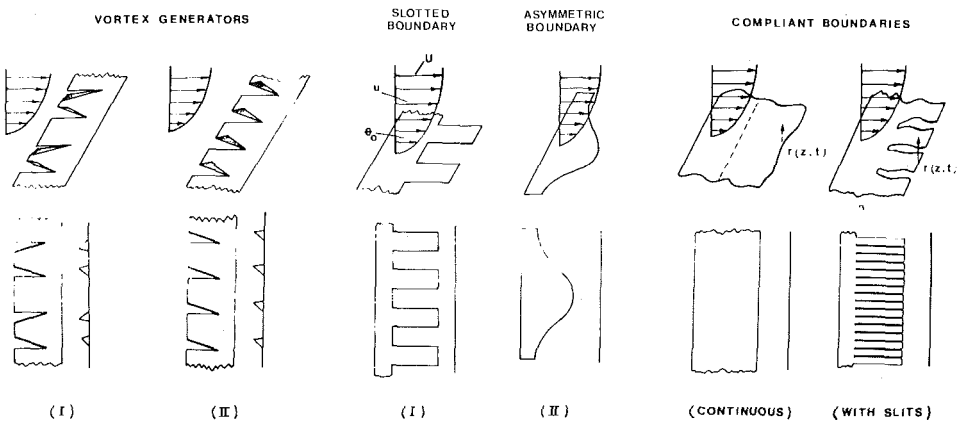

Fig. 2 Attenuator configurations: vortex generators, slotted boundary; asymmetric boundary; and compliant boundaries

Nomenclature

$\tilde{u}$ = root-mean-square velocity fluctuation in cavity on centerline of jet
U_0 = time-averaged centerline velocity in pipe at entrance of cavity
f = frequency
$\tilde{P}_{b_{rms}}$ = root-mean-square pressure taken in cavity at $x=0$ (see Fig. 1)
$\Delta\phi$ = $\phi_{\tilde{u}} - \phi_{\tilde{u}_0}$ Phase (difference) angle (reference $\phi_{\tilde{u}_0}$)
θ_0 = boundary layer momentum thickness at separation
L = length of cavity
m/s = meters per second
D_c = inner diameter of cavity
D = inner diameter of pipe ($D=2R$)

Oscillation modes with attenuators:
△ = 2nd mode (90 Hz)
○ = 3rd mode (135 Hz)
□ = 4th mode (179 Hz)
▽ = 5th mode (226 Hz)
○ = Helmholtz mode (250 Hz)

Oscillation modes without attenuators:
● = 3rd mode (135 Hz)
■ = 4th mode (179 Hz)
▼ = 5th mode (226 Hz)

Fig. 3 Plots of representative attenuators mounted within exit of plexiglas pipe: vortex generators-I; slotted boundary; and asymmetric boundary

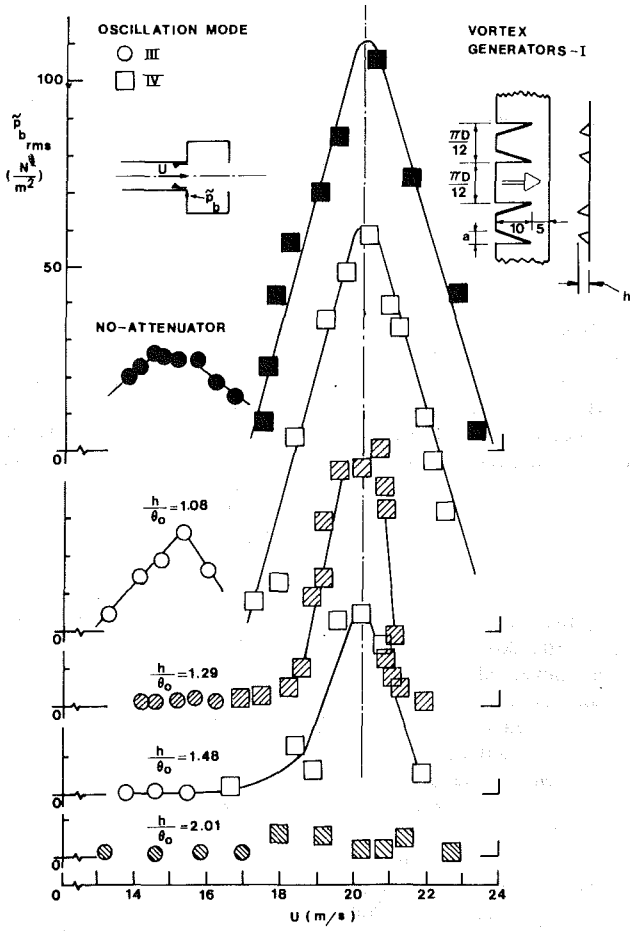

Fig. 4 Pressure amplitude in cavity ($\tilde{P}b_{rms}$) versus velocity (U) as a function of size (h) of vortex generators-I $2061 \leq Re_{\theta_0} \leq 3805$; $L/\theta_0 = 36.03$

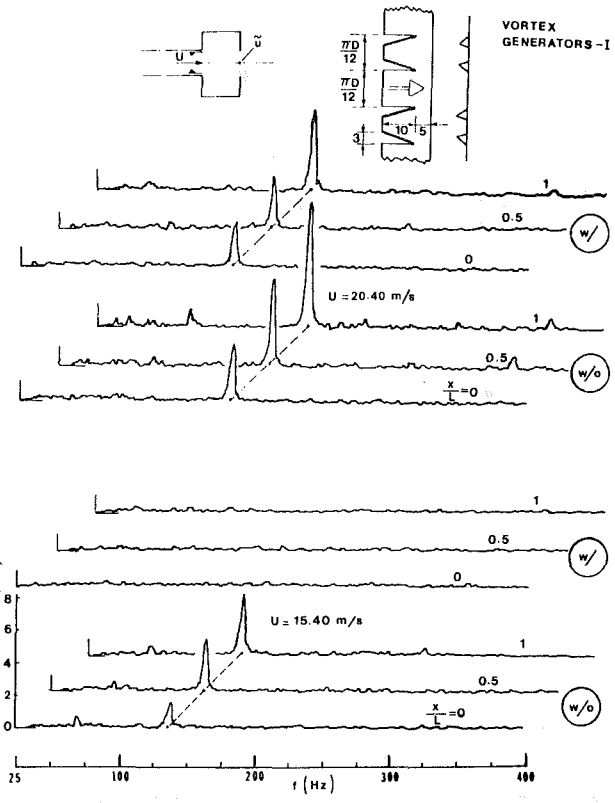

Fig. 5(*a*) Effect of vortex generators on spectra of velocity fluctuations ($\tilde{u}_{rms}(f)/df$), taken along centerline of jet ($r/R = 0$), at velocities corresponding to maximum amplitude response without generators (U = 15.40 m/s and 20.40 m/s) $Re_{\theta_0} = 2442, 3234$, $L/\theta_0 = 36.03$. w/: with generators; w/0; without generators.

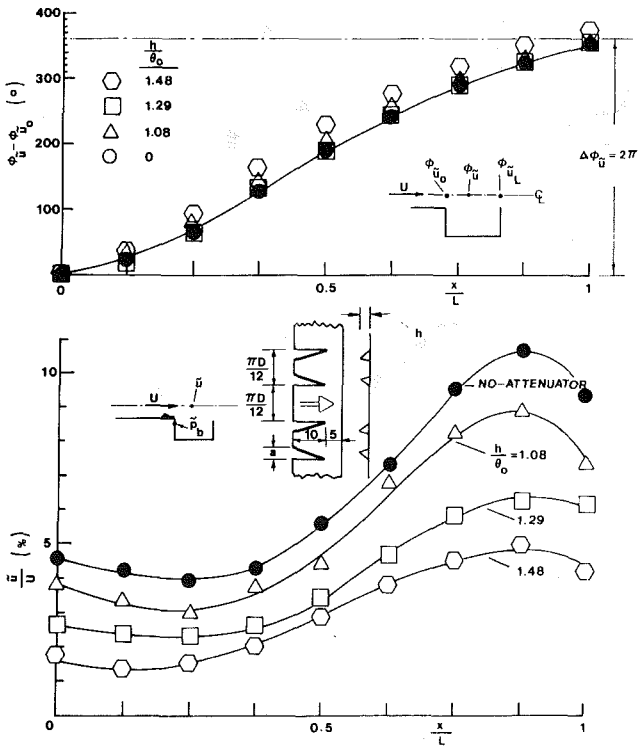

Fig. 5(*b*) Variation of phase ($\phi_{\tilde{u}} - \phi_{\tilde{u}_0}$) and amplitude ($\tilde{u}/U$) of velocity fluctuation at centerline of jet ($r/R = 0$) for various size of vortex generators-I at velocity of maximum amplitude response. $Re_{\theta_0} = 3234$; $L/\theta_0 = 36.03$.

Attenuator Effectiveness

Vortex Generators. Figure 4 depicts the effect of attenuator height on the amplitude of the organized pressure oscillation for two modes of oscillation, the peak amplitude in the fourth mode being considerably higher than the third

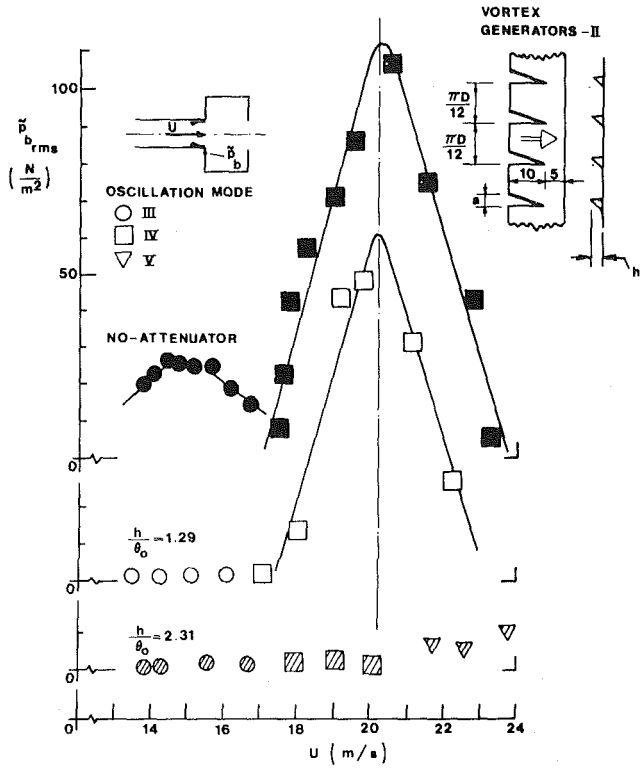

Fig. 6 Pressure amplitude in cavity. ($\tilde{P}_{b_{rms}}$) versus velocity (U) as a function of size (h) of vortex generators-II. $2061 \leq Re_{\theta_0} \leq 3805$; $L/\theta_0 = 36.03$.

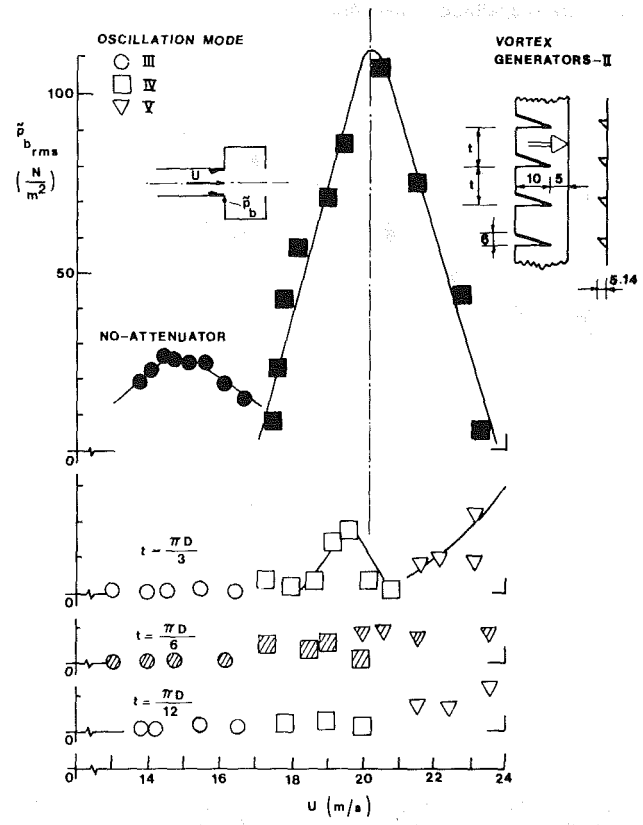

Fig. 7 Pressure amplitude in cavity ($\tilde{P}_{b_{rms}}$) versus velocity (U) as a function of pitch (t) of vortex generators-II. $2061 \leq Re_{\theta_0} \leq 3805$; $L/\theta_0 = 36.03$.

mode (at $U = 20.4$ m/s). (As discussed by Rockwell and Schachenmann (1982 [10]), the damping of each acoustic

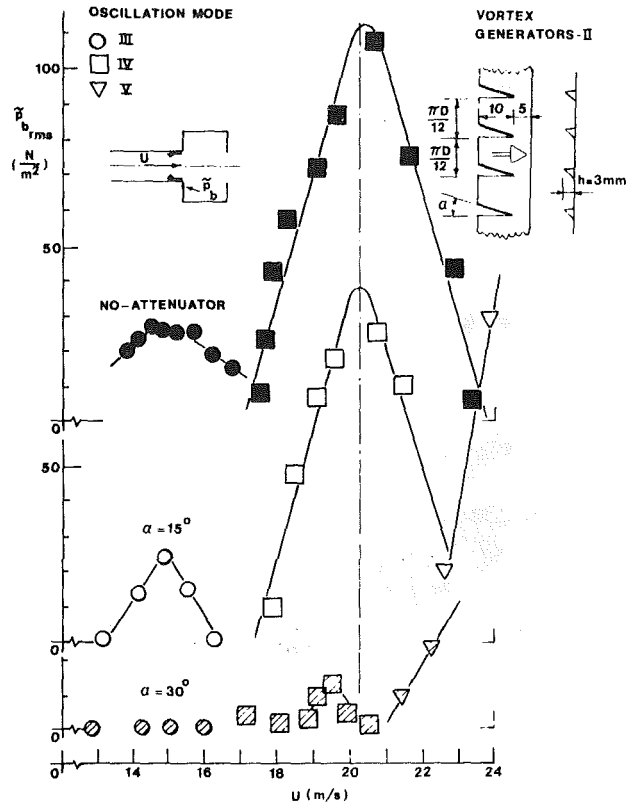

Fig. 8 Pressure amplitude in cavity ($\tilde{P}_{b_{rms}}$) versus velocity (U) as a function of angle (α) of vortex generators-II. $2061 \leq Re_{\theta_0} \leq 3805$; $L/\theta_0 = 36.03$.

mode varied significantly with mode number.) Although generator height $h/\theta_0 = 1.08$ has little effect, increasing the height to $h/\theta_0 = 2.01$ attenuated the oscillation. (All dimensions in the inset are in mm; note that the vertical axis is broken to save space.)

The effect of the attenuator on the streamwise evolution of the velocity spectra is shown in Fig. 5(a). For the oscillation in mode III ($U = 15.40$ m/s), the attenuator ($a = 3$ mm; $h/\theta_0 = 1.29$) completely eradicates any sign of organized oscillation in velocity spectra along the entire streamwise extent of the jet (i.e., from cavity inlet ($x = 0$) to outlet ($x = L$)). However, for the stronger oscillation of the fourth mode ($U = 20.40$ m/s), peak amplitudes of the spectra are proportionately decreased, rather than being completely attenuated.

This behavior prompted a detailed study of the effect of attenuator height on streamwise distributions of amplitude and phase of the organized velocity fluctuation. Shown in Fig. 5(b) is the downward shifting of the amplitude distributions with increased height of the generator. However, the streamwise distributions of phase are nearly coincident for all values of generator height, and the overall phase difference of 2π is maintained. This means that the *phase speed of the disturbance along the centerline of the jet and the 2π phase criterion for maximum relative amplitude are insignificantly affected by attenuation of absolute amplitude of oscillations via the vortex generator.*

The fact that vortex generators of configuration II (see Fig. 2) are as effective as those of configuration I (Fig. 4) is evidenced in Fig. 6. Nearly complete attenuation is achieved with an attenuator height of only $h/\theta_0 = 2.31$.

The effect of pitch (t) of the vortex generators is depicted in Fig. 7. Nearly complete attenuation of the mode IV oscillation can be achieved with $t = \pi D/3$, though there is onset of oscillation energy in mode V at the expense of attenuating mode IV! Residual energy of mode V is, in fact, evident for higher values of pitch where attenuation is more complete.

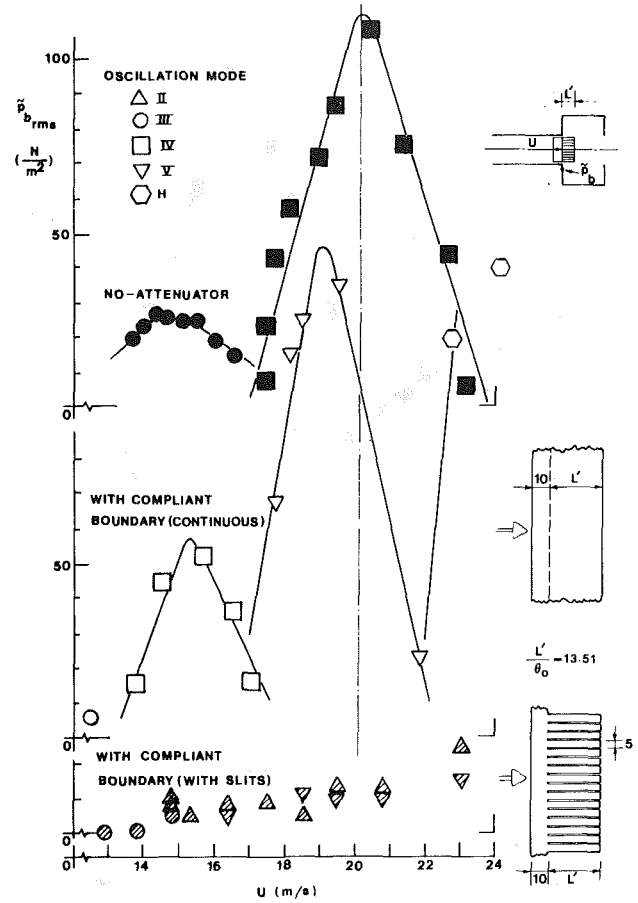

Fig. 9 Pressure amplitude in cavity ($\tilde{P}_{b_{rms}}$) versus velocity (U) for continuous boundary and compliant boundary with slits. $2061 \leq Re_{\theta_0} \leq 3805$; $L/\theta_0 = 36.03$.

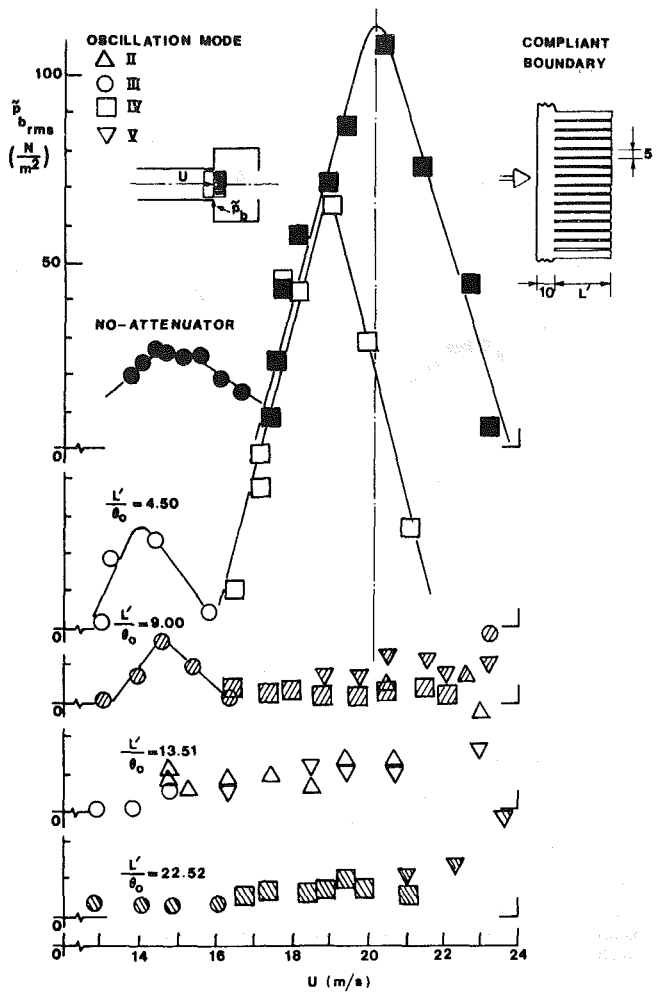

Fig. 10 Pressure amplitude in cavity ($\tilde{P}_{b_{rms}}$) versus velocity (U) as a function of length (L') of compliant boundary with slits. $2061 \leq Re_{\theta_0} \leq 3805$; $L/\theta_0 = 36.03$.

The importance of angle of inclination of the attenuator is high-lighted in Fig. 8, showing little change in amplitude for $\alpha = 15$ deg, but a drastic decrease in amplitude for $\alpha = 30$ deg. Also evident at $\alpha = 30$ deg is the shifting of the amplitude peak of mode IV to lower velocity and onset of mode V oscillations at higher values of velocity.

Compliant Boundaries: Effectiveness of the compliant boundary, extending a distance L' downstream of the cavity lip, is depicted in Figs. 9 and 10. For the case of a continuous boundary (having no slits; see Fig. 9), the modes of oscillation are shifted to higher values, and the peak amplitudes increased. However, in the case of the compliant boundary with slits, substantial attenuation is achieved, as depicted at the bottom of Fig. 9. The effect of length of the slitted compliant boundary is given in Fig. 10. Substantial attenuation can be achieved with a boundary length of $L'/\theta_0 = 13.51$; the effect of a short length ($L'/\theta_0 = 4.50$) is to shift the peak amplitudes to lower velocity. It should be noted that, for the peak amplitudes of oscillation in absence of an attenuator, the wavelength of the jet instability (λ) was 36 momentum thicknesses (θ_0) long, i.e., $\lambda/\theta_0 = 36$. Consequently, for $L'/\theta_0 = 13.5$ corresponding to effective attenuation, $L'/\lambda \simeq 1/3$.

Slotted Boundary. The effect of a slotted separation boundary is depicted in Fig. 11. Though there is a tendency to shift the peak amplitudes to lower velocity, it is evident that little attenuation can be achieved. The explanation of this ineffectiveness may lie in the mixing layer visualization of Breidenthal (1980 [2]), who found that the three-dimensionality induced by spanwise dephasing at a slotted trailing edge did not persist; there was rapid recovery to two-dimensional vortical structures within a short streamwise distance.

Asymmetric Boundary. In the case of the nonaxisymmetric configuration (see Fig. 12), a substantial reduction in peak amplitude is possible only for relatively long lengths, $L' = 2L/3$. At shorter lengths, i.e., $L' = 1/3$, there is substantial shift of peak amplitudes to lower values of velocity and inducement of large amplitudes at a higher mode (V). Consequently, both types of these separation boundaries are relatively ineffective.

Conclusions

Of the various categories of attenuators, the most effective are vortex generators and compliant boundaries:

(*a*) Vortex generators having either the same angle, or alternating angle, of incidence with respect to the mean flow were found to be equally effective. The height of the generators should be (at least) two momentum thicknesses of the separating boundary layer, their angle of incidence at least 30 deg, and their pitch no more than one-sixth the jet circumference.

(*b*) Compliant boundaries involving highly flexible extensions of the jet nozzle exit are most effective when slitted in the streamwise direction. The length of these boundaries should be at least one-third wavelength of the developing instability wave of the jet.

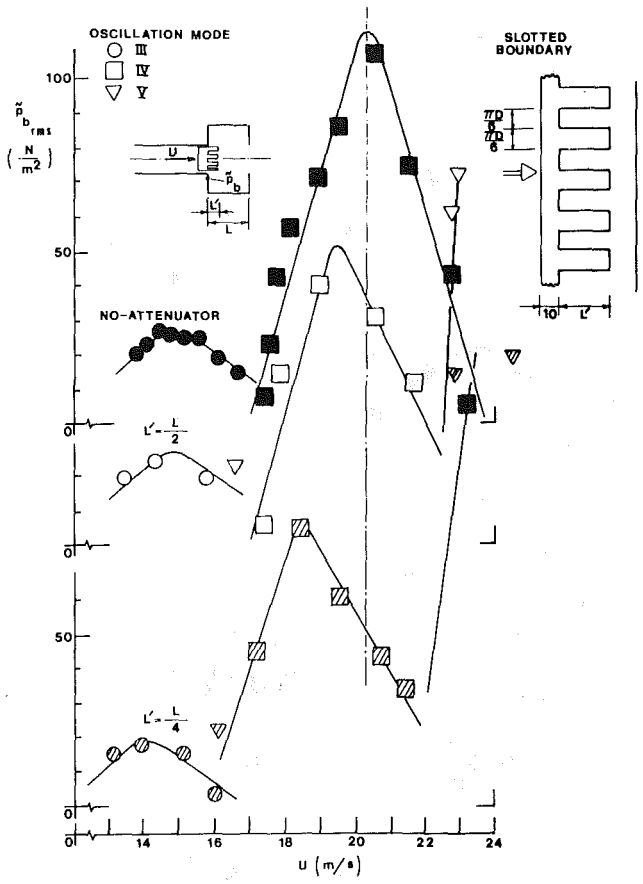

Fig. 11 Pressure amplitude in cavity ($\tilde{P}_{b_{rms}}$) versus velocity (U) as a function of length (L) of slotted boundary; $2061 \leq Re_{\theta_0} \leq 3805$; $L/\theta_0 = 36.03$.

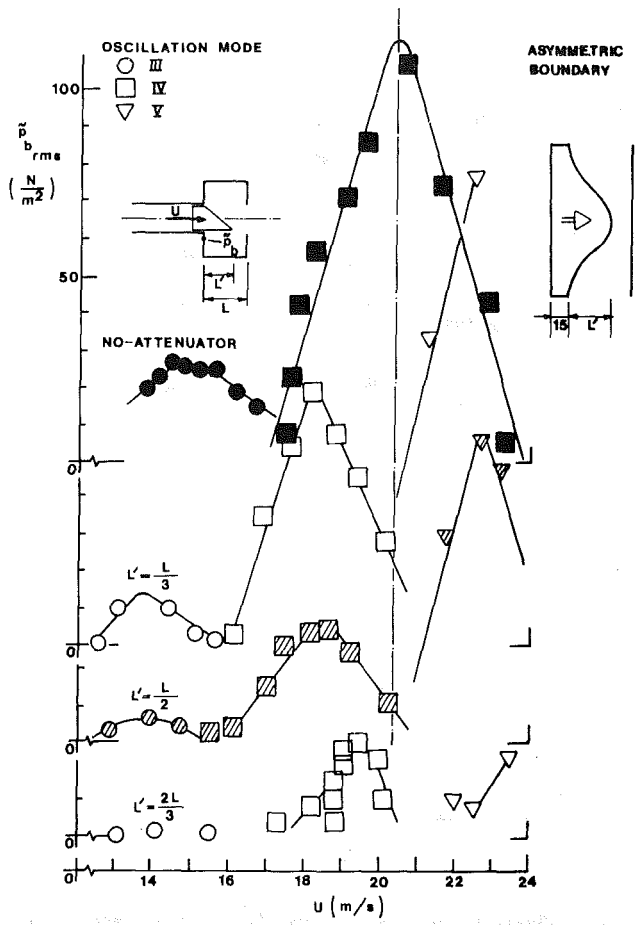

Fig. 12 Pressure amplitude in cavity ($\tilde{P}_{b_{rms}}$) versus velocity (U) as a function of length (L') of asymmetric boundary; $2061 \leq Re_{\theta_0} \leq 3805$; $L/\theta_0 = 36.03$.

Attenuation of the amplitude of oscillation is associated with a proportional reduction of velocity amplitude along the *entire* streamwise extent of the jet, including the amplitude level at the separation edge. Regardless of the degree of attenuation (excepting complete attenuation), the phase speed of the jet disturbance remains essentially unaltered; moreover, the condition of 2π phase difference between separation and impingement occurring at maximum *relative* amplitude of oscillation, is always maintained.

Depending upon the oscillation technique employed, there is the possibility that attenuation of a given mode of oscillation will lead to the onset of a higher mode. Although this is not a significant problem for those attenuators that are highly effective, marginally effective attenuators can, in some cases, yield a higher amplitude at the same or a higher mode; moreover, they may shift the peak amplitude of oscillation to a lower value of velocity.

Acknowledgments

The authors wish to express their appreciation to the National Science Foundation and the Volkswagen Foundation for support of this investigation.

References

1 Bradbury, L. J. S. and Khadem, A. H., "The Distortion of a Jet by Tabs," *J. Fluid Mech.*, Vol. 70, part 4, 1974, pp. 801–813.

2 Breidenthal, R., "Response of Plane Shear Layers and Wakes to Strong Three-dimensional Disturbances," *Phys. Fluids*, Vol. 23, No. 10, Oct. 1974.

3 Keller, J., and Escudier, M., "Periodic Flow Aspects of Throttles, Cavities, and Diffusers," Brown Boveri Research Center Report KCR-79-144B, Nov. 1979.

4 Kuethe, A. M., "Effect of Streamwise Vortices on Wake Properties Associated with Sound Generation," *J. Aircraft*, Vol. 9, No. 10, Oct. 1972.

5 Laufer, J., "The Structure of Turbulence in Fully-Developed Pipe Flow," NASA Report 1174, 1953.

6 Morkovin, M. V., Private communication, July 1980.

7 Naudascher, E., and Rockwell, D., *Practical Experiences with Flow-Induced Vibrations, Proceedings of 1979 IAHR/IUTAM Symposium*, Springer Verlag, Berlin, 1980.

8 Pannu, S. S., and Johannesen, N. H., "The Structure of Jets from Notched Nozzles," *J. Fluid Mech.*, Vol. 74, Part 3, 1975, pp. 515–528.

9 Rockwell, D., "Invited Lecture: Oscillations of Impinging Shear Layers," 20th Aerospace Sciences Meeting, AIAA, January 11–13, Orlando, Fl., 1982. To be published in *AIAA Journal*.

10 Rockwell, D., and Schachenmann, A., "Self-Generation of Organized Waves in an Impinging Turbulent Jet at Low Mach Number," *J. Fluid Mech*, Vol. 117, Apr. 1982, pp. 425–441.

11 Schachenmann, A., and Rockwell, D., "Self-Sustained Oscillations of a Turbulent Pipe Flow Terminated by an Axisymmetric Cavity," *J. Sound and Vibration*, Vol. 73, No. 1, 1980 pp. 61–72.

Y. Tomita
Research Assistant.

A. Shima
Professor.
Mem. ASME

K. Takahashi
Graduate Student.

Institute of High Speed Mechanics,
Tohoku University,
Sendai, Japan

The Collapse of a Gas Bubble Attached to a Solid Wall by a Shock Wave and the Induced Impact Pressure

An experimental study was made on the collapse of a gas bubble attached to a solid wall by a shock wave. The collapse process of the bubble and the induced impact wall pressure were measured simultaneously by means of a high speed camera and a pressure transducer, respectively. Consequently, it was found that the impact wall pressure was very sensitive to the factors such as the bubble size, the strength of shock wave and the distance from the origin of shock wave to the gas bubble, and in some cases it became larger than that generated by a shock wave directly impinging on the solid wall without a gas bubble.

Introduction

It is well known that cavitation damage is attributed predominantly to an impact pressure produced by a collapsing bubble. In order to clarify the mechanism of the impact pressure generation, many works were done on bubble dynamics [1-30]. As a result of the previous works, two factors were found to be predominant in generating the impact pressure. One is a liquid jet developed from the instability of a collapsing bubble, and the other is a shock wave generated at the instant of the rebound of a bubble. When a bubble locates both on and very close to a solid wall, it collapses nonspherically and a microjet flowing toward the solid wall is formed. This fact was confirmed experimentally as well as theoretically, so it was supposed that the microjet would mainly contribute to an impulsive force acting on the solid wall. Recently Fujikawa and Akamatsu [13, 14] showed that the presence of a solid boundary did not inhibit the shock wave radiation and an impulsive pressure accompanying the bubble collapse was caused by the impact of shock waves, and the jet impingement did not produce any detectable effects. Shima et al. [15] reconfirmed the generation of shock waves during the rebound of spark bubbles, and observed the coexistence of a shock wave and a liquid jet in the case where a bubble almost touched a solid wall at its maximum expansion. The experimental evidence like the generation of shock waves is of significance to investigate the cavitation phenomena. In fact in actual cavitation such as flow cavitation and acoustic cavitation, it is possible that a shock wave generated from one bubble acts on another nearby bubble in collapsing phase. Therefore it is important to clarify the interactions between bubbles and also between a bubble and a shock wave. Nevertheless only a few papers were reported to this problem, for example, as to the interactions between a bubble and a shock wave in the references [7, 8, 20] and between bubbles in the reference [10]. Tulin [20] theoretically suggested that the formation of ultra-jet [31] on cavity surfaces by impinging shocks might be an important mechanism in the cavitation damage. On the other hand, Smith and Mesler [10] experimentally investigated the interaction of a growing and collapsing vapor bubble with a neighbouring gas bubble. They concluded that the transfer of energy from the vapor bubble to the gas bubble and the repulsion of the vapor bubble by the gas bubble were important factors in the protection of the boundary. However, they did not refer to the interaction of the gas bubble with a shock wave produced by the initiation of the vapor bubble. Further, we have never seen the systematic investigation with respect to the impact wall pressure resulted from the interaction between a bubble and a shock wave.

In the present paper, therefore, an experimental study is made on the collapse of a single gas bubble attached to a solid wall by a shock wave. To simulate a shock wave generated at the instant of the re-expansion of a bubble, one generated at the instant of the spark discharge in water is used here. The collapse of the gas bubble and the induced impact wall pressure are measured simultaneously by means of an Imacon high speed camera and a pressure transducer, respectively. Consequently, the results obtained here are as follows; The collapse of an attached gas bubble by a shock wave is very intensive. When a shock wave impinges on the surface of a gas bubble from different direction with the axis of symmetry of the bubble, an oblique liquid jet may be formed. The impact wall pressure is strongly depending on the bubble size, the shock strength and the distance from the origin of shock wave to the gas bubble. According to the combinations of these factors, a gas bubble acts as either the energy absorber from a

Contributed by the Fluids Engineering Division and presented at the ASME Applied Mechanics, Bioengineering and Fluids Engineering Conference, Houston, Texas, June 20-22, 1983, of THE AMERICAN SOCIETY OF MECHANICAL ENGINEERS. Manuscript received by the Fluids Engineering Division, January 15, 1982. Paper No. 83-FE-3.

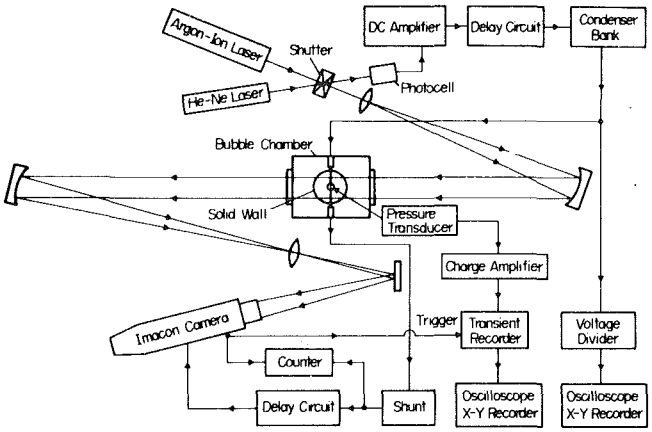

Fig. 1 Schematic diagram of the experimental apparatus

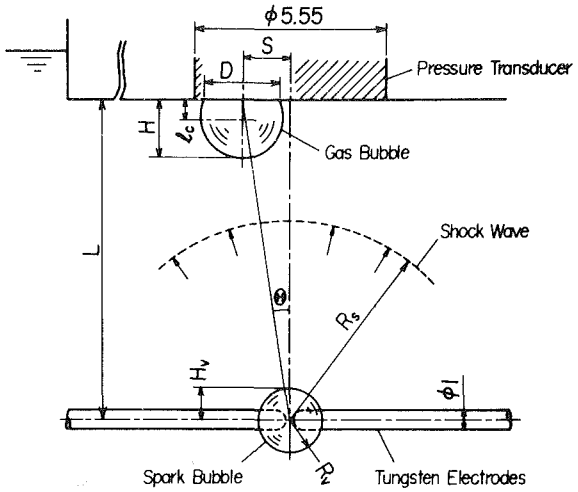

Fig. 2 Detail of the test section

shock wave or the source of more intensive impact wall pressure than one generated by a shock wave directly impinging on the solid wall without a gas bubble.

Experimental Equipment and Methods

A schematic diagram of the experimental set up is shown in Fig. 1. A 300 mm × 240 mm × 240 mm stainless steel bubble chamber with 100 mm diameter observation windows was used, and tap water at room temperature was filled in it. At the center of the chamber a pair of tungsten electrodes of 1 mm diameter which was utilized to generate a shock wave impinging on a gas bubble was placed facing each other. A condenser bank of $C = 0.5\ \mu F$ and variable charging voltage V_C was used here. A solid lucite wall of 40 mm diameter was settled above and parallel to the axis of the electrodes. A Swiss Kistler Model 603 B quartz transducer was mounted flush to the solid surface. The transducer has a diameter of 5.55 mm, a resonant frequency of 400 kHz with a rise time of about 1 μs to step changes in pressure and is capable of measuring pressure up to 25 MPa with a resolution of 0.5 kPa.

A gas bubble (i.e., an air bubble) was carefully placed on the surface of the pressure transducer by means of a syringe as shown in Fig. 2. Here L is taken as the distance between the origin of a shock wave and the solid wall. The collapse process of the gas bubble was observed by using an Imacon high speed camera (John Hadland Type 700). An Argon-ion laser equipped with a 1 msec opening duration mechanical shutter was used as a light source for the Imacon camera. Three kinds of a framing rate of 10^5 frames/s, 2×10^5 frames/s and 10^6 frames/s were used for photographing in this experiment. Output signals from the pressure transducer were displayed on an oscilloscope or an X-Y recorder through a transient recorder (Iwatsu DM 901). A discharge current appearing at the spark bubble initiation was used as trigger signals of photographing the bubbles and of measuring the pressure histories. The radius R_e of an equivalent sphere having the same volume of an attached gas bubble and the center of gravity l_C of the gas bubble measured from the solid wall were

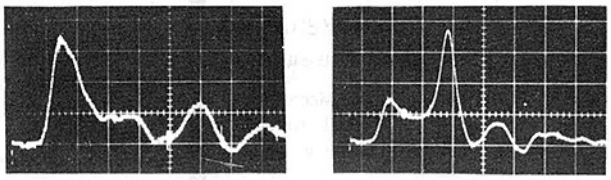

Fig. 3 Oscilloscope trace of the impact wall pressure ($V_C = 6.0$ kV, $L = 5.0$ mm)
(a) Without a gas bubble
(b) With a gas bubble ($R_e = 0.6$ mm, $lc/R_e = 0.70$)

Nomenclature

C_∞ = sound velocity of liquid
D = base diameter of a gas bubble attached to a solid wall
D_0 = initial value of D
D^* = D/D_0
F_t = impulse
H = height of an attached gas bubble
H_0 = initial value of H
H_v = height of a spark bubble (see Fig. 2)
H^* = H/H_0
H_v^* = H_v/L
l_C = center of gravity of a gas bubble measured from a solid wall
L = distance from an origin of a shock wave to a solid wall
p_0 = initial pressure inside a gas bubble
$p_{G,\max}$ = maximum impact wall pressure
$p_{r=R}$ = pressure at bubble wall
p_s = peak pressure of a shock wave
$p_{s,a}$ = peak pressure of a shock wave through a gas bubble
$p_{\infty,0}$ = pressure in liquid at infinity
$p_\infty(t)$ = ambient pressure around a gas bubble
R = bubble radius
R_e = equivalent bubble radius
$R_{v,0}$ = spark bubble radius without a gas bubble
$R_{v,0}^*$ = $R_{v,0}/L$
S = position of a gas bubble
t = time
T_C = Rayleigh's collapse time
$T_{C,G}$ = collapse time of an attached gas bubble
$T_{C,G\infty}$ = collapse time of a gas bubble far from a solid wall
V_C = charging voltage
w = pulse width of an impact wall pressure
w_s = pulse width of a shock wave received on a solid wall
γ = polytropic index
θ = angle
Θ = $\tan^{-1}(S/L)$
ρ_∞ = liquid density at infinity
σ = surface tension of liquid

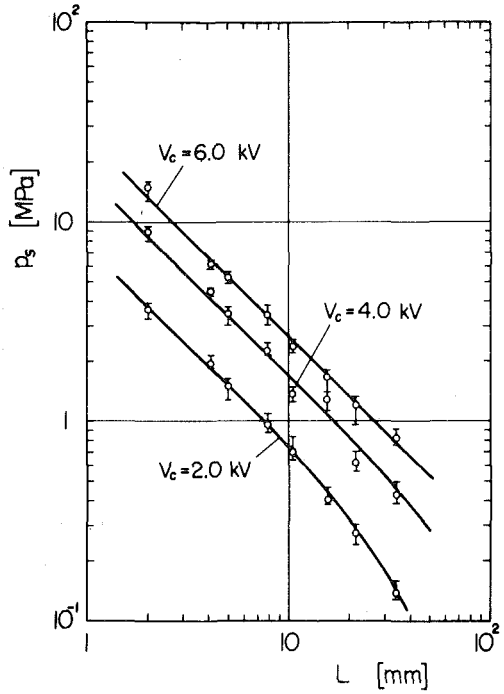

Fig. 4 Variation of the peak pressure of a shock wave p_s with the distance L

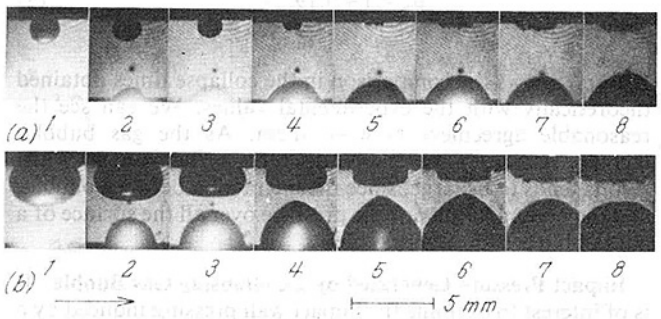

Fig. 5 Collapse of an attached gas bubble by a shock wave (V_C = 6.0 kV, L = 5.0 mm, $S \simeq 0$)
(a) R_e = 0.9 mm, l_C/R_e = 0.71; 2×10^5 frames/s, frame interval 5 μs, exposure 1 μs/frame
(b) R_e = 1.9 mm, l_C/R_e = 0.56; 10^5 frames/s, frame interval 10 μs, exposure 2 μs/frame

numerically determined by measuring points on the bubble surface from a stationary bubble photograph and assuming the gas bubble to be axial symmetry.

Figures 3(*a*) and (*b*) show examples of the pressure trace received on the solid wall without and with a gas bubble. In the case without a gas bubble, the peak pressure and the pulse width are defined as p_s and w_s, respectively. Figure 4 shows the variation of p_s with L for various values of V_C. It is clearly seen that p_s is inversely proportional to distance L for each charging voltage V_C. This fact indicates that the shock wave spherically propagates in water. The shock wave velocity was measured as 1460 m/s.

Results and Discussion

The study is focussed at first on the $S \simeq 0$ case where a gas bubble situates on almost the center of the pressure transducer and a shock wave impinges on the top side of the bubble surface from the direction of the axis of symmetry of the bubble. Secondly the experiment is advanced to the $S \neq 0$ case and the influence of the position of a gas bubble S on the impact wall pressure is investigated.

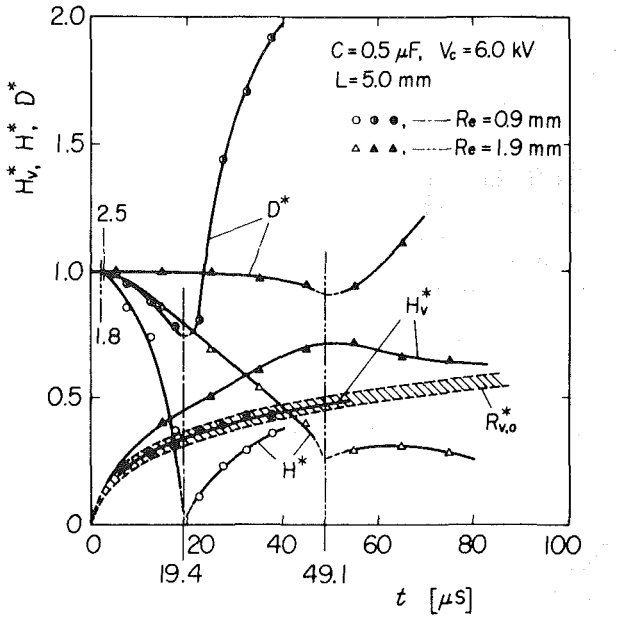

Fig. 6 Variations of nondimensional quantities for both a gas bubble and a spark bubble with time corresponding to Figs. 5(*a*) and (*b*)

Collapse of Attached Gas Bubbles by Shock Waves and Interaction of Gas Bubbles With Spark Bubbles. Figures 5(*a*) and (*b*) show typical photographs of the interaction between bubbles for $V_C = 6.0\,kV$ and $L = 5$ mm. The framing rate of 2×10^5 frames/s is used for Fig. 5(*a*) where $R_e = 0.9$ mm, $l_C/R_e = 0.71$ and that of 10^5 frames/s used for Fig. 5(*b*) where $R_e = 1.9$ mm, $l_C/R_e = 0.56$. The solid wall can be seen at the top of each frame, and gas bubbles are attaching to that wall due to the buoyancy. Figure 5(*a*) shows the case where the interaction between bubbles is small, so the gas bubble is intensively collapsing. The collapse time of this bubble with $R_e = 0.9$ mm was measured as $T_{C,G} = 16.9$ μs. Therefore, it is immediately understood that the collapse process of a gas bubble by a shock wave is very intensive, since in general the collapse time of a spherical bubble with radius of 1 mm is about 100 μs under the stepwise change in pressure of 0.1 MPa. At the final stage of the bubble collapse, the radial velocity at the base of the gas bubble attains to the value of about 30 m/s, while the collapsing velocity at the top side of its bubble is extremely rapid and exceeds 200 m/s. The formation of a liquid jet during the bubble collapse can be conjectured from the observation of a counterjet which is detected in sixth frame in Fig. 5(*a*). Therefore the latter value should be much larger than that estimated here, because the liquid jet is accelerated. By the way, Plesset and Chapman [21] calculated a maximum jet velocity of 130 m/s in the case where an initially spherical vapor cavity in contact with a solid boundary collapsed under the stepwise change in pressure of 0.1 MPa.

On the other hand, Fig. 5(*b*) shows the case where the interaction between bubbles becomes significant. The collapse time of the gas bubble with $R_e = 1.9$ mm was measured as $T_{C,G} = 47.3$ μs which was longer than that for $R_e = 0.9$ mm due to the interaction between bubbles. From this figure it can be seen that the surface of the spark bubble closest to the solid wall is attracted along the flowing of the liquid jet which is formed during the collapse of the gas bubble, then it tends to flatten during the rebound of the gas bubble. In both cases of Figs. 5(*a*) and (*b*), it is clearly seen that the radial flows at the bases of the gas bubbles rapidly spread outward after the rebound. Figure 6 shows the variations of nondimensional quantities for both the gas and spark bubbles with time corresponding to Figs. 5(*a*) and (*b*). In this figure the non-

dimensional radii of spark bubbles without gas bubbles, $R^*_{v,0}(=R_{v,0}/L)$, are indicated by hatching with including five trials. For $R_e = 0.9$ mm the interaction between bubbles is so weak that H^*_v lies in the range of $R^*_{v,0}$. On the contrary, for $R_e = 1.9$ mm, H^*_v deviates from $R^*_{v,0}$ at the initial stage of the collapse due to the attractive effect between them. Two groups of values in pairs are also seen in the figure. A pair of earlier times corresponds to the arriving times of shock waves from sources to gas bubbles and another pair of later times corresponds to the collapse times of gas bubbles measured from spark initiations, and chained lines with one dot and with two dots indicate for the cases of $R_e = 0.9$ mm and $R_e = 1.9$ mm, respectively.

Collapse Times of Gas Bubbles Attached to a Solid Wall by Shock Waves. As mentioned in the preceding section, the collapse of a bubble by a shock wave is so intensive that the collapse time of it will become shorter.

For the case of the stepwise change in pressure ($p_{\infty,0} \rightarrow p_\infty$, $\Delta p = p_\infty - p_{\infty,0}$ = const.), in general, the collapse time of a spherical bubble with radius of R_e far from a solid wall, T_C, is given by Rayleigh [16] as follows:

$$T_C = 0.915 R_e \sqrt{\frac{\rho_\infty}{\Delta p}} \tag{1}$$

This relation is fulfilled also for a rectangular pressure wave with a pulse duration of t_s as long as the condition of $t_s > T_C$ is satisfied. A shock wave, however, has a very short pulse duration in general, say $t_s << T_C$. Therefore the collapse time of a bubble far from a solid wall by a shock wave always satisfies the relation of $T_{C,G\infty} > T_C$.

We now consider the theoretical treatment. Assuming that the pressure change surrounding the bubble is uniform over all the bubble surface, the collapse time $T_{C,G\infty}$ can be determined from the following equation [18].

$$R\ddot{R}\left(1-\frac{2\dot{R}}{C_\infty}\right)+\frac{3}{2}\dot{R}^2\left(1-\frac{4\dot{R}}{3C_\infty}\right)+\frac{1}{\rho_\infty}\left\{p_\infty(t)-p_{r=R}+\frac{R}{C_\infty}(\dot{p}_\infty-\dot{p}_{r=R})\right\}=0 \tag{2}$$

where

$$p_{r=R}=p_0\left(\frac{R_e}{R}\right)^{3\gamma}-\frac{2\sigma}{R} \tag{3}$$

In the above expression, R is the bubble radius, R_e the initial bubble radius, γ the polytropic index, σ the surface tension of the liquid, $p_0(=p_{\infty,0}+2\sigma/R_e)$ the initial pressure inside the bubble, and C_∞, ρ_∞ and $p_{\infty,0}$ are the sound velocity, the density and the pressure in the liquid at infinity, respectively. The pressure change resulted from a shock wave is introduced into the pressure term $p_\infty(t)$ in equation (2). In numerical calculations the time dependence of the shock pressure was approximated by a rectangular or triangular impulse by using the impulse of shock pressure $F_i(=\int_0^t p dt)$ obtained experimentally. On the other hand, in the case of the presence of boundaries like a solid wall and a free surface, the motion of a bubble is strongly affected by these boundaries, for example, the collapse time of a bubble near a solid wall becomes longer. As for this matter there are some theoretical studies such as obtained by Rattray [17] using a perturbation method and Sato and Shima [28] using a variational method in which the surface tension is included. Consequently, it was confirmed that the effect of a solid wall on the collapse time was sufficiently satisfied by a linear equation with R_e/l_C in the range of $0 \leqq R_e/l_C \leqq 1$ [30]. Supposing the previous relation to be extrapolated for $R_e/l_C > 1$, and using it as a correcting factor about the effect of the solid wall, we finally obtain the collapse time as follows:

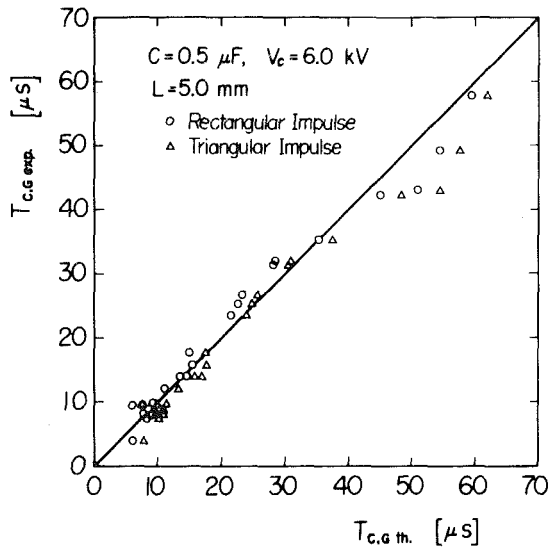

Fig. 7 Comparison between the theory and the experiment with respect to $T_{C,G}$ ($V_C = 6.0$ kV, $L = 5.0$ mm)
o Rectangular impulse,
Δ Triangular impulse

$$T_{C,Gth}=\psi_w T_{C,G\infty} \tag{4}$$

where

$$\psi_w = 1+0.19\frac{R_e}{l_C} \tag{5}$$

Figure 7 shows the comparison in the collapse times obtained theoretically with the experimental values. We can see the reasonable agreement between them. As the gas bubbles increase in size, however, the discrepancy between both the results tends to be large, since the interaction between bubbles and the nonuniformity of the pressure over all the surface of a gas bubble become remarkable.

Impact Pressure Generated by a Collapsing Gas Bubble. It is of interest to examine the impact wall pressure induced by a collapsing gas bubble in connection with the cavitation damage.

As seen in Fig. 3(*b*), in general, two peaks appear in the impact wall pressure history in the presence of a gas bubble. The first peak pressure is contributed from a shock wave through an attached gas bubble and the second one contributed from a collapsing gas bubble, which are defined as $p_{s,a}$ and $p_{G,\max}$, respectively.

The variations of $p_{G,\max}/p_s$ and $p_{s,a}/p_s$ for various equivalent radii R_e are shown in Fig. 8. Here p_s is the peak pressure of a shock wave received on the solid wall without a gas bubble, and three cases for p_s are discussed in the figure, that is, $p_s = 5.26$ MPa ($V_C = 6$ kV), 2.34 MPa ($V_C = 3$ kV) and 1.44 MPa ($V_C = 2$ kV). If $p_{G,\max} < p_s$, a gas bubble seems to be energy absorber from a shock wave, while if $p_{G,\max} > p_s$, one to be source of more intensive impact pressure. From the figure, we can readily see the existence of the region for $p_{G,\max} > p_s$.

The tendency of $p_{G,\max}$ curve is strongly depending upon the peak pressure of shock wave as well as the size of gas bubble. In the case where the shock wave has a relatively small peak pressure, no intensive compression of the gas inside the bubble occurs due to the small amount of energy transferred to the gas bubble. When p_s is smaller, there is a region where $p_{G,\max}$ is smaller than p_s for all R_e. On the contrary, when p_s is larger, $p_{G,\max} - R_e$ curve has a maximum at a certain point of R_e. This means that $p_{G,\max}$ decreases with decreasing R_e for smaller gas bubbles than those

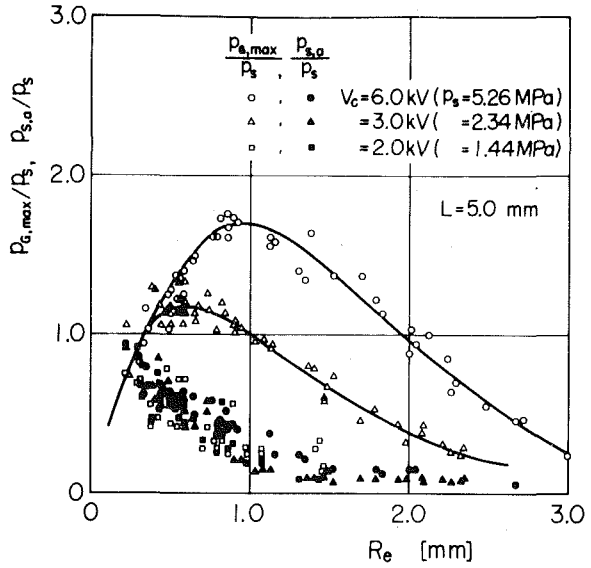

Fig. 8 Variations of the maximum impact wall pressure $p_{G,max}/p_s$ and the first peak pressure $p_{s,a}/p_s$ with the equivalent radii R_e (L = 5.0 mm) ○, △, □ $p_{G,max}/p_s$; ●, ▲, ■ $p_{s,a}/p_s$; ○, ● V_C = 6.0 kV(p_s = 5.26 MPa); △, ▲ V_C = 3.0 kV(p_s = 2.34 MPa); □, ■ V_C = 2.0 kV(p_s = 1.44 MPa)

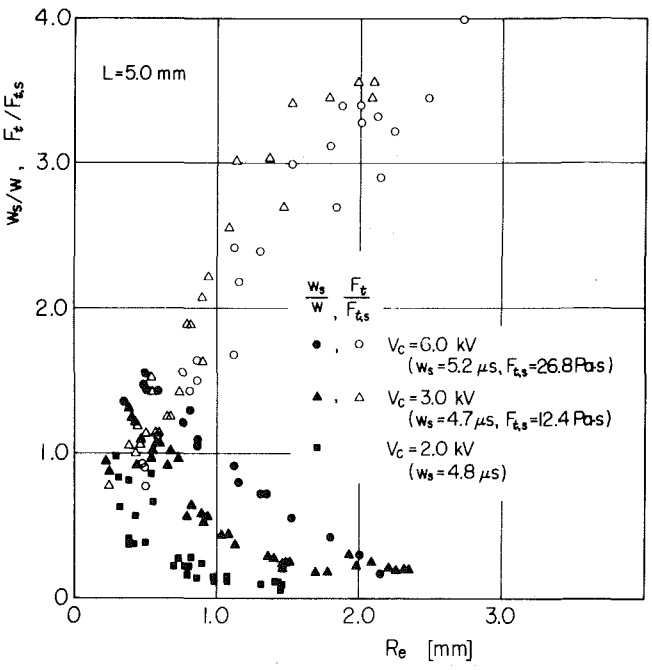

Fig. 9 Variations of the nondimensional pulse width w_s/w and the nondimensional impulse $F_t/F_{t,s}$ with the equivalent radii R_e (L = 5.0 mm)

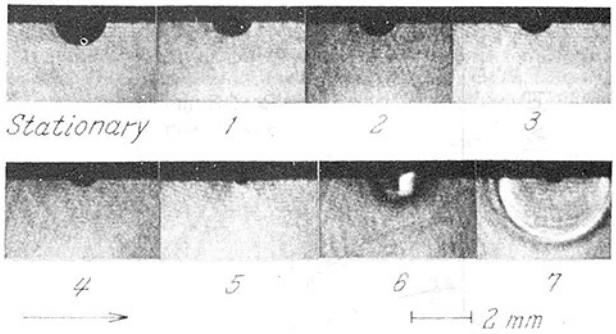

Fig. 10 Shock wave generated at the instant of the rebound of a gas bubble (V_C = 7.0 kV, L = 5.0 mm, R_e = 0.6 mm, l_C/R_e = 0.45; 10^6 frames/s, frame interval 1 μs, exposure 0.2 μs/frame)

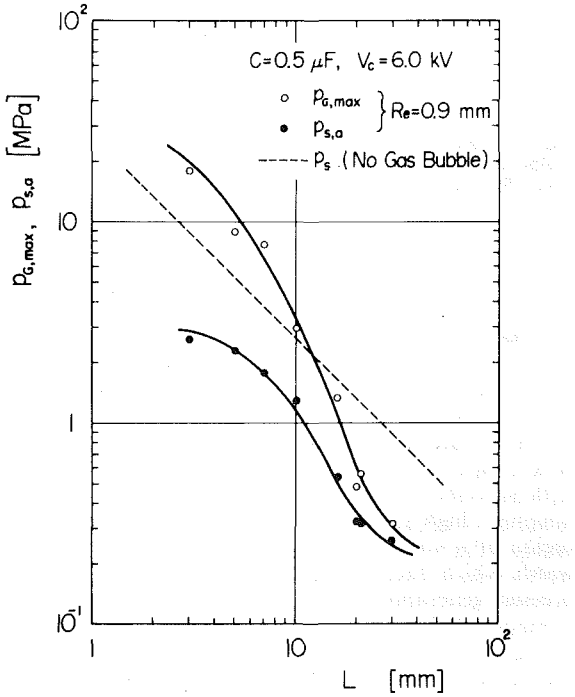

Fig. 11 Variation of the maximum impact wall pressure $p_{G,max}$ with the distance L (V_C = 6.0 kV, R_e = 0.9 mm)
○ $p_{G,max}$, ● $p_{s,a}$
------ p_s (without gas bubble)

corresponding to the maximum of $p_{G,\max}$. However, it is well-known that for the bubble collapse in water under the same conditions the peak pressure produced at the bubble surface increases with decreasing the bubble radius because of the effect of surface tension [23, 24, 29]. The difference between the result in Fig. 8 and the well-known fact is to be resulted from the following. In the present study the distance L and the shock strength p_s are kept with constants in order to examine the effect of the existence of a gas bubble on $p_{G,\max}$. Since the height of an attached gas bubble, H, is proportional to the bubble size R_e, the shock pressure just arriving on the surface of the gas bubble decreases with decreasing R_e. Of course the fact is no doubt that the impact wall pressure measured here will be underestimated compared with the real value of it in particular when the bubble becomes smaller in size. In the same figure, further, it is found that when R_e approaches to zero, $p_{s,a}$ is asymptotic to the shock pressure, i.e., p_s, and that $p_{s,a}$ is monotonously decreasing, independent of p_s with increasing R_e. This experimental evidence indicates that the energy absorbed by the gas bubble increases with bubble-size increase and this is obviously seen from Fig. 9.

Figure 9 shows the impulse $F_t/F_{t,s}$ which increases monotonously with increasing R_e. In the same figure, the nondimensional pulse width of the impact wall pressure, i.e., w_s/w, is also plotted. The pulse width of $p_{G,max}$ at the maximum almost corresponds with one of the shock pressure received on the solid wall without a gas bubble, that is $w_s/w \simeq 1$. For smaller gas bubbles than those corresponding to the maximum of $p_{G,\max}$, the relation of $w < w_s$ is satisfied and vice versa. In the region $w > w_s$ where the interaction between bubbles becomes significant in proportion to increasing R_e, the liquid jet should be predominant in generating the impact

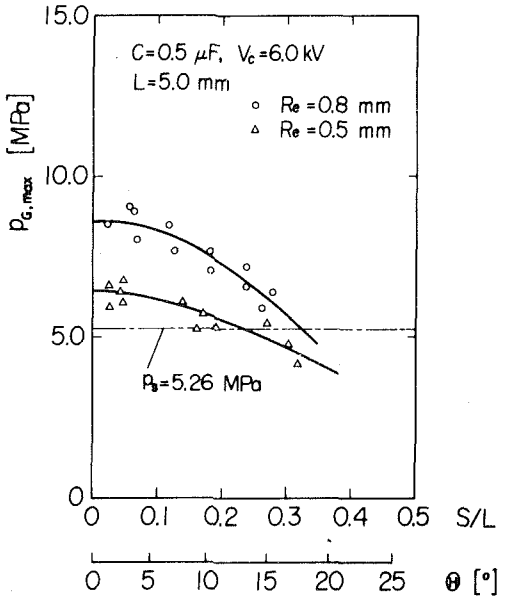

Fig. 12 Variation of the maximum impact wall pressure $p_{G,max}$ with the position of a gas bubble S/L ($V_C = 6.0$ kV, $L = 5.0$ mm) ○ $R_e = 0.8$ mm, △ $R_e = 0.5$ mm, ——— $p_s = 5.26$ MPa

wall pressure. On the other hand, a sharp pressure pulse occurs in the region of $w < w_s$. In this region we could frequently photograph a shock wave generated at the rebound of an attached gas bubble. An example of photographing a shock wave is shown in Fig. 10. However in the same region a counterjet is also observed during the rebound. The existence of this counterjet demonstrates the formation of a liquid jet. It is shown in references [31, 32] that a sharp pressure pulse with very short duration appeared on the solid wall by impinging a high speed liquid jet. In view of these facts in the region of $w < w_s$, it is difficult to judge from only the pulse width which factors are the sources for the impact wall pressure generation.

Figure 11 shows the variation of $p_{G,\max}$ with the distance L for $R_e = 0.9$ mm, in which a broken line represents a locus of the average values of p_s for variable L. It is clearly seen that $p_{G,\max} - L$ curve intersects with $p_s - L$ curve at a certain point of L. When L is smaller than this point, a gas bubble acts as the source of more intensive impact pressure than the shock pressure p_s, while in the case of L apart from this point, it acts as the energy absorber from a shock wave.

Next the case for $S \neq 0$ is discussed. In this case a gas bubble contracts with a part of its surface being flattened in the shock direction, i.e., $\Theta = \tan^{-1}(S/L)$. Therefore an oblique liquid jet may be formed at the final stage of the bubble collapse. In fact Singer and Harvey [33] performed an experiment on the cavitation damage of plasticine specimens by using an ultrasonic vibrator, and observed an interesting experimental evidence such that the axis of some of pits was as much as 35 deg from the vertical.

Figure 12 shows the variation of $p_{G,\max}$ with S/L (or Θ). As a gas bubble situates apart from the original point, $p_{G,\max}$ decreases smaller than that in $S \simeq 0$ case due to the decrease of p_s according as the increase of the propagating distance of shock wave to the surface of the gas bubble. Further, $p_{G,\max}$ decreases as the angle Θ becomes larger, since an effective value to the solid wall is measured as the vertical component of it. It should be mentioned here that the pressure transducer used in the present experiment has a diameter of 5.55 mm which is fairly larger than the size of a minimum gas bubble. A real value of a maximum impact wall pressure released from the shock wave and/or the liquid jet during the bubble collapse should be larger than the one measured here. This is more so as the bubble becomes smaller, since the measured value is one averaged over the diameter of the pressure transducer.

Conclusions

In order to clarify the collapse process of a gas bubble attached to a solid wall by a shock wave and the mechanism of its induced impact wall pressure generation, a detailed experiment was performed by means of the photographing with a high speed camera and the pressure measurement. The results obtained here are summarized as follows:

1. The impact wall pressure generated by a collapsing gas bubble attached to the solid wall is strongly dependent on the bubble size, the shock strength and the distance from the origin of shock wave to the gas bubble. A gas bubble acts as either the energy absorber from a shock wave or the source of more intensive impact wall pressure than one generated by a shock wave directly impinging on the solid wall without a gas bubble according to the factors mentioned above.
2. The collapse process of a gas bubble by a shock wave is very intensive and the collapsing velocity at the top side of its bubble is extremely rapid with exceeding of 200 m/s.
3. In the region where the significant interaction between a spark bubble and an attached gas bubble occurs, the source of the impact wall pressure is predominantly contributed from a liquid jet, whereas in the region where the interaction is weaker, both a shock wave and a counterjet are observed.
4. The theoretical result with respect to the collapse time of a gas bubble attached to the solid wall by a shock wave coincides with the experimental result obtained here satisfactorily.
5. When a shock wave impinges on the surface of a gas bubble from different direction with the axis of symmetry of the bubble, an oblique liquid jet developing in the direction of the impinging shock may be formed.

Experimental Uncertainty

Each open circle shown in Fig. 4 is averaged value with ten data. The length data shown in Fig. 6 are measured from the photographs which have an uncertainty of ±2 percent except at the final stage of the bubble collapse with that of ±6 percent. The experimental values comparing with the theoretical values in Fig. 7 have the uncertainty of ±2 percent. The uncertainty in the data presented in Figs. 8, 9, and 11 are ±6 percent, whereas the data in Fig. 12 have the uncertainty of ±10 percent.

Acknowledgments

Finally, authors would like to express their thanks to the late Professor Emeritus F. Numachi of Tohoku University for his encouragement throughout the course of the present study. They are also thankful to Assistant Professor K. Takayama of Tohoku University for his helpful suggestions in this works. Assistances received from Mr. N. Miura, Mrs. Y. Ohoka, Miss M. Sekii and also the members of Factory of the Institute of High Speed Mechanics, Tohoku University are acknowledged with thanks. The present project was financially supported by Science and Research Grant in Aid offered by Ministry of Education in 1980 and 1981.

References

1 Harrison, M., "An Experimental Study of Single Bubble Cavitation Noise," *Journal of Acoustical Society of America*, Vol. 24, Nov. 1952, pp. 776–782.

2 Mellen, R. H., "An Experimental Study of the Collapse of a Spherical Cavity in Water," *Journal of Acoustical Society of America*, Vol. 28, May 1956, pp. 447–457.

3 Jones, I. R., and Edwards, D. H., "An Experimental Study of the Forces Generated by the Collapse of Transient Cavities in Water," *Journal of Fluid Mechanics*, Vol. 7, Part 4, Apr. 1960, pp. 596–609.

4 Naudé, C. F., and Ellis, A. T., "On the Mechanism of Cavitation Damage by Nonhemispherical Cavities Collapsing in Contact with a Solid Boundary," ASME *Journal of Basic Engineering*, Vol. 83, No. 4, Dec. 1961, pp. 648–656.

5 Shutler, N. D., and Mesler, R. B., "A Photographic Study of the Dynamics and Damage Capabilities of Bubbles Collapsing Near Solid Boundaries," ASME *Journal of Basic Engineering*, Vol. 87, No. 3, Sept. 1965, pp. 648–656.

6 Ellis, A. T., "On Jets and Shock Waves from Cavitation," *Proceedings of Sixth Symposium on Naval Hydrodynamics*, Washington, 1966, pp. 137–161.

7 Brunton, J. H., Wilson, M. P. W., and Camus, J. J., "The High-Speed Photography of Liquid Flow in Collapsing Cavities and Impinging Liquid Drops," *Proceedings of the 8th International Congress on High-Speed Photography*, Stockholm, 1968, pp. 467–470.

8 Lauterborn, W., "High-Speed Photography of Laser-Induced Breakdown in Liquids" *Applied Physics Letters*, Vol. 21, No. 1, July 1972, pp. 27–29.

9 Kling, C. L., and Hammitt, F. G., "A Photographic Study of Spark-Induced Cavitation Bubble Collapse," ASME *Journal of Basic Engineering*, Vol. 94, No. 4, Dec. 1972, pp. 825–833.

10 Smith, R. H., and Mesler, R. B., "A Photographic Study of the Effect of an Air Bubble on the Growth and Collapse of a Vapor Bubble Near a Surface," ASME *Journal of Basic Engineering*, Vol. 94, No. 4, Dec. 1972, pp. 933–942.

11 Lauterborn, W., and Bolle, H., "Experimental Investigations of Cavitation Bubble Collapse in Neighbourhood of a Solid Boundary," *Journal of Fluid Mechanics*, Vol. 72, Part 2, Nov. 1975, pp. 391–399.

12 Chahine, G. L., "Interaction between an Oscillating Bubble and a Free Surface," ASME JOURNAL OF FLUIDS ENGINEERING, Vol. 99, No. 4, Dec. 1977, pp. 709–716.

13 Fujikawa, S., and Akamatsu, T., "Experimental Investigations of Cavitation Bubble Collapse by a Water Shock Tube," *Bulletin of the JSME*, Vol. 21, No. 152, Feb. 1978, pp. 223–230.

14 Fujikawa, S., and Akamatsu, T., "Effects of the Non-Equilibrium Condensation of Vapour on the Pressure Wave Produced by the Collapse of a Bubble in a Liquid," *Journal of Fluid Mechanics*, Vol. 97, Part 3, Apr. 1980, pp. 481–512.

15 Shima, A., Takayama, K., Tomita, Y., and Miura, N., "An Experimental Study on Effects of a Solid Wall on the Motion of Bubble and Shock Waves in Bubble Collapse," *Acustica*, Vol. 48, No. 5, 1981, pp. 293–301.

16 Rayleigh, Lord., "On the Pressure Developed in a Liquid During the Collapse of a Spherical Cavity," *Philosophical Magazine*, Vol. 34, 1917, pp. 94–98.

17 Rattray, M., Jr., "Perturbation Effects in Cavitation Bubble Dynamics," California Institute of Technology, Ph.D. thesis, 1951.

18 Trilling, L., "The Collapse and Rebound of a Gas Bubble," *Journal of Applied Physics*, Vol. 23, No. 1, Jan. 1952, pp. 14–17.

19 Shima, A., "The Behavior of a Spherical Bubble in the Vicinity of a Solid Wall," ASME *Journal of Basic Engineering*, Vol. 90, No. 1, Mar. 1968, pp. 75–89.

20 Tulin, M. P., "On the Creation of Ultra-Jets," L. I. Sedov 60th Anniversary Volume, Problems of Hydrodynamics and Continuum Mechanics, Moscow, 1969, pp. 725–747.

21 Plesset, M. S., and Chapman, R. B., "Collapse of an Initially Spherical Vapour Cavity in the Neighbourhood of a Solid Boundary," *Journal of Fluid Mechanics*, Vol. 47, Part 2, May 1971, pp. 283–290.

22 Mitchell, T. M., and Hammitt, F. G., "Asymmetric Cavitation Bubble Collapse," ASME *Journal of Basic Engineering*, Vol. 95, No. 1, Mar. 1973, pp. 29–37.

23 Shima, A., and Tomita, Y., "On the Impulse Pressure Accompanying Spherical Bubble Collapse in Liquids," Reports of the Institute of High Speed Mechanics, Tohoku University, Vol. 31, No. 281, 1975, pp. 97–135.

24 Tomita, Y., and Shima, A., "On the Behavior of a Spherical Bubble and the Impulse Pressure in a Viscous Compressible Liquid," *Bulletin of the JSME*, Vol. 20, No. 149, Nov. 1977, pp. 1453–1460.

25 Shima, A., and Nakajima, K., "The Collapse of a Non-Hemispherical Bubble Attached to a Solid Wall," *Journal of Fluid Mechanics*, Vol. 80, Part 2, Apr. 1977, pp. 369–391.

26 Tomita, Y., and Shima, A., "The Effect of Heat Transfer on the Behavior of a Bubble and the Impulse Pressure in a Viscous Compressible Liquid," *ZAMM*, Bd. 59, Heft 7, Juli 1979, S. 297–306.

27 Shima, A., and Sato, Y., "The Collapse of a Bubble Attached to a Solid Wall," Ingenieur-Archiv, Bd. 48, Heft 2, 1979, S. 85–95.

28 Sato, Y., and Shima, A., "The Collapse of an Initially Spherical Bubble Near a Solid Wall," Reports of the Institute of High Speed Mechanics, Tohoku University, Vol. 42, No. 325, 1980, pp. 1–24.

29 Fujikawa, S., and Akamatsu, T., "On the Mechanisms of Cavitation Bubble Collapse," *Proceedings of the 10th IAHR Symposium*, Tokyo, Vol. 1, 1980, pp. 91–102.

30 Shima, A., and Tomita, Y., "The Behavior of a Spherical Bubble Near a Solid Wall in a Compressible Liquid," Ingenieur-Archiv, Bd. 51, Heft 3/4, 1981, S. 243–255.

31 Bowden, F. P., and Brunton, J. H., "The Deformation of Solids by Liquid Impact at Supersonic Speeds," *Proceedings of the Royal Society of London*, Series A, Vol. 263, No. 1315, Oct. 1961, pp. 433–450.

32 Hancox, N. L., and Brunton, J. H., "The Physics of Impact and Deformation: Multiple Impact, The Erosion of Solids by the Repeated Impact of Liquid Drops," *Philosophical Transactions of the Royal Society of London*, Series A, Vol. 260, 1966, pp. 121–139.

33 Singer, B. G., and Harvey, S. J., "Cavitation Damage Studies Using Plasticine," *International Journal of Mechanical Science*, Vol. 21, 1979, pp. 409–416.

3 Jones, I. R., and Edwards, D. H., "An Experimental Study of the Forces Generated by the Collapse of Transient Cavities in Water," *Journal of Fluid Mechanics*, Vol. 7, Part 4, Apr. 1960, pp. 596–609.

4 Naudé, C. F., and Ellis, A. T., "On the Mechanism of Cavitation Damage by Nonhemispherical Cavities Collapsing in Contact with a Solid Boundary," ASME *Journal of Basic Engineering*, Vol. 83, No. 4, Dec. 1961, pp. 648–656.

5 Shutler, N. D., and Mesler, R. B., "A Photographic Study of the Dynamics and Damage Capabilities of Bubbles Collapsing Near Solid Boundaries," ASME *Journal of Basic Engineering*, Vol. 87, No. 3, Sept. 1965, pp. 648–656.

6 Ellis, A. T., "On Jets and Shock Waves from Cavitation," *Proceedings of Sixth Symposium on Naval Hydrodynamics*, Washington, 1966, pp. 137–161.

7 Brunton, J. H., Wilson, M. P. W., and Camus, J. J., "The High-Speed Photography of Liquid Flow in Collapsing Cavities and Impinging Liquid Drops," *Proceedings of the 8th International Congress on High-Speed Photography*, Stockholm, 1968, pp. 467–470.

8 Lauterborn, W., "High-Speed Photography of Laser-Induced Breakdown in Liquids" *Applied Physics Letters*, Vol. 21, No. 1, July 1972, pp. 27–29.

9 Kling, C. L., and Hammitt, F. G., "A Photographic Study of Spark-Induced Cavitation Bubble Collapse," ASME *Journal of Basic Engineering*, Vol. 94, No. 4, Dec. 1972, pp. 825–833.

10 Smith, R. H., and Mesler, R. B., "A Photographic Study of the Effect of an Air Bubble on the Growth and Collapse of a Vapor Bubble Near a Surface," ASME *Journal of Basic Engineering*, Vol. 94, No. 4, Dec. 1972, pp. 933–942.

11 Lauterborn, W., and Bolle, H., "Experimental Investigations of Cavitation Bubble Collapse in Neighbourhood of a Solid Boundary," *Journal of Fluid Mechanics*, Vol. 72, Part 2, Nov. 1975, pp. 391–399.

12 Chahine, G. L., "Interaction between an Oscillating Bubble and a Free Surface," ASME JOURNAL OF FLUIDS ENGINEERING, Vol. 99, No. 4, Dec. 1977, pp. 709–716.

13 Fujikawa, S., and Akamatsu, T., "Experimental Investigations of Cavitation Bubble Collapse by a Water Shock Tube," *Bulletin of the JSME*, Vol. 21, No. 152, Feb. 1978, pp. 223–230.

14 Fujikawa, S., and Akamatsu, T., "Effects of the Non-Equilibrium Condensation of Vapour on the Pressure Wave Produced by the Collapse of a Bubble in a Liquid," *Journal of Fluid Mechanics*, Vol. 97, Part 3, Apr. 1980, pp. 481–512.

15 Shima, A., Takayama, K., Tomita, Y., and Miura, N., "An Experimental Study on Effects of a Solid Wall on the Motion of Bubble and Shock Waves in Bubble Collapse," *Acustica*, Vol. 48, No. 5, 1981, pp. 293–301.

16 Rayleigh, Lord., "On the Pressure Developed in a Liquid During the Collapse of a Spherical Cavity," *Philosophical Magazine*, Vol. 34, 1917, pp. 94–98.

17 Rattray, M., Jr., "Perturbation Effects in Cavitation Bubble Dynamics," California Institute of Technology, Ph.D. thesis, 1951.

18 Trilling, L., "The Collapse and Rebound of a Gas Bubble," *Journal of Applied Physics*, Vol. 23, No. 1, Jan. 1952, pp. 14–17.

19 Shima, A., "The Behavior of a Spherical Bubble in the Vicinity of a Solid Wall," ASME *Journal of Basic Engineering*, Vol. 90, No. 1, Mar. 1968, pp. 75–89.

20 Tulin, M. P., "On the Creation of Ultra-Jets," L. I. Sedov 60th Anniversary Volume, Problems of Hydrodynamics and Continuum Mechanics, Moscow, 1969, pp. 725–747.

21 Plesset, M. S., and Chapman, R. B., "Collapse of an Initially Spherical Vapour Cavity in the Neighbourhood of a Solid Boundary," *Journal of Fluid Mechanics*, Vol. 47, Part 2, May 1971, pp. 283–290.

22 Mitchell, T. M., and Hammitt, F. G., "Asymmetric Cavitation Bubble Collapse," ASME *Journal of Basic Engineering*, Vol. 95, No. 1, Mar. 1973, pp. 29–37.

23 Shima, A., and Tomita, Y., "On the Impulse Pressure Accompanying Spherical Bubble Collapse in Liquids," Reports of the Institute of High Speed Mechanics, Tohoku University, Vol. 31, No. 281, 1975, pp. 97–135.

24 Tomita, Y., and Shima, A., "On the Behavior of a Spherical Bubble and the Impulse Pressure in a Viscous Compressible Liquid," *Bulletin of the JSME*, Vol. 20, No. 149, Nov. 1977, pp. 1453–1460.

25 Shima, A., and Nakajima, K., "The Collapse of a Non-Hemispherical Bubble Attached to a Solid Wall," *Journal of Fluid Mechanics*, Vol. 80, Part 2, Apr. 1977, pp. 369–391.

26 Tomita, Y., and Shima, A., "The Effect of Heat Transfer on the Behavior of a Bubble and the Impulse Pressure in a Viscous Compressible Liquid," *ZAMM*, Bd. 59, Heft 7, Juli 1979, S. 297–306.

27 Shima, A., and Sato, Y., "The Collapse of a Bubble Attached to a Solid Wall," Ingenieur-Archiv, Bd. 48, Heft 2, 1979, S. 85–95.

28 Sato, Y., and Shima, A., "The Collapse of an Initially Spherical Bubble Near a Solid Wall," Reports of the Institute of High Speed Mechanics, Tohoku University, Vol. 42, No. 325, 1980, pp. 1–24.

29 Fujikawa, S., and Akamatsu, T., "On the Mechanisms of Cavitation Bubble Collapse," *Proceedings of the 10th IAHR Symposium*, Tokyo, Vol. 1, 1980, pp. 91–102.

30 Shima, A., and Tomita, Y., "The Behavior of a Spherical Bubble Near a Solid Wall in a Compressible Liquid," Ingenieur-Archiv, Bd. 51, Heft 3/4, 1981, S. 243–255.

31 Bowden, F. P., and Brunton, J. H., "The Deformation of Solids by Liquid Impact at Supersonic Speeds," *Proceedings of the Royal Society of London*, Series A, Vol. 263, No. 1315, Oct. 1961, pp. 433–450.

32 Hancox, N. L., and Brunton, J. H., "The Physics of Impact and Deformation: Multiple Impact, The Erosion of Solids by the Repeated Impact of Liquid Drops," *Philosophical Transactions of the Royal Society of London*, Series A, Vol. 260, 1966, pp. 121–139.

33 Singer, B. G., and Harvey, S. J., "Cavitation Damage Studies Using Plasticine," *International Journal of Mechanical Science*, Vol. 21, 1979, pp. 409–416.

DISCUSSION

A. Prosperetti[1]

The authors are to be congratulated for reporting in this paper results of interest for their bearing on the mechanism of cavitation damage and bubble dynamics in general.

The shock wave which in a real flow situation is irradiated by collapsing bubbles is obtained here by means of a spark discharge and subsequent growth of a vapor bubble. This results in a good simulation of the real process if the parameters of the shock wave (notably its width and strength) are comparable in the two cases. Maybe the authors can comment on this point referring to their collapse shock results shown e.g. in Fig. 10.

I was also interested in the bubble-bubble interaction results shown in Fig. 5 in view of some numerical work based on potential flow which we did on the problem some time ago (L. Guerri, G. Lucca, and A. Prosperetti, "A Numerical Method for the Dynamics of Nonspherical Cavitation Bubbles," in *Proceedings of the Second International Colloquium on Drops and Bubbles*, Monterey, November 19–21, 1981, D. H. Le Croissette Ed., Jet Propulsion Laboratory Publication 82-7, pp. 175–181). The figure reproduced here shows some results for the case of axisymmetric collapse of one spherical and one hemispherical bubble attached to a solid wall (or, by reflection in the horizontal plane, of three equally spaced bubbles). Successive shapes of the bubbles are shown by thick lines, while the thin lines indicate particle paths. The situation is different from that of the paper because the bubbles begin to collapse at the same time. However these results show that the hemispherical bubble is impeded in its collapse by the neighbouring one and takes on an elongated shape qualitatively similar to that of the vapor bubble in the experiments (Fig. 5(*b*), frames 4-6). The numerical results also show that the time to collapse is affected by the presence of other bubbles, a factor which is not taken into account in the calculations of the paper. I would suggest that the discrepancy between calculated and measured collapse times for large R_e which can be seen in Fig. 7 is caused by the flow field of the spark-generated bubble. When the bubbles come close together (which, for the conditions of the experiment, implies large radii and greater collapse times) the interaction is not only due to the pressure wave but also to the actual flow field. Maybe some other effects depending on R_e reported in the paper are due to this factor.

Finally I would like to make a remark, and ask the authors' opinion, on the difficult question of shock waves versus microjets as agents of cavitation damage. The unambiguous identification of a shock wave irradiated by the bubble upon rebound and a failure to identify pressure pulses caused by the microjet does not necessarily demonstrate that cavitation damage is not to be imputed to the latter. If the action of the microjets is to cause very minute fractures of the surface of the solid, they could have such an effect without producing

[1] Istituto di Fisica, 20133 Milano, Italy.

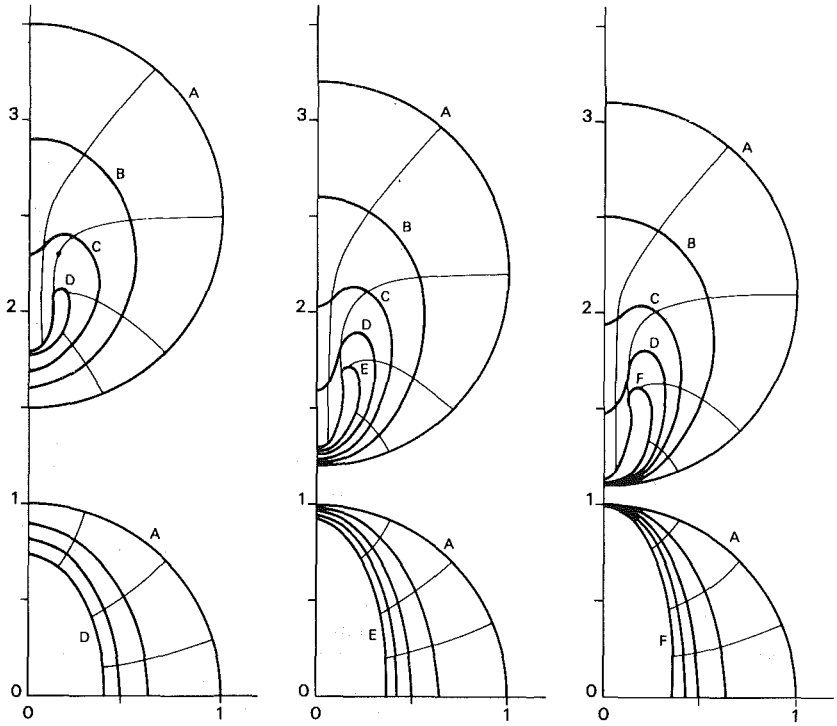

Fig. 12 Simultaneous axisymmetric collapse of one hemispherical and one spherical bubble in an inviscid incompressible liquid. The figures show successive bubble shapes (thick lines) and particle paths (thin lines). The initial distance between the bubble centers is, from left to right, 2.5, 2.2, and 2.1 initial radii. The shapes shown are for: *A*, $t = 0$; *b*, $t = 0.950$; *C*, $t = 1.063$; *D*, $t = 1.105$ (left and right), $t = 1.103$ (center); *E*, $t = 1.130$; *F*, $t = 1.135$. Distances are made dimensionless with respect to the initial radius R_0 and times with respect to $R_0\{\rho/(p_\infty - p_i)\}^{1/2}$, where ρ is the liquid density and p_∞ and p_i denote the ambient and internal pressure taken as constants.

notable pressures. It is possible that shock waves become effective in causing weight loss only after the surface has been exposed to "working" by the microjets? In this case both mechanisms would be important and, once more, the truth would be in the middle.

Authors' Closure

The authors wish to thank Professor Prosperetti for his useful discussions.

In the present experiment, shock waves with strength $p_s <$ about 5 MPa and pulse width $w_s \approx 5$ μs are used in order to study the sock wave-bubble interaction. These values were determined by referring to the experimental study on the ultrasonic cavitation [34] in which the shock amplitudes of about 5 MPa were measured at the position of 1 mm apart from the center of collapse by means of optical methods. By the way, parameters of the shock wave produced in Fig. 10 are measured as $p_{G,\max} = 10.4$ MPa and $w = 2.6$ μs. The peak pressure $p_{g,\max}$ will reduce to the value of about 3 MPa at $L =$ 5 mm along a $1/L$ decrease curve.

The authors are also thankful to Professor Prosperetti for his suggestion concerning the bubble-bubble interaction, and believe that the numerical results obtained by him and co-worker provide valuable addition to this paper. As a gas bubble increases in size, the interaction of it with a spark bubble becomes remarkable. This relation is shown in Fig. 13, where $\bar{R}_{v,0}$ indicates an averaged curve of five trials. It is clearly seen that when R_e increases, the discrepancy of H_v from $\bar{R}_{v,0}$ becomes larger. This means that a gas bubble will be affected by a spark bubble with increasing R_e. In general, there exists Bjerknes force between pulsating bubbles at a distance $2d$ apart. Two bubbles pulsating in phase attract each other, and bubbles pulsating 180 deg out of phase repel each other. These are mathematically equivalent to the motion of a bubble at a distance d from a solid wall for the former and from a free surface for the latter, respectively. The periods of collapse will be lengthened near a solid wall and shortened near a free surface. In our experiment the motions of two bubbles are 180 deg out of phase in the initial stage of their motions. As a result, the calculated collapse times would be overestimated than measured collapse times because the interaction of a gas bubble with a spark bubble is not taken

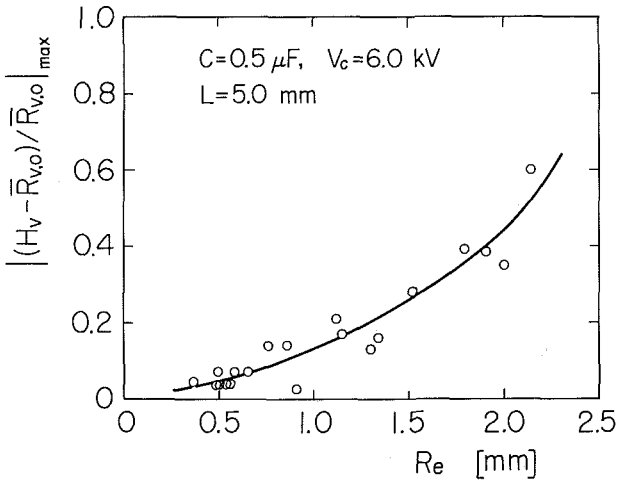

Fig. 13 Interaction between a gas bubble and a spark bubble

into account in our calculations, and thus the discrepancy between them becomes larger with increasing R_e.

Now the authors would make a remark on the mechanism of impact pressure generation. We do believe that three types of damage forces are possible, and basically agree with the discussor's opinion. They are resulted from a shock wave, from a liquid jet and from both a shock wave and a liquid jet. The induced impact wall pressure modes are fairly corresponding to the bubble collapse modes depending on L/R_{max}, where L is the distance between the electrodes and the solid wall and R_{max} a maximum bubble radius (see reference [35] for details).

Additional References

34 Hinsch, K., and Brinkmeyer, E., "Investigation of Very Short Cavitation Shock Waves by Coherent Optical Methods," *Proceedings of the Society of Photo-optical Instrumentation Engineers*, Vol. 97, 1977, pp. 166–171.

35 Shima, A., Takayama, K., Tomita, Y. and N. Ohsawa, "Mechanism of Impact Pressure Generation from Spark-Generated Bubble Collapse Near a Wall," *AIAA Journal*, Vol. 21, No. 1, Jan. 1983, pp. 55–59.

The Flow States of Liquid Through Two Series-Connected Diffusers Subject to Cavitation

J. R. Tippetts

G. H. Priestman

Department of Chemical Engineering and Fuel Technology, University of Sheffield, Sheffield, England

A "diffuser" is a venturi-like element with a well-formed contraction followed by a small-angle diffuser. When liquid flows through two diffusers connected in series various flow states are possible depending on whether or not cavitation occurs in the diffusers. It is shown that, in the absence of strong "Reynolds-number effects," one of just two possible sequences of flow states can occur for a particular pair of diffusers. Denoting the diffusers by "upstream" and "downstream," cavitation can occur as follows with increasing flow:

1. *Neither; upstream only; both.*
2. *Neither; downstream only (and upstream never).*

Once this classification is known it is easy to predict the characteristics of the circuit which can then be used to define an "equivalent single diffuser" to represent the pair of diffusers. Experimental data verifying the theory are included.

Introduction

If liquid flows through a converging and then gradually diverging channel (as shown in Fig. 1), like a metering venturi, the onset of cavitation greatly alters its pressure-drop ~ flow characteristics. The effect is strongest when the diverging section is designed to provide good pressure recovery. Cavitation limits the degree of recovery and results in an abrupt demarcation between the cavitating and noncavitating characteristics. The significance of cavitation in metering venturis is described in [1, 2, and 3]. Despite this complicating factor, it is not difficult to characterize flow through a single "diffuser" (as these elements will be called). Is it, however, more difficult to characterize the flow through two diffusers in series. Is it inevitable that both diffusers will cavitate when the flow is sufficiently large? If one diffuser cavitates, which is it, the upstream or the downstream diffuser? These are qualitative questions which are answered in this paper thereby facilitating the quantitative characterization of the two-diffuser system.

The results are of great practical importance in determining the operation of fluidic diodes (usually vortex diodes) because their forward (low resistance) state operation can be modelled as two series-connected diffusers.

Characteristics of a Single Diffuser

Under noncavitating conditions the pressure P_u upstream of a diffuser can be expressed in terms of the flow q and the downstream pressure P_d by

$$P_u = k\,q^2 + P_d \tag{1}$$

where k is a coefficient incorporating fluid and geometrical variables, and an overall noncavitating discharge coefficient C_n as follows:

$$k = 8\rho/\pi^2 C_n^2 d^4 \tag{2}$$

where d is the throat diameter. For a diffuser with good pressure recovery C_n would be between 2.5 and 3.

When cavitation occurs the pressure at the throat drops to the vapor pressure P_v and the flow becomes independent of the downstream pressure. The upstream pressure can be expressed by

$$P_u = j\,q^2 + P_v \tag{3}$$

where j is given by

$$j = 8\rho/\pi^2 C_c^2 d^4 \tag{4}$$

In this case the discharge coefficient C_c refers to flow accelerating to the throat of the diffuser and is expected to have a value similar to that of a good nozzle, i.e., circa .97.

The two characteristics are shown in Fig. 2. There is an abrupt change from one characteristic to the other at the onset

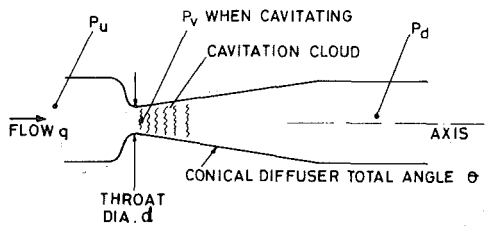

Fig. 1 Converging-diverging duct referred to as a "diffuser"

Contributed by the Fluids Engineering Division and presented at the ASME Applied Mechanics, Bioengineering, and Fluids Engineering Conference, Houston, Texas, June 20-22, 1983. Manuscript received by the Fluids Engineering Division, May 10, 1982. Paper No. 82-FE-4.

of cavitation. The sudden increase in resistance is because increasing the flow beyond the cavitation point ceases to be accompanied by increased pressure recovery.

Explicit Characterization of a Single Diffuser. The operating state of a single diffuser can easily be found:

1) Given the flow find the pressures:
Use equations (1) and (2) and select the greater value of P_u. The cavitating state is determined, of course by which equation gives the higher value.
2) Given the pressures find the flow:
The pressures may be a pair selected from P_u, P_d or pressure drop.

Equations (1) and (3) are simply inverted to give flow explicitly, i.e.: noncavitating (from equation (1))

$$q=\sqrt{\frac{P_u-P_d}{k}} \tag{5}$$

cavitating (from equation (3))

$$q=\sqrt{\frac{P_u-P_v}{j}} \tag{6}$$

In this case the lower value should be chosen.

The intersection point of the two characteristics, i.e., the onset point of cavitation is given by

$$q_c=\sqrt{\frac{P_d-P_v}{j-k}} \tag{7}$$

(by equating equations (1) and (3))

$$P_{uc}=\frac{P_d-P_v}{1-k/j}+P_v \tag{8}$$

(by substituting in equation (3)) where q_c and P_{uc} are the coordinates of the intersection point.

The Output Characteristics of a Diffuser Acting as a Source. The foregoing equations adequately describe the operation of a single diffuser but it is helpful for the two-diffuser circuit to have another characterization. This is the pressure P_d downstream of a diffuser as a function of the flow when the upstream pressure is constant. This is, in effect, an "output characteristic" available from a constant pressure source via the diffuser. As shown in Fig. 3, the characteristic is a curve which drops away from the horizontal line representing the constant upstream pressure. At the onset of cavitation the flow reaches a maximum value and at this point the "output pressure" (i.e., P_d) drops abruptly. At different upstream pressures the characteristic would be similar but shifted vertically by the appropriate amount. The onset point

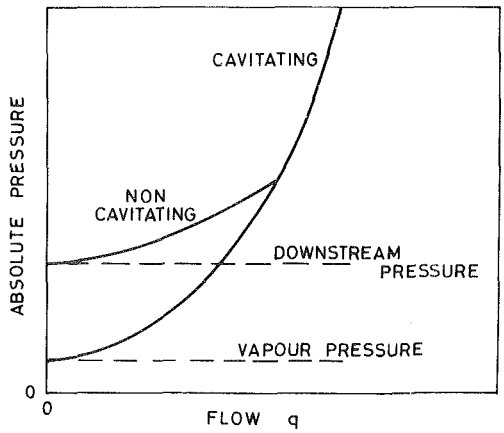

Fig. 2 Pressure upstream of a diffuser

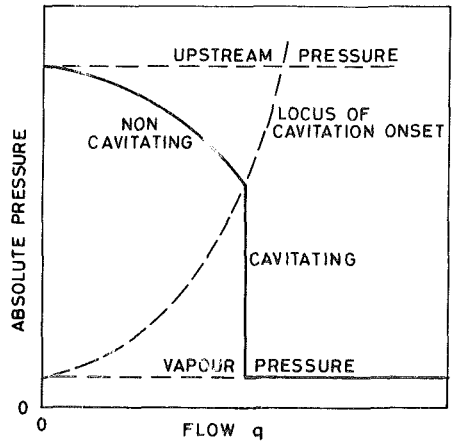

Fig. 3 Pressure downstream of a diffuser

of cavitation however, would move along a parabolic locus "L" which is particularly important in the subsequent analysis.

The equations defining the output characteristics and the cavitation-onset locus in Fig. 3 are simply a rearrangement and a combination of previous equations. Nevertheless it is useful to write them explicitly:

Noncavitating Output Characteristic. This gives the downstream pressure as a function of q and P_u

$$P_d=P_u-k\,q^2 \tag{9}$$

Nomenclature

C_c = discharge coefficient for cavitating flow
C_{cu}, C_{cd} = values of C_c for upstream and downstream diffusers
C_n = discharge coefficient for noncavitating flow
C_{nu}, C_{nd} = values of C_n for upstream and downstream diffusers
d = diameter of diffuser throat
E = ratio of k/j for upstream diffuser
F = ratio of k/j for downstream diffuser
j = gradient of cavitating characteristic: pressure drop/flow^2
k = gradient of noncavitating characteristic: pressure drop/flow^2
k_l = calculated loss coefficient for flow emerging from diffuser: dynamic pressure /flow^2
P = pressure, pressure in between the two diffusers
P_v = vapor pressure
q = flow
q_m = cavitation-limited flow
Q = normalized flow equal to $q\sqrt{j_u}$
Q_m = cavitation-limited value of Q
S = relative resistance ratio of diffusers, equal to j_d/j_u

Subscripts

c = value for cavitating flow
d = value for downstream diffuser
e = value for equivalent single diffuser
u = value for upstream diffuser
n = value for noncavitating flow

Locus of Cavitation-onset

$$P=(j-k)q^2+P_v \tag{10}$$

Cavitation-Limited Maximum Flow. The cavitation-limited maximum flow, q_m, at which the pressure falls abruptly in Fig. 3 is given by equation (6).

Analysis of Two Series-Connected Diffusers

The series-connection of two diffusers is shown in Fig. 4. They are referred to as "upstream" or "downstream." The circuit can be represented by superimposing the input characteristics of the downstream diffuser onto the output characteristics of the upstream diffuser. The pressure upstream of the downstream diffuser is the output pressure downstream of the upstream diffuser so intersections of the two sets of characteristics represent operational states of the circuit. To simplify this process of superimposition and subsequent analysis it is helpful to define some simplifying variables.

In the superimposition of the two sets of characteristics the downstream diffuser is characterized by equations (1) and (3) and the upstream diffuser by equations (3), (9) and (10). (The appropriate values of k and j distinguish between the two diffusers and between the two applications of equation (3).) These equations can be rewritten in terms of the following variables which are defined so as to give direct measures of the major quantities determining the results. Minor effects (such as variations of coefficients with Re) can be regarded as perturbations.

Normalized Variables

$E=\dfrac{k_u}{j_u}$ also equal to $\left(\dfrac{C_{cu}}{C_{nu}}\right)^2$ for the upstream diffuser

$S=\dfrac{j_d}{j_u}$ also equal to $\left(\dfrac{C_{cu}}{C_{cd}}\right)^2\left(\dfrac{d_u}{d_d}\right)^4$

$F=\dfrac{k_d}{j_d}$ also equal to $\left(\dfrac{C_{cd}}{C_{nd}}\right)^2$ for the downstream diffuser

$Q^2=j_u q^2$

The variables E and F are nondimensional quantifiers of the performance of each individual diffuser. They are equivalent to a ratio of Euler numbers or pressure-drop coefficients. If the diffusers had the same geometric design and operated at similar Reynolds numbers, the two variables E and F would be equal.

The variable S is primarily a measure of relative size. Here again if the diffusers have similar designs and operating Re, then the ratio of the discharge coefficients would be unity and size (i.e., d) would be the sole determining factor.

The definition of Q is made to remove a multiplying factor (i.e., j_u) throughout the analysis.

Normalized Equations Representing the Two Diffusers

Downstream Diffuser. Noncavitating Characteristic

$$P=F\,S\,Q^2+P_d \tag{11}$$

Cavitating Characteristic

$$P=S\,Q^2+P_v \tag{12}$$

Upstream Diffuser. Noncavitating Output Characteristic

$$P=P_s-E\,Q^2 \tag{13}$$

Cavitation Onset Locus

$$P=(1-E)\,Q^2+P_v \tag{14}$$

Cavitation-Limited Flow

$$Q_m^2=P_s-P_v \tag{15}$$

These relationships become straight lines when plotted on a P versus Q^2 coordinate grid as shown in Figs. 5 and 6. The characteristics of the upstream diffuser are represented by two line segments. One segment UN slopes down from a value of P_s on the P axis to a point on the cavitation-onset locus L. From this point the other segment UC drops vertically to the P_v line. The downstream diffuser is characterized by another pair of line segments; one, DN, slopes up from a value of P_d on the P axis to a point on the cavitating characteristic; the other DC is the cavitating characteristic extending beyond this

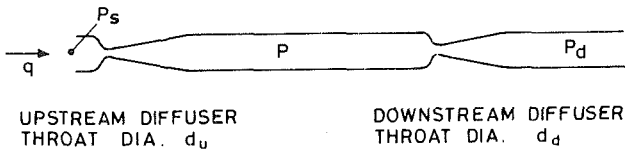

Fig. 4 Two series-connected diffusers

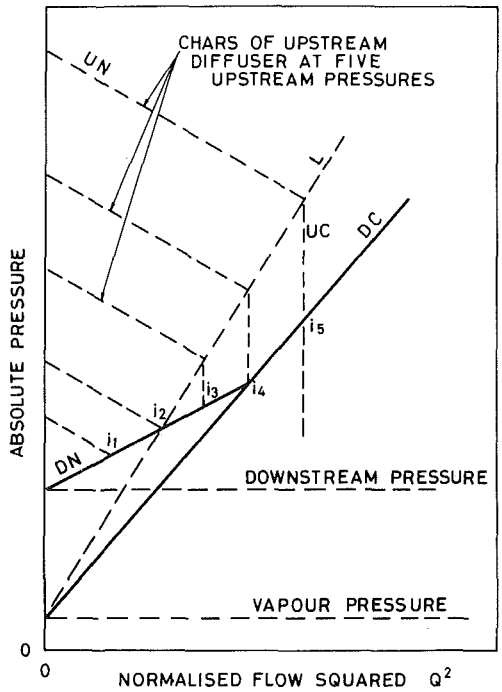

Fig. 5 Representation of type-1 circuits

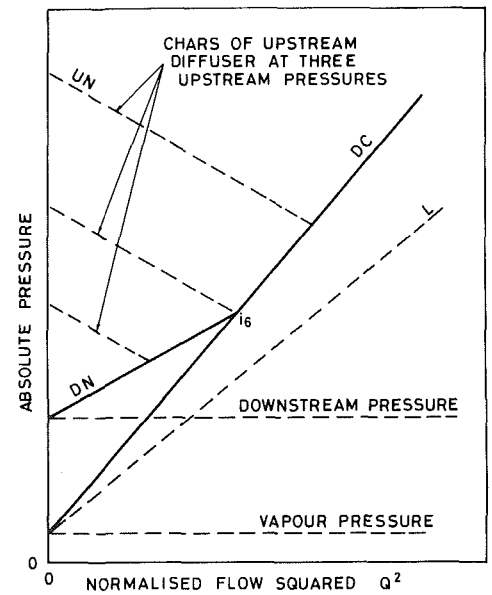

Fig. 6 Representation of type-2 circuits

point. The state of the circuit is represented by intersections of these two pairs of line segments.

Consideration of the superimposed characteristics shows that there are two types of circuit: in type 1 represented by Fig. 5 the cavitation-onset locus L for the upstream diffuser is above the cavitating characteristic of the downstream diffuser DC. In type 2, represented by Fig. 6, L is below DC. Since intersection points of the two sets of characteristics must be on or above the DC line the fact that L is below it means that the upstream diffuser never cavitates in circuits of type 2. Because of the convexity of the configuration of line segments comprising the characteristics there is no other distinctive qualitative classification of circuit types. The characteristics of the two types of circuit are considered next.

Characteristics of Type 1 Circuits (L above DC). Suppose the downstream pressure P_d is fixed and the flow is gradually increased. At first the supply pressure to the circuit P_s is small and the system is represented by intersection point i_1 in Fig. 5 where the two noncavitating characteristics cross. As the flow increases a point i_2 is reached where the locus L intersects DN. The upstream diffuser starts to cavitate and at higher flows all intersection points must be on the vertical segment UC representing the cavitating state of the upstream diffuser. This means that for circuits of this type (type 1) the downstream diffuser cannot be the only one cavitating; the upstream diffuser must already be cavitating for this to happen. A typical state with cavitation in the upstream diffuser but not in the downstream one is indicated by intersection point i_3.

As the flow is further increased point i_4 is reached at which the downstream diffuser cavitates and for flows beyond this both diffusers cavitate. A typical point in this ultimate regime is i_5.

The sequence of cavitating states in the diffuser is

Neither, Upstream only, Both.

Quantitative Characteristics of Type 1 Circuits. The algebraic criterion for a type 1 circuit is that the gradient of L should be greater than the gradient of DC, i.e.

$$\text{type 1 if } (1-E) > S \tag{16}$$

In this circuit the supply pressure as a function of flow consists of two segments, a noncavitating segment up to intersection point i_2 and another segment determined solely by the cavitating characteristics of the upstream diffuser. The transition to cavitation of the downstream diffuser does not affect the characteristics. The $P_s \sim Q$ characteristics are given by these equations

Noncavitating (from equations (11) and (13))

$$P_s = (E+FS)Q^2 + P_d \tag{17}$$

Cavitating (from equations (13) and (14))

$$P_s = Q^2 + P_v \tag{18}$$

Point of Cavitation Onset in Upstream Diffuser (from equations (11) and (14))

$$Q = \sqrt{\frac{P_d - P_v}{1-E-FS}} \tag{19}$$

This is the transition point from the noncavitating to the effective cavitating characteristic for the circuit.

Equivalent Single Diffuser. Since the characteristics of the two-diffuser circuit of type 1 consist of two segments it can be regarded as a single diffuser with suitably defined "effective" characteristics. The "equivalent diffuser" can be defined as having the same size (i.e., d) as the upstream diffuser, and the same value of C_c but having a lesser value of C_n. This effective value of C_n is given by comparing the noncavitating characteristics of a single diffuser and those of the circuit as given by equation (17). This yields

$$k_e = k_u + k_d \tag{20}$$

$$\frac{1}{C_{ne}^2 d_u^4} = \frac{1}{C_{nu}^2 d_u^4} + \frac{1}{C_{nd}^2 d_d^4} \tag{21}$$

Note that the diameter of the equivalent diffuser is made equal to d_u.

Table 1 Main dimensions of diffusers

Diffuser	Throat bore mm	Exit dia mm	Total angle°
1	8.2	29	5.7
2	9.77	29	5.9
3	9.77	29	5.9
Uncertainty at 20 to 1 odds	± .02	± .1	± .1

Characteristics of Type 2 Circuits (L below DC). The operation of type 2 circuits can be seen by considering the effect of gradually increasing the flow while keeping the downstream pressure constant. The circuit is represented in Fig. 6. At low flows neither diffuser cavitates. As the flow is increased point i_6 is reached at which the downstream diffuser cavitates and at higher flows the operating point simply moves further up the cavitating characteristic of the downstream diffuser but always within the noncavitating regime of the upstream diffuser. The sequence of cavitating states for this type 2 circuit is therefore

Neither, Downstream only (upstream never).

Quantitative Characteristics of Type 2 Circuits. In this circuit, like the type 1 circuit, the $P_s \sim Q$ characteristics have just two segments which can be referred to again as "cavitating" and "noncavitating." In this case it is the onset of cavitation in the downstream diffuser which determines the state. The noncavitating characteristic is given by the same equation as for the type 1 circuit, i.e., equation (17).

The cavitating characteristic is the sum of the cavitating pressure drop in the downstream diffuser and the noncavitating pressure drop through the upstream diffuser. Its equation is therefore

$$P = (S+E)Q^2 + P_v \tag{22}$$

The flow at which cavitation occurs is given by

$$Q = \sqrt{\frac{P_d - P_v}{S(1-F)}} \tag{23}$$

Equivalent Single Diffuser. Again, like the type 1 circuit, the type 2 circuit can also be regarded as a single diffuser. By comparing equations (17) and (22) defining the type 2 circuit, with equations (13) and (15) representing a single diffuser (or equations (1) and (3)) the effective coefficients k_e and j_e defining the hypothetical equivalent diffuser can be found, i.e.:

$$k_e = k_u + k_d \tag{24}$$

$$j_e = j_d + k_u \tag{25}$$

These can be put alternatively in terms of the equivalent diameter and discharge coefficient.

$$\frac{1}{C_{ne}^2 d_e^4} = \frac{1}{C_{nu}^2 d_u^4} + \frac{1}{C_{nd}^2 d_d^4} \tag{26}$$

$$\frac{1}{C_{ce}^2 d_e^4} = \frac{1}{C_{cd}^2 d_d^4} + \frac{1}{C_{nu}^2 d_u^4} \tag{27}$$

Since there are 3 effective variables, the two discharge

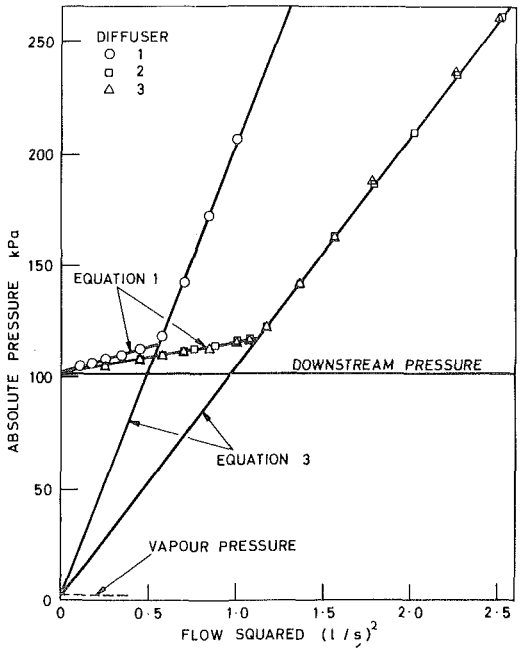

Fig. 7 Characteristics of three single diffusers. Uncertainty at 20:1 odds, flow ± .0167 liter/s pressure ± 0.3 kPa

coefficients and the diameter, and only two equations, it is arbitrary how the equivalent diffuser is defined. The main fact is that such a diffuser can be defined but its defining parameters are subject to a degree of choice.

Experimental Verification

Three diffusers, with dimensions shown in Table 1, were tested with water at 17°C to verify the predicted results. Measurements were made with a mercury-in water manometer with an uncertainty of ± .3 kPa and with a Rotameter-type flowmeter with an uncertainty of ± 1 liter/min at 20 to 1 odds.

Water Quality and Related Effects. The objective of our research is to develop liquid-handling systems for industrial applications so the gross changes in performance caused by cavitation are the main interest rather than cavitation per se. The water was not specially treated so that its air and nuclei content would be similar to that in the application. The "vapor pressure" is therefore less well-defined than for pure water since its effective value could be raised by the air content (a typical value might be circa 18 kPa). Despite this possibility, the theoretical pure-water-value for P_v is used in the ensuing analysis of the experimental results but, in fact, a degree of uncertainty in the value for P_v would not seriously affect the results. The angle of lines DC and L in Figs. 5 and 6 would be changed and a slightly less convincing coincidence of data and theory would be expected.

Another effect that might occur is some degree of interaction: i.e., if the upstream diffuser cavitates and thereby changes the nucleation properties of the flow entering the downstream diffuser. The results show that such interaction was absent or that it was insignificant. This is in agreement with the results got by Numachi et al. [4] who were worried about the same topic in tests on venturi meters.

In a general sense, the relationship of the results to the properties of the water is similar to that in large turbomachines for which useful cavitation data are obtained despite the need to use unrefined water.

Results for Single Diffusers. First the diffusers were tested singly by measuring the pressure upstream as flow was increased covering both cavitating and noncavitating regimes. The outflow from the diffusers emerged into a large tank so the downstream pressure was constant and close to atmospheric. Also, the relatively small dynamic head of the outflow contributes to the noncavitating measured pressure drop. The results are shown in Fig. 7 where the upstream pressure is plotted against the flow squared. The straight lines drawn in Fig. 7 correspond to equations (1) and (3). The constants P_v and P_d are the same for all cases and had values of $P_v = 1.93$ kPa and $P_d = 101.4$ kPa. The values of k, j and the consequent values of C_n and C_c for these lines characterizing the diffusers are given in Table 2. Also included is the loss factor k_l calculated for the component of dynamic head emerging from the 29 mm diameter exit of each diffuser. It is small but not negligible.

Table 2 Data for single diffusers

Diffuser	k	j	C_n	C_c
	kPa/(liter/s)^2			
1	23.5	206	2.76	.933
2	14.2	104	2.51	.924
3	12.9	104	2.62	.924
Uncertainty at 20:1 odds	± 1.6	±2.1	± .02	± .012

Calculated exit loss = 1.15 kPa/(liter/s)^2.

Evidently, equations (1) and (3) are good representations of the performance. The sharp transition to cavitating flow implied by the intersection of the lines is reflected in the measurements near that point and by the appearance of cavities in the flow (which could be seen through the transparent diffusers). The cavitation appeared first around the periphery of the throat. With increasing flow, the zone of cavitation progressively extended downstream from the throat in the same way as reported by other researchers (e.g., [3]). These results were not new but they show that the diffusers were not abnormal in any way. The difference between the noncavitating characteristics of diffusers 2 and 3 appeared to be caused by a slight difference in throat length (although they were nominally the same).

Experiments on Series-Connected Diffusers. The results from tests on three circuits will be considered. The circuits were formed by connecting the diffusers by a 38 mm bore pipe with a separation of 0.25 m. In the numerical calculations it has been assumed that half of the dynamic head leaving the 29 mm bore exit of the upstream diffuser is recovered by the interconnecting pipe. Hence the k and j coefficients for the downstream diffuser have been reduced by subtracting $\frac{1}{2} k_l$.

The pressure upstream of the series-connected diffusers was measured as the flow was increased. The flow discharged into a large tank at near-atmospheric pressure in the same way as for the tests on the diffusers singly. The objective was to show that the characteristics of both types of two-diffuser circuit could be calculated from those of the single diffusers, and that an "equivalent diffuser" could be defined.

Results of Tests on Series Connected Diffusers. The results are shown in Fig. 8 where the upstream pressure is plotted against the flow squared. The straight lines drawn in Fig. 8 correspond to equations (1) and (3) with equivalent values of k and j derived in accordance with equations (17), (18), and (22) (but with the small dynamic head correction as described). The values of these coefficients and the parameters E, S, F, circuit type and the discharge coefficients of the effective diffusers are shown in Table 3.

The equivalent diffusers were defined as having a throat bore equal to that of the smallest diffuser in the pair. This imposed constraint enables the coefficients to be unambiguously defined for the type-2 circuits.

The results for the series-connected diffusers show the

Table 3 Characteristics of series-connected diffuser circuits

Circuit	Upstream diff.	Downstream diff.	S	E	F	Circuit type	Data for equivalent single diffuser				
							k kPa/(liter/s)^2	j	C_{ne}	C_{ce}	Bore mm
1	1	2	.114	.502	.132	1	37.13	206	2.2	.933	8.2
2	2	1	.136	1.97	.111	2	37.13	219	2.2	.903	8.2
3	2	3	.136	.994	.119	2	26.5	117	1.83	.868	9.77
Uncertainty at 20:1 odds			±.036	±.006			±2	±3	± .03	±.02	± .02

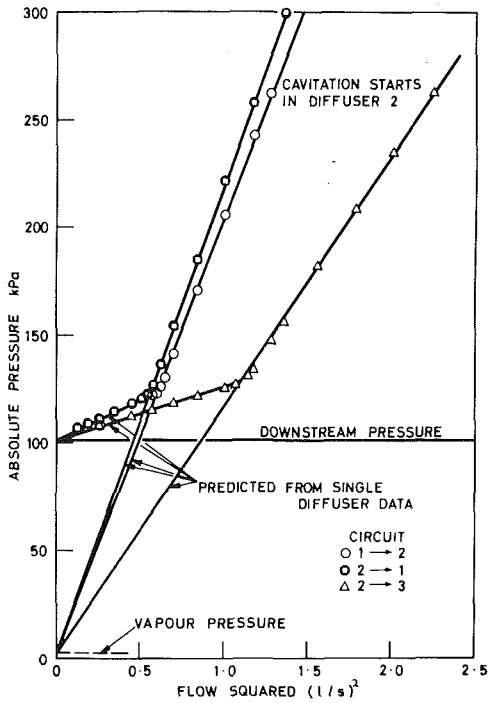

Fig. 8 Characteristics of three 2-diffuser circuits. Uncertainty at 20:1 odds, flow ± 0.167 liter/s pressure ± 0.3 kPa

predicted two-segment type of characteristics. The transition point is where the upstream diffuser cavitates in circuit 1 and where the downstream diffuser cavitates in circuits 2 and 3. In circuit 1 the upstream pressure is unaffected by the onset of cavitation in the downstream diffuser (as expected); in fact the cavitating characteristic is identical to that of the upstream diffuser alone. In circuits 2 and 3, cavitation was suppressed in the upstream diffuser because of the back pressure caused by the downstream diffuser. In this case the cavitating characteristic is the sum of the appropriate single diffuser characteristics as predicted.

It is interesting to note that circuit 3 using two nearly identical diffusers is definitely a type 2 circuit, it is not a borderline case.

Consideration of the Reynolds Number and Related Effects. The clear-cut results demonstrated so far are a result of the distinct two-segment geometry of the characteristics of the single diffusers. Some well-documented influences might complicate this situation, however. One such influence is the variation in the discharge coefficient as a function of Reynolds number as described by Hall [5]. The discharge coefficient increased from .95 to .99 as Re increased from 20000 to 200000 in a typical well-formed nozzle for example. Consideration of this however shows that although it is significant in regard to flowmetering applications, its effect on the results derived here is rather small because of the large difference in the gradients of the cavitating and non-cavitating characteristics. The effect would in fact be more noticeable in devices with a poor pressure recovery which would imply a lesser distinction between the two characteristics and therefore more chance of an ill-defined transition point. A design feature likely to promote this complicating influence is a long parallel section at the throat of the diffuser. The diffusers tested however all had virtually no parallel section at the throat so no specific tests have been done to investigate such details.

Analogous Treatment for Orifices

Usually when flow passes through an orifice plate in a pipe there is some degree of pressure recovery downstream. The orifice can therefore be regarded as a degenerate diffuser characterized by two equations like equations (1) and (3). The values of k and j would be closer than for the diffuser and would be equal in the extreme case of an orifice with no downstream pressure recovery. The theory developed for diffusers therefore encompasses numerous other systems.

Conclusion

Two series-connected diffusers can be characterized by equations analogous to those for a single diffuser. These are simple because they are represented by two distinct segments: cavitating and noncavitating. The quantitative details of this analogy depend on whether the upstream or the downstream diffuser cavitates first. This fact can be prediced fairly easily, however, so the analysis is straightforward. The experimental results corresponded well with the theory.

Acknowledgments

This work is sponsored by the United Kingdom Atomic Energy Authority and British Nuclear Fuels Ltd. being part of their programme of Power Fluidics Development.

References

1 Randall, L. N., "Rocket Applications of the Cavitating Venturi," *J. Am Rocket Soc.*, Vol. 22, 1952.

2 Escande, L., and Castex, L., "Limiting Device of Discharge in Cavitation," Paper 4.21, IAHR Congress, 1963.

3 Hutton, S. P., "Cavitating Venturimeter as a Flow Limiter," *Proc. 6th Conf. on Fluid Machinery*, Vol. 1, Akad. Kiado, Budapest, 1979, p. 494.

4 Numachi, F., Kobayashi, R., and Kamiyama, S., "Effect of Cavitation on the Accuracy of Herschel-Type Venturi Tubes," ASME Journal of Basic Engineering, Vol. 84, Sept. 1962, pp. 351–360.

5 Hall, G. W., "Application of Boundary Layer Theory to Explain some Nozzle and Venturi Flow Peculiarities," *Proc. Inst. Mech. Engrs.*, Vol. 173, No. 36, 1959, p. 837.

Pressure Field Generated by Nonspherical Bubble Collapse

G. L. Chahine
Hydronautics, Incorporated,
Laurel, Md. 20707

A. G. Bovis
STCAN, Bassin des Carenes,
Paris, France

The method of matched asymptotic expansions is used to investigate the behavior of a collapsing bubble near a solid wall. Cases are studied in which the ratio ϵ between the initial spherical bubble radius and its distance from the wall is small. Expansions in powers of ϵ lead to a simple system of differential equations which is solved numerically. The bubble shape, the velocity potential and the pressure field are determined as functions of time. The deformation of the bubble is a singular perturbation of the pressure field around it. An increase in the value of ϵ augments the pressure on the solid wall by orders of magnitude. The influence of surface tension and the proximity of the wall, gas content and its law of compression, are investigated. The results are compared to previous investigations. One advantage of the method employed is the fact that it leads to a numerical solution which costs very little computer time. In addition, it can be extended very easily to more complex cases such as multibubble configurations or to walls coated with elastomeric coatings.

Introduction

The modeling of cavitation erosion and noise, as well as the related scaling effects, requires the knowledge of individual and collective bubble behavior. Most of the presently used modeling approaches are of a statistical nature and are based on a spherical bubble collapse theory developed by Rayleigh. This spherical model was extended by Plesset [1] to the case of a gas and vapor filled spherical bubble moving with the surrounding fluid. However, in practical situations where cavitation is harmful, collective bubble collapse and the presence of nearby solid boundaries are fundamental. Observations of nonspherical bubble collapse have been made experimentally using high-speed photography [2–4]. A high-speed re-entering jet is seen to be formed at the final stage of collapse. Pressure waves of higher maximum amplitude than those obtained in the spherical case are expected to be generated and to contribute to the jet's damaging effect.

Despite its great practical importance, nonspherical bubble dynamics studies are not very advanced due to the complexity of the free boundary problem involved. Analytical solutions are unlikely at present. However, several important contributions do exist [5–8] which are either purely numerical or numerical with some analytical simplifications. These investigations succeeded in describing the re-entering jet formation, as well as its early evolution. The final stage of collapse could not be obtained, due either to numerical instabilities or to failure of the analytical model. These calculations are very time consuming; thus they have not been extended to investigate the influence of different parameters, or to study complex configurations. In previous publications [4, 9], we proposed and used matched asymptotic expansions to study the problem when the bubble radius is small compared to its distance from nearby boundaries. The behavior in the more complicated case where the two lengths are of the same order of magnitude, can be at least qualitatively deduced from the behavior of the solution when the small parameter approaches unity. This method is used here for the analysis of the collapse of an isolated bubble near a solid wall. A moving coordinate system attached to the bubble allows to follow the bubble deformation during the collapse for a long period of time. The potential flow is determined and then used to describe the pressure field evolution around the collapsing bubble. One attractive advantage of this method is its small computer run time. Less than forty seconds of a Univac 1110 are needed to describe the whole bubble collapse as well as the pressure field.

Formulation of the Problem

Let us consider the classical problem of the collapse of an initially spherical bubble near a solid wall. R_0 is the initial radius of the sphere and l_0 is the initial distance from its center to the solid wall. Due to a change in the ambient pressure $P_\infty(t)$, the bubble shape changes. Our aim is to determine, at a subsequent time t, the equation of the bubble wall, $R(\theta, t)$, as well as, the pressure field around it, $p(r, \theta, t)$. To do so, let $0_0X_0Y_0Z$ be the initial coordinate system and $0XYZ$ a coordinate system moving in the z direction. If $b(t)$ is the distance 00_0, the distance from the origin to the wall at the time t is given by $l(t) = l_0 - b(t)$. A point M on the bubble surface is defined by the angle θ (Fig. 1) and the distance $R(\theta, t)$ from 0.

If the fluid is assumed to be inviscid and the flow irrotational there exists a velocity potential ϕ such that the

Contributed by the Fluids Engineering Division and presented at the Proceedings on Cavitation Erosion in Fluid Systems, Boulder, Colo., June 22-24, 1981, of THE AMERICAN SOCIETY OF MECHANICAL ENGINEERS. Manuscript received by the Fluids Engineering Division, June 21, 1982.

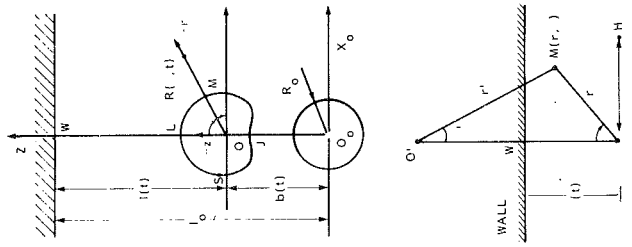

Fig. 1 Definition of different characteristic lengths

velocity field is given by $\mathbf{V} = \nabla\phi$. If the fluid is also incompressible, it satisfies the Laplace equation,

$$\Delta\phi = 0. \tag{1}$$

To determine the bubble wall motion one has to solve equation (1) subjected to the following kinematic and dynamical conditions on the bubble surface and on the solid wall:

$$\nabla\phi \cdot \mathbf{n}|_{r=R(\theta,t)} = [\dot{R}\mathbf{e}_r + \dot{b}\mathbf{e}_z]\cdot\mathbf{n}, \tag{2}$$

$$\rho[\dot{\phi} - \dot{b}\,\mathbf{e}_z\cdot\nabla\phi + \tfrac{1}{2}|\nabla\phi|^2]_{r=R(\theta,t)} = P_\infty(t) - P_g(t) - P_v + 2\gamma C(\theta,t), \tag{3}$$

$$\nabla\phi\cdot\mathbf{n}|_{r=l(t)/\cos\theta} = 0, \tag{4}$$

where C and $\mathbf{n}$ are, respectively, the curvature of the bubble surface and its unit normal vector at the point $M(\theta, t)$. γ is the surface tension and dots denote time differentiation. ϕ and the operator ∇ are expressed in the moving system $0XYZ$. P_∞, P_v, and P_g are the imposed ambient pressure, the vapor pressure and the pressure of the gas inside the bubble. If we assume a polytropic behavior, P_g is related to its initial value by the equation

$$P_g(t) = P_{g_0}\frac{{R_0}^{3k}}{V^k(t)}\cdot\frac{4}{3}\pi, \tag{5}$$

where $V(t)$ is the volume of the bubble at the time t, and k is the polytropic coefficient ($1 < k < c_p/c_v$).

To these conditions, we have to add the initial condition and the boundary condition at infinity:

$$\phi(r,\theta,0) = 0,$$

$$P_\infty(0) = P_0 = P_{g_0} + P_v - \frac{2\gamma}{R_0}, \tag{6}$$

$$\lim_{r\to\infty}\phi(r,\theta,t) = 0.$$

The pressure field is then determined by the Bernoulli equation which can be written in the moving system as follows:

$$p(r,t) = -\dot{\phi} + \dot{b}\,\mathbf{e}_z\cdot\nabla\phi - \tfrac{1}{2}|\nabla\phi|^2 + P_\infty(t). \tag{7}$$

With no further simplifications or assumptions, this general problem is not easily solved analytically. As mentioned above, numerical computations, can be used, the most attractive ones being based on a variational formulation. However, when the ratio R_0/l_0 is small, analytical calculations using matched asymptotic expansions dramatically simplify the problem leading to a low time-consuming numerical resolution.

Matched Asymptotic Problem

When the orders of magnitude of R_0 and l_0 are different (i.e., $R_0/l_0 = \epsilon << 1$), the problem has two different characteristic lengths, and depending on whether one is interested in the vicinity of the bubble "inner region," or in the vicinity of the solid wall "outer region," R_0 or l_0 should be, respectively, choosen as the length scale, L. By doing so, the problem (1) to (6) is divided into two easier subproblems, the "inner" ($L = R_0$) and the "outer" ($L = l_0$), with matching conditions in between. Before giving the details let us notice that, to the first order of approximation ($\epsilon = 0$) in the inner problem the solid wall is effectively at infinity. The bubble reacts to a change $P_\infty(t)$ in the ambient pressure as if it were in an infinite medium. It therefore behaves spherically, its wall motion $a_0(t)$ being given by the Rayleigh-Plesset [1] equation. To the same order of approximation the bubble appears as a spherical singularity of strength $q_0(t) = a_0^2\,\dot{a}_0$ in the presence of a solid wall. The solution is easily obtained by the use of the method if images. The resultant flow is that due to the superposition of two sources—one the actual

Nomenclature

$a_0, a_1, \ldots a_n$ = spherical contributions to the bubble wall equation
$b(t)$ = distance between the fixed and the moving coordinate system
$\dot{b}_s$ = velocity of an oscillating sphere
c_p, c_v = specific heat of the gas at constant pressure, volume.
D_{ep} = multiplicative constant to $\dot{b}_s$
f_2, f_3 = amplitude of nonspherical perturbations of type $\cos\theta$ of $R(\theta, t)$
g_3 = amplitude of nonspherical perturbtion of type $P_2(\cos\theta)$ of R
h_2, h_3 = amplitude of nonspherical perturbation of type $\cos\theta$ of ϕ
K_3 = amplitude of nonspherical perturbations of type $P_2(\cos\theta)$ of R
k = polytropic coefficient
l_0 = initial bubble center to wall distance
$p(r,\theta,t)$ = pressure field
$P_\infty(t)$ = imposed ambient pressure
P_0, p_{g_0} = initial ambient pressure, and gas pressure
p_v = vapor pressure
$P_g(t)$ = noncondensable gas pressure
ΔP = characteristic value of the imposed pressure $\Delta P = P_{\max} - P_0$
$q_0, q_1, \ldots q_n$ = strengths of first and successive spherical sources
r = spherical coordinate
r' = $(r^2 + 4l^2 - 4rl\cos\theta)^{1/2}$
R_0 = initial bubble radius
t = time
T = characteristic time scale $T = R_0\sqrt{\rho/\Delta P}$
P = $(P_0 - P_v)/\Delta P$
$P_n(\cos\theta)$ = Legendre polynomial of order n
$R(\theta,t)$ = bubble wall equation
ρ = liquid density
γ = surface tension
ϵ = $R_0/l_0 << 1$
$\phi(r,\theta,t)$ = velocity potential in the moving system
$\phi_0, \phi_1, \ldots \phi_n$ = successive expansions of ϕ
$\Phi.$ = characteristic velocity potential
W_e = $R_0 \cdot \Delta P/2\gamma$

Superscripts

$\dot{}$ = time differentiation
$\bar{}$ = nondimensional outer variable
$\tilde{}$ = nondimensional inner variable

source at 0 and the other an identical one symmetrical to 0 with respect to the wall. To the following orders one has to solve in the "inner problem" the Laplace equation and satisfy the boundary conditions on the bubble surface. The conditions at infinity are to be replaced by a matching condition with the "outer solution." This is obtained by applying the "Asymptotic Matching Principle" [14] which, in the case of a series expansion as here, stipulates: "the n-term inner expansion of (the m-term outer expansion) = the m-term outer expansion of (the n-term inner expansion)." This can be written in an intuitive physical way as follows:

$$\underset{r=r/l_0\to 0}{\text{Expansion}}\ \phi_{\text{out}} = \underset{r=r/R_0\to\infty}{\text{Expansion}}\ \phi_{\text{in}} \tag{8}$$

Nondimensionalizations

In order to make asymptotic expansions (and thus to compare orders of magnitudes) an accurate choice of characteristic scale variables is fundamental. For the length scales the choice is obvious: R_0 in the inner problem, l_0 in the outer. The time scale has to be the same for the two problems and, since we are interested in the collapse history, the Rayleigh time based on R_0 and the characteristic value of the imposed pressure perturbation, Δp, is taken as this time scale:

$$T = R_0\sqrt{\rho/\Delta P}. \tag{9}$$

ΔP, which is also taken as the characteristic scale for the pressures, can be defined as the difference between the maximum value of $P_\infty(t)$ and the initial value $P_\infty(0) = P_0$.

$$\Delta P = P_{\max} - P_0. \tag{10}$$

If surface tension is neglected and if the cavity contains only liquid vapor, then $P_0 = P_v$ and T is the classical Rayleigh time. In the more general case considered here P_0 is given by (6).

The only variable left is the characteristic velocity potential Φ_0. As we have mentioned before, in both regions the flow in the first approximation is due to the presence of a source (and its image for the outer problem) of strength $q_0(t)$ (characteristic scale R_0^3/T). Then, the velocity potential has the scale $q_0(t)/r$. That is to say, $\Phi_0 = R_0^2/T$ for the inner problem and $\Phi_0 = R_0^3/l_0 T$ for the outer problem.

With these characteristic scales, non-dimensional variables all of order unity are introduced through the following definitions, where bars denote outer non-dimensional variables and tildes inner ones.

$$\begin{aligned}
&\tilde r = r/R_0 \quad ; \quad \bar r = r/l_0,\\
&\tilde\phi = \phi T/R_0^2 \quad ; \quad \bar\phi = \epsilon\,\phi\, T/R_0^2,\\
&\tilde p(t) = \bar p(t) = p(t)/\Delta P,\\
&\tilde t = \bar t = t/R_0\sqrt{\rho/\Delta P},\\
&\bar l = l/l_0,\\
&\tilde b = b/R_0 \quad ; \quad \bar b = b/l_0.
\end{aligned} \tag{11}$$

Each of the unknowns is then expanded in power series of ϵ as follows:

$$\begin{aligned}
\phi &= \bar\phi_0 + \epsilon\bar\phi_1 + \epsilon^2\bar\phi_2 + \epsilon^3\bar\phi_3 + \ldots,\\
\tilde\phi &= \tilde\phi_0 + \epsilon\tilde\phi_1 + \epsilon^2\tilde\phi_2 + \epsilon^3\tilde\phi_3 + \ldots,\\
\tilde b &= \tilde b_0 + \epsilon\tilde b_1 + \epsilon^2\tilde b_2 + \epsilon^3\tilde b_3 + \ldots,\\
\tilde R &= \tilde a_0 + \epsilon\tilde R_1 + \epsilon^2\tilde R_2 + \epsilon^3\tilde R_3 + \ldots.
\end{aligned}$$

Analytical Solution

First Order of Approximation (ϵ^0). As stated before, the bubble behaves spherically to the first order of approximation, and its radius is given by the following non-dimensional Rayleigh-Plesset equation:

$$\tilde a_0\ddot{\tilde a}_0 + \frac{3}{2}\dot{\tilde a}_0^2 = -\tilde p(\tilde t) + P(\tilde a_0^{-3k} - 1) + W_e^{-1}(\tilde a_0^{-3k} - \tilde a_0^{-1}) \tag{12}$$

where

$$\begin{aligned}
W_e &= R_0\cdot\Delta P/2\gamma\\
P &= \frac{P_0 - P_v}{\Delta P} = \frac{P_{g0}}{\Delta P} - W_e^{-1} = \tilde P_{g0} - W_e^{-1}
\end{aligned} \tag{13}$$

The parameter P is a measure of the initial nondimensional gas pressure inside the bubble. The potential flow in the inner problem can then be written:

$$\tilde\phi_0 = \frac{-\tilde a_0^2\dot{\tilde a}_0}{\tilde r} = \frac{-\tilde q_0(\tilde t)}{\tilde r}, \tag{14}$$

In the outer problem, the potential flow is that due to the superposition of two symmetrical sources relative to the wall (Fig. 1) and can be written:

$$\bar\phi_0 = -\tilde q_0(\tilde t)\left[\frac{1}{\bar r} + \frac{1}{\bar r'}\right]. \tag{15}$$

To this order, due to the spherical symmetry of the problem, no bubble motion occurs and if we fix the origin of coordinates to the bubble we can write:

$$\bar l_0 = 1, \quad \tilde b_0 = 0 \tag{16}$$

Second Order of Approximation (ϵ^1): Lengthening Effect. The matching condition (8) shows that the first correction to the order-zero inner solution (14) is of order ϵ. By taking Definitions (11) into account, equation (8) can be written:

$$\underset{\bar r\to\infty}{\text{Expansion}}\ (\tilde\phi_0 + \epsilon\tilde\phi_1 + \ldots.) = \epsilon\ \underset{\bar r\to\infty}{\text{Expansion}}(\bar\phi_0 + \epsilon\bar\phi_1 + \ldots.)$$

which with (15) implies the already-known condition,

$$\lim_{\bar r\to\infty}\ \tilde\phi_0 = 0,$$

as well as

$$\lim_{\bar r\to\infty}\ \tilde\phi_1 = \frac{\tilde q_0(\tilde t)}{2}. \tag{17}$$

$\tilde\phi_1$ has to satisfy the Laplace equation, as well as the boundary conditions on the bubble wall (the contribution to order ϵ of the expansion of (2) and (3) nondimensionalized).

To this order all boundary conditions are spherical so that the solution $\tilde\phi_1$ can be written as:

$$\tilde\phi_1 = -\frac{\tilde q_1}{\tilde r} - \frac{\tilde q_0}{2}, \tag{18}$$

where $\tilde q_0$ and $\tilde q_1$ are functions of time. $\tilde q_0$ has been defined earlier, (14), and

$$\tilde q_1 = \tilde a_0^2\dot{\tilde a}_1 + 2\tilde a_0\dot{\tilde a}_0\tilde a_1. \tag{19}$$

The first spherical correction, $\tilde a_1$, of the bubble radius is obtained by solving the following differential equation.

$$\tilde a_0\ddot{\tilde a}_1 + 3\dot{\tilde a}_0\dot{\tilde a}_1 + \tilde a_1\left(\ddot{\tilde a}_0 - \frac{W_e^{-1}}{\tilde a_0^2} + 3k\frac{\tilde P_{g0}}{\tilde a_0 3k+1}\right) = -\frac{\dot{\tilde q}_0}{2}, \tag{20}$$

$$\tilde R_1(\theta,\tilde t) = \tilde a_1(\tilde t)$$

If the surface tension and the pressure of noncondensable gas are neglected, equations (20) and (12) can be integrated to give the corrected period of oscillation of the bubble, which can be written:

$$\bar\tau = \bar\tau_0 + \epsilon\bar\tau_1 = 0.915\left(1 + \frac{\epsilon}{4}\int_0^1 \tilde a_0\, d\tilde t\right), \tag{21}$$

where $\bar\tau_0$ is the nondimensional time needed for a spherical void to collapse. A solid wall is therefore seen to have a

lengthening effect on the bubble collapse time (a free surface gives a shortening effect). This result has been predicted by energy considerations by Herring [10] as early as 1941.

The outer solution of the problem is obtained by the use of the method of images, which consists of adding a symmetrical image to the correction-source, to give,

$$\tilde{\phi}_1 = -\tilde{q}_1\left[\frac{1}{\tilde{r}} + \frac{1}{\tilde{r}'}\right]. \tag{22}$$

As the problem is still spherical to this order, no motion is involved, and

$$\tilde{l}_1 = \tilde{b}_1 = 0. \tag{23}$$

Third Order of Approximation (ϵ^2): Motion and First Nonspherical Deformation. The first nonspherical term in the equations appears to the order ϵ^2, in the expansion of the matching condition (8). This term varies as $\cos\theta$. Since the nonspherical terms involving the motion of the origin of coordinates in the boundary conditions on the bubble ((2) and (3)) are also of the form $\cos\theta$, the principle of less degeneracy leads to the choice,

$$\tilde{b} = \epsilon^2 \tilde{b}_2 + \ldots\ldots$$

The equations to this order then take the form:

$$\Delta\tilde{\phi}_2 = 0, \tag{24}$$

$$\frac{\partial\tilde{\phi}_2}{\partial\tilde{r}}\bigg|_{\tilde{r}=\tilde{a}_0} = 2\,\tilde{R}_2\,\frac{\dot{\tilde{a}}_0}{\tilde{a}_0} + \dot{\tilde{R}}_2 + \dot{\tilde{b}}_2\cos\theta + F_1(\tilde{a}_1,\tilde{a}_0), \tag{25}$$

$$-\tilde{a}_0\,\frac{\partial\tilde{\phi}_2}{\partial\tilde{r}} - \frac{\partial\tilde{\phi}_2}{\partial\tilde{t}}\bigg|_{\tilde{r}=\tilde{a}_0} = \tilde{R}_2\ddot{\tilde{a}}_0 + \frac{W_e^{-1}}{\tilde{a}_0^2}\left(2\,\tilde{R}_2 + \frac{\partial\tilde{R}_2}{\partial\theta}\,\mathrm{cotg}\theta + \frac{\partial^2\tilde{R}_2}{\partial\theta^2} - \frac{2a_1^2}{\tilde{a}_0^2}\right) - \dot{\tilde{a}}_0\dot{\tilde{b}}_2\cos\theta + F_2(\tilde{a}_1,\tilde{a}_0,\tilde{P}_{g_0},k), \tag{26}$$

$$\lim_{\tilde{r}\to\infty}\ \tilde{\phi}_2 = -\frac{\tilde{q}_0}{4}\,\tilde{r}\cos\theta + \frac{\tilde{q}_1}{2}, \tag{27}$$

where F_1 and F_2 are known functions of $\tilde{a}_1$, $\tilde{a}_0$, k, and $\tilde{P}_{g_0}$.

This problem is more complex than those already solved in the two preceding orders. A solution can be obtained by means of an infinite spherical harmonic series expansion of $\tilde{\phi}_2$. Fortunately, due to the condition (27) and to the initial condition $\tilde{\phi}_2$ $(r, \theta, 0) = 0$, all the terms of the expansion are shown to be identically zero except the following ones:

$$\tilde{\phi}_2 = -\frac{\tilde{q}_2}{\tilde{r}} + \left(\frac{\tilde{h}_2}{\tilde{r}^2} + \frac{\tilde{q}_0}{4}\,\tilde{r}\right)\cos\theta - \frac{\tilde{q}_1}{2}. \tag{28}$$

This leads to,

$$\tilde{R}_2(\theta,t) = \tilde{a}_2(t) + \tilde{f}_2(t)\cos\theta. \tag{29}$$

$\tilde{a}_2$ and $\tilde{f}_2$ are given by the following differential equations:

$$\tilde{a}_0\ddot{\tilde{a}}_2 + 3\dot{\tilde{a}}_0\dot{\tilde{a}}_2 + \tilde{a}_2\cdot\left(\ddot{\tilde{a}}_0 - \frac{W_e^{-1}}{\tilde{a}_0^2} + \tilde{P}_{g_0}\,\frac{3k}{\tilde{a}_0 3k+1}\right) = -\frac{\dot{\tilde{q}}_1}{2} + F_3(\tilde{a}_0,\tilde{a}_1,W_e^{-1},\tilde{P}_{g_0},k), \tag{30}$$

$$\tilde{a}_0\ddot{\tilde{f}}_2 + 3\dot{\tilde{a}}_0\dot{\tilde{f}}_2 = -\tilde{a}_0\ddot{\tilde{b}}_2 - 3\dot{\tilde{a}}_0\dot{\tilde{b}}_2 - \frac{3}{4}\,(\dot{\tilde{a}}_0\tilde{q}_0 + \tilde{a}_0\dot{\tilde{q}}_0). \tag{31}$$

Once $\tilde{a}_2$ and f_2 are known, $\tilde{q}_2$ and $\tilde{h}_2$ are given by the following relations,

$$\tilde{q}_2 = 2\,\frac{\tilde{a}_1}{\tilde{a}_0}\,\tilde{q}_1 + \left(2\,\frac{\tilde{a}_2}{\tilde{a}_0} - 3\,\frac{\tilde{a}_1^2}{\tilde{a}_0^2}\right)\tilde{q}_0 + \dot{\tilde{a}}_2\tilde{a}_0^2, \tag{32}$$

$$\tilde{h}_2 = -\tilde{q}_0\left(\frac{\tilde{a}_0^3}{8} + \tilde{f}_2\right) - \frac{\tilde{a}_0^3}{2}\,(\dot{\tilde{f}}_2 + \dot{\tilde{b}}_2). \tag{33}$$

The only remaining unknown, needed to solve equations (30) and (31) is the imposed motion of the origin of coordinates $\tilde{b}_2(t)$. The aim of this arbitrary motion, as stated before, is to provide at each time $\tilde{t}$ a system of coordinates which can describe the bubble wall equation correctly. With no motion of 0, the part of the bubble surface farthest from the wall can reach 0 early in the collapse history. For subsequent times, 0 is outside the domain bounded by the bubble surface and the spherical coordinate system used (r, θ, ϕ) is no longer adequate to describe this surface. Therefore, the coordinate motion should be chosen in order to delay this limit, if not to avoid it. The first idea which comes to mind is to attach 0 to the center of gravity G of the bubble by writing its equation of motion. This motion is such that the net pressure thrust on the massless moving bubble is zero. The equation obtained is not an additional one and gives again (3) (or to this order (30) and (31)). Thus, the position of G is known once the whole problem is solved. An iterative procedure can be used by taking the position of the center of gravity of the bubble, at a given time step, as the new origin for the following step. Another approach has been used here because it appeared more practical. If a cavity is assumed to remain spherical while oscillating near a solid wall as a source of strength $\tilde{q}_0$ (t), its center moves toward the wall with the velocity $\tilde{b}_s(t)$ given by:

$$2\tilde{a}_0\ddot{\tilde{b}}_s + 6\dot{\tilde{a}}_0\dot{\tilde{b}}_s = -\dot{\tilde{a}}_0\tilde{q}_0 - \tilde{a}_0\dot{\tilde{q}}_0. \tag{34}$$

To obtain (34), only the source-image relative to the wall is taken into account. The images relative to the bubble wall are neglected and hence the conditions (2, 3) on the bubble surface are not satisfied. A motion of the origin of coordinates proportional to $\tilde{b}_s$, such that $\tilde{b}_2 = D_{ep} \cdot \tilde{b}_s$, is applied and gives good results for $1 < \mathrm{Dep} < 1.5$.

Order ϵ^3 and Following. As we have seen above, the choice of $\tilde{b}$ is somewhat arbitrary. We will then restrict the motion of the origin to $\tilde{b}$ $(\tilde{t})$ and treat the following orders of approximation with no correction of this motion. One can show that to each order, as for the preceding orders, the radius R_n (θ,t) is of the form:

$$R_n(\theta,\tilde{t}) = \tilde{a}_n(\tilde{t}) + \tilde{f}_n(\tilde{t})\cos\theta + \tilde{g}_n(\tilde{t})P_2(\cos\theta) + \ldots\,\tilde{y}_n(\tilde{t})P_{n-1}(\cos\theta),$$

where P_n $(\cos\theta)$ is the Legendre polynomial of order n. For $n = 3$, we have:

$$R_3(\theta,t) = \tilde{a}_3(\tilde{t}) + \tilde{f}_3(\tilde{t})\cos\theta + \tilde{g}_3(t)\cdot(3\cos^2\theta - 1)/2. \tag{35}$$

$\tilde{a}_3$ $(\tilde{t})$, $\tilde{f}_3$ $(\tilde{t})$ and $\tilde{g}_3$ $(\tilde{t})$ are obtained by solving the following differential equations:

$$\tilde{a}_0\ddot{\tilde{a}}_3 + 3\dot{\tilde{a}}_0\dot{\tilde{a}}_3\tilde{a}_3(\ddot{\tilde{a}}_0 - W_e^{-1}\tilde{a}_0^{-2} + 3K\,\tilde{P}_{g_0}\cdot\tilde{a}_0^{-3k-1}) = F_4(\tilde{a}_0,\tilde{a}_1,\tilde{a}_2,W_e^{-1},\tilde{P}_{g_0}) - \dot{q}_2, \tag{36}$$

$$\tilde{a}_0\ddot{\tilde{f}}_3 + 3\dot{\tilde{a}}_0\dot{\tilde{f}}_3 = F_5(\tilde{a}_0,\tilde{a}_1,\tilde{f}_2), \tag{37}$$

$$\tilde{a}_0\ddot{\tilde{g}}_3 + 3\dot{\tilde{a}}_0\dot{\tilde{g}}_3 - \tilde{g}_3(\ddot{\tilde{a}}_0 - 6W_e^{-1}\tilde{a}_0^{-2}) = -5(\tilde{a}_0^4\ddot{\tilde{a}}_0 + 4\tilde{a}_0^3\dot{\tilde{a}}_0^2)/8, \tag{38}$$

where F_4 and F_5 are known functions of variables determined in the preceding orders of approximation. For the sake of conciseness the complete expressions are not given here but can be found along with more details of the calculations in [11].

Pressure Field. To sum up, the velocity potential in the outer problem can be written as follows:

$$\tilde{\phi}(\tilde{r},\theta,t) = -(\tilde{q}_0 + \epsilon\tilde{q}_1 + \epsilon^2\tilde{q}_2 + \epsilon^3\tilde{q}_3 + \epsilon^4\tilde{q}_4)(r^{-1} + \tilde{r}'^{-1}) + (\epsilon^3\tilde{h}_2 + \epsilon^4\tilde{h}_3)(\tilde{r}^{-2}\cos\theta - \tilde{r}'^{-2}\cos\theta') \tag{39}$$

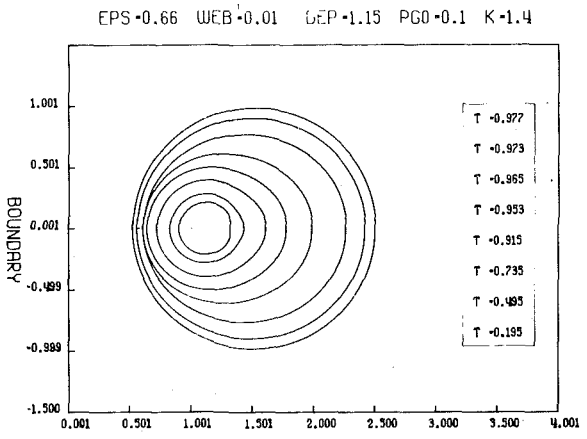

Fig. 2 Shape of the bubble at different times

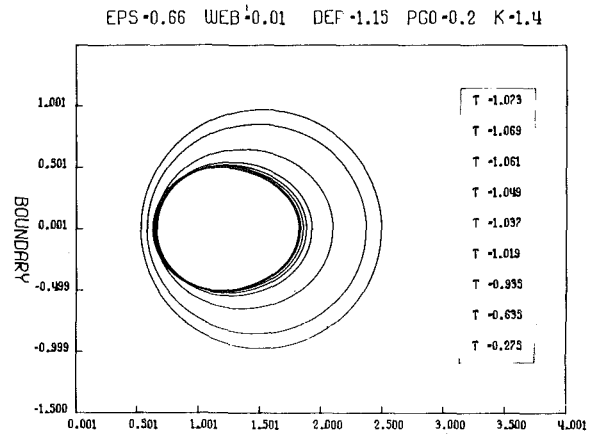

Fig. 3 Shape of the bubble at different times

$$+\epsilon^4 \tilde{K}_3(\tilde{r}^{-3}P_2(\cos\theta)+\tilde{r}'^{-3}P_2(\cos\theta')+0(\epsilon^4).$$

The pressure field is obtained by replacing $\tilde{\phi}$ by its value in the Bernoulli equation to give:

$$\tilde{p}=p_\infty - A_s\left[\epsilon\dot{\tilde{q}}_0+\epsilon^2\dot{\tilde{q}}_1+\epsilon^3\dot{\tilde{q}}_2+\epsilon^4\dot{\tilde{q}}_3\right] - \epsilon^4\Big[(\dot{\tilde{q}}_0\tilde{l}_2+\tilde{q}_0\dot{\tilde{l}}_2)E + \dot{\tilde{h}}_2(\cos\theta\cdot r^{-2}-B)+\tilde{q}_0\dot{\tilde{l}}_2\cos\theta\, A_e - \tilde{q}_0\dot{\tilde{l}}_2\sin\theta\, A_F+\tilde{q}_0^2 A_p\Big]+0(\epsilon^4) \tag{40}$$

where

$$A_s=\tilde{r}^{-1}+\tilde{r}'^{-1} \quad ; \quad A_e=\tilde{r}^{-2}+(\tilde{r}-2\cos\theta)\tilde{r}'^{-3}$$

$$E=2(2-\tilde{r})\cos\theta\cdot\tilde{r}'^{-3} \quad ; \quad A_F=2\sin\theta\cdot\tilde{r}'^{-3}$$

$$B=(2-\tilde{r}\cos\theta)\tilde{r}'^{-3} \quad ; \quad A_p=(A_e^2+A_F^2)/2$$

Once the evolution of the surface of the bubble and the velocity potential are determined, (41) allows a complete description of the pressure field and of its evolution with time.

Numerical Results

The equations (12), (20), (30), (36) to (38) constitute a system of seven equations with seven unknowns. Each of these equations is a differential equation of the second order which can be solved numerically by a Runge-Kutta procedure. Particularly the Rayleigh Plesset equation (12), and the origin of coordinates motion equation (34) are independent and can be solved easily to give $\tilde{a}_0$ and $\tilde{b}_2$. Equations (20) and (38) which depend on $\tilde{a}_0$ and equation (31) which depend on $\tilde{a}_0$ and $\tilde{b}_2$ can then be solved by the same procedure. The results are used to solve the remaining equations. This "multi-Runge Kutta" procedure is convergent and gives in few seconds of run on a Univac 1110 computer the collapse history of the bubble in some two thousands steps of time.

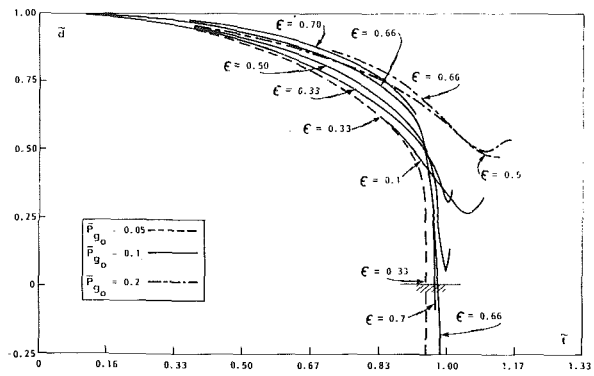

Fig. 4 Motion of the re-entering point on the bubble surface influence of ϵ and $\bar{P}_{g_0}, D_{ep} = 1.15, W_e^{-1} = 0.01$

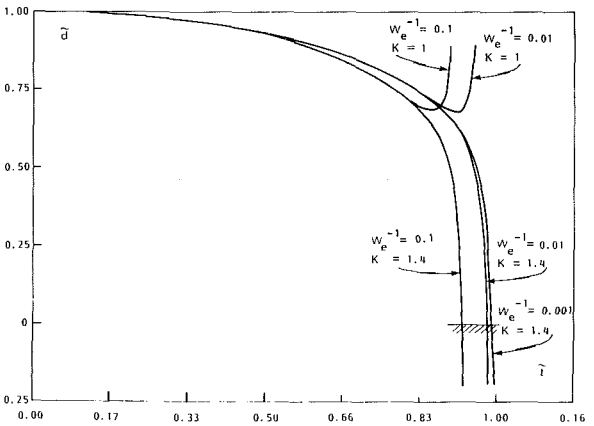

Fig. 5 Motion of the re-entering point on the bubble surface influence on K and W_e^{-1} $D_{ep} = 1.15, \epsilon = 0.66, \bar{P}_{g_0} = 0.1$

The results are illustrated in Figs. 2 and 3. In both figures the initial bubble-center to wall distance is 1.5 R_0. This is a classical case which was investigated in previous publications [5, 6, 7]. The numerical results of [5] were checked experimentally in [3]. This is an extreme case for the application of the method, considering the higher value of ϵ. However a qualitative agreement with the previous results and experiments is observed. Quantitatively, the time needed by the bubble wall to attain the initial position of the sphere's center is only five percent smaller than the results of reference [5]. As can be seen from the comparison between the two figures the influence of P_{g0} is very important. $\bar{P}_{g0} = 0.2$ gives a cushioned collapse followed by a rebound without the formation of a re-entering jet. On the other hand when $P_{g0} = 0.1$, a re-entering jet is clearly formed. At the time-step following $t = 0.977\ (\rho/P_0 - P_v)^2$, the motion of the jet overtakes that of the origin of coordinates, and the method no longer describes the bubble equation correctly. In order to investigate the influence of different parameters on the bubble wall motion, Figs. 4 and 5 compare the motion of the re-entering point on the bubble surface (point J in Fig. 1) in different cases. Figures 6 and 7 compare the motion of the origin of coordinates 0. We can see from Fig. 4, that decreasing the initial pressure of noncondensable gases inside the bubble $\bar{P}_{g_0}$ is as effective in increasing the violence of the bubble collapse as decreasing the bubble wall distance. This result also applies to the pressure field generated around the bubble, and thus to the erosive effect of collapse. Such

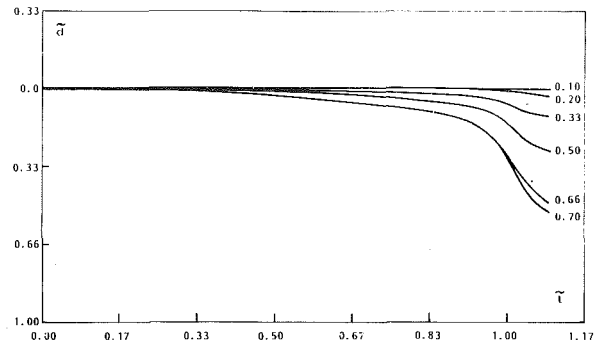

Fig. 6 Bubble center motion • influence of ϵ D_{ep} = 1.15 $\bar{P}_{g_0}$ = 0.1 W_e^{-1} = 0.01 K = 1.4

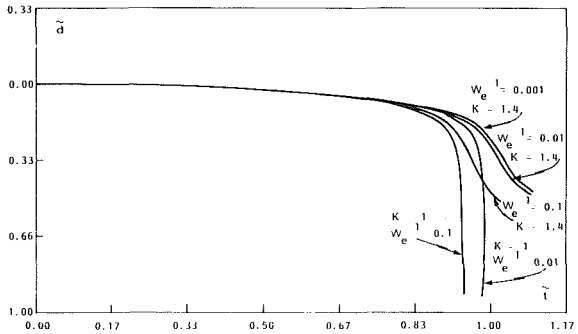

Fig. 7 Bubble center motion • influence of K, W_e^{-1} D_{ep} = 1.15, $\bar{P}_{g_0}$ = 0.1, ϵ = 0.66

behavior is expected since the gas acts as a spring cushioning the bubble implosion. The importance of the law of behavior of this gas, shown analytically in [4], is remarkably illustrated in Fig. 5 where the re-entering jet behavior is completely different between K = 1 and K = 1.4. However, the interpretation of the result is complicated: One would expect a faster collapse for the isothermal law. This is the case for the first order of approximation a_0. However, the corrections a_1, a_2, a_3, which are inversely dependent on a_0, are greater than in the more realistic adiabatic case. The isothermal collapse remains more energetic since the attraction of the bubble toward the wall is much higher (Fig. 7). This is reflected in the results obtained for the pressure field. Let us note, however, that the solution in the isothermal case loses its validity earlier in the collapse history since the ratio of the bubble radius to its distance from the wall increases faster than for the adiabatic case.

The influence of the surface tension can be reduced from Figs. 5 and 7. For high Weber numbers (W_e > 100) the motion of the re-entering point and of the center of the bubble are not very sensitive to a change of W_e. These motions become highly dependent on W_e for smaller values of this parameter. Surface tension effects are thus expected to become important with typical fluids for very small values of (R_0 • ΔP). A similar effect is known for spherical bubbles. The most interesting result concerning nonspherical bubble dynamics is the influence of ϵ (proximity of the wall) on the behavior of the re-entering jet and on the duration of collapse. As shown above, from considerations on the spherical corrections of the Rayleigh Plesset solution, a lengthening effect on the bubble collapse time is obtained with presence of a solid wall: The increase in the bubble life is directly proportional to ϵ. However, one would expect intuitively that the jet velocity would increase with ϵ and that the time needed for this jet to reach the opposite bubble wall can be smaller than the time needed for a spherical bubble to attain its maximum radius. This reasoning has been confirmed ex-

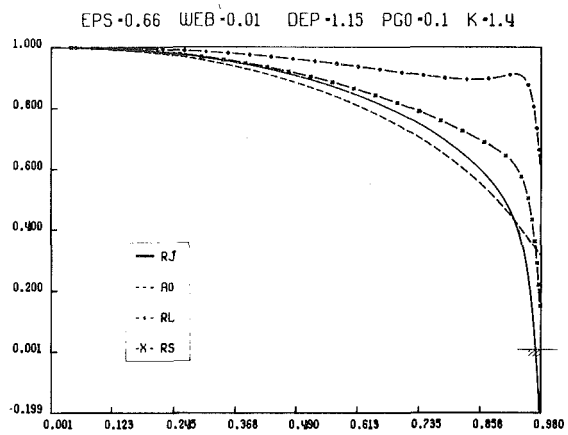

Fig. 8 Motion of characteristic points on the bubble

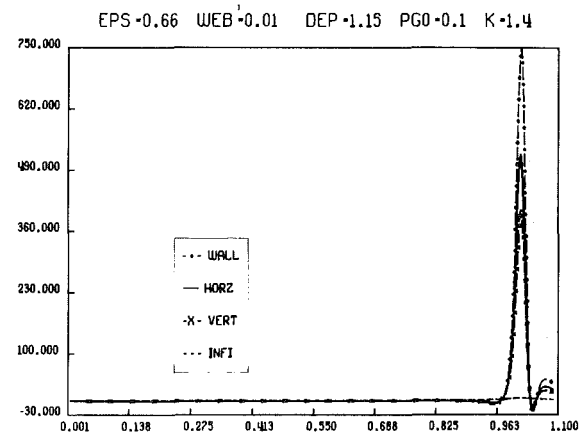

Fig. 9 Pressure versus time at different locations

perimentally [4, 12]. Figure 4 (and in more detail, Fig. 8) shows this effect: Unitl the latest stage of collapse, increasing ϵ increases, at a given time, the distance OJ (Fig. 1). This shows the tendency towards lengthening the bubble life. However, this tendency is reversed later. The speed of the jet increases with ϵ and the overall effect is to shorten the time needed for the re-entering jet to pierce the bubble. At the same time the attraction of the bubble towards the wall increases (Fig. 6). The effect of ϵ on O_0J is greater than on OJ since the effects on OJ and the wall distance are then added. A similar shortening effect has been reported in the case of a moving spherical bubble [13]. In Fig. 8, the evolution with time of the distances OJ, OL, OS (Fig. 1) as well as the spherical solution, a are plotted simultaneously. These lengths are, respectively, noted in the figure as RJ, RL, RS, and AO. The lengthening effect is clearly seen on RL and would be greater if the curve represented O_0L. On the contrary the collapse is faster for OS and especially of OJ, even without taking into account the motion of the origin. Let us note, however, that this is an extreme case, correspoding to Fig. 2. For nonviolent collapses (low values of ϵ or high values of $\bar{P}_{g_0}$) a lengthening effect exists.

In the last four figures we consider the pressure field around the collapsing bubble. This subject is a matter of concern, since earlier results seem to be contradictory. Mitchell and Hammitt [6] found that there was little pressure increase above ambient between the bubble and the wall. However Korovkin and Levkovskii [13] found, without taking into account the bubble deformation that the maximum value of the pressure on the nearby wall can be much higher than in the infinite medium case, if $\bar{P}_{g_0}$ is small. Here, we confirm this result without contradicting that of [6]. Figure 9 shows the evolution with time of the pressure on the

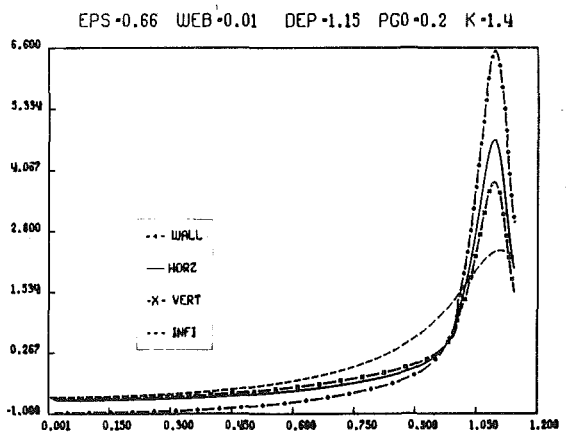

Fig. 10 Pressure versus time at different locations

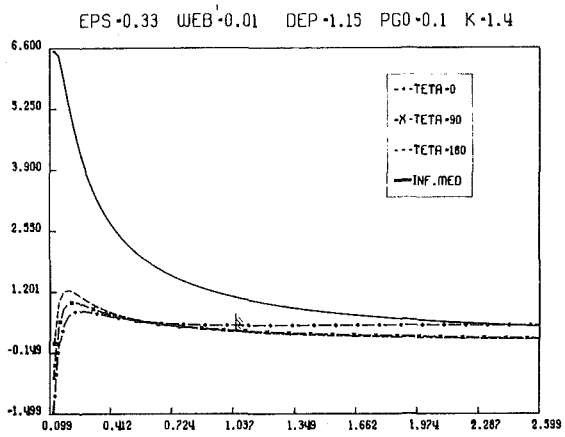

Fig. 11 Pressure versus radius for dif. angles at $\bar{T} = 0.914$

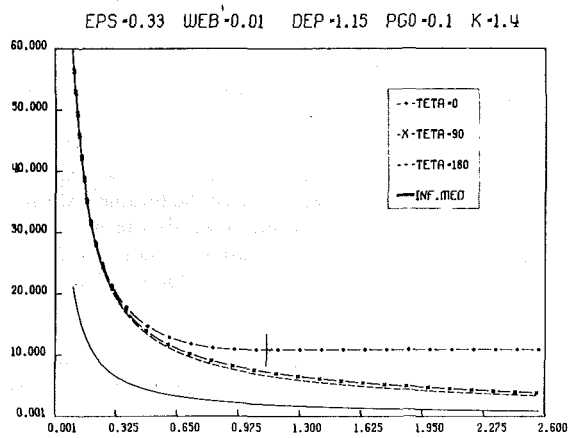

Fig. 12 Pressure versus radius for dif. angles at $\bar{T} = 0.949$

wall (point W, Fig. 1) and at two other points at a distance l_0 from 0—one on the axis of symmetry (noted VERT) and one in the plane parallel to the wall and passing through 0 (noted HORZ). These pressures are compared to that in an infinite medium (noted INFI). The presence of the wall greatly modifies the pressure field especially at W where the maximum pressure is two orders of magnitude higher than in the infinite medium. This maximum value drops significantly for a less violent collapse: Figure 10 shows that for $\bar{P}_{g_0} = 0.2$, it is only three times that in an infinite medium. For $\bar{t} < 1$, the pressure is reduced in the presence of the wall. This explains the results of [6] where the largest time in the calculations is smaller than the limiting time after which the pressures increase. These remarks are confirmed in Figs. 11 and 12. Where the variations of the pressure perturbation $\bar{p}$ with $\bar{r}$ are represented for different angles θ, at two times (0.914 and 0.949); $\theta = 0$ corresponds to the direction of the wall. We can see that in Fig. 11 the pressure field is smaller than that in an infinite medium and is very similar to that presented in [6]. However at $\bar{t} = 0.949$ (Fig. 12) the pressure in the entire field is higher than in the infinite medium case.

Conclusion

1. The method of matched asymptotic expansions is seen to be successful in describing the nonspherical bubble dynamics near a solid wall, including the generated pressure field during the bubble collapse. To study more complex boundaries one need only change the second member of the differential equations solved numerically.
2. The influence of the initial gas pressure and of its law of compression is as important as the proximity of the wall (ϵ).
3. Higher jet velocities are obtained for greater ϵ and smaller $\bar{P}_{g_0}$. An overall shortening effect of the bubble collapse time is obtained for intense collapses.
4. Pressures, orders of magnitude higher than in the spherical case, are generated on the nearby wall when the bubble is very close to it.
5. An amelioration of the method can be obtained by a closer look at the last stage of collapse. In particular, a change in the lengths and the time scales is needed, since the problem becomes singular in time at the end of the collapse.

Acknowledgments

The main part of this work was done while both authors were members of Groupe GPI at the Ecole Nationale Supérieure de Techniques Avancées, 32 Bd Victor Paris. We wish to thank the three organizations for their support.

References

1 Plesset, M. S., "Dynamics of Cavitation Bubbles," ASME *Journal of Applied Mechanics*, No. 16, 1948, pp. 228–231.

2 Naude, C. F., and Ellis, A. T., "On the Mechanisms of Cavitation Damage by Non-hemispherical Cavities Collapsing in Contact With a Solid Boundary," ASME *Journal of Basic Engineering*, Vol. 83, 1961, pp. 648–656.

3 Lauterborn, W., and Bolle, H., "Experimental Investigation of Cavitation Bubble Collapse in the Neighbourhood of a Solid Boundary," *Journal of Fluid Mechanics*, Vol. 2, No. 72, 1975, pp. 391–399.

4 Chahine, G. L., "Etude Locale du Phénomène de Cavitation: Analyse des Facteurs Régissant la Dynamique des Interfaces," Docteur es-sciences Thesis, University Pierre et Marie Curie, Paris, Mar. 1979.

5 Plesset, M. S., and Chapman, R. B., "Collapse of an Initially Spherical Vapor Cavity in the Neighbourhood of a Solid Boundary," *Journal of Fluid Mechanics*, Vol. 47, Part 2, 1971, pp. 283–290.

6 Mitchell, J. M., and Hammitt, F. G., "Asymmetric Cavitation Bubble Collapse," ASME *Journal of Fluids Engineering*, Mar. 1973, pp. 29–37.

7 Lenoir, M., "Calcul Numérique de l'Implosion d'une Bulle de Cavitation au Voisinage d'une Paroi on d'une Surface Libre," *Journal de Mécanique*, Vol. 15, No. 5, 1976, pp. 725–751.

8 Shima, A., and Nakajima, K., "The Collapse of a Non-hemispherical Bubble attached to a Solid Wall," *Journal of Fluid Mechanics*, Vol. 80, Part 2, pp. 386–391.

9 Chahine, G. L., and Bovis, A. G., "Oscillation and Collapse of a Cavitation Bubble in the Vicinity of a Two-Liquic Interface," *Proceedings Cavitation and Inhomogeneitis in Underwater Acoustics*, Göttingen, 1980, cd. Springer-Verlag.

10 Herring, C., "Theory of the Pulsations of the Gas Bubbles Produced by an Underwater Explosion," Columbia Univ., NDRC Report C4SR20-010, 1941.

11 Bovis, A. G., "Etude Asymptotique du Phénomène de Cavitation Cavités non sphériques," Docteur-Ingenieur Thesis, University et Marie Curie, Paris, June 1980.

12 Chahine, G. L., and Fruman, D. H., "Dilute Polymer Solution Effects on Bubble Growth and Collapse," *Physics of Fluids*, Vol. 22, No. 7, 1979, pp. 1406–1407.

13 Korovkin, A. N., and Levkovskii Yu. L., "Study of the Collapse of a Cavitation Cavity Close to a Solid Wall," *Journal of Engineering Physics*, Vol. 12, No. 2, 1967, pp. 246–253. (in Russian)

14 Van Dyke, M., *Perturbation Methods in Fluid Mechanics*, Academic Press, 1964.

DISCUSSION

F. G. Hammitt[1]

This paper concerning the analysis of the collapse of nonspherical bubbles near solid walls, using a method of matched asymptotic expansions rather than a full numerical treatment of the problem, which is very expensive in machine time, is most welcome, and I believe a highly important contribution to this extremely complex, and also important problem. As the authors suggest, I hope they will have the opportunity to carry further this valuable approach to the cases of several bubbles in close proximity to each other, and also to an elastic rather than rigid wall. Both cases are certainly highly important to the understanding of the actual cavitation damage process, and also to the use of elastomeric coatings for alleviating damage.

It is encouraging that they find that their method produces reasonably valid results when bubble wall distance is only 1.5 × original bubble radius, by comparing with more exact past numerical treatments (authors' [5–7]). I wonder what is the minimum distance ratio for which they feel their method could be applied?

I am happy they they have resolved a previous disagreement between our previous treatment (authors' reference [6]) and another earlier work (authors' reference [13]), which had appeared to disagree. They now conclude that the pressure near the wall can be very large indeed under certain conditions, which we had not previously predicted (reference [6]).

Their conclusion that initial gas pressure and its law of compression can be more important than wall proximity is interesting, and I believe unexpected, since the volume collapse ratio is usually not enormous before the generation of a microjet.

[1] W. E. Lay Auto Lab - North Campus, Mechanical Engineering, The Univ. of Michigan, Ann Arbor, Mich. 48109

[2] Ivany, R. D., and Hammitt, F. G., "Cavitation Bubble Collapse in Viscous, Compressible Liquids," *Journal of Basic Engineering*, Vol. 87, No. 4, 1965, pp. 977–985.

Authors' Closure

We very much appreciate Professor Hammitt's comments and would like to thank him for giving us the opportunity to present an update on the progress made using the method described here. We first presented this paper at the ASME Symposium on Cavitation Erosion in Fluid Systems, Boulder, Colo., June 1981. Since then, the method has proven successful in studying the nonspherical behavior near a free surface [1], and more importantly, has been extended to the study of the interaction of a cloud of bubbles [2, 3]. A major influence of the collective behavior on the bubble dynamics and on the generated pressure field has been shown. We share Professor Hammitt's view on the importance of the study of elastomeric coatings. Unfortunately, we have not yet had the chance to pursue our initial approach [4] of that problem and hope to do it soon.

The matched asymptotic method we have used in this paper is valid as long as the bubble radius to wall distance ratio, ϵ, is small compared to one. We have pushed the method a little too far by applying it to a value of ϵ, of 2/3. The last phase of the collapse is the hardest to describe, and depending on the bubble gas content and on ϵ, the method fails earlier or later in the bubble history. Here we address the last comment of the discussant. We believe that the volume collapse ratio before the generation of a microjet is a function of both the wall proximity and gas content; for a given bubble wall configuration, the less noncondensible gas the bubble contains, the earlier the microjet forms. Thus, the formation of a microjet and of large bubble deformations (limit of application of the method) is function as much of gas content as of bubble wall proximity.

Additional References

1 Bovis, A., and Chahine, G. L., "Etude Asymptotique de l' Interaction d' une Bulle Oscillante avec une Surface Libre Voisine," *Journal de Mécanique*, Vol. 20, No. 3, 1981, pp. 537–556.

2 Chahine, G. L., "Pressures Generated by a Bubble Cloud Collapse," ASME *Cavitation and Polyphase Flow Forum*, St. Louis, Mo. 1982, pp. 27–31.

3 Chahine, G. L., "Cloud Cavitation: Theory," *Proceedings 14th Symposium on Naval Hydrodynamics*, Ann Arbor, Mich. 1982, pp. 165–195.

4 Chahine, G. L., Cohen D., Ducasse, P. and Ligneul, L., "Influence d' un Revêtement Elastique sur le Collapse d' une Bulle au Voisinage d' une Paroi Solide," *Proceedings 4th Int.* Meeting on Water Column Separation, Cagliari, Italy, Sept. 1982.

Journal of Fluids Engineering

Technical Briefs

On the Skin Friction Coefficient for a Fully Rough Flat Plate

A. F. Mills[1] and Xu Hang[1]

A comparison of the Prandtl-Schlichting formula for skin friction of a fully rough plate with recently obtained experimental data shows an average error of 17.5 percent. It is suggested that the reason for this discrepancy is a failure to account for the wake component of the velocity profile. The integral momentum equation is used to derive a new skin friction theory which when compared to the same data gives an average error of 2.7 percent. A new skin friction formula is proposed which is valid over a wide parameter range.

Nomenclature

- C_f = local skin friction coefficient $= \tau_w/\frac{1}{2}\rho u_e^2$
- C_D = $1/L\int_0^L C_f dx$, drag coefficient for plate of length L
- k_s = equivalent sand grain roughness
- L = plate length
- u = streamwise velocity component
- u_e = freestream velocity
- v^* = $(\tau_w/\rho)^{1/2}$, friction velocity
- x = streamwise coordinate
- y = coordinate perpendicular to plate
- y^+ = yv^*/ν
- δ = boundary layer thickness, as defined by wake velocity component
- κ = von Karman's constant
- ν = kinematic viscosity
- θ = $\int_0^\delta \frac{u}{u_e}\left(1-\frac{u}{u_e}\right)dy$, momentum thickness
- ρ = density
- τ_w = wall shear stress

The need to calculate skin friction for a turbulent boundary layer on a flat plate is encountered in many areas of technology, e.g., ships, aircraft, and turbines. Widely used for this purpose are charts originally calculated by Prandtl and Schlichting in 1934, and conveniently found in Schlichting's text on boundary layer theory [1]. The charts are based on the velocity profiles measured by Nikuradse for pipes roughened with uniform sand grains [2]. For the fully rough regime ($k_s^+ \gtrsim 60$) the charts may be used for other types of roughness pattern by invoking the concept of an equivalent sand grain roughness: indeed it is in this manner that the charts find their widest use since sand grain roughness is seldom encountered in practice. For the fully rough regime simple interpolation formulae are recommended by Schlichting, viz.,

$$C_f = \left(2.87 + 1.58 \log \frac{x}{k_s}\right)^{-2.5} \tag{1}$$

$$C_D = \left(1.89 + 1.62 \log \frac{L}{k_s}\right)^{-2.5} \tag{2}$$

which are claimed to be valid for $10^2 < L/k_s < 10^6$. Also White [3] has presented an analysis in which C_f is determined using his inner-variable approach and a velocity profile

$$u^+ = \frac{1}{\kappa} ln y^+ + 5.5 - \frac{1}{\kappa} ln(1 + 0.3 k_s{}^+) \tag{3}$$

which for a fully rough wall and $\kappa = 0.40$ recovers Nikuradse's velocity profile,

$$u^+ = 2.5 ln\left(\frac{y}{k_s}\right) + 8.5 \tag{4}$$

while giving a smooth transition between the smooth and fully rough regimes. For the fully rough regime White obtains

$$C_f = \left(1.4 + 3.7 \log \frac{x}{k_s}\right)^{-2} \tag{5}$$

for $x/k_s > 100$ and claims this result to be equivalent to the Prandtl-Schlichting formula to within about 5 percent.

Recently there has been an extensive investigation into turbulent boundary layers of air on surfaces roughened with close-packed spheres at Stanford University [4, 5]. In the fully rough regime Pimenta et al. [5] obtained skin-friction data in the range $750 < x/k_s < 2750$, and found deviations from equation (1) of up to 25 percent. No reason for the discrepancy was advanced. The purpose of this note is to show why the Prandtl-Schlichting formula is inadequate in this parameter range, and to give a new improved formula in its place.

The shortcoming of the Prandtl-Schlichting and White formulas for C_f is that they both ignore the wake component of the velocity profile. The fact that the same velocity defect law is valid for both smooth and rough wall flat plate boundary layers is well known, based on the experimental data of, for example, Hama [6]. Pimenta et al. [5] showed that the defect law based on Coles' law of wake [7], viz.,

$$u_e{}^+ - u^+ = -\frac{1}{\kappa} ln\left(\frac{y}{\delta}\right) + \frac{\Pi}{\kappa}\left[2 - 2\sin^2\left(\frac{\pi}{2}\frac{y}{\delta}\right)\right] \tag{6}$$

was in good agreement with their measured velocity profiles,

School of Engineering and Applied Science, University of California, Los Angeles, Calif. 90024. Mr. Hang's permanent address is the Wangting Power Plant, Shanghai, Peoples Republic of China.

Contributed by the Fluids Engineering Division of THE AMERICAN SOCIETY OF MECHANICAL ENGINEERS. Manuscript received by the Fluids Engineering Division, May 11, 1982.

Table 1 Comparison of the Prandtl-Schlichting formula and the new theory with the skin friction data of Pimenta et al. [5]

		Equation (1)		Equation (10)	
x/k_s	$C_f/2$, experiment	$C_f/2$	% error	$C_f/2$	% error
758	0.00267	0.00333	24.9	0.00286	7.0
1145	0.00252	0.00304	20.0	0.00262	4.0
1532	0.00239	0.00285	19.2	0.00247	3.4
1919	0.00231	0.00271	17.4	0.00236	2.3
2306	0.00226	0.00261	15.5	0.00228	0.8
2694	0.00222	0.00253	13.8	0.00221	−0.3
838	0.00261	0.00326	24.8	0.00280	7.2
1226	0.00252	0.00299	18.7	0.00258	2.5
1613	0.00243	0.00282	15.9	0.00244	0.0
2000	0.00236	0.00269	14.0	0.00234	−0.8
2387	0.00229	0.00259	13.2	0.00226	−1.2
2774	0.00224	0.00251	12.1	0.00220	−1.8

for $\kappa=0.41$ and $\Pi=0.55$. The corresponding velocity profile in terms of inner variables is, for fully rough walls,

$$u^+ = \frac{1}{\kappa} ln\left(\frac{y}{k_s}\right) + 8.5 + \frac{\Pi}{\kappa} 2\sin^2\left(\frac{\pi}{2}\frac{y}{\delta}\right) \tag{7}$$

The use of Nikuradse's result of $u^+=8.5$ at $y=k_s$ implies definition of equivalent sand grain roughness such that $u^+=8.5$ at $y=k_s$. Schlichting [8] used this definition to deduce $k_s=0.627$ times diameter for closely packed spheres, which for Pimenta's surface gives $k_s=0.79$ mm. Checking Pimenta's velocity profiles gives a range of u^+ (k_s) from 8.24 to 8.95 with a mean of 8.49. Thus $k_s=0.79$ mm appears to be a reasonable characterization of Pimenta's surface.

The velocity profile may be used to calculate the momentum thickness to give

$$\frac{\theta}{k_s} = \left(\frac{3.78}{u_e{}^+} - \frac{25.0}{u_e{}^{+2}}\right) e^{0.41(u_e{}^+ - 11.18)};\ u_e{}^+ = \sqrt{2/C_f} \tag{8}$$

for $\kappa=0.41$, $\Pi=0.55$. The integral momentum equation is $C_f/2=d\theta/dx$: substituting equation (8) and rearranging gives

$$\frac{d}{du_e{}^+}\left(\frac{x}{k_s}\right) = e^{0.41(u_e{}^+ - 11.18)}\left(\frac{50}{u_e{}^+} - 14.03 + 1.55u_e{}^+\right) \tag{9}$$

which was solved using a Runge-Kutta integration routine, with x measured from the virtual origin of the turbulent boundary layer. The resulting C_f distribution was curve-fitted for convenience as

$$C_f = \left(3.476 + 0.707 ln\frac{x}{k_s}\right)^{-2.46} \tag{10}$$

which is accurate to within 1 percent in the range $150 < x/k_s < 1.5\times10^7$. A further numerical integration yields the drag coefficient C_D which was curve fitted as

$$C_D = \left(2.635 + 0.618 ln\frac{L}{k_s}\right)^{-2.57} \tag{11}$$

Table 2 Comparison of the Prandtl-Schlichting formula for skin friction with equation (10) over a large range of x/k_s

	$C_f/2$		
x/k_s	Equation (1)	Equation (10)	% Difference
1×10^2	0.00560	0.00459	22.02
2	0.00463	0.00386	19.92
5	0.00368	0.00313	17.74
1×10^3	0.00313	0.00269	16.19
2	0.00269	0.00274	14.88
5	0.00223	0.00197	13.31
1×10^4	0.00195	0.00174	12.14
2	0.00172	0.00155	11.28
5	0.00147	0.00133	10.23
1×10^5	0.00131	0.00120	9.22
2	0.00118	0.00108	8.90
5	0.00103	0.00095	8.07
1×10^6	0.00093	0.00087	7.06

which is about as accurate as equation (10). Table 1 compares equation (10) with the experimental data of Pimenta et al. The average absolute deviation for equation (1) is 17.5 percent while for equation (10) it is only 2.7 percent. Thus it is concluded that the theory underlying equation (11) is in good accord with experiment in this parameter range. Table 2 compares equation (1) and equation (10) over a wide range of x/k_s.

To examine the impact of using equation (11) versus equation (2) consider a high speed underwater vehicle of length 3 m and equivalent sand grain roughness 0.25 mm, giving $L/k_s=12{,}000$. Equation (11) gives $C_D/2=0.00208$ while equation (2) gives 0.00237 which is 14% higher. Since skin drag contributes in excess of 80 percent of the total drag of such vehicles, such a discrepancy has a significant effect on estimates of vehicle speed.

References

1 Schlichting, H., *Boundary Layer Theory*, 6th ed., McGraw-Hill, New York, 1968, pp. 611–612.

2 Nikuradse, J., "Laws of Flow in Rough Pipes," NACA TM 1292, 1950.

3 White, F. M., *Viscous Fluid Flow*, McGraw-Hill, New York, 1974, p. 503.

4 Healzer, J. M., Moffat, R. J., and Kays, W. M., "The Turbulent Boundary Layer on a Rough Porous Plate: Experimental Heat Transfer with Uniform Blowing," Report No. HMT-18, Thermosciences Division, Department Mechanical Engineering, Stanford University, 1974.

5 Pimenta, M. M., Moffat, R. J., and Kays, W. M., "The Turbulent Boundary Layer: An Experimental Study of the Transport of Momentum and Heat with the Effect of Roughness," Report No. HMT-21, Thermosciences Division, Department of Mechanical Engineering, Stanford University, May 1975.

6 Hama, F. R., "Boundary-Layer Characteristics for Smooth and Rough Surfaces," *Trans. Soc. Naval Arch. and Marine Eng.*, Vol. 62, 1954, pp. 333–358.

7 Coles, D., "The Law of the Wake in the Turbulent Boundary Layer," *Journal of Fluid Mech.*, Vol. 1, Part 2, 1956, pp. 191–226.

8 Schlicting, H., *Boundary Layer Theory*, 6th ed., McGraw-Hill, New York, 1968, pp. 586–587.

Journal of Fluids Engineering

Discussion

LDV Measurements Near a Vortex Shedding Strut Mounted in a Pipe[1]

Z. D. Husain.[2] Reported results reflect a very carefully conducted experiment, and data are precise, for which authors must be commended. Since these data were not addressing azimuthal effects of the circular pipe, results from similar experiments in a rectangular test-section could possibly resolve the question on the existence of any noticeable three-dimensional or azimuthal influence of this flow facility.

In "Apparatus and Techniques," the authors stated "Throughout most of the pipe, the nonlinearity of the position was smaller than the length of the measuring volume . . ." This statement is vague. Relatively large errors due to nonlinearity is expected near the wall, especially at $y/D \approx \pm 0.5$. Again, those locations are not of major concern to data presented here. Hence, defining regions of large errors in the probe-volume location could be expressed in terms of y/D.

Data over $y/D < 0$ were generated by assuming symmetry or antisymmetry (as the case may be), hence lines over that region should not be drawn with any data symbol. Plotting with symbols over the entire flow field tend to imply that actual data were obtained. Again, the same symbol is used for all x/D locations, hence symbols are not essential to the plot. Please refer to plots by Kovasznay (reference [1]) and Durgin and Karlson (reference [2]), where one-half of the plot does not have any data symbol because data were not actually acquired.

It is stated that to handle data uncertainty in both time and space due to randomness associated with high-Reynolds number flows, the velocity power-spectral density was obtained to measure different fluctuating-velocity components relating to vortices. Since conventional true-RMS meters do not distinguish between the random part from the periodic part, how did authors measure the random part of the turbulence intensity? The total turbulence intensity can be obtained from the velocity power spectrum. From Fig. 10, it appears that the total turbulence intensity u_T is the vector sum of the random and two periodic components. A statement relating to the actual data acquisition method of different fluctuating-velocity components would be helpful. Please note that spectral averaging does not resolve the uncertainty in space/time randomness.

Figure 9 is a presentation of typical plot of the power spectral density, but has no reference to locations in y/D. I presume that the probe volume is near the path of the vortex center, because the spectrum shows noticeably large peaks at the fundamental vortex shed-frequency. A velocity signal which is not exactly sinusoidal in the frequency domain, through Fourier decomposition will show peaks at higher harmonics of the fundamental. Authors state that the "worst" spectrum in Fig. 9 is at x/D of 0.63. The velocity signal at that x/D location is expected to have high energy at the fundamental mode in the frequency domain. Hence, randomness in strength, shape and size of the vortex along with space/time dependence will result in peaks at higher harmonics of the fundamental mode in the frequency domain. From the controlled excitation study of a circular jet, Zaman and Hussain [8] reported nonsinusoidal velocity signals in the time domain even when very repetitive vortex structures were shed at the exit of an axisummetric jet. Note that velocity signals behind a cylinder is also nonsinusoidal (reference [1]). Spectra of such velocity signals show peaks at higher harmonics (Zaman and Hassain). Hence, there is nothing wrong with the "worst" spectrum in Fig. 9. Velocity signals at locations away from the path of the vortex center is not an exact sinusoid. Figure 10 showing peaks at the first harmonic of the fundamental and associated with decrease in the fundamental at $y/D \approx 0$ and $y/D \approx 0.5$ is consistent with the flow phenomenon.

Figure 14 shows that with increasing x/D there is a continual decrease in u_1/U_b values and increase in u_2/U_b values. Note also that with increasing distances from the strut, alternately shed vortices effectively double the vortex-passage frequency, thereby in the frequency domain a noticeable peak is observed at the first harmonic of the fundamental. Similar velocity signals were reported by Kovasznay (reference [1], Fig. 12), and Zaman and Hussain.

Conditionally sampled data could provide further insight into the vortex structure in space and in time domain when sampled at different phases of their evolution.

Additional Reference

8 Zaman, K. B. M. Q., and Hussain, A. K. M. F., "Vortex Pairing in a Circular Jet Under Controlled Excitation. Part I. General Jet Response," *J. Fluid Mechanics*, Vol. 101, 1980, pp. 449-491.

Note: Definition reads $v_T = (\Sigma v_n^2 + v_n^2)^{1/2}$; second subscript on the right-hand side of the equation should be "t" and not "n".

Authors' Closure

We thank Dr. Z. D. Husain for his discussion. We will answer paragraph by paragraph the questions he raised.

The azimuthal dependence of the incoming flow in our facility has been tested by comparing two perpendicular profiles at $x/D = -0.71$. The profiles were both symmetric and agreed with each other within better than 0.5 percent except within 2mm of the wall, where the agreement was within 1 percent. This shows that our facility produces axisymmetric flow. Also, profiles of the longitudinal velocity were taken along horizontal diameters at $x/D = 0.63$, 0.83, and 3.13 with the splitter plate vertical. Then the strut was rotated 90 degrees, and the same profiles were taken along vertical diameters with the splitter plate horizontal. The

[1] By T. T. Yeh, B. Robertson, and W. M. Mattar, published in the June 1983 issue of the JOURNAL OF FLUIDS ENGINEERING, Vol. 105, No. 2, pp. 185-196.

[2] Corporate R&D, Daniel Industries Inc., Houston, Texas 77224.

corresponding profiles agreed within better than one percent, showing again that the upstream flow from our flow facility is axisymmetric.

The point closest to the wall for which the velocities were measured is at $y/D = 0.48$ and $z/D = 0$ (with the splitter plate horizontal). At this point the nonlinearity in y/D is about 0.008 and in z/D about 0.004. At other points where the velocities were measured, the nonlinearity in the position calibration was too small to be measured. The largest contribution to position uncertainty is the approximately 1.5 mm $\times$ 0.15 mm size of the measuring volume in the 52 mm diameter pipe.

We agree it would have been better to plot symbols only where data were actually taken.

To determine the magnitudes of the periodic velocity components, we measured the area under the corresponding peak in the power spectrum as described on page 192. The level of random signal subtracted was determined by averaging 5 data points on each side of the 21 points and interpolating linearly between the two averages.

The spectra of Fig. 9 were taken at $y/D = 0.096$ ($y = 5$mm) and $z/D = 0$ for all three values of x/D listed. The 3rd harmonic of the velocity signal was smaller than about 1 percent of the larger of the 1st or 2nd harmonics at all points where data were taken. We chose the word "worst" only to express this point, not to suggest that anything was wrong. Harmonics higher than the third were too small to be measured. We agree that periodic signals in general exhibit higher harmonics. We would certainty have observed them in our experiment if they were larger than the turbulence at that frequency. To a good approximation, the only components that are there are just the mean, the fundamental, the second harmonic, and broadband turbulence.

As noted on page 194, vortices passing on both sides of the centerline cause a maximum in the second harmonic u_2 of the longitudinal velocity but a zero value for the second harmonic v_2 of the transverse velocity on the centerline. By second harmonic, we mean the component at twice the frequency of the first harmonic or fundamental.

Interference Between Two Circular Cylinders of Finite Height Vertically Immersed in a Turbulent Layer[1]

M. M. Zdravkovich.[2] The authors are to be complimented for an excellent and detailed pressure measurement on one of two interferring cylinders at $R_e = 1.55 \times 10^4$. The height to diameter ratio of both cylinders was only 3 and the thickness of the turbulent boundary layer along the wall on which the cylinders were attached was 0.86 of the cylinder height. At the base of the cylinders near the ground, the turbulent boundary layer presumably rolled down and formed a strong horse-shoe eddy. At the free-end, the flow was deflected upwards on the upstream side and pressure coefficient could not reach the value of one. The extent of these two regions probably overlapped for short $h/d = 3$ and it *should* have resulted in a complete suppression of eddy shedding in the wakes of both cylinders. This inference seems to be supported by the measured values of the base pressure coefficient, C_{p180} being in the range -0.3 to -0.6. These are considerably above the values of -1.2 to -1.4 found behind the nominally two-dimensional cylinder at the same Reynolds number. The overall drag coefficient of 0.65 is almost half of that produced by the nominally two-dimensional cylinder. However, the authors did not mention eddy shedding and my first question is whether they found that the eddy shedding was suppressed for all arrangements tested.

If my inference about the suppressed eddy shedding is correct then the authors demonstration of a qualitative similarity of the interference effects between the short finite cylinders and nominally two-dimensional ones gives a new insight into the phenomena involved. The biased jet in side-by-side arrangements reappeared between the short cylinders despite the absence of eddy shedding and presence of the strong horse-shoe eddy and end-effects. The bistable nature of that phenomenon was demonstrated in Fig. 10, but single values for C_D and C_L were plotted in Figs. 13 and 14. There must have been intermittent occasions when the monitored cylinder experienced the jet-switch and produced different pressure distribution. My second question to the authors concerns the effect of bistable jet swich on the overall C_L and C_D.

There is another flow instability in slightly staggered arrangements when the strong gap flow between the cylinders may suddenly cease and result in a discontinuous change of C_L. This gap flow switch was a prominent feature of the interference between the two nominally two-dimensional cylinders. The authors chain-dot line $C_{L\max}$ in Fig. 13 is located in the region where the gap flow instability should be expected. The question is whether similar gap flow switch was observed by the authors.

The tandem arrangements displayed a typical change in pressure distribution on the upstream side as seen in Fig. 8(*a*) for $s/d = 3$ and 4. This always produced discontinuous jump in C_D (reference [10]). This jump, however, is not shown in Fig. 14 and the authors comment's will be helpful.

The effect of Reynolds number was not mentioned in the paper. The beautiful flow visualization photographs shown in Fig. 10 were obtained at R_e about 620. The flow pattern should not be expected to be identical for $R_e = 1.55 \times 10^4$ at which pressure distributions were measured. The difference of two flows is caused not only by the laminar boundary layer along the wall, as stated by the authors, but also due to long laminar free-shear layers separated from the cylinders. The transition in free shear layers at $R_e = 1.55 \times 10^4$ is expected to be not further than 0.5D from the separation. The simulation of turbulent boundary layers on both cylinders in reference [11], was done with the aim of simulating post-critical flow regime. However, despite the strong Reynolds number effect an extremely valuable qualitative insight can be gained from Fig. 10. May I ask the authors what was the height of the smoke-wire relative to the height of the cylinders and could they show some photographis for $y/h = 0.11$ and $y/h = 0.89$? The first will reveal three-dimensional flow due to the horse-shoe eddy (as in reference [14]), while the second equally intriguing one will show three-dimensional flow around the free end.

Finally the inferred double flow structure by the discusser along the height of the short cylinders can be proved or disproved by presenting equilift and equidrag lines for local sections. The horse-shoe flow structure will strongly affect local C_D and C_L at $y/H = 0.11$ while the free-end effect will dominate local C_L and C_D at $y/H = 0.89$. The present Figs. 13 and 14 hide these two separate effects.

Additional Reference

14 Taniguchi, S., Sakamoto, H., and Arie, M., "Flow Around a Circular Cylinder of Finite Height Placed Vertical in Turbulent Boundary Layers," *Bull. J.S.M.E.*, Vol. 24, No. 187, 1981, pp. 37–44.

[1] By Taniguchi, S., Sakamoto, H., and Arie, M., published in the December 1982 issue of the ASME JOURNAL OF FLUIDS ENGINEERING, Vol. 104, No. 4, pp. 529–536.

[2] University of Salford, Salford, U.K. Mem. ASME.

corresponding profiles agreed within better than one percent, showing again that the upstream flow from our flow facility is axisymmetric.

The point closest to the wall for which the velocities were measured is at $y/D = 0.48$ and $z/D = 0$ (with the splitter plate horizontal). At this point the nonlinearity in y/D is about 0.008 and in z/D about 0.004. At other points where the velocities were measured, the nonlinearity in the position calibration was too small to be measured. The largest contribution to position uncertainty is the approximately 1.5 mm $\times$ 0.15 mm size of the measuring volume in the 52 mm diameter pipe.

We agree it would have been better to plot symbols only where data were actually taken.

To determine the magnitudes of the periodic velocity components, we measured the area under the corresponding peak in the power spectrum as described on page 192. The level of random signal subtracted was determined by averaging 5 data points on each side of the 21 points and interpolating linearly between the two averages.

The spectra of Fig. 9 were taken at $y/D = 0.096$ ($y = 5$mm) and $z/D = 0$ for all three values of x/D listed. The 3rd harmonic of the velocity signal was smaller than about 1 percent of the larger of the 1st or 2nd harmonics at all points where data were taken. We chose the word "worst" only to express this point, not to suggest that anything was wrong. Harmonics higher than the third were too small to be measured. We agree that periodic signals in general exhibit higher harmonics. We would certainty have observed them in our experiment if they were larger than the turbulence at that frequency. To a good approximation, the only components that are there are just the mean, the fundamental, the second harmonic, and broadband turbulence.

As noted on page 194, vortices passing on both sides of the centerline cause a maximum in the second harmonic u_2 of the longitudinal velocity but a zero value for the second harmonic v_2 of the transverse velocity on the centerline. By second harmonic, we mean the component at twice the frequency of the first harmonic or fundamental.

Interference Between Two Circular Cylinders of Finite Height Vertically Immersed in a Turbulent Layer[1]

M. M. Zdravkovich.[2] The authors are to be complimented for an excellent and detailed pressure measurement on one of two interferring cylinders at $R_e = 1.55 \times 10^4$. The height to diameter ratio of both cylinders was only 3 and the thickness of the turbulent boundary layer along the wall on which the cylinders were attached was 0.86 of the cylinder height. At the base of the cylinders near the ground, the turbulent boundary layer presumably rolled down and formed a strong horse-shoe eddy. At the free-end, the flow was deflected upwards on the upstream side and pressure coefficient could not reach the value of one. The extent of these two regions probably overlapped for short $h/d = 3$ and it *should* have resulted in a complete suppression of eddy shedding in the wakes of both cylinders. This inference seems to be supported by the measured values of the base pressure coefficient, C_{p180} being in the range -0.3 to -0.6. These are considerably above the values of -1.2 to -1.4 found behind the nominally two-dimensional cylinder at the same Reynolds number. The overall drag coefficient of 0.65 is almost half of that produced by the nominally two-dimensional cylinder. However, the authors did not mention eddy shedding and my first question is whether they found that the eddy shedding was suppressed for all arrangements tested.

If my inference about the suppressed eddy shedding is correct then the authors demonstration of a qualitative similarity of the interference effects between the short finite cylinders and nominally two-dimensional ones gives a new insight into the phenomena involved. The biased jet in side-by-side arrangements reappeared between the short cylinders despite the absence of eddy shedding and presence of the strong horse-shoe eddy and end-effects. The bistable nature of that phenomenon was demonstrated in Fig. 10, but single values for C_D and C_L were plotted in Figs. 13 and 14. There must have been intermittent occasions when the monitored cylinder experienced the jet-switch and produced different pressure distribution. My second question to the authors concerns the effect of bistable jet swich on the overall C_L and C_D.

There is another flow instability in slightly staggered arrangements when the strong gap flow between the cylinders may suddenly cease and result in a discontinuous change of C_L. This gap flow switch was a prominent feature of the interference between the two nominally two-dimensional cylinders. The authors chain-dot line $C_{L\max}$ in Fig. 13 is located in the region where the gap flow instability should be expected. The question is whether similar gap flow switch was observed by the authors.

The tandem arrangements displayed a typical change in pressure distribution on the upstream side as seen in Fig. 8(*a*) for $s/d = 3$ and 4. This always produced discontinuous jump in C_D (reference [10]). This jump, however, is not shown in Fig. 14 and the authors comment's will be helpful.

The effect of Reynolds number was not mentioned in the paper. The beautiful flow visualization photographs shown in Fig. 10 were obtained at R_e about 620. The flow pattern should not be expected to be identical for $R_e = 1.55 \times 10^4$ at which pressure distributions were measured. The difference of two flows is caused not only by the laminar boundary layer along the wall, as stated by the authors, but also due to long laminar free-shear layers separated from the cylinders. The transition in free shear layers at $R_e = 1.55 \times 10^4$ is expected to be not further than 0.5D from the separation. The simulation of turbulent boundary layers on both cylinders in reference [11], was done with the aim of simulating post-critical flow regime. However, despite the strong Reynolds number effect an extremely valuable qualitative insight can be gained from Fig. 10. May I ask the authors what was the height of the smoke-wire relative to the height of the cylinders and could they show some photographis for $y/h = 0.11$ and $y/h = 0.89$? The first will reveal three-dimensional flow due to the horse-shoe eddy (as in reference [14]), while the second equally intriguing one will show three-dimensional flow around the free end.

Finally the inferred double flow structure by the discusser along the height of the short cylinders can be proved or disproved by presenting equilift and equidrag lines for local sections. The horse-shoe flow structure will strongly affect local C_D and C_L at $y/H = 0.11$ while the free-end effect will dominate local C_L and C_D at $y/H = 0.89$. The present Figs. 13 and 14 hide these two separate effects.

[1] By Taniguchi, S., Sakamoto, H., and Arie, M., published in the December 1982 issue of the ASME JOURNAL OF FLUIDS ENGINEERING, Vol. 104, No. 4, pp. 529–536.

[2] University of Salford, Salford, U.K. Mem. ASME.

Additional Reference

14 Taniguchi, S., Sakamoto, H., and Arie, M., "Flow Around a Circular Cylinder of Finite Height Placed Vertical in Turbulent Boundary Layers," *Bull. J.S.M.E.*, Vol. 24, No. 187, 1981, pp. 37–44.

Authors' Closure

The aim of this study was to make clearer the time-averaged fluid forces caused by the interference between the two circular cylinders of finite height. At present, we leave the measurements of the eddy shedding for the further experiment, so that we cannot answer correctly whether the eddy shedding was suppressed for all arrangements tested.

In this experiment, we got two values of the pressure on the back surface of the monitor cylinder, which were caused by the bistable jet switch in case of the side-by-side arrangement when $s/d=1.2$. The coefficients C_D and C_L in Figs. 13~16 were computed by the lower pressure distributions. These values formed the continuous curves, as seen in these figures. The higher values of C_D and C_L were 0.72 and 0.22, respectively. However, similar gap flow in the other arrangements were not measured by Betz type manometer used in this experiment.

Appended Fig. 1 shows the back pressure coefficients $-c_{pb}$ at the height of the two cylinders $y/h=0.44$ and the overall drag coefficients C_D of the upstream cylinder in the tandem arrangement. Each curve has its maximum value at $s/d=1.35$-1.5 and rapidly decreases as s/d increases, and then becomes almost constant over $s/d=2.0$. However, we cannot find the discontinuous jump in C_D which has always occurred in a two dimensional case.

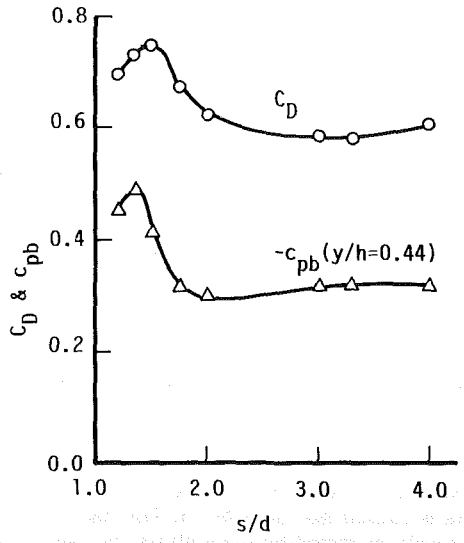

Appended Fig. 1 C_D and c_{pb} of the upstream cylinder

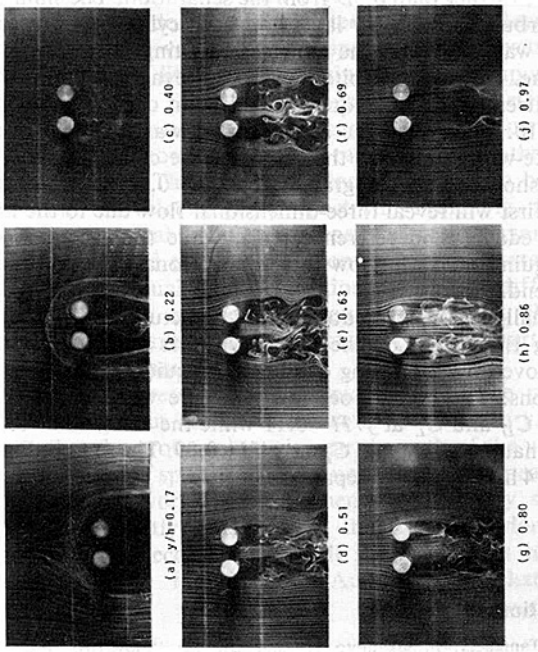

Appended Fig. 2 Flow patterns around two cylinders in side-by-side arrangement. $d=10$ mm, $h/d=3.5$, $s/d=2.0$

We didn't investigate the effects of Reynolds number on the flow around the two cylinders. Figure 10 visualized the flow patterns around the two cylinders when the wire element was set horizontally at the height $y/h=0.5$. The flow patterns around a three dimensional body such as two cylinders cited in this study are markedly different along its height. Therefore it is very important to investigate the variation of the flow patterns with respect to the height of the body. From this point of view, we present some photographs at the several heights of the two cylinders in the side-by-side arrangement in Appended Fig. 2 and the surface flow patterns in the various arrangements in Appended Fig. 3, respectively.

The three dimensionality of the flow around the two cylinders causes the different pressure distributions along the height of the two cylinders, as seen in Fig. 6. We can roughly

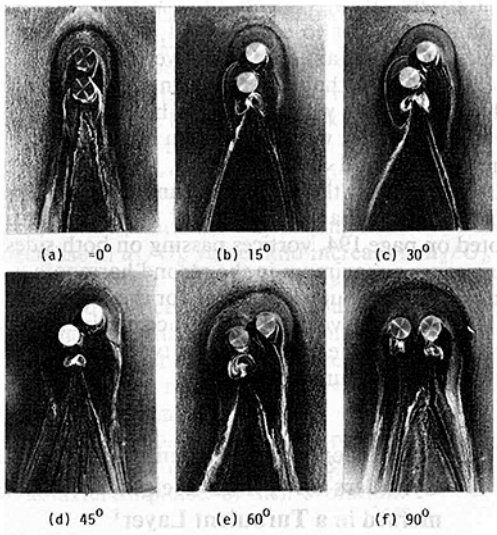

Appended Fig. 3 Surface flow patterns around two cylinders in various arrangements. $s/d=1.5$, $U_0=16$ m/s

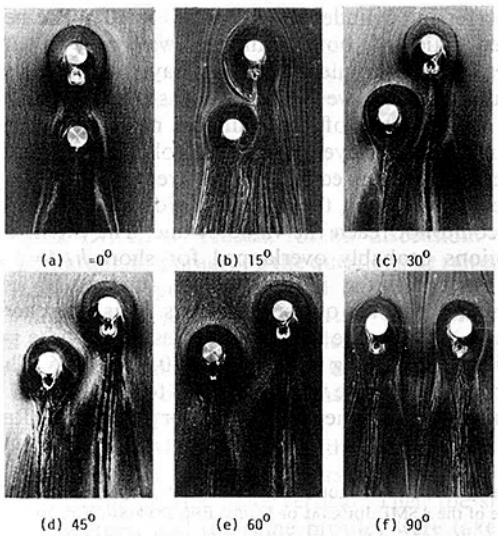

Appended Fig. 3 (cont.) $s/d=4.0$, $U_0=16$ m/s

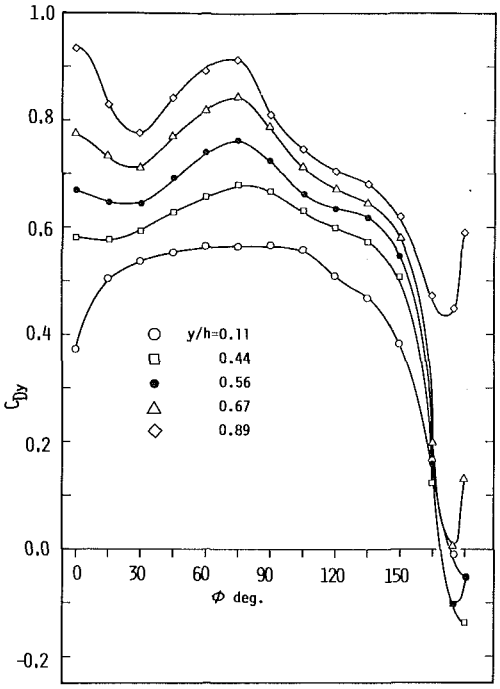

Appended Fig. 4 Local drag coefficient, $s/d = 2.0$

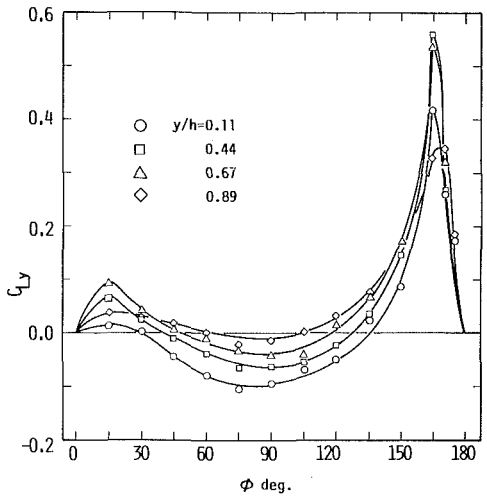

Appended Fig. 5 Local lift coefficient $s/d = 2.0$

estimate the trend of the variations in the local coefficient C_{Dy} and C_{Ly} from these pressure distributions. Appended Figs. 4, 5 show the local drag coefficient C_{Dy} and the local lift coefficient C_{Ly} at several heights of the two cylinders in case of $s/d = 2.0$. It can be noticed the whole trends of these coefficients are almost similar to one another.